# AN OVERVIEW OF CATALYTIC FUEL PROCESSING FOR HYDROGEN PRODUCTION AND FUEL CELL APPLICATIONS

*Chunshan Song**

Clean Fuels and Catalysis Program, The Energy Institute, and
Department of Energy & Geo-Environmental Engineering
The Pennsylvania State University, University Park, PA 16802
*E-mail: csong@psu.edu; Fax: 814-865-3248

This paper presents a brief overview of the recent trends for hydrogen energy development, methods of hydrogen production, and fuel processing for hydrogen and fuel cell applications. A brief discussion will be made on the major problems and challenges in energy utilization in 21st century, and the advantages of hydrogen energy development, followed by the principles of hydrogen production processes.

Table 1 shows the worldwide use of various energy sources, world population, per capita energy consumption and $CO_2$ emissions in the 20th century (from 1900 to 2001) estimated based on published data (SAUS. 1998; Flavin and Dunn 1999; USBC. 1999; NCFHS, 2003; SAUS 2004; Keeling and Whorf, 2004). The 20th century is characterized by the tremendous growth with respect to consumption of all energy resources including coal, petroleum, natural gas, and nuclear energy. Coal has played a key role as a primary source of organic chemical feedstocks in the world till 1950s, and maintained its large share as a primary energy source in the 20th century. Although the percentage contribution of coal decreased from 55% in 1900 to 24% in 2001, the amount of coal consumption in 2001 has increased to 478%, and the per capita energy use has risen to 315% of the world's 1900 levels, as can be seen from Table 1.

Figure 1 presents a personal vision for energy and fuels research, which was developed by the author for developing and directing the clean fuels and catalysis research at the Pennsylvania State University in the past decade (modified from Song 2002).

Related to Figure 1 is a long-term consideration that hydrogen energy and fuel cells have great potential to decouple the link between energy utilization and environmental pollution in the future.

Table 2 shows the principal energy sources, hydrogen atom sources, and reaction processes for production of molecular hydrogen (Song, 2003). The principle and advantages of different types of fuel cells will be briefly mentioned. Then the discussions will focus on fuel processing for applications in both high-temperature fuel cells (SOFC, MCFC) and low-temperature fuel cells (PEMFC and PAFC). Hydrocarbon fuels and alcohol fuels can both be used as fuels for reforming on-site or on-board. Alcohol fuels can be reformed at lower temperatures, but hydrocarbon fuels have the advantages of existing infrastructure of production and distribution.

Figure 2 shows the concepts and steps for catalytic fuel processing of gaseous, liquid and solid fuels for high-temperature and low-temperature fuel cell applications (Song, 2002). Further research and development is necessary on fuel processing for improved energy efficiency and reduced size of fuel processor.

Catalysis and adsorption play a major role in many of the processes related to hydrogen production and fuel processing for fuel cell applications. More effective ways of deep removal of sulfur before or after fuel reforming, and more energy-efficient and stable catalysts and processes for reforming hydrocarbon fuels are necessary for both high- and low-temperature fuel cells. In addition, more active and robust catalysts for water-gas-shift, more selective and active catalysts for preferential CO oxidation at lower temperature, more CO-tolerant anode catalysts would contribute significantly to development and implementation of low-temperature fuel cells, particularly proton-exchange membrane fuel cells.

**Table 1. Worldwide energy use, population and per capita consumption in 20th century**

| Energy Source | 1900 Use (Million tons of oil equivalent)[1,2] | 1900 Distn Percentage (%) or Unit | 2001 Use (Million tons of oil equivalent)[2,3] | 2001 Distn Percentage (%) or Unit |
|---|---|---|---|---|
| Coal | 501 | *55* | 2,395 | 24 |
| Petroleum | 18 | 2 | 3,913 | 39 |
| Natural gas | 9 | 1 | 2,328 | 23 |
| Nuclear | 0 | 0 | 662 | 6 |
| Renewables[4] | 383 | 42 | 750 | 8 |
| **Total** | **911** | **100 %** | **10,048** | **100 %** |
| Population[1,2] | 1,762 | million | 6,153 | million |
| Per Capita E Use | 0.517 | TOE | 1.633 | TOE |
| Global $CO_2$ emission[2,3] | 534 | MMTCE | 6,607 | MMTCE |
| Per capita $CO_2$ emission | 0.30 | MTCE | 1.07 | MTCE |
| Atmospheric $CO_2$[5] | 295 | ppmV | 371 | ppmV |
| Life expectancy[6] | 47.3 | Years | 77.2 | Years |

1) Source for energy in 1900: C. Flavin and S. Dunn of Worldwatch Institute [Flavin and Dunn, 1999]. 2) Sources: 2001 data from Statistical Abstract of the United States 2003 (SAUS 2004); 1900 population and $CO_2$ data from U.S. Census Bureau-Historical Estimates of World Population from different sources for years up to 1950 (USBC, 1999). 3) Sources for 2001 $CO_2$ data: International Energy Annual 2002 (EIA/IEA 2004). 4) Including hydroelectric power, biomass, geothermal, solar and wind energy. 5) Carbon Dioxide Information Analysis Centre (Keeling and Whorf, 2004). 6) Data for the US from National Center for Health Statistics (NCFHS, 2003).

**Table 2**. **Principal energy sources, hydrogen atom sources, and reaction processes for production of molecular hydrogen**

| Hydrogen Source | Energy Source | Reaction Process |
|---|---|---|
| **Fossil Hydrocarbons** | **Primary** | **Existing Processes** |
| Natural gas | Fossil energy | Steam reforming and water-gas-shift* |
| Petroleum | Biomass | Partial oxidation, Autothermal reforming* |
| Coal | Organic Waste | Dehydrocyclization or naphtha reforming* |
| Tar Sands, Oil Shale, | Nuclear energy | Gasification* |
| Natural Gas Hydrate | Solar-thermal | Decomposition, dehydrogenation, coking* |
| **Biomass** | Photovoltaic | Electrolysis* |
| **Water (H2O)** | Hydropower | **Emerging Processes** |
| Organic/Animal Waste | Wind, Wave, Geothermal | Plasma Reforming |
| **Synthetic Clean Fuels** | **Secondary** | Photocatalytic; Solar-thermal |
| MeOH, EtOH, FT-HCs | Electricity | Membrane reactors; Ion-conducting membranes |
| Organic Chemicals | Hydrogen | Thermochemical cycling |
| Metal hydride | Special Cases | Biological; Bio-inspired process |
| Hydrogen sulfide | Metal bonding | Electrocatalytic |
| Ammonia | Chemical bonding | Hydrolysis |
| Others | Others | Others |

Note: current processes that produces hydrogen as main product or by-product in commercial processes are denoted by * mark.

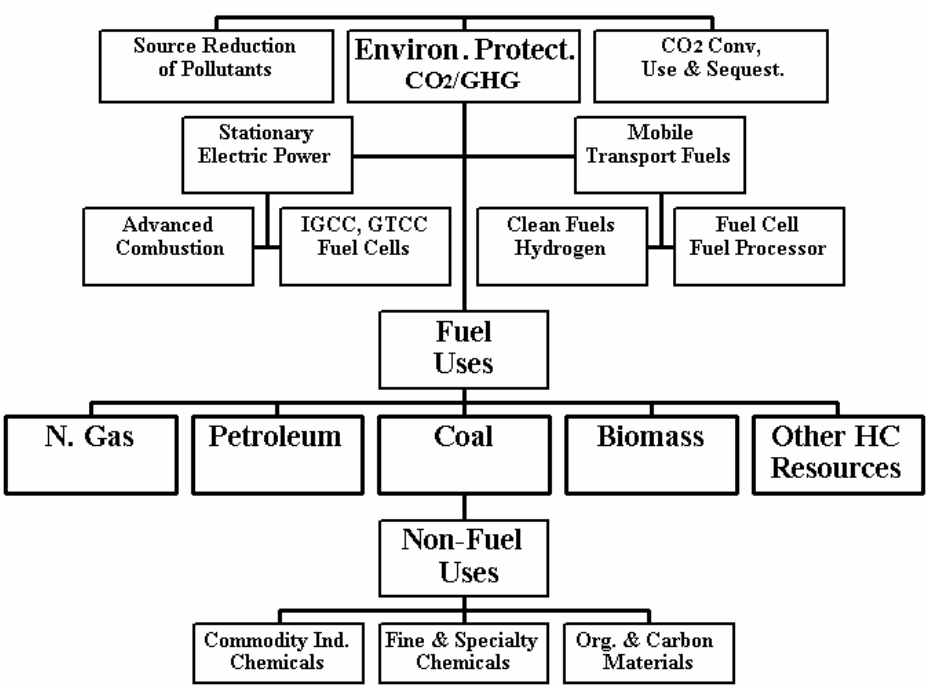


**Figure 1**. A personal vision for energy chemical and catalytic research involving clean fuels, chemicals, and organic materials (Song, 2002, 2003).

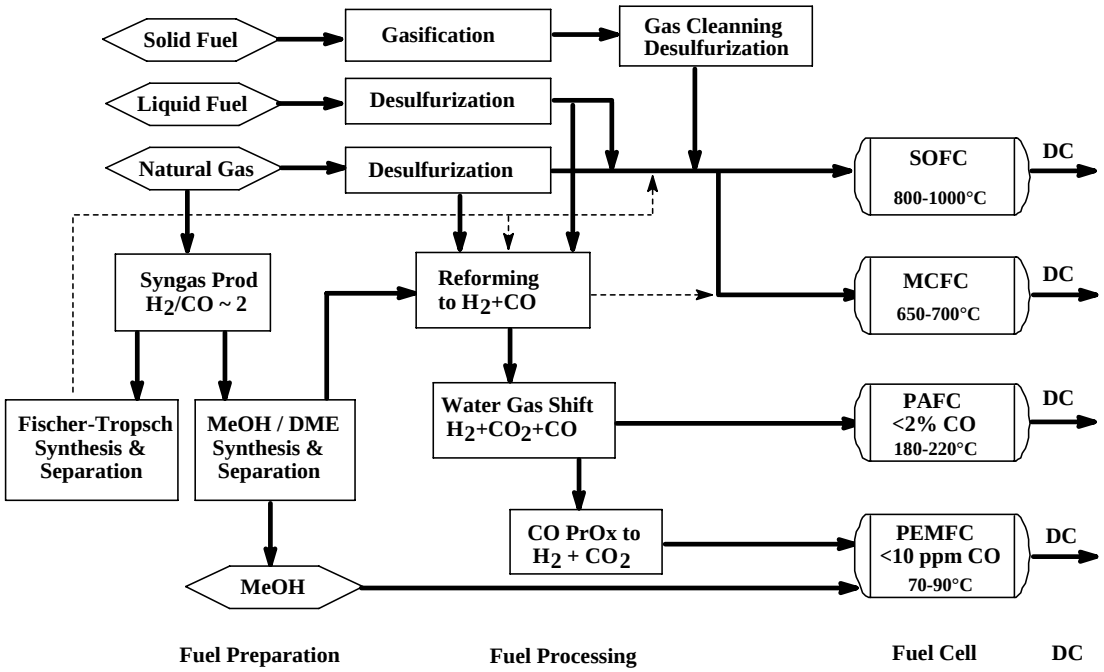


**Figure 2.** The concepts and steps for fuel processing of gaseous, liquid and solid fuels for high-temperature and low-temperature fuel cell applications (Song, 2002).

On-going work in our laboratory will be briefly discussed on selective adsorption for removing sulfur from hydrocarbon fuels (Ma et al., 2002; Velu et al., 2003), on catalytic reforming of liquid fuels at lower temperatures (Strohm et al., 2003; Shen et al., 2002), oxygen-assisted water-gas shift for CO removal (Bickford et al., 2004), $H_2S$ removal after reforming (Novochinskii et al., 2004), and $CO_2$ separation for $H_2$ production (Xu et al., 2002, 2003).

**Acknowledgement.** The author gratefully acknowledges the US Department of Energy, US Department of Defense, US Air Force Office of Scientific Research, and US Environmental Protection Agency for supporting various research projects in our laboratory related to hydrogen and synthesis gas production and fuel processing for fuel cells. The author also wishes to thank his current and former coworkers at Penn State, particularly X. Ma, S. Velu, J. Strohm, X. Xu, I. Novochinskii, J. Shen, W. Pan, J. Zheng, W. Gu, E. Bickford, S. Watanabe, J. Clemons, and A. Glass and his collaborators at Air Products and Chemicals (J. Armor), Engelhard Corporation (R. Farrauto, J. Lampert, L. Shore); Conoco Phillips (E. Esen, J. Allison), and Altex Technology(M. Namazian and S. Sethuraman).

## References

Bickford E S, Velu S, Song C (2004) Nano-Structured $CeO_2$ Supported Cu-Pd Bimetallic Catalysts for the Oxygen-Assisted Water-Gas-Shift Reaction. Catalysis Today, 2004, in press.

Flavin C, Dunn S (1999) in "State of the World 1999", A Worldwatch Institute Report, Norton and Company, New York, p. 22.

Keeling C D, Whorf T P (2004) Atmospheric $CO_2$ records from sites in the SIO air sampling network. In Trends: A Compendium of Data on Global Change. Carbon Dioxide Information Analysis Centre, Oak Ridge National Laboratory, Oak Ridge, TN, USA.

Ma X, Sun L, Song C (2002) A new approach to deep desulfurization of gasoline, diesel fuel and jet fuel by selective adsorption for ultra-clean fuels and for fuel cell applications. Catalysis Today, 77, 107-116.

Ma X, Velu S, Kim J H, Song C (2004) Deep Desulfurization of gasoline by selective adsorption over solid adsorbents and impact of analytical methods on PPM-level sulfur quantification for fuel cell applications. Applied Catalysis B: Environmental, 2004, in press.

NCHS (2003) Life expectancy at birth, United States selected years 1900-2001. National Center for Health Statistics, Center for Disease Control and Prevention, U.S. Department of health and Human Services, Hyattsville, MD, 2003.

Novochinskii I, Song C, Ma X, Liu X, Shore L, Lambert J, Farrauto R J (2004) Low-temperature $H_2S$ removal from steam-containing gas mixtures with ZnO for fuel cell application. 1. ZnO particles and extrudates. Energy & Fuels, 18 (2), 576-583.

Novochinskii I, Song C, Ma X, Liu X, Shore L, Lambert J, Farrauto R J (2004) Low-temperature $H_2S$ removal from steam-containing gas mixtures with ZnO for fuel cell application. 2. Wash-coated Monolith. Energy & Fuels, 18 (2), 584-589.

SAUS (1998) Statistical Abstract of the United States 1998. Bureau of Census, U.S., Washington DC

SAUS (2004) Statistical Abstract of the United States 2003. Bureau of Census, U.S., Washington DC

Shen J P, Song C (2002) Influence of preparation method on performance of Cu/Zn-based catalysts for low–temperature steam reforming and oxidative steam reforming of methanol for $H_2$ production for fuel cells. Catalysis Today, 77, 89-98

Song C (2002) Fuel processing for low-temperature and high-temperature fuel cells. Challenges, and Opportunities for Sustainable Development in the 21st Century. Catalysis Today, 77, 17-50.

Song C (2003) An overview of new approaches to deep desulfurization for ultra-clean gasoline, diesel and jet fuel. Catalysis Today, 86, 211-263.

Song C, Ma X (2003) New design approaches to ultra-clean diesel fuels by deep desulfurization and deep dearomatization. Applied Catalysis B: Environmental, 41 (1-2), 207-238

Velu, S., Song C, Ma X (2003) Selective adsorption for removing sulfur from jet fuel over zeolite-based adsorbents. Industrial and Engineering Chemistry Research, 42, 5293-5304

USBC (1999) Historical estimates of world population. U.S. Bureau of Census, U.S. Department of Commerce

Xu X, Song C, Andresen J M, Miller B G, Scaroni A W (2002) Novel polyethyleneimine-modified mesoporous molecular Sieve of MCM-41 Type as Adsorbent for $CO_2$ Capture. Energy & Fuels, 16, 1463-1469

Xu X, Song C, Andresen J M, Miller B G, Scaroni A W (2003) Preparation and characterization of novel $CO_2$ "molecular basket" adsorbents based on polymer-modified mesoporous molecular sieve MCM-41. Microporous and Mesoporous Materials, 62, 29-45

# DIRECT CRACKING OF METHANE USING AN AUTO-CATALYTICALLY REDUCED NICKEL CATALYST

*Richard A. Couttenye,[a] Marianela Hoz De Vila[a]*
*Steven L. Suib [a,b,c]*

[a] Department of Chemical Engineering, [b] Institute of Material Science, and [c] Department of Chemistry, University of Connecticut, Storrs, CT 06269

## Introduction

The search for alternative energy sources has been propelled by the reduction of petroleum reserves around the world, and by pollution caused by the increase in energy consumption. Compared to other options, e.g.: solar, the use of hydrogen ($H_2$) to satisfy the future energy demand emerges as an attractive choice.

Direct cracking of methane over supported metal catalysts (Ni-Co-Cu), produces very pure $H_2$ without the formation of carbon oxides. Nickel nitrate has been the preferred source of nickel for direct cracking of methane. The thermal decomposition of nickel nitrate (T > 400$^o$C) produced nickel oxide (NiO). In order to reduce the nickel from oxide to nickel metal, pretreatment of the catalysts was required (using $H_2$ at high temperature (> 500$^o$C) for at least 2 h). In contrast, thermal decomposition (T>300$^o$C) of nickel acetate ($Ni(CH_3COO)_2.4H_2O$) produced a mixture of $Ni^o$ and NiO.

The present investigation evaluated the application of the $Ni^o$/NiO mixture obtained after thermal decomposition of nickel acetate, for CO-free hydrogen production by means of direct cracking of methane, using $SiO_2$ as catalyst support. The relationship between nickel oxide (NiO) mean crystallite sizes and catalyst deactivation due to carbon deposition, was also studied.

## Experimental

**Catalyst preparation.** Nickel catalyst supported on $SiO_2$ (Davisil 35-60 mesh, grade 646, type 150 A, Fisher) was prepared by conventional wet-impregnation with a nominal metal loading of 8, and 40 wt%. 1) Nickel (II) acetate tetrahydrate ($Ni(CH_3COO)_2.4H_2O$), CAS # 6018-89-9, Aldrich Chemical company Milwaukee, WI), and 2) nickelous nitrate hexahydrate ($Ni(NO_3)_2.6H_2O$, JT Baker, Phillipsburg, NJ) were used as a source of nickel. After impregnation at room temperature, the catalysts were dried overnight at 120$^o$C, and then calcined, in air, at 600$^o$C for 2 h.

**X-ray Diffraction (XRD).** XRD data were collected using a Scintag 2000 XDS diffractometer with CuKa X-ray radiation. Powder samples were placed on aluminum slides and scanned at 4$^o$ 2θ/min. The beam voltage and beam current were 45 kV and 40 mA, respectively.

**Scanning Electron Microscopy, and Field Emission Scanning Electron Microscopy (FE-SEM).** The morphology of the catalyst, was recorded using scanning electron microscopy (SEM), and field emission scanning electron microscopy (FE-SEM). SEM micrographs were taken in an Amray 1810 microscope, and high-resolution micrographs were taken in a Zeiss DSM982 Gemini FE-SEM microscope.

**Textural Properties.** The catalyst surface areas were measured, using nitrogen physisorption at liquid nitrogen temperature with a Micrometrics ASAP 2010 System. Before the analysis samples were out-gassed at 300$^o$C under vacuum for 2 h. Surface areas were determined by nitrogen adsorption data, with Brunauer-Emmett-Teller (BET) methods.

**Catalytic activity.** The catalysts were tested for the direct cracking of methane using a gas-flow quartz tube reactor, operating at atmospheric pressure. Methane (99% [Airgas]) was fed to the reactor at 40 mL/min. Before reaction started, the catalysts prepared using $Ni(NO_3)_2.6H_2O$ were reduced with pure hydrogen at 550$^o$C, for 2 h – unless otherwise mentioned. During the reaction, the product stream was analyzed using mass spectrometry (MS) with an MKS-UTI PPT quadrupole residual gas analyzer. Methane conversion was calculated from the hydrogen concentration in the product mixture. Each experiment was performed three times using catalysts prepared in different batches (B1-B2-B3).

## Results and Discussion

**Influence of Nickel Precursor on Catalysts Surface Area and Activity**. Table 1 summarized the effect of nickel precursor on the catalyst surface area. $Ni(CH_3COO)_2.4H_2O$ was used as nickel precursor and led to materials with higher surface areas than those obtained with $Ni(NO_3)_2.6H_2O$. In addition, the amount of nickel (wt %) used had an inverse effect on the catalyst surface area – i.e.: the higher the Ni wt% the lower the surface area.

The changes in methane conversion with time during the catalytic cracking of methane at 550$^o$C, are showed in Figure 1. The activity of the catalyst prepared using nickel acetate - without reduction pretreatment (Fig.1: curve - 2), was very close to the activity obtained with the catalysts prepared using nickel nitrate – pre-reduced with $H_2$ at 550$^o$C for 2 h (Fig. 1: curve – 1). Additionally, the methane conversion data for the unreduced SNi1 catalyst were also included in Figure 1. Clearly, the conversion of methane using this non-treated catalyst (Fig.1-3) was lower than the one obtained with the pre-reduced SNi1 (Fig.1-1). This difference in activity illustrated the reduction effect on the catalysts prepared from the nitrate salt, and the advantage of using nickel acetate as a precursor (reduction free).

**Table 1. Effect of Nickel Precursor and Support on Catalysts Surface Area.**

| Catalyst | Nickel precursor | Nickel wt% | BET surface area, $m^2g^{-1}$ | | |
|---|---|---|---|---|---|
| | | | B1 | B2 | B3 |
| SNi1 | $Ni(NO_3)_2.6H_2O$ | 40 | 179 | 170 | 173 |
| SNi2 | $Ni(CH_3COO)_2.4H_2O$ | 40 | 250 | 230 | 256 |
| SNi3 | $Ni(NO_3)_2.6H_2O$ | 8 | 274 | 278 | 266 |
| SNi4 | $Ni(CH_3COO)_2.4H_2O$ | 8 | 286 | 295 | 281 |

**XRD Characterization.** Decomposition of nickel (II) acetate tetrahydrate in air at 600$^o$C for 2 h resulted in the formation of a mixture of $Ni^o$/NiO as indicated by the XRD pattern ($Ni^o$: 2θ =43.7$^o$, 51.1$^o$, 75.6$^o$, NiO: 2θ = 36.4$^o$, 42.5$^o$, 62.0$^o$, 78.6$^o$). On the other hand, thermal decomposition of nickelous nitrate hexahydrate in air at 600$^o$C for 2 h resulted in the formation of NiO (NiO: 2θ = 36.4$^o$, 42.5$^o$, 62.0$^o$, 78.6$^o$). However, when the nickel precursors (acetate, nitrate) were impregnated on $SiO_2$, and calcined in air at 600$^o$C for 2h, the main product obtained was NiO regardless of the nickel wt%.

**Effect of Nickel Oxide (NiO) Mean Crystallite Size on Catalyst Carbon Yield (gC/gNi).** The mean crystallite size of NiO was estimated using the Sherrer equation based on half-width of the diffraction peaks assigned to [200], and [111] NiO. Figure 2 shows the effect of NiO mean crystallite size on the carbon yield of the catalysts. For instance, in the case of type 2 catalysts, as the crystallite size increased the carbon yield of the catalysts also increased (see Fig. 2).

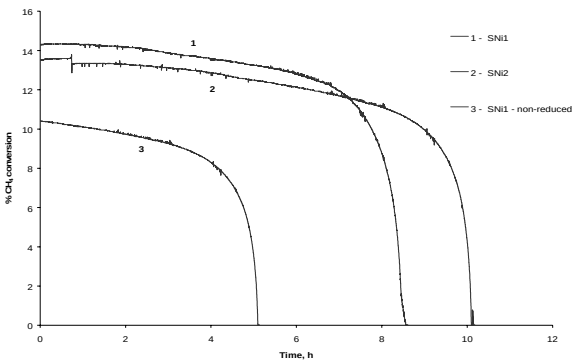


**Figure 1.** Changes in methane conversion during methane decomposition using B1 nickel catalysts. Experimental conditions: Temperature = 550$^{o}$C, Pressure = 1 atm, and Flow rate = 40 mlmin-1

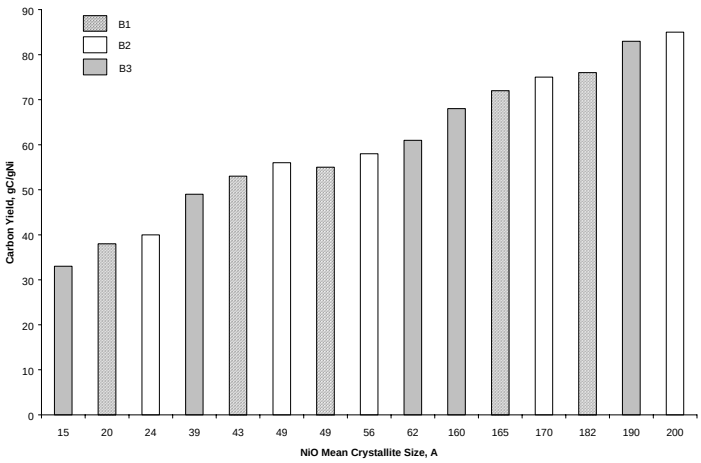


**Figure 2.** Effect of NiO mean crystallite size on the catalysts carbon yield

## Conclusions

1) For the first time, the Ni$^{o}$/NiO mixture obtained by thermal decomposition of nickel acetate has been successfully used for catalytic cracking of methane to produce CO-free hydrogen suitable for hydrogen fuel cells. The use of nickel acetate as a nickel precursor, for the preparation of the catalysts, saves not only hydrogen (our product of interest) but also time, and energy by eliminating the pretreatment step (i.e. using $H_2$ at high temperature (>500$^{o}$C) for at least 2 h).

2) The use of nickel acetate as the catalysts nickel precursor led to materials with a higher surface area than those obtained when nickel nitrate were used.

3) For catalyst supported on SiO2 (sa. ~ 200 – 300 m2g-1), the carbon yield (gC/gNi) attained during methane decomposition increased with an increase in the catalysts NiO mean crystallite size.

**Acknowledgement.** The authors are grateful to the Connecticut Global Fuel Cell Center and the US-Army for financial support.

## References

(1) J. Armor, Appl. Catal. Gen. **1999,** 76, 159.
(2) R. Cortright, R. Davda, J. Dumesic, Nature, **2002,** 418, 964.
(3) T. Zhang, M. Amiridis, Appl. Catal. Gen. **1998** , 167, 161.
(4) R. Aiello, J. Fiscus, H. Loye, M. Amiridis, Appl. Catal. Gen. **2000,** 192, 227.
(5) A. Diks, J. Power. Sourc. **1996**, 61, 113.
(6) M.Matsukata , T. Matsushita, K. Ueyama, Chem. Eng. Sci. **1996,** 51, 2769.
(7) M. Ermakova, D. Ermakov, G. Kuvshinov, L. Plyasova, J. Catal. **1999,** 187, 77.
(8) J.-W. Snoeck, G. Froment, M. Fowles, J. Catal. **1997,** 169, 240.
(9) S. Takenaka, S. Kobayashi, H. Ogihara, K. Otsuka, J. Catal. **2003,** 217, 79.
(10) S. Takenaka, Y. Shigeta, E. Tanabe, K. Otsuka, J. Catal. **2003,** 220, 468
(11) V. Choudhary, S. Banerjee, A. Rajput, J. Catal. **2001,** 198, 136.
(12) V. Choudhary , S. Banerjee, A. Rajput Appl. Catal. Gen. **2002,** 234, 259.
(13) T. Choudhary, C. Sivadinarayana, C. Chusuei, A. Klinghoffer, D. Goodman, J. Catal. **2001,** 199, 9
(14) P. Gronchi, P. Kaddouri, P. Centola, R. Del Rosso, J. Sol-Gel. Sci. Tech. **2003,** 26, 843.
(15) V. Recupero, L. Pino, R. Di Leonardo, M. Lagana, G. Maggio, J. Power. Sourc. **1998,** 71, 208.
(16) A. Da Silva, M. De Moura, L. Mercuri, A. Santo, J. Matos, An. Assoc. Bras. Quim. **1998,** 47, 133.
(17) M. Elmasry, A. Gaber, E. Khater, J. Therm. Anal. Cal. **1996,** 47, 757.
(18) G. Hussein, A. Nohman, K. Attyia, J. Therm. Anal. Cal. **1994,** 42, 1155.
(19) M. Mohamed, S. Halawy, M. Ebrahim, J. Anal. Appl. Pyrol. **1993,** 27 109.
(20) A. Gadalla, H. Yu, Thermochim. Acta. **1990,** 164, 21.
(21) A. Galwey, S. McKee, T. Mitchell, M. Brown, A. Bean, React. Solid. **1988,** 6, 173.
(22) W. Pease, R. Segall, R. Smart, P. Turner, J. Chem. Soc. Faraday Trans. **1986,** 82 747.
(23) J. Doremieux, Compt. Rend. **1965,** 261, 4426.
(24) J. Leicester, M. Redman, J. Appl. Chem. **1962,** 12, 357.
(25) C. Louis, Z. Cheng, M. Che, J. Phys. Chem. **1993,** 97, 5703

# CERIA BASED NANOSIZED WATER-GAS SHIFT CATALYSTS FOR FUEL CELL APPLICATIONS

*Ranjan K. Pati[1], Ivan C. Lee[2], Deryn Chu[2], Sicong Hou[1], Osifo Akhuemonkhan[1] and Sheryl H. Ehrman[1]*

[1]Department of Chemical Engineering, University of Maryland, College Park, MD 20770
[2]Sensors and Electron Devices Directorate, US Army Research Lab, Adelphi, MD 20783

**Abstract**

This paper describes our research efforts towards the preparation of high surface area ceria containing catalysts for fuel cell applications. In the present work, we present a simple, single step flame synthesis method to prepare high surface area ceria based water gas shift (WGS) catalyst using aqueous solutions of metal acetate precursors. The specific surface areas of the synthesized powders are in the range of 130 and 163 $m^2/g$. High-resolution transmission electron microscopic (TEM) characterization showed that the particle sizes for the ceria materials are in the range of 3 and 10 nm. X-ray diffraction (XRD) and X-ray photoelectron spectra show the presence of transition metal oxide in the as prepared catalysts.

**Keywords**

Flame synthesis; WGS catalysts; transition metal supported ceria; TEM; XPS

**Introduction**

Cerium oxide ($CeO_2$) / ceria is an important inorganic material having the cubic fluorite type crystal structure (1). Ceria either in the pure form or doped with other metals (Cu, Ni, etc) / metal ions ($Mg^{2+}$, $La^{2+}$, $Sc^{2+}$, $Gd^{3+}$, $Y^{3+}$, $Zr^{4+}$ etc.), potentially has a wide range of vast applications including gas sensors (2), electrode materials for solid oxide fuel cells (3, 4) oxygen pumps, amperometric oxygen monitors and three way catalytic supports for automobile exhaust gas treatment (5,6).

In recent years, nanocrystalline particles have attracted much attention because of their improved physical and chemical properties compared to those of bulk materials. Various solution-based techniques have been used for the preparation of pure ceria and transition metals, rare earth metals, or metal ions doped ceria materials, including coprecipitation (7, 8), hydrothermal (9-11), microemusion (12, 13), sol-gel (14), solution combustion (15) and electrochemical methods (16). In addition, solid-state reaction, mechano-chemical methods, chemical vapor deposition (CVD), sputtering have also been used to make ceria-based materials (17-19). These methods are either multi step and time-consuming (e.g. solution based techniques) or control of the product composition may be difficult (e.g. CVD).

In the present paper we report a single step alternative route for synthesizing $CeO_2$ based nanoparticles. The process involves the pyrolysis of aqueous solutions of the metal acetate without addition of any extra fuel in a methane oxygen flame.

**Experimental**

The precursors used were cerium acetate as the cerium source.The transition metal salts used were copper as the copper source, nickel acetate, iron acetate, manganese acetate, cobalt acetate, chromium nitrate, and rhodium acetate. The precursors were dissolved in deionized water to make 0.3 M solutions of each. For the transition metal supported ceria, a series of solutions have been prepared starting from 5, 10, 20, 30 and 40 mole % of transition metal in ceria. The solutions were filtered through a membrane filter before filling the nebulizer (Gemini Scientific Corporatation, Inc.). Liquid precursor feed was then atomized with compressed air resulting in a fine spray. In the reactor the flame was made by methane, oxygen and nitrogen. The flow rate for each gas was methane 0.9 l/min, oxygen 1.81 l/min and nitrogen 2.75 l/min. The flow rate of the precursor solution into the flame was 0.5ml/min. After burning the fine spray, the particles were collected on a water-cooled surface by thermophoresis, which was kept on the top of the flame. The distances of the water-cooled surface from the burner and the flame were 6.5 cm and 2 cm respectively.

**Characterization**

The synthesized materials were then characterized by powder X-ray diffraction (XRD) using $CuK_\alpha$ ($\lambda$ = 1.5408Å) for the phase analysis and crystal structure determination. Thermogravimetric analysis (TGA) was used to determine the amount of unwanted materials such as water and carbononaceous compounds in the sample. Atomic bonding was analyzed using Fourier transformed infrared spectroscopy (FTIR). Brunauer, Emmett and Teller (BET) gas absorption method was applied to investigate the surface area of the sample. Transmission electron microscopy (TEM) was used for the particle size analysis and surface morphology of the material. X-ray photoelectron spectroscopy (XPS) was utilized to determining the oxidation state of the transition metal used in the ceria system.

**Results and discussion**

Thermogravimetric analysis was performed in air at a heating rate of 10ºC/min. The TGA curve for the pure ceria sample indicates that there were two stage of weight loss. The first weight loss (between 20 to 200ºC) was due the removal of water molecules, which probably come from the condensation of water molecule on the water-cooled surface. The second stage weight loss (between 300 to 600ºC) resulted from the burning and oxidation of carbon compounds (combustion by-product) likely from incomplete combustion of the metal acetate precursor, which is confirmed by FTIR. Similarly, the TGA of the as prepared $Cu/CeO_2$ showed the same weight loss behavior with the presence of more carbon in the sample.

The IR absorption bands in the region of 2800-2900 $cm^{-1}$ are typical of the C-H stretching mode of hydrocarbons. The C=O stretching band at ~1400 $cm^{-1}$ confirms the presence of unburned acetic acid in the final product.

Residual water and hydroxyl group are detected with a large band at around 3500$cm^{-1}$, corresponding to O-H stretching frequency, and a broad band at around 1600 $cm^{-1}$, due to the bending vibrations of associated water. Another species of strong bands is located at around 1000 $cm^{-1}$, which may be either associated with the formation of carbonate like species (20) or the formation of nanocrystalline $CeO_{2-x}$ (21).

The X-ray diffraction pattern of 40% Cu doped $CeO_2$ is shown in Figure 1. The diffraction lines corresponding to the fluorite type structure and the d values agree well with those expected for $CeO_2$. The peaks corresponding to Cu or CuO could not be detected even with the increase of Cu content. This suggests that metallic Cu or $Cu^{2+}/Cu^{+}$ may not be substituted for $Ce^{4+}$ in $CeO_2$. Increasing the Cu content increases the line width compared to the pure $CeO_2$ and the absence of Cu or Cu-oxide phase suggest that the metallic Cu or $Cu^{2+}$ /$Cu^{+}$ ions are dispersed on the surface of $CeO_2$. Diffraction patterns of Ni and Fe doped $CeO_2$ prepared by the flame synthesis method are similar to those of pure $CeO_2$ and Cu doped $CeO_2$.

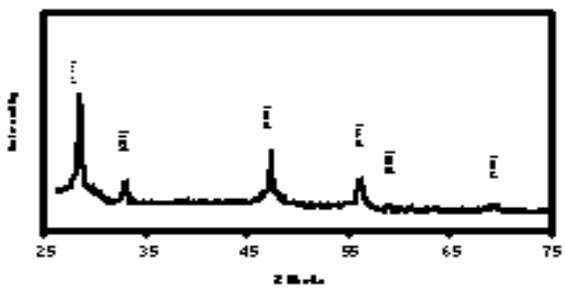


**Figure 1.** X-ray diffraction spectra of the as prepared 40% $Cu/CeO_2$ powder

The XPS of as prepared $Ni(2p_{3/2})$ shows that Ni is in the +2 oxidation state as seen from the $Ni^{2+}$ $(2p_{3/2})$ binding energy as well as the satellite peaks. The $Ni/CeO_2$ catalyst after the water-gas shift treatment shows the zero oxidation state of Ni, which indicates the reduction of $Ni^{2+}$ to Ni happens in the reducing atmosphere.

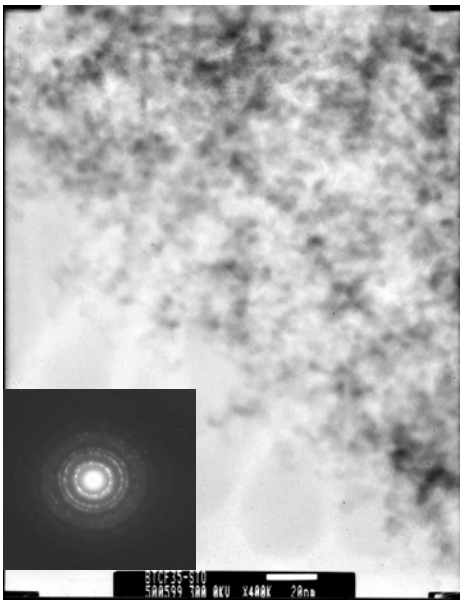

**Figure 2.** Transmission electron micrograph and the selected area electron diffraction pattern of the as prepared $Cu/CeO_2$ powder

Transmission electron microscopic image of 40%$Cu/CeO_2$ is shown in Figure 2. The particles are spherical in size with particle size in the range of 3-5 nm. The absence of big particle suggests that the precursor droplets are vaporized completely in the flame. The selected area electron diffraction (SAED) pattern is indexed to polycrystalline $CeO_2$ in the fluorite structure and no line corresponding to Cu or any of the oxides of Cu is detected. This again suggests the dispersion of $Cu^{2+}$ on the $CeO_2$ surface. A particle size and BET surface area analysis of pure ceria and $M/CeO_2$ (M=Cu, Ni, Fe) is given in Table-1.

**Table 1. Particle size and the BET surface area of the synthesized pure ceria and transition metal supported ceria**

| Material | particle size (nm) | Surface area ($m^2/g$) |
|---|---|---|
| Pure $CeO_2$ | 3-5 | 153 |
| 5% $Cu/CeO_2$ | 3-5 | 135 |
| 10% $Cu/CeO_2$ | 3-5 | 153 |
| 15% $Cu/CeO_2$ | 3-5 | 128 |
| 30% $Cu/CeO_2$ | 3-5 | - |
| 40% $Cu/CeO_2$ | 3-10 | 156 |
| 40% $Fe/CeO_2$ | - | 127 |
| 5% $Ni/CeO_2$ | 5 | 163 |

**Conclusions**

Flame synthesis is an easy, single step method for the preparation of pure $CeO_2$ and the transition metal doped $CeO_2$ materials starting from aqueous solution of metal salts. The process is time and possibly cost efficient compared to other wet chemical methods. From XPS it is clear that the transition metals in the $CeO_2$ are in an oxidized state and the metal ions may be on the surface of the $CeO_2$ lattice. Preliminary results show that the flame made transition metals doped $CeO_2$ powders are active for the water-gas shift reaction (22). A small amount of carbon is present in the as prepared sample, which is confirmed by TGA and FTIR. The particle sizes of the synthesized materials are in the range of 3-10 nm and the BET surface area are in the range of 127-163 $m^2/g$.

**Acknowledgements**. We thank Amy Wingfield, Jason Repac, Radhika Char for additional help in making the materials, and Dr. Bindhu Varughese for the XPS measurements. Ranjan K. Pati and Sheryl H. Ehrman would like to thank U.S. Army Research Laboratory for the financial and instrumental support.

**References**

1. M. Hirano, M. Inagaki, J. Mater. Chem., 10 (2000) 473
2. B.C.H. Steele, Solid State Ionics, 129 (2000) 95
3. T. Kubo, H. Obayasi, J.Electrochem. Soc., 122 (1975) 42
4. H. Yahiro, Y. Bab, K. Eguchi, H. Arai, J.Electrochem. Soc., 135 (1988) 2077
5. P. Fornasiero, G. Balducci, R. DiMonte, J. Kaspar, V. Sergo, G. Gubitosa, A. Ferrero, G. Maziani, J.Catal., 164 (1996) 173
6. G.R. Rao, P. Fornasiero, R. DiMonte, J. Kaspar, G. Vlaic, G. Balducci, S. Meriani, G. Gubitosa, A. Cremona, M. Graziani, J.Catal., 162 (1996) 1
7. J. Van herle, T. Horita, T. Kawada, N. Sakai, H. Yokokawa, M. Dokiya, J. Am. Ceram. Soc., 80 (1997) 933
8. K. Higashi, K. Sonoda, H. Ono, S. Sameshima, Y. Hirata, J. Mater. Res., 14 (1999) 957
9. M. Hirano, E. Kato, J. Am. Ceram. Soc., 82 (1999) 786
10. P. Shuk, M. Greenblatt, Solid State Ionics, 116 (1999) 217
11. Y.C. Zhou, M.N. Rahaman, J. Mater. Res., 8 (1993) 1680
12. A. Martinez-Arias, M. Fernandez-Garcia, V. Ballesteros, L.N. Salamanca, J.C. Conesa, C. Otero, J. Soria, Langmuir**,** 15 (1999) 4796
13. T. Masui, K. Fujiwara, Y.M. Peng, T. Sakata, K. Machida, H. Mori, G. Adachi, J. Alloys. Compd., 269 (1998) 116
14. L. Li, X. Lin, G. Li, H. Inomata, J. Mater. Res., 16 (2001) 3207
15. P. Bera, S.T. Aruna, K.C. Patil, M. S. Hegde, J.Catal., 186 (1999) 36

16. Y. Zhou, R.J. Phillips, J.A. Switzer, J. Am. Ceram. Soc., 78 (1995) 981
17. X.R. Ye, D.J. Jia, J.Q. Yu, X.Q. Xin, Z. Xue, Adv. Mater., 11 (1999) 941
18. W. Bai, K.L. Choy, N.H.J Stelzer, J. Schoonman, Solid State Ionics, 116 (1999) 225
19. M. Hasegawa, Y. Kato, M. Kagawa, Y. Syono, J.Mater. Sci. Lett., 15 (1996)1608
20. D. Terribile, A. Trovarelli, J. Llorca, C.D. Leitenburg, G. Dolcetti, J. Catal., 178 (1998) 299
21. J.Y. Ying, A. Tschöpe, The Chem. Engg. J., 64 (1996) 225
22. I.C. Lee, R.K. Pati, S.H. Ehrman, D. Chu, (Unpublished work).

# HYDROGEN PRODUCTION VIA THE HIGH-TEMPERATURE WATER-GAS SHIFT REACTION OVER CHROMIUM-FREE IRON-BASED CATALYSTS

*Sittichai Natesakhawat, Lingzhi Zhang, Xueqin Wang, and Umit S. Ozkan*

Department of Chemical and Biomolecular Engineering
The Ohio State University
Columbus, OH 43210

## Introduction

Hydrogen generation technologies have become increasingly important due to recent attention focusing on fuel cells. The water-gas shift reaction, which is performed in two stages as high- and low-temperature shift, is of central significance to produce high-purity hydrogen. Generally, the high-temperature water-gas shift reaction (HTS) is conducted on Fe-Cr catalysts. However, these catalytic systems possess many drawbacks such as low activity at low temperatures, sintering of magnetite ($Fe_3O_4$), and a pyrophoric nature. Moreover, the use of Cr poses additional complications due to harmful effects of $Cr^{6+}$ on human health. Thus, development of chromium-free catalytic systems is necessary. Also, it is apparent that innovative chromium-free iron-based catalysts that can overcome those drawbacks would have a significant impact on widespread applications of fuel cell systems. Araujo and Rangel[1] investigated the catalytic performance of Al-doped Fe-based catalyst with small amounts of copper (%wt Cu ≈ 3) in the HTS reaction. The aluminum and copper-doped catalysts showed similar catalytic activity compared to a commercial Fe-Cr catalyst at 350 $^oC$ and $H_2O/CO = 0.4$. Costa et al.[2] examined the use of thorium instead of chromium in iron- and copper-based catalysts for the HTS reaction. It was found that thorium and copper-doped catalyst was more active than a commercial Fe-Cr catalyst at $H_2O/CO = 0.6$ and 370 $^oC$, possibly due to an increase in surface area by thorium.

In this work, various chromium-free iron-based catalysts promoted with first row transition metals have been synthesized and studied for the HTS reaction. The effect of synthesis variables on physical, chemical, and structural properties and, in turn, on catalyst performance has been examined.

## Experimental

**Catalyst preparation.** Catalysts were prepared using a coprecipitation method. All metal precursors (Aldrich) used were in nitrate form. Ammonium hydroxide (29.63 vol%, Fisher Scientific) was used as the precipitating agent. Initially, 0.5 M aqueous solutions of metal nitrates were prepared and mixed in a beaker in appropriate proportion to keep the Fe/promoter molar ratio constant at 10. $NH_4OH$ was subsequently added drop-wise to the mixed solution until the final pH was 9. The resulting dark brown solution was stirred vigorously for an additional 30 min. The precipitate was washed with demineralized distilled water and filtered several times to remove ammonium ions. The remaining solid was then dried overnight in an oven at 110 $^oC$. The dry samples were ground to a fine powder and were calcined under air at 450 $^oC$ (ramp rate = 2.5 $^oC$/min) for 4 h. For catalysts promoted with first-row transition metals, they were synthesized by a coprecipitation-impregnation method. Before drying, the precipitate obtained after washing was further impregnated with a calculated amount of 0.5 M aqueous solution of the first row transition metal and stirred for 30 min.

**Catalyst characterization.** BET surface areas of freshly calcined catalysts were measured by $N_2$ adsorption-desorption at 77 K using a Micromeritics ASAP 2010 instrument. Pore size distributions were also calculated from the desorption isotherms using the BJH method. *In situ* X-ray diffraction (XRD) during reduction under 5% $H_2/N_2$ of the catalysts pre-calcined at 450 $^oC$ was performed using a Bruker D8 Advance X-ray diffractometer equipped with atmosphere and temperature control stage and using Cu $K_\alpha$ radiation operated at 40 kV and 50 mA.

Temperature-programmed reduction (TPR) of catalysts was conducted using a laboratory-made gas flow system with 10% $H_2$/Ar (40 $cm^3$/min) as a reducing agent. The temperature of the catalysts was raised using a ramp rate of 10 $^oC$/min to 950 $^oC$ and held for 30 min. $H_2$ consumption was measured using a thermal conductivity detector (TCD) connected to a data-acquisition computer. X-ray photoelectron spectroscopy (XPS) of catalysts was performed with an AXIS Ultra XPS spectrometer with an Al anode operated at 14 kV and 10 mA. Spectra were corrected using the C 1s signal located at 284.5 eV. Diffuse reflectance infrared Fourier transform spectroscopy (DRIFTS) experiments were performed using a Bruker IFS66 instrument equipped with an MCT detector and a KBr beamsplitter. Prior to the collection of spectra, the catalysts were reduced *in situ* under 20% $H_2$/He at 350 $^oC$ for 2 h followed by flushing under He for 30 min.

**Reaction studies.** The steady-state reaction experiments were performed using a fixed-bed flow stainless steel reactor (1/4 in. OD). The reaction conditions were as follows: 300-400 $^oC$, $CO/H_2O/N_2$ = 1/1/8, GHSV = 3,200-9,500 $h^{-1}$. Prior to the reaction, catalysts were reduced *in situ* under 20% $H_2/N_2$ (50 $cm^3$/min) at 350 $^oC$ for 2 h. The feed and effluent were analyzed on-line using an automated Shimadzu GC-14A equipped with FID and TCD detectors. Separations were performed under Ar using 2 columns: Porapak Q (12 ft x 1/8 in. SS, 80/100 mesh) and molecular sieve 13X (5 ft x 1/8 in. SS, 60/80 mesh). The catalytic activity is defined as moles of CO converted per moles of Fe present per hour.

## Results and Discussion

It is believed that the function of chromium in commercial HTS formulations is to stabilize magnetite from sintering, thus enhancing the activity and stability of iron catalysts [3,4]. In this study, aluminum, manganese, and gallium were chosen as potential replacements for chromium. Our reaction results indicate that the presence of Mn and Ga caused a decrease in WGS activity whereas the addition of Al in Fe catalysts improved WGS activity. This suggests that Al could be a potential chromium replacement.

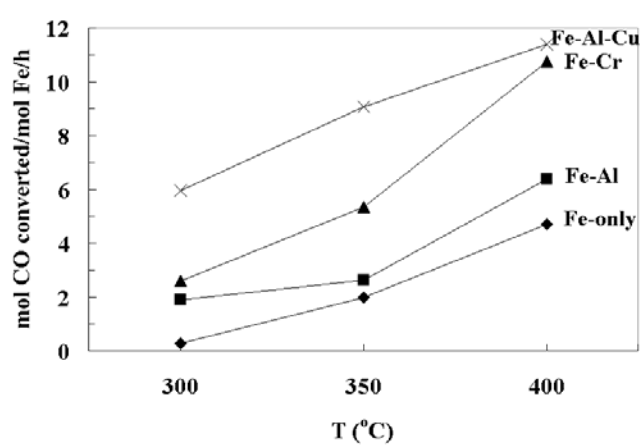


**Figure 1.** Reaction comparison of various reduced Fe-based catalysts in the HTS reaction [Reaction conditions: 300-400 $^oC$, $CO/H_2O/N_2$ = 1:1:8, GHSV = 9,500 $h^{-1}$].

As shown in **Figure 1**, although Fe-Al catalysts were not as active as Fe-Cr catalysts, the addition of Cu in Fe-Al catalysts (Fe/Cu = 20) resulted in a significant enhancement of WGS activity. More importantly, Fe-Al-Cu catalysts not only matched the activity of Fe-Cr catalysts, but surpassed them. In addition, the beneficial effect of Cu promotion is much more pronounced at lower temperatures. This indicates that formulations of highly active and chromium-free iron-based catalysts can be achieved by adding both aluminum and copper.

It is noted that all promoted catalysts exhibited higher surface area (54-88 $m^2/g$) compared to Fe-only catalyst (19 $m^2/g$). The pore size corresponding to the maximum of Fe-only catalyst (24 nm) was considerably higher than that of Al- and Cr-containing samples (8 and 6 nm, respectively). This suggests that the presence of aluminum or chromium retards the growth of hematite crystallites during calcination. Moreover, *in situ* XRD during reduction indicated that the all promoted catalysts possessed smaller crystallite sizes of magnetite at the reduction temperatures ranging from 300 to 450 $^oC$.

It is conceivable that reduction behaviors of Fe-based catalysts could play a major role on catalytic performance in the HTS reaction. To further examine the change in catalyst reducibility with promotion, TPR was performed with 10% $H_2$/Ar over various pre-calcined Fe-based catalysts. A low-temperature (LT) reduction peak around 420 $^oC$ is assigned to the reduction of hematite ($Fe_2O_3$) to magnetite ($Fe_3O_4$). A broad high-temperature (HT) reduction peak is attributed to the reduction of magnetite ($Fe_3O_4$) to FeO and metallic Fe. The addition of Cr or Al helps stabilize magnetite and prevents its further reduction to inactive FeO and metallic Fe. The presence of Cu facilitates the formation of magnetite, leading to a significant improvement in WGS activity. An additional peak is also observed on Cr- and Cu-containing samples, possibly due to the reduction of $Cr^{6+}$ to $Cr^{3+}$ (270 $^oC$) and $Cu^{2+}$ to metallic Cu (220 $^oC$), respectively.

XPS was conducted to investigate the nature of active sites and oxidation states of species present on the catalyst surface. For all calcined catalysts, only the hematite phase (710.9 eV) was observed. After reduction at 350 $^oC$, magnetite (710.3 eV) was the major species detected. Metallic (706.3 eV) phase is clearly seen on reduced Fe-only catalysts while it was markedly suppressed on both Al- or Cr-containing catalysts. Consistent with TPR results, the addition of Al or Cr in Fe catalysts helps retard the formation of metallic Fe. Furthermore, the oxidation state of chromium after reduction was found in +3 state whereas all copper oxide was converted to a metallic copper phase. This is also consistent with our TPR peak assignments.

DRIFTS experiments of the CO+$H_2O$ TPReaction were further conducted to investigate adsorbed species during the WGS reaction and to elucidate the reaction mechanism. Our *in situ* DRIFTS results indicated that the WGS reaction over Fe-based catalysts occurs via the redox mechanism. The catalyst surface undergoes successive reduction and oxidation cycles by CO and $H_2O$ to produce $CO_2$ and $H_2$, respectively, with $Fe^{3+}$ and $Fe^{2+}$ occupying the octahedral sites in the magnetite structure constituting a redox pair. More interestingly, $CO_2$ bands grew stronger under CO flow on reduced Fe-Al-Cu catalyst after $H_2O$ exposure at 400 $^oC$ for 1 h compared to reduced Fe-only catalyst. This suggests that Cu promotes the redox cycle, thus improving the catalytic activity of iron-based catalysts.

## Conclusions

Various chromium-free iron-based catalyst were synthesized and studied in the HTS reaction at 300-400 $^oC$ and $H_2O/CO = 1$. Our reaction results have suggested that aluminum is a potential chromium replacement. Promotion with Cu of Fe-Al catalysts further enhances WGS activity significantly. Characterization results have indicated that the differences in catalytic performance could be due to changes in catalyst reducibility and magnetite crystallite growth as well as rate differences in redox steps of the WGS reaction over iron-based catalysts.

**Acknowledgement.** The financial support provided by Ohio Coal Development Office (OCDO) is gratefully acknowledged.

## References

(1) Araujo, G.C.; and Rangel, M.C. *Catal. Today*, **2000**, *62*, 201.
(2) Costa, J.L.R.; Marchetti, G.S.; and Rangel, M.C. *Catal. Today*, **2002**, *77*, 205.
(3) Ridler, D.E.; and Twigg, M.V. In *Catalyst Handbook*; Twigg, M.V., Ed.; Wolfe: London,1989 ; pp.
(4) Newsome, D.S. *Catal. Rev. -Sci. Eng.* **1980**, *21*, 275.

# HYDROGEN STORAGE AND DELIVERY BY REVERSIBLE HYDROGENATION OF LIQUID-PHASE HYDROGEN CARRIERS

*Alan C. Cooper, Larry D. Bagzis, Karen M. Campbell, Guido P. Pez*

Corporate Science and Technology Center
and Advanced Materials Division
Air Products and Chemicals, Inc.
7201 Hamilton Blvd.
Allentown, PA 18195

## Introduction

Hydrogen storage system development is a key enabling technology for the widespread introduction of hydrogen fuel cells. None of the existing technologies used for industrial hydrogen storage meet all or even most of the necessary performance criteria such as volume and gravimetric hydrogen density while providing inherent safety at a competitive price. While demonstration activity for PEM (proton exchange membrane) fuel cell applications is progressing using these and other early promising storage technologies, the performance targets required to enable hydrogen fuel cell vehicles is one of the most demanding applications with the largest potential impact. Significant work is progressing on technologies that show promise to improve storage densities by adsorption, absorption, or hydrogenation of hydrogen to various materials for storage onboard a vehicle. Novel liquid-phase hydrogen storage materials have been developed that enable the storage of hydrogen by reversible catalytic hydrogenation. Our proposed approach for hydrogen storage provides improved benefits that will be discussed.

## Discussion

**Hydrogen Storage System Approach.** The proposed reversible liquid-phase hydrogen carrier (LQH) approach, illustrated in Figure 1, provides a scenario that integrates the fuel distribution with the onboard vehicle storage technology.[1] Storage technologies being investigated, which include hydrogen stored as cryogenic liquid, compressed hydrogen, and reversible solid hydrogen sorbents, all currently fall short of the challenging benchmark expectation of consumers set by gasoline. Targets have been developed by the U. S. Department of Energy with input from the automotive companies to address these challenges.

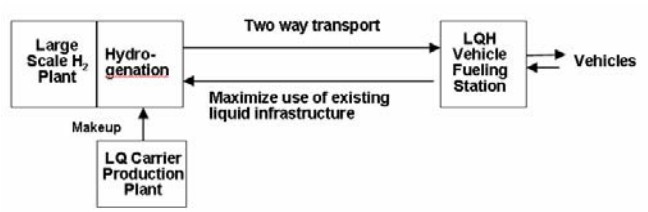


**Figure 1**. Schematic for the integrated approach of liquid-phase hydrogen carriers (LQH).

The LQH approach provides some potential benefits compared to the other storage technologies. The areas of distribution, infrastructure cost, onboard system requirements, energy efficiency, and safety will be addressed.

(1) Distribution. The liquid carrier is hydrogenated at the hydrogen production site and delivered ultimately to the fuel tank of a hydrogen powered vehicle with no intermediate transformations in the delivery chain as would be required if a reversible solid hydrogen storage technology were utilized. Because the LQH can be stored at atmospheric conditions without spontaneous evolution of hydrogen, the transfer of the liquid through pipelines, tanker trucks, or conventional liquid storage tanks is consistent with today's fuel distribution system.

(2) Infrastructure Cost. By carrying hydrogen in an atmospheric liquid, we expect this approach can utilize the existing liquid fuels infrastructure. Fueling stations will dispense a liquid fuel in the same manner they do today without requiring hydrogen production, compression, or heat exchange capabilities. Pipeline systems and tanker truck fleets can be utilized as well. While the carrier must be returned, since the fuel distribution trucking fleet currently returns empty there is available capacity at minimal incremental cost to facilitate the return. This approach has the potential for transition amongst the current fuel distribution providers as hydrogen slowly builds demand. The level of upfront speculative capital that will be required to build an infrastructure should be significantly less than gaseous and cryogenic distribution approaches.

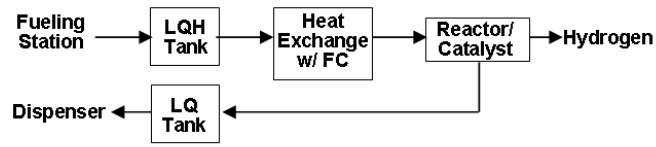


**Figure 2.** Schematic for the integration of a dehydrogenation reactor with a fuel cell onboard a vehicle. The system consists of a tank for a hydrogenated liquid (LQH), a heat exchanger to utilize waste heat from the fuel cell for the endothermic dehydrogenation, a catalyst bed, and a holding tank for the dehydrogenated liquid (LQ).

(3) Onboard System. A conformable storage tank like that used for gasoline today is expected. Current compressed hydrogen tanks for onboard storage are cylindrical or spherical in shape to contain the very high pressures. It is anticipated that conformability should allow for easier vehicle design. The volume required onboard the vehicle for hydrogen transfer, storage, and generation is only starting to be addressed by storage technology developers. Because the LQH is hydrogenated at a central location instead of onboard the vehicle like in many solid sorbent systems, the automotive system is simplified. There will be no need for heat exchange during fueling and the fueling can occur at a rate comparable to today's gasoline pumping. The LQH and dehydrogenation system are being designed to utilize waste heat from the fuel cell for hydrogen generation without supplemental heating (Figure 2). By accomplishing this, it will also significantly reduce the radiator requirement for the vehicle. The work to develop this dehydrogenation system is underway and is critical to the success of this approach.

(4) Energy Efficiency. Hydrogen powered fuel cells have the potential to provide energy advantages over today's petrochemical vehicle fuel supply. However, in order to achieve these advantages, the storage of hydrogen must also be energy efficient. As just discussed, the dehydrogenation will utilize the waste heat from the fuel cell. The hydrogenation of the liquid carrier is an exothermic process with anticipated heats of hydrogenation of -8 to -18 kcal/mol (Figure 3). In a commercial industrial hydrogenation process, some portion of this heat can be captured and utilized for economic benefit for utilization in the hydrogen production process such as for steam generation.

(5) Safety. While hydrogen can be handled safely, it requires different considerations than today's vehicle fuels that could greatly affect the acceptance and adoption rate of hydrogen vehicles. These are dominated by consumer acceptance for the fueling experience,

but also include vehicle repair and maintenance, parking considerations, and security considerations for tunnels. The LQH fueling experience, by its nature, will appear the same to the consumer as today's "one way" transfer of gasoline or diesel fuel with simultaneous transfer of two liquids. The transfer of hydrogenated liquid into the vehicle and dehydrogenated liquid off of the vehicle can happen automatically without any additional action by the consumer. The consumer will never come into contact with hydrogen gas itself nor be at risk of an equipment failure that could create an incident since the liquid carrier is an atmospheric liquid that will not spontaneously generate gaseous hydrogen. The onboard system is expected to generate hydrogen on demand, so the vehicle repair and maintenance industry, while still requiring new mechanical training, should not require additional safety considerations for the individuals or for detectors and other safety systems in the garages. In our ongoing work, our objective is to develop liquid systems that will provide improved environmental and safety considerations than that of gasoline and diesel.

**Liquid-phase Hydrogen Carriers.** The possibility of storing and transporting hydrogen for energy storage via the catalytic hydrogenation and dehydrogenation of common aromatic molecules such as benzene or toluene has long been discussed.[2] The dehydrogenation of saturated aromatics to provide hydrogen to a fuel cell or hydrogen internal combustion engine (ICE) has also been investigated for these chemically simple systems.[3] With a theoretical gravimetric hydrogen storage capacity of over 7 weight percent, the systems seem attractive. But while this chemistry is carried out routinely in chemical plants, there are numerous engineering difficulties in utilizing it in a practical hydrogen storage device.

With the appropriate metal catalysts, the hydrogenation of benzene, toluene, naphthalene and related one or two six-membered ring aromatics to the corresponding saturated cyclic hydrocarbons, cyclohexane, methylcyclohexane and decalin, respectively, can be conducted at relatively mild conditions, e.g. ~100°C and ~100 psi (6.9 bar) of hydrogen pressure, where it is thermodynamically very favorable. However, dehydrogenation of the above cited corresponding alkanes to produce hydrogen gas at the about 20 psia (1.5 bar) and higher delivery pressures as required for use in today's PEM fuel cells,is a highly endothermic process. They require the use of higher reaction temperatures that are not easily obtainable from the fuel cells as well as a significant input of energy. For example, the dehydrogenation of decalin in a membrane reactor gives only a very low conversion (~15%) of decalin, even at 300°C, and is only greatly enhanced by the selective separation of hydrogen by the membrane and removal from the reactor.[4]

For the hydrogenation of benzene to cyclohexane, the experimental enthalpy change at standard conditions (1 atm. pressure, 25°C), $\Delta H°$, is -16.4 kcal/mol $H_2$; $\Delta G$ at 80°C is -6.2 kcal/mol $H_2$, with a corresponding $K=2.9 \times 10^{11}$ $atm^{-3}$ and approaches the ideal $\Delta G$ value only at about 280°C (where K = 1.1 $atm^{-3}$). For the hydrogenation of naphthalene (liquid), $C_{10}H_8$, to *cis*-decalin (liquid), $C_{10}H_{18}$, the experimental $\Delta H°$= -15.1 kcal/mol $H_2$ and $\Delta G$ at 80°C is –4.9 kcal/mol $H_2$ and approaches zero only at about 235°C (where K = 0.8 $atm^{-5}$). Therefore, it is very clear that with the reversible hydrogenation of simple aromatics a recovery of hydrogen that is stored by hydrogenation will only be possible at quite elevated temperatures.

Additionally, the common one or two six-membered ring aromatic molecules are quite volatile as are their hydrogenated products. While the hydrogenation can be conducted in a closed system, the production of product hydrogen from the reverse reaction fundamentally requires that there be some means of totally separating the gas from the reaction's organic volatile components. While technically possible, this requires a further unit operation which increases the complexity and cost of the hydrogen storage process.

There have been several attempts to provide practical processes for storing hydrogen via a reversible hydrogenation of aromatics. Jensen et al. have described a means of dehydrogenating a hydrocarbon to an aromatic and hydrogen in the presence of a particular iridium-based homogeneous catalyst at temperatures of 190°C or higher.[5] Specifically described hydrocarbons are methylcyclohexane, decalin, dicyclohexyl, and cyclohexane (for which the corresponding aromatic products are toluene, naphthalene, biphenyl and benzene). These substrates are clearly volatile at these reaction temperatures and the reaction chamber is thus necessarily provided with a membrane that is highly selective for the passage of hydrogen as compared to the other volatile reaction components which are retained in the reaction chamber.

Kariya, Ichikawa *et al.* have recently reported what is described to be an efficient generation of hydrogen from liquid cycloalkanes such as cyclohexane, methylcyclohexane and decalin over platinum and other platinum-containing catalysts supported on carbon. The processes are carried out at from about 200°C to 400°C under either "wet-dry multiphase conditions"[6] or using pulse-spray mode reactors[7], which involve intermittently contacting the saturated liquid hydrocarbon with a heated solid catalyst in a way such that the catalyst is alternately wet and dry. Because of local superheating and other cited factors the dehydrogenation reaction is rendered more efficient in terms of improved reaction kinetics but because of the reaction thermodynamics, it still requires the use of relatively high temperatures for a high conversion of the cyclohexane to the corresponding aromatic molecule.

**Thermodynamics.** In the hydrogen storage system approach discussed here, the hydrogen is "contained" in liquid-phase hydrogen carriers. Hydrogenation of the LQH is an exothermic process, while the release of hydrogen by dehydrogenation requires at least the corresponding input of thermal energy which can ideally be met from the fuel cell's or internal combustion engine's waste heat. Thus, in contrast to compressed hydrogen or liquid hydrogen-based storage systems, the necessary energy needed for containing the hydrogen (i.e. its heat of hydrogenation) can thus largely be met without significant consumption of higher grade electrical energy for compression.

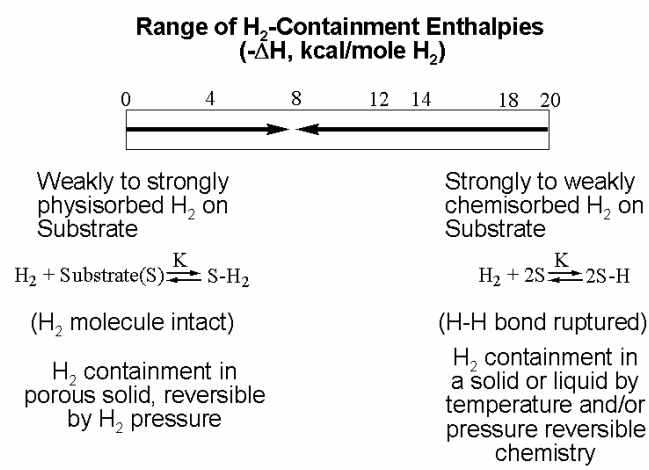


**Figure 3**. The range of known $H_2$-containment enthalpies including physical adsorption and chemical adsorption (eg. metal hydrides and hydrogenation of aromatic molecules).

This concept can be quantified in terms of the basic thermodynamic parameters, enthalpy (ΔH), entropy (ΔS), Gibbs free energy (ΔG), and the equilibrium constant K, for the reversible hydrogenation reaction of substrate A to A-$H_{2n}$:

$$A + nH_2 \xleftrightarrow{K} A - H_{2n}$$

by the familiar thermodynamic relationship:

$$\Delta G = -RT\ln K = \Delta H - T\Delta S \qquad (1)$$

where R is the ideal gas constant, T is the reaction temperature (K), and

$$K = [A\text{-}H_2]/[A]P^{n}_{H2} \qquad (2)$$

where the terms in [ ] refer to concentration and $P_{H2}$ designates the hydrogen partial pressure.

For an ideally reversible process, ΔG should ideally be about zero at a temperature (T) of ~80°C, the approximate temperature of operation of present day polymer electrolyte membrane (PEM) fuel cells.

From Equation 1, the ideal requirement of ΔG~0 would be met with ΔH~TΔS. The entropy change for a hydrogenation (ΔS) of pi-conjugated substrates, which is largely representative of the loss of the $H_2$ molecules' translational entropy, is typically on the order of ~30 cal/deg/mol $H_2$. Thus, for ΔG=0 at 80°C, ΔH should be about –10.6 kcal/mol $H_2$; at 200°C, ΔH will be approximately –14.2 kcal/mol $H_2$; and at 250°C, ΔH will be approximately –15.7 kcal/mol $H_2$. For a practical hydrogen storage device that operates via a reversible hydrogenation of an aromatic molecule, the change in enthalpy at standard conditions (ΔH°, with standard conditions being 25°C and 1 atm.) of hydrogenation of the substrate as determined experimentally should be within the range of about –8 to -14 kcal/mol $H_2$, (a range of hydrogenation enthalpies enthalpy changes that does not encompass the ΔH° for benzene or the ΔH° for naphthalene to their corresponding hydrocarbons). Those substrates having a lower modulus (absolute value) of the negative standard enthalpy change of hydrogenation, will be more easily dehydrogenated.

## Conclusions

The reversible liquid-phase hydrogen carrier approach provides a scenario that integrates the fuel distribution with the onboard vehicle storage technology into a total system approach. While all proposed hydrogen storage technologies currently fall short of the ultimate commercialization targets, the LQH approach provides some unique benefits compared to the other storage technologies. The thermodynamics of the system provide potential maximum energy efficiency by (a) utilizing the waste heat from the exothermic carrier hydrogenation reaction and (b) a close integration of the endothermic dehydrogenation step which would thus be essentially driven by the waste heat from the $H_2$ consuming power source.

Progress in demonstrating the feasibility of producing hydrogen by the dehydrogenation of saturated aromatic molecules has been reported in the literature. However, it is evident from these results and our calculated thermodynamics that the use of molecules with a heat of hydrogenation >15 kcal/mol $H_2$ will not allow for the dehydrogenation catalysis to operate at a temperature that enables the direct utilization of PEM fuel cell waste heat. The challenge of discovering liquid-phase hydrogen carriers for onboard hydrogen storage with both a suitable hydrogen capacity and heat of hydrogenation still remains.

## References


(1) http://www.eere.energy.gov/hydrogenandfuelcells/pdfs/solid_liquid_carriers_pres_air_prod.pdf

(2) Scherer, G. W. H.; Newson, E.; Wokaun, A. *Int. J. Hydrogen Energy* **1999**, *24*, 1157.

(3) Taube, M.; Rippin, D.; Knecht, W.; Hakimifard, D.; Milisavljevic, B.; Gruenenfelder, N. *Int. J. Hydrogen Energy* **1985**, *10*, 595.

(4) Loufty, R. O.; and Vekster, E. M. In *Proceedings of the International Hydrogen Energy Forum 2000*; Munich, **2000**; pp. 335.

(5) Jensen, C. M., U. S. Pat., No. 6,074,447, **2000**.

(6) Kariya, N.; Fukuoka, A.; Ichikawa, M. *Appl. Cat. A* **2002**, *233*, 91.

(7) Kariya, N.; Fukuoka, A.; Utagawa, T.; Sakuramoto, M.; Goto, Y.; Ichikawa, M. *Appl. Cat. A* **2003**, *247*, 247.

# HYDROGEN SPILLOVER MODELING: APPLICATIONS IN HYDROGEN STORAGE

*Angela D. Lueking*

Department of Energy & Geo-Environmental Engineering
Pennsylvania Stat University
University Park, PA 16801

**Abstract**

The objective of the proposed work was to develop a model of hydrogen spillover that provides a mechanistic understanding of the resulting surface concentration attributed to hydrogen spillover. We have developed four models to describe this process, including (1) a chemical kinetics model, (2) a kinetic Monte Carlo analysis, (3) a dimensional analysis of the process, and (4) use of a Langmuirian model to provide a simplified chemical kinetics analysis. Each model has led us to some degree of insight to the hydrogen spillover process, and we anticipate that successful development of a model for hydrogen spillover will lead to a better design of hydrogen storage materials and provide insight into the field of heterogeneous catalysis as well. Here, we discuss the fourth model in detail and its resulting "spillover isotherm" which has allowed comparison of recent experimental results in hydrogen storage of doped carbon nanomaterials at pressures up to 20 bar.

**Introduction**

Recently, the term hydrogen spillover was used by Lueking & Yang to describe a synergistic effect between a multi-wall carbon nanotube (MWNT) and a $Ni_{0.4}Mg_{0.6}O$ catalyst left from synthesis: Hydrogen spillover increased the uptake of the MWNT by up to 40% [1] and high-pressure studies with this material showed adsorption and desorption to be 3.7% and 3.6% hydrogen by weight respectively at 69 bar and 300 K [2]. Temperature-programmed desorption showed a secondary low temperature desorption peak attributed to hydrogen spilled over to the carbon surface; integration of these desorption peaks indicates that hydrogen bound carbon exceeds hydrogen bound catalyst by a factor of two at atmospheric pressure. This hydrogen uptake was comparable to similar studies reported concurrently for carbon-based materials with uncharacterized metal content. Similar work suggests that the original 5-10% report of hydrogen storage in SWNT was also a result of carbon-metal synergy and theoretical studies of Fe-doped bucky balls suggest that application of pressure to doped nanocarbons may induce defects that lead to additional carbon adsorption sites with a hydrogen binding energy between classic physical and chemical adsorption [3]. Development of a solid state hydrogen storage material remains a key hurdle to realize a hydrogen fuel economy, yet no current materials meet storage targets established by the DOE. Despite a general skepticism about hydrogen storage reports in carbon based materials, the study of carbon-metal hybrids remains largely unexplored.

The objective of this paper was to provide the theoretical framework to properly analyze and interpret hydrogen spillover data beyond the limit of low surface coverage, such that a theoretical basis can be used to guide experimental efforts. To this end, a simple utilitarian model with a limited number of parameters requiring estimation and/or extrapolation is desired. We have developed four separate conceptual models that are useful in describing hydrogen spillover and are not limited to low pressure and low coverage conditions. The final model, a simple kinetic analysis based on an extended Langmuir-like derivation, proved the most utilitarian for interpreting high-pressure hydrogen adsorption isotherms; and thus this final "hydrogen spillover isotherm" is discussed here in detail, fit and validated with experimental data, and used to interpret spillover trends on various carbon supports. The corresponding "hydrogen spillover isotherm" has implications not only in hydrogen storage, but also in the field of hetoergeneous catalysis.

**Methods**

**Materials.** HiPCO single wall carbon nanotubes (SWNTs) were obtained from Carbon Nanotechnologies (CNI) Inc. and further treated with 4M HCl followed by 6M HNO3 to remove residual metals. Treated SWNT were doped with platinum ($H_2PtCl_5.6H_2O$, STREM Chemicals) by refluxing in ethylene glycol. Prior to adsorption measurements, samples were reduced *in situ* in 100 cc (STP)/min hydrogen gas at 573 K followed by vacuum treatment at 573 K to remove hydrogen prior to cooling to room temperature for adsorption measurements.

**Hydrogen adsorption.** Total hydrogen uptake was quantified at 300K for 40-50 mg samples gravimetrically through adsorption isotherms on a Hiden IGA-003 microbalance with a sensitivity of $\pm 1$ μg at pressures up to 20 bar. Ultra-high purity hydrogen was used and further purified with an in-line molecular sieve. Buoyancy corrections were based on preliminary helium densitometry measurements which showed a density of 1.9 g/cm$^3$. The hydrogen monolayer coverage was calculated by extrapolating to zero pressure, using standard procedures. The hydrogen adsorption for the 1% Pt/SWNT was compared to data obtained in reference [4].

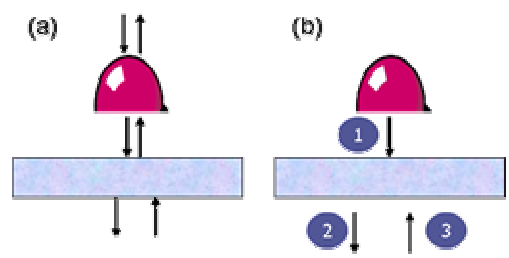


**Figure 1.** Hydrogen spillover includes (a) adsorption/desorption from a supported catalyst followed by surface diffusion to the catalyst support. In our simplified Langmuiran analysis (b) we have incorporated the assumption that the metal remains saturated and the flux is only from the metal to the support (see text and Equation 1)

**Model Development.** To arrive at active metal surface area, a common method is to extrapolate low pressure data to zero pressure. The assumption is that metal remains saturated at intermediate pressures. We have incorporate this assumption in the development of our spillover model illustrated in Figure 1. Combining a mass balance around the support with a surface diffusion term, *Ds*, ultimately leads to the Langmuiran-type expression for overall uptake, $\eta$, normalized per number of surface sites, Z:

$$\Theta = \frac{\eta}{Z} = \beta_1 + (1-\beta_1)\left(\frac{\beta_1\theta_M + \lambda_1\rho^{1/2}}{(1-\beta_1)(\lambda_2+1) + \lambda_1\rho^{1/2}}\right) \qquad (1)$$

Where de-dimensionalization of the equation has led to the following dimensionless parameters: (2)

$$\rho = \frac{P}{P^o}$$

$$\lambda_1 = \frac{\chi a_S \kappa P_o^{1/2}}{D_s Z} \sim \frac{r_3}{r_1}$$

$$\lambda_2 = \frac{\chi \nu_S e^{-q/RT}}{D_s} \sim \frac{r_2}{r_1}$$

Thus, this Langmuiran approach has led to a "spillover isotherm" represented in Equation 1 which incorporates dimensionless parameters that relate hydrogen adsorption, desorption (to/from the support) to the rate of interfacial transfer to the support ($\lambda_1$ and $\lambda_2$). The parameters $\beta_1$ and Z represent the fractional number of catalyst surface sites and the total number of sites per surface; these parameters are characteristic of the support and should be easily determined through experimental analysis.

**Results and Discussion**

Hydrogen spillover is often cited to be proportional to the square root of pressure. In his seminal work, Langmuir discussed a fifth case of adsorption which involved dissociation of the adsorbate and, we believe, ultimately led to this common assertion. However, Langmuir clear states that this equation is valid only in the limiting case where surface coverage approaches zero. Hydrogen uptake on supported catalyst is generally limited to measurements between 0-1 bar. Over this limited pressure regime, overall uptake can be fit reasonably well to any number of exponential type expressions, including that indicating a square root pressure dependence. In contrast, defining spillover as an increase in uptake over that expected for the undoped supported showed little pressure dependence for metals supported on nano-carbons [4].

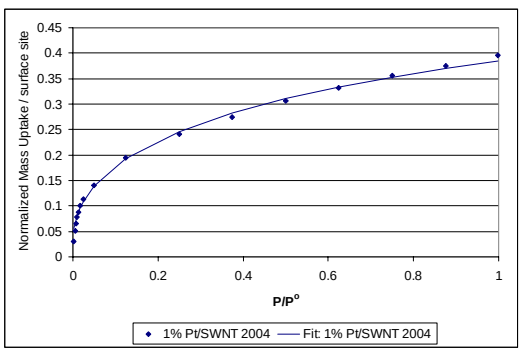


**Figure 2.** The hydrogen spillover isotherm fits experimental hydrogen uptake data for 1% Pt supported on SWNT at high pressures (here $P^o$ = 20 bar).

The spillover isotherm fits experimental data for a 1% Pt/SWNT very well at pressures up to 20 bar (Figure 2); previous models we have developed relying on simple square root pressure dependence do not fit the data over this range of pressures. It is interesting to note that the spillover isotherm reduces to square root pressure dependence when $\lambda_2$ is large; this corresponds to a large desorption rate relative to the mass transfer rate (see Equation 2). The spillover isotherm also exhibits properties similar to that of the classic Langmuir isotherm, in that it has a limiting value at high pressure. This limiting capacity provides a more realistic view of potentially applying carbon-metal hybrids to hydrogen storage applications, than the common statement that uptake is proportional to the square root of pressure.

The direct need for a hydrogen spillover model to characterize and understand experimental data has been discussed previously [7]. Simple additive analysis commonly used to interpret data makes no concession for synergistic effects upon the addition of a catalyst. When comparing the overall uptake of a catalyst-support combination, it is difficult to draw meaningful conclusions about the ability of a support to accept spiltover hydrogen when the surface may—either by design or inadvertently—have different catalyst loading and dispersion. Chemical methods that modify the support ultimately affect metal dispersion, thus systematic attempts to study the role of chemical modifications on hydrogen spillover are difficult at best. Plots of hydrogen uptake before (Figure 3a) and after (Figure 3b) illustrate how the normalization procedure via the spillover isotherm facilitate data analysis. Prior to normalization, it is unclear whether the ~2-fold increase in hydrogen uptake for the 5% Pt/SWNT is due to greater Pt or due to chemical properties of the support (Figure 3a). Normalization and use of the spillover isotherm allows a meaningful comparison between the chemical treatments and synthesis of the different SWNTs shown (Figure 3b). The 1% Pt/ SWNT was synthesized as described in the methods section, whereas the data for the 5% Pt/SWNT is from reference [4]. Thus, the two SWNT were synthesized and pretreated with very different procedures. This normalization via the spillover isotherm leads to initial speculations that the $HNO_3$ treatment was detrimental to hydrogen uptake via hydrogen spillover.

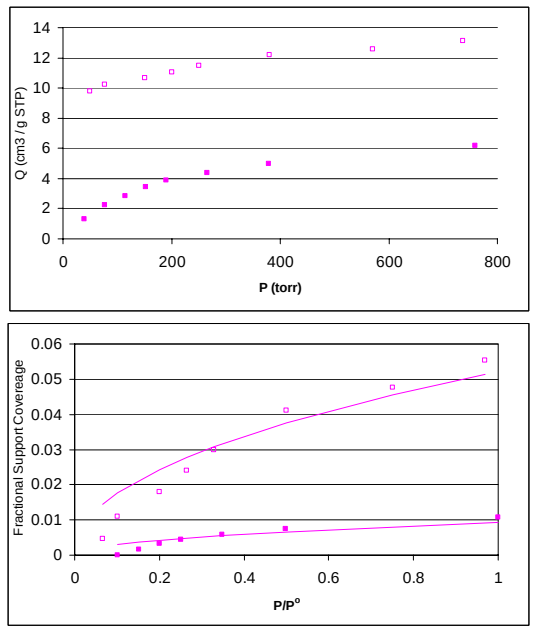


**Figure 3.** Hydrogen uptake of 5% Pt/SWNT is greater than 1% Pt/SWNT (a), but it is unclear if this is due to metal content, loading, or support chemistry. Treatment of the data through the hydrogen spillover isotherm (b) suggests the surface chemistry of the 5% Pt/SWNT contributes to its higher uptake.

**References**


1. Lueking, A. and R.T. Yang, *J Catal*, 2002. **206**: 165.
2. Lueking, A. and R.T. Yang, *AIChE Journal*, 2003. **49**: 1556.
3. Dillon, A.C., et al. *Nanostructured Carbon and Carbon/Metal Hybrid Materials for Vehicular Hydrogen Storage*. in *National Hydrogen Association's 15th annual U.S. Hydrogen Conference*. 2004. Los Angeles, CA.
4. Lueking, A. and R.T. Yang, *Appl. Catal. A*, 2004. **265**: 259.

# INVESTIGATIONS INTO THE CONVERSION OF SOLAR ENERGY TO CHEMICAL ENERGY *via* LONG-LIVED CHARGE SEPARATION

*Prabir K. Dutta* and Yanghee Kim,*

Department of Chemistry, The Ohio State University,
Columbus, OH 43210

## Introduction

In the past several decades there has been considerable interest in efficiently harnessing solar energy to generate chemical energy.[1,2] However, significant progress is still needed to reach this goal. Natural photosynthesis represents the conversion of solar energy to chemicals via a complex array of light-harvesting pigments and redox species arranged spatially across membranes.[3] It is necessary to create long-lived accessible photogenerated charge-separated species for building up an efficient energy conversion system. The thermal back-electron-transfer reaction makes this difficult; e.g., with the photosensitizer tris(bipyridine)ruthenium-(II) ($Ru(bpy)_3^{2+}$ ) and the electron acceptor methyl viologen ($MV^{2+}$), the forward- and back-electron-transfer rate constants are reported to be $5.6 \times 10^{9}$ and $2.4 \times 10^{9}$ $M^{-1}$ $s^{-1}$, respectively.[4]

Various heterogeneous supports have been examined for the $Ru(bpy)_3^{2+}$ and viologen system such as micelles,[5] vesicles,[6] silica gel,[7] clays,[8] and zeolites.[9,10] Zeolite-based systems have shown promise for generation of long-lived charge-separated species. Using dyad molecules exchanged on the surface of zeolites, it was found that intramolecular back-electron-transfer reactions between $Ru(bpy)_3^{3+}$ and viologen radical could be $10^5$ times slower than in solution.[11] Several groups have shown that the back electron transfer between zeolite-entrapped $Ru(bpy)_3^{3+}$ and viologen radical can be slowed, and charge hopping between intrazeolitic viologen molecules can lead to permanent photoinduced charge separation.[12-15] However, in these latter cases, Ru-$(bpy)_3^{2+}$ was within the zeolite and not accessible for possible chemical utilization.

Here we would like to address the accessibility problem by examining a system in which a polypyridine-ruthenium moiety is covalently bonded to entrapped-bipyridinium acceptors on the surface of the zeolite.[10] By adapting a zeolite membrane, which can keep apart two chemical systems that interfere with each other, yet still allow for transport of specific species through the membrane, a spatial separation of the photogenerated hole and electron can be achieved.[16,17] In our study a prototype zeolite-membrane-based artificial photosynthetic assembly, which is a Ru polypyridyl complex decorated on the surface of the zeolite with intrazeolite bipyridinium ions and propylviologen sulfonate in solution, will be proposed as an attractive feature in mimicking natural photosynthesis.

## Experimental

**Chemicals:** $(Ru(bpy)_2^{3+}$, Strem Chemicals), $Na_2EDTA$ (GFS Chemicals), triethanolamine (Sigma), 1,3-dibromopropane (Aldrich), 1,4-dibromobutane (Aldrich), 2,2'-bipyridine (Aldrich), 4,4'-dipyridyl hydride (Aldrich) and 1,3 propane sulfone (Aldrich) were purchased with the highest purity available and used as received. Acetonitrile, toluene, dichloromethane and acetone were obtained from Mallinckrodt (reagent grade) and used without further purification. N,N' -trimethyl-2,2' –bipyridinium dibromide ($3DQ^{2+}$/, N,N'-tetramethyl-2,2' -bipyridinium dibromide ($4DQ^{2+}$/ and propyl viologen sulfonate (PVS) were synthesized following a procedure published elsewhere.[18]

**Preparations of zeolite and its membrane:** As a support, porous $\alpha$-$Al_2O_3$ disks prepared according to the literature procedures were used.[19] Nanocrystalline zeolites Y were used as a seed crystal and were synthesized from clear solutions of tetramethylammonium (TMA)-aluminate according to the literature.[20,21] The synthesis solution had the following molar composition; 0.037 $Na_2O$, 1.0 $Al_2O_3$, 3.13 $(TMA)_2O$, 4.29 $SiO_2$, 497 $H_2O$. Zeolite Y membrane was prepared by secondary growth method and a detailed procedure was discussed in a previous report.[16] X-ray powder diffraction (XRD) patterns of nanocrystalline zeolite Y and its membranes were recorded with a Rigaku Geigerflex diffractometer using Ni-filtered Cu $K_\alpha$ radiation (40 kV and 25 mA). Figure 1 shows a typical XRD pattern of zeolite Y membrane.

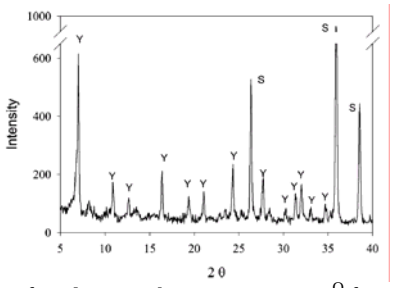


**Figure 1.** XRD of zeolite membrane grown at 45$^{O}$ for 7 days (Y-due to zeolite, S-due to substrate).[16]

**Synthesis of Ru complex and fabrication of zeolite- based artificial photosynthetic assemblies:** Ligand L (1,4-Bis[2-(4'-methyl-2,2'-bipyrid-4-yl)ethenyl]-benzene) and $[Ru(bpy)_2(L)](PF_6)_2$ were prepared by following methods described in the literature with slight modifications.[22] Analytical and spectroscopic data recorded for these compounds were in agreement with the proposed structures. To accomplish the prototype of zeolite-based artificial photosynthetic assemblies, each reaction step was properly modified. Their $^1H$ NMR and UV-Vis absorption spectra matched with those of the presynthesized one. Pore size engineering technique was also applied to accomplish ideal model assembly by means of reducing the ion-exchange of $3\text{-}DQ^{2+}$ by $Na^+$.

**Photolysis:** A xenon arc lamp equipped with a water filter, a 420 nm cut-off filter and a reflecting mirror (420–650 nm) was used as a light source. The power of the incident radiation on the membrane side of the cell was 250 mW/cm$^2$, measured by a Coherent 210 power meter. For suspension and membrane photolysis, a vacuum-sealed NMR tube and a cell,[10] which has a built-in (1 cm internal length) cuvette for *in situ* absorption spectro-scopic study were used respectively.

## Results and Discussion

To examine charge transport through the zeolite membrane, a reaction that involves electron transfer by a self-exchange process was considered.

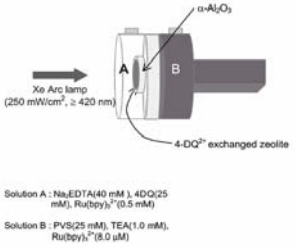


**Scheme 1.** A schematic representation of the cell for photochemical charge transport studies[16]

A schematic description of the cell in which the reaction was carried out, and has two compartments separated by the zeolite membrane[17] is shown in scheme 1. The zeolite was ion-exchanged with $4DQ^{2+}$ and the following process was carried out:

$$\text{Zeolite side: } Ru(bpy)_{3\,s}^{2+} + DQ_s^{2+} \xrightarrow{h\nu} Ru(bpy)_{3\,s}^{2+*} + DQ_s^{2+} \quad (1)$$

$$Ru(bpy)_{3\,s}^{2+*} + DQ_s^{2+} \longrightarrow Ru(bpy)_{3\,s}^{3+} + DQ_s^{+\cdot} \quad (2)$$

$$Ru(bpy)_{3\,s}^{3+} + EDTA \longrightarrow Ru(bpy)_{3\,s}^{2+} + EDTA_{ox}^{+} \quad (3)$$

$$DQ_s^{+\cdot} + DQ_z^{2+} \longrightarrow DQ_s^{2+} + DQ_z^{+\cdot} \quad (4)$$

$$\text{Intrazeolitic membrane: } DQ_{1z}^{+\cdot} + DQ_{2z}^{2+} \longrightarrow DQ_{1z}^{2+} + DQ_{2z}^{+\cdot} \quad (5)$$

$$\text{Substrate side: } DQ_z^{+\cdot} + PVS_s \longrightarrow DQ_z^{2+} + PVS_s^{-\cdot} \quad (6)$$

where the subscripts s and z represent solution and zeolite, respectively. Reaction (1) initiates the charge-transfer process on the zeolite side, and EDTA acts as a sacrificial electron donor. If charge transport through the zeolite membrane can occur by electron hopping via the self-exchange of ion-exchanged $DQ^{2+}$, as shown in reaction (5), then illumination of the zeolite side should lead to creation of $PVS^{-\bullet}$ radical on the substrate side of the membrane and measure of this radical (characteristic absorption bands at 390 and 605 nm) was the focus of these experiments. Even though $O_2$ from leaking into the cell was not fully prevented, 0.018 mM of $PVS^{-\bullet}$ radical was observed on the substrate side of the membrane as a resultant of charge propagation through zeolite membrane.

In terms of achieving efficient charge transfer, however, the electron donor and acceptor should be as close as possible. Therefore an electron donor and acceptor dyad would be required and $[Ru(bpy)_2(L\text{-}4DQ)]^{4+}$-Y zeolite was chosen as a model system. $[Ru(bpy)_2(L\text{-}4DQ)]^{4+}$-Y ion-exchanged with $MV^{2+}$ upon exposure to ambient light in an anaerobic environment exhibited new bands at 390 and 605 nm. Further, these spectral changes disappeared when the zeolite sample was subsequently exposed to $O_2$. These observations are consistent with formation of the $MV^{\bullet-}$ radical. $Ru(bpy)_2(L\text{-}4DQ)^{4+}$ -Y ion-exchanged with $3DQ^{2+}$ was dispersed in a PVS solution and irradiated with visible light. A growth in bands at 390 and 605 nm signifying the formation of $PVS^{\bullet-}$ radical in solution was noted, as shown in the insert of Figure 2. The formation of the viologen radical as measured by the absorbance at 390 nm for two zeolite samples $[Ru(bpy)_2(L\text{-}4DQ)]^{4+}$-$3DQ^{2+}$-Y and $[Ru\text{-}(bpy)_2(L\text{-}4DQ)]^{4+}$-Na-Y are contrasted. The data show that the growth of $PVS^{\bullet-}$ is considerably accelerated with intrazeolitic $3DQ^{2+}$. After 3 h of photolysis, 12 nmol of $PVS^{\bullet-}$ was formed, though the amount of the ruthenium complex on the zeolite was 10 nmol. The yield of $PVS^{\bullet-}$ could be increased further with photolysis time, as is obvious from the slope of $PVS^{\bullet-}$ generation in Figure 2.[10]

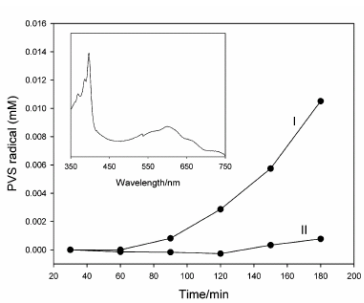


**Figure 2.** Growth of $PVS^{\bullet-}$ during photolysis of I, $[Ru(bpy)_2(L\text{-}4DQ)^{4+}]$- $3DQ^{2+}$-zeolite Y, and II, $[Ru(bpy)_2(L\text{-}4DQ)^{4+}]$-$Na^+$-Y, in aqueous solution of 0.01 M PVS (inset shows the spectrum after 180 min of illumination for I).[10]

Several experiments were done with the solution recovered from the photolysis sample and measured their excitation (measured at 530 nm) and emission spectrum ($\lambda_{max}$: 530 nm). A new species was being created during photolysis with characteristic absorption and emission maximum at 390 and 530 nm indicated the presence of 3,4-dihydro-1,1'-dimethyl-3-oxo-4,4'-bipyridinium cation (3-one), which originates from be the oxidation of PVS in solution. The question that arises is what species oxidizes PVS to the pyridones?

In aqueous solution at neutral pH, the half-life for Ru-$(bpy)_3^{3+}$ is of the order of 200 s in the dark and is considerably faster in the presence of visible light.[23] Illumination within the ligand to metal charge-transfer band of $Ru(bpy)_3^{3+}$ increases the nucleophilicity of the bpy ligand and thereby promotes the attack by water. In earlier studies,[24,25] we concluded that the covalent hydrates and hydroxylated species of the ruthenium complex formed by the attack of water on $Ru(bpy)_3^{3+}$ oxidize methyl viologen to pyridones and regenerate $Ru(bpy)_3^{2+}$. We propose that, in the $[Ru(bpy)_2(L\text{-}4DQ)]^{4+}$ -$3DQ^{2+}$ -zeolite sample, photo-excitation leads to electron transfer from the tethered Ru complex to intrazeolitic $3DQ^{2+}$.

The photolyzed solution was also tested to examine if it had any sacrificial electron donor properties for photolysis with $Ru(bpy)_3^{2+}$ and viologen, and the result was found to be negative. This experiment also confirmed that if any of the zeolite-tethered $[Ru(bpy)_2(L\text{-}4DQ)]^{4+}$ complex was decomposing, then such soluble species did not have the ability to generate $PVS^{-\bullet}$ in solution.

On the basis of data, we concluded that, in the $[Ru(bpy)_2(L\text{-}4DQ)]^{4+}$ -$3DQ^{2+}$ -zeolite sample, photoexcitation leads to electron transfer from the tethered Ru complex to intrazeolitic $3DQ^{2+}$. Several studies in zeolites have demonstrated that if the bipyridinium ions in zeolite are well packed, then the electron can migrate through the zeolite by self-exchange,[14,15,26,27] and this is the purpose $DQ^{2+}$ serves. Such a process will lead to the formation of Ru(III) on the zeolite surface, which in the presence of light and water will lead to rapid adduct formation that can react with PVS in solution to form the pyridones and regenerating Ru-(II). The electron on the $3DQ^{2+/+}$ can migrate through the zeolite and upon coming to the surface of the zeolite is vectorially transferred (because of the difference in reduction potentials) to PVS in solution forming $PVS^{\bullet-}$ , a feature that has also been reported by other groups.[14,15] These ideas are represented by scheme 2 and the following equations:

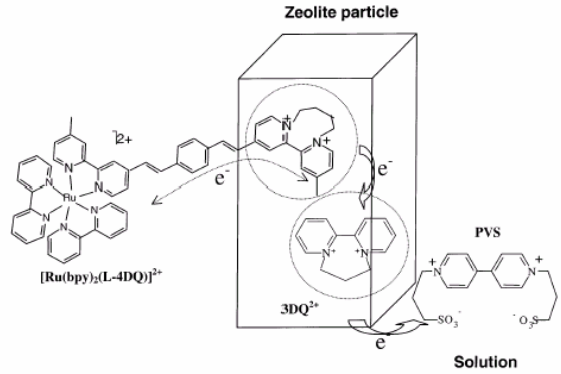


**Scheme 2.** Photoelectron-Transfer Scheme of $[Ru(bpy)2(L\text{-}4DQ)]^{4+}$-$3DQ^{2+}$-Zeolite Y in Aqueous Solution of PVS.[10]

$$Ru^{II}\text{–zeolite} \xrightarrow{h\nu} Ru^{II*}\text{–zeolite}$$

$$Ru^{II*}\text{–zeolite} + 3DQ^{2+}\text{–zeolite} \rightarrow Ru^{3+}\text{–zeolite} + 3DQ^{\bullet+}\text{–zeolite}$$

$$Ru^{3+}\text{–zeolite} + H_2O \xrightarrow{h\nu} Ru^{3+}(OH_2)\text{–zeolite}$$

$$Ru^{3+}(OH_2)\text{–zeolite} + PVS \rightarrow Ru^{2+}\text{–zeolite} + \text{pyridones}$$

$$3DQ^{\bullet+}\text{–zeolite} + PVS(soln) \rightarrow 3DQ^{2+}\text{–zeolite} + PVS^{\bullet-}(soln)$$

In the scheme above, the $Ru^{3+}$ $(OH_2)$-zeolite represents the complex formed by water attack on the Ru(III) complex and its actual form is more complicated than the representation. [23-25] The reason the electron at the interface (on $3DQ^{2+}$) does not recombine with the ruthenium complex is because Ru(III) has reacted with water and PVS and is regenerated as Ru(II). Thus, both water and PVS are necessary to regenerate Ru(II). PVS also plays a second role as the electron acceptor from $DQ^{\bullet+}$ in the zeolite. Eventually, the formation of $PVS^{\bullet-}$ will stop when all the PVS is converted to the pyridone, but since we have a 2500-fold excess of PVS over ruthenium, such a situation is not reached within the times for which we have photolyzed the samples. Water attack on the photogenerated Ru(III) complex will result in degradative processes and destruction of the Ru complex in the absence of PVS.[23,24] Zeolite-based $RuO_2$ catalytic systems that can result in $O_2$ generation are currently being incorporated into the molecular assembly and will assist in regeneration of the Ru(II) complex.[28] Also, in the present system (Scheme 2), there is a sacrifice in photochemical efficiency due to quenching of [Ru(bpy)2(L-4DQ)]* by PVS in solution.

Here, it is suggested that using a zeolitic membrane to separate the redox species would alleviate this problem.[16,17] A prototype zeolite-based artificial photosynthetic assembly is proposed for demonstrating efficient long-lived charge transfer and separation. The assembly will be configured to have Ru polypyridyl complex decorating the surface of the zeolite membrane with intrazeolitic bipyridinium ions ($3\text{-}DQ^{2+}$). Its photochemical and photophysical properties will be examined in the same manner as with zeoltie particles and it is expected that a long-lived charge separation across a membrane will be possible. This successful demonstration should lead to interesting chemistry, including the possibility of splitting water into hydrogen and oxygen.[9] More details will be discussed in the symposium.

**Acknowledgement.** We acknowledge funding from NASA, NSF (Grant INT 0096798) and The Ohio State University.

**References**

(1) Maas, H.; Huber, S.; Khatyr, A.; Pfenniger, M.; Meyer, M.; Calzaferri, G. *Mol. Supramol. Photochem.* **2003,** *9*, 309.
(2) Dutta, P.K.; Kim, Y. *Current Opinion in Solid State Material Science* **2003**, *7*, 483
(3) Lawlor, D. W. Photosynthesis: Molecular, Physiological, and Environmental Processes, 2nd ed.; Longman: Essex, U.K., 1993.
(4) Kalyanasundaram, K. *Coord. Chem. Rev.* **1982**, *46*, 159.
(5) Kunjappu, J. T.; Somasundaran, P.; Turro, N. J. *J. Phys. Chem.* **1990**, *94*, 8464.
(6) Lanne, C.; Ford, W. E.; Otvos, J. W.; Calvin, M. *Proc. Natl. Acad. Sci. U.S.A.* **1981**, *78*, 2017.
(7) Castellano, F. N.; Meyer, G. J. *J. Phys. Chem.* **1995**, *99*, 14742.
(8) Colon, J. L.; Yang, C.; Clearfild, A.; Martin, C. R. *J. Phys. Chem.* **1990**, *94*, 874.
(9) Vaidyalingam, A. S.; Coutant, M. A.; Dutta, P. K *Electron-Transfer In Chemistry*; Balzani, V., Ed.; Wiley-VCH: Weinheim, Germany, 2001; Vol. 4, pp 412-486.
(10) Kim, Y.; Lee, H.; Dutta, P.K.; Das, A. *Inorg Chem* **2003,** *42*, 4215.
(11) Yonemoto, E. H.; Kim, Y. I.; Schmehl, R. H.; Wallin, J. O.; Shoulders, B. A.; Richardson, B. R.; Haw, J. F.; Mallouk, T. E. *J. Am. Chem. Soc.* **1994**, *116*, 10557.
(12) Vitale, M.; Castagnola, N. B.; Ortins, N. J.; Brooke, J. A.; Vaidyalingam, A.; Dutta, P. K. *J. Phys. Chem. B* **1999**, *103*, 2408.
(13) Borja, M.; Dutta, P. K. *Nature* **1993**, *362*, 43.
(14) Sykora, M.; Kincaid, J. R. *Nature* **1997**, *387*, 162.
(15) Yong, S. P.; Lee, E. J.; Chun, Y. S.; Yoon, Y. D.; Yoon, K. B. *J. Am. Chem. Soc.* **2002**, *124*, 7123.
(16) Kim, Y.; Dutta, P.K. *Res. Chem. Intermed.* **2004**, *30*, 147.
(17) Lee, H.; Dutta, P.K. *J. Phys. Chem. B* **2002,** *106*, 11898.
(18) Homer, R. F.;Tomilson, T. E. *J. Chem. Soc.,* **1960,** 2498.
(19) Pan, M.; Lin, Y. S. *Micropor. Mesopor. Mater.* **2001**, *43*, 319.
(20) Otterstedt, J. E.; Sterte, J.; Schoeman, B. J. *International Patent WO* 94/05597 **1994.**
(21) Schoeman, B. J.; Sterte, J.; Otterstedt, J. E. *Zeolites* **1994,** *14*, 110
(22) Shaw, J. R.; Webb, R. T.; Schmehl, R. H. *J. Am. Chem. Soc.* **1990**, *112*, 1117.
(23) Ghosh, P. K.; Brunschwig, B. S.; Chou, M.; Creutz, C. Sutin, N. *J. Am. Chem. Soc.* **198**4, *105*, 4832.
(24) Ledney, M.; Dutta, P. K. *J. Am. Chem. Soc.* **1995**, *117*, 7687.
(25) Das, S. K.; Dutta, P. K. *Langmuir* **1998**, *14*, 5121.
(26) Krueger, J. S.; Mayer, J. E.; Mallouk, T. E. *J. Am. Chem. Soc.* **1988**, *110*, 8232.
(27) Li, Z.; Mallouk, T. E. *J. Phys. Chem.* **1987**, *91*, 643.
(28) Das, S. K.; Dutta, P. K. *Microporous. Mesoporous. Mater.* **1998**, *22*, 475.

# STABILITY AND ACTIVITY OF Au CATALYSTS SUPPORTED ON FUNCTIONALIZED OXIDE SUPPORTS

*S. H. Overbury, Wenfu Yan, Bei Chen and Sheng Dai*

Chemical Sciences Division
Oak Ridge National Laboratory
Oak Ridge, TN 37931

## Introduction

Au catalysts have recently been the subject of great interest because they may be highly active but only when the Au particles are in a certain size range[1] or thickness.[2,3] Elucidation of the causes of this extreme structure sensitivity has been obfuscated by the role of the support in the reaction mechanism and the effect of the support upon the growth and stability of the Au precursor and *in situ* particle sizes.[4] Conversely, tailoring of the support could lead to improved control of Au structure and stability and therefore inhibit thermal deactivation of the catalyst. In the following we summarize research to study the effects of variation in the support properties upon the catalytic performance of the resulting Au catalysts. The crystallographic structure and surface composition of the support has been varied to determine the effect upon activity for CO oxidation reaction after various pre-treatments. In particular, Au catalysts were prepared using different structures of $TiO_2$, and two different morphologies of $SiO_2$ were functionalized with single and double overlayers of Ti- and Al oxides.

## Synthesis of catalysts

A variety of methodologies have been used to prepare catalyst supports which included three different pure allotropes of $TiO_2$ (rutile, anatase and brookite), commercial $TiO_2$-p25, mesoporous $TiO_2$, mesoporous silica and silica supports functionalized by single or double monolayers. Pure rutile and anatase were obtained using sonication synthesis with tetraisopropyltitanate and titanium tetrachloride used as precursors for anatase and rutile respectively. Brookite was obtained by hydrothermal synthesis using titanium tetrachloride as a precursor. Commercial $TiO_2$ P25 was obtained from Alfa Aesar. Phase purity of the $TiO_2$ supports was checked by XRD.

Monolayer synthesis of catalyst were performed using non-aqueous deposition of oxide precursors onto fumed silica (Cabosil) or mesoporous silica (SBA-15) using methods described by Kunitake.[5,6] In this approach, an alkoxide precursor ($Ti(OBu^n)_4$ or $Al(OBu^s)_3$ ) is dissolved in solvent (mixture of toluene and dry methanol). The dried support was added and the resulting mixture was refluxed for 3 hours resulting in substitution of surface hydroxyl by the alkoxide precursor with loss of the corresponding alcohol. Following removal of the pre-cursor, the resulting functionalized support was washed in water to hydrolyze surface alkoxides. Repeating these two steps permits layer-by-layer deposition of single monolayers of oxide precursor (hydroxide). Using this approach single or double monolayers were obtained. For example, deposition first of Al onto Cabosil, followed by deposition of Ti yielded the support designated $Ti^2$-$Al^1$ -$SiO_2$ (Cabosil). Analysis of Al and Ti uptakes on the Cabosil samples by ICP were consistent with the density of surface hydroxyls and the surface area of the silica supports.

Following preparation of the supports, Au was deposited using deposition-precipitation (DP) at pH 10. DP stoichiometry were targeted to a high Au loading (near 13 wt%) but the actual Au loading determined by ICP or XANES were normally lower. Catalysts were dried at low temperature (50 °C). To minimize on-shelf deactivation of reduced Au catalysts, no subsequent treatments were performed until the catalysts were put on-line. Catalysts were tested in a flow reactor (Altamira Instruments AMI-200) outfitted with QMS and GC detection of reaction products. CO oxidation (typically 1%CO in air) was used as a bench-mark test to compare activity and stability of the catalysts. A reaction mixture of 1% CO in air at SV of 40,000 ml/g cat hr was typically used.

## Reduction of Au precursor

Stability of Au catalysts is strongly affected by sintering and growth of Au clusters, a thermally driven process dependent upon the surface on which the Au precursors are supported. Our interest was to establish the effects of thermal and chemical pretreatments upon the Au cluster growth and the resulting effect upon activity of the catalyst for CO oxidation. Results are presented for the evolution of the Au precursors during reduction at 150 °C (in 20% $H_2$-Ar) and calcination at 300 and 500 °C (in 8%$O_2$-He). Following DP at high pH it is expected that the Au is present on the surface primarily as a hydroxide and is accompanied by hydroxyl or water chemisorbed on the support. TGA and temperature programmed desorption in He demonstrate evolution of water occurs in two peaks near 100 and 200 °C and tails off at higher T, attributed in part to de-hydrolysis of the Au hydroxide (Fig. 1). Oxygen evolution occurs in a sharp peak at 350 °C due to decomposition of Au oxide remaining from the dehydrolysis.

Reduction of Au by CO and $H_2$ occurs readily at temperatures well below the TPD peak temperatures, as determined by color change and XANES. In the as-dried state the catalysts are light colored (brown or tan) and readily turn to a dark blue or black when treated in the reactor at room temperature in reaction mixture (CO in air) or in $H_2$. XANES at the Au $L_{III}$ edge conclusively demonstrates reduction of the Au precursor to metallic Au under reaction conditions. Once reduced, the Au clusters will not reoxidize by treatment with air at room temperature or 300 °C. These catalysts with reduced Au clusters may be highly active for CO oxidation, depending upon Au loading and the size of the resulting Au particles.

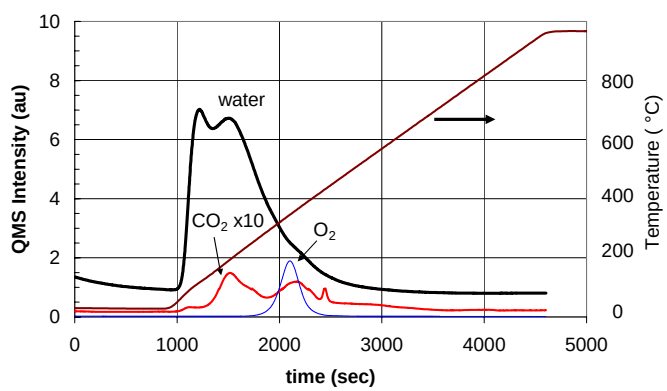


**Figure 1.** Temperature programmed desorption in He from as-dried Au on $TiO_2$ (anatase), heating rate 15 °C / min.

## Catalytic activity and stability

Catalysts were all tested to compare their activities for CO oxidation after various pre-treatments. The goal was to compare the effect of sequentially higher treatments upon the catalyst activity and to therefore measure their stability to thermal deactivation. Following each pre-treatment, the activity was measured as a function of reaction temperature. Arrhenius plots of the data at low conversion were used to obtain rates and apparent activation energies. Selected activity results are shown in Table 1. For

comparison, the activities are expressed as the temperature at which 50% conversion of CO to $CO_2$ is achieved.

Au catalysts prepared on pure $TiO_2$ gave reaction rates comparable to published values when compared at the same temperatures. Catalysts are already active in the as-dried form in spite of water present on the support and initially oxidized Au. Upon first introducing the reaction stream, $CO_2$ is generated from reduction of the Au hydroxide and contributes to $CO_2$ produced catalytically, presumably by the newly reduced Au. All forms of $TiO_2$ supported Au had comparable activities in as-dried state and after reduction at 150 °C. The supports are differentiated by the stability of the Au catalyst following calcination, and the brookite is least affected by calcination at 300 or 500 °C while the pure rutile is the most strongly deactivated.[7]

Although Au on Cabosil or SBA-15 by DP has low activity, functionalizing the silica with a single monolayer of Ti before Au deposition yields a very active catalyst which remains active after calcination up to 300 °C. A double layer of Ti behaves similarly (the very low $T_{50}$ after 150 °C reduction may be a heat transfer effect). Interposing an Al layer under the Ti has the major effect of destabilizing the catalyst after calcination at 300 °C or above. Most interesting is the behavior of the Al terminated supports. A single layer of Al on the silica does not lead to a good catalyst, although addition of a second silica layer leads to an improvement. Remarkably, interposing a buffer layer of Ti under the Al layer leads to a catalyst which is more active and stable than the Al layered catalysts and as stable as the most stable $TiO_2$ (brookite).

**Table 1. Activity ($T_{50}$ °C) for Catalysts after Various Pretreatments.**

| Support | Au load wt% | As dried | Reduce 150° C | Calcine 300° C | Calcine 500° C |
|---|---|---|---|---|---|
| $TiO_2$ p25 | 8<br>5.7 | n/a<br>-48 | -30<br>-25 | -15<br>21 | 120<br>n/a |
| $TiO_2$ anatase | 12.6<br>2.8 | -38<br>n/a | -38<br>n/a | 7<br>6 | n/a<br>96 |
| $TiO_2$ brookite | 3.2 | -20 | -38 | -26 | 31 |
| $TiO_2$ rutile | 13. | -31 | -35 | 48 | n/a |
| $Ti^1$-$SiO_2$ (SBA-15) | n/a | -34 | n/a | -25 | n/a |
| $Ti^1$-$SiO_2$ (Cabosil) | 5 | -44 | -32 | -5 | >100 |
| $Ti^2$-$Ti^1$ $SiO_2$ (Cabosil) | 6.8 | -45 | -95 | -25 | n/a |
| $Ti^2$-$Al^1$ $SiO_2$ (Cabosil) | 11.7 | -22 | -11 | 65 | 127 |
| $Al^1$ $SiO_2$ (Cabosil) | 8 | unstable | inactive 100 C | -- | -- |
| $Al^2$-$Al^1$ $SiO_2$ (Cabosil) | 10 | 7 | 12 | Inactive at 30 C | -- |
| $Al^2$-$Ti^1$ $SiO_2$ (Cabosil) | 10.3 | -31 | <-93 | -28 | 35 |

These results suggest that tailoring the support functionality can lead to a route to stabilizing Au catalysts to deactivation. Addition of oxide overlayers serve to alter the acidity (the iso-electric point), the electronegativity, structure, valency and defect types at the surface. This can be achieved on silica with a single specific morphology. Alternatively, variation of the support morphology by use of different nanoparticulate or mesoporous forms of silica may be used with particular functionalizing overlayers leading to independent control of support morphology and surface properties.

**Structural characterization of catalysts**

Active catalysts were examined by Z-contrast STEM and by conventional TEM. In particular the brookite and anatase supported Au catalysts were examined using ORNL's aberration corrected Z-STEM. In the precursor state, clusters of gold atoms were visible and resolvable on the anatase support. Images obtained after reduction at 150 °C were consistent with large quantities of Au thin rafts 1 to 2 nm in diameter. Since scattering in dark field is quantifiable, it was possible to determine that the majority of rafts were one or two layers thick. Au atoms were not resolvable in the rafts suggesting that Au atoms were dynamic, although the rafts were stably anchored to the support.

Au particle sizes were analyzed by EXAFS analysis for Au supported on $TiO_2$-p25 following a sequence of annealing steps. Simultaneous measurement of the catalyst activity was obtained to assure activity, although mass transfer limitations prevented accurate rate measurements. Instead, separate aliquots of the catalyst were tested in the reactor under identical protocols. Coordination numbers (and corresponding mean particle sizes) obtained from EXAFS and reaction rates data were correlated following each anneal. EXAFS confirmed decrease in Au particle diameter, d, with increasing annealing temperature, correlating with decrease in reaction rates. Reaction rate (on a *total* Au basis) decreased with particle size faster than the $d^{-1}$ dependence expected from simple loss of surface area. This correlation supports a size effect in Au catalysis, but does not agree with a $d^{-3}$ dependence suggested previously.[8]

**Acknowledgement.** The authors acknowledge contributions from Steve Pennycook and Andy Lupini for Z-STEM and Shannon Mahurin for TEM, Viviane Schwartz and David R. Mullins for EXAFS and XANES measurements. Research sponsored by the Division of Chemical Sciences, Geosciences, and Biosciences, Office of Basic Energy Sciences, U.S. Department of Energy, under contract DE-AC05-00OR22725 with Oak Ridge National Laboratory, managed and operated by UT-Battelle, LLC

**References**

1. Bamwenda, G. R.; Tsubota, S.; Nakamura, T.; Haruta, M., *Catalysis Letters* 1997, 44, (1-2), 83-87.
2. Chen, M. S.; Goodman, D. W., *Science* 2004, 306, 252.
3. Lupini, A. R.; Franceschetti, A.; Chen, B.; Yan, W.; Mullins, D. R.; Schwartz, V.; Dai, S.; Peng, Y.; Pantelides, S. T.; Pennycook, S. J.; Overbury, S. H., *Nature* 2004, submitted.
4. Haruta, M., *Catalysis Today* 1997, 36, (1), 153-166.
5. Yan, W. F.; Chen, B.; Mahurin, S. M.; Hagaman, E. W.; Dai, S.; Overbury, S. H., *Journal of Physical Chemistry B* 2004, 108, (9), 2793-2796.
6. Ichinose, I.; Senzu, H.; Kunitake, T., *Chemistry of Materials* 1997, 9, (6), 1296-&.
7. Yan, W. F.; Chen, B.; Mahurin, S. M.; Dai, S.; Overbury, S. H., *Chemical Communications* 2004, (17), 1918-1919.
8. Lopez, N.; Janssens, T. V. W.; Clausen, B. S.; Xu, Y.; Mavrikakis, M.; Bligaard, T.; Norskov, J. K., *J. Catalysis* 2004, 223, 232-235.

# AN EVALUATION OF PT SULFITE ACID (PSA) AS PRECURSOR FOR SUPPORTED PT CATALYSTS

John R. Regalbuto[1]*, Jeff T. Miller[2], and A. Jeremy Kropf[3]

[1]*Dept. of Chem. Eng., U. of Illinois at Chicago, 810 S. Clinton Street, Chicago, IL 60607*
[2]*BP Research Center, 150 W. Warrenville Rd., Naperville, IL 60563*
[3]*Argonne National Laboratory, 9700 Cass Ave., Argonne, IL 60439*
*jrr@uic.edu

## Introduction

Platinum sulfite acid is a traditional precursor in the synthesis of Pt/carbon black fuel cell electrocatalysts [1]. Easy to use and not relatively expensive, it is a potentially attractive precursor for many other types of supported catalysts. The ultimate usefulness for many applications, however, will depend on the extent that Pt can be dispersed and sulfur eliminated.

To this end a series of supports including alumina, silica, magnesia, niobia, titania, magnesia and carbon were synthesized with PSA solutions and subsequently analyzed with extended x-ray absorption fine structure (EXAFS) and x-ray absorption near edge structure (XANES) analysis to characterize the Pt species formed upon impregnation, calcination, and reduction. It was found almost impossible, by any pretreatment, to eliminate all sulfur from the Pt phase over any support; high temperature calcinations followed by reduction in hydrogen eliminated most but not all S, at the expense of increasing Pt particle size.

## Materials and Methods

Platinum sulfite acid was obtained from Heraeus and was diluted such that impregnation by pore filling (dry impregnation) into the various oxide and carbon supports yielded about 1.5 wt% Pt. EXAFS measurements were performed at the MRCAT undulator beam-line equipped with a double-crystal Si (111) monochromator with resolution of better than 4 eV at 11.5 keV (Pt $L_3$ edge). Spectra were taken in both the fluorescence and transmission modes using pressed powder samples. Phase-shift and backscattering amplitudes were obtained from various solid reference compounds. Details of the experimental and fitting procedures can be found in references 2 and 3.

## Results and Discussion

EXAFS results are shown in Figure 1 for a progression of pretreatments of PSA impregnated alumina. The dried state (solid line), which was virtually identical to the solution species, could be fit with two Pt-S bonds and two Pt-O bonds. After a 300°C calcination, there were six Pt-O bonds (dotted line), while a 300°C reduction of the dried sample yielded only Pt-S bonds (dashed line).

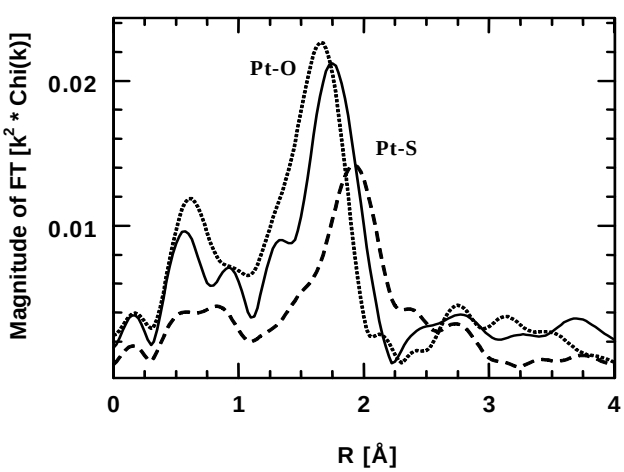


**Figure 1.** Magnitude of Fourier transform of PSA on alumina ($k^2$: $\Delta k = 3.0 – 13.0$ Å$^{-1}$), solid: dried at RT, dotted: calcined at 300°C, dashed: reduced at 300°C

The removal of sulfur from the Pt phase was attempted by higher temperature reduction (at 500°C), and by a 300°C calcination followed by a 300°C reduction. The retention of sulfur after these pretreatments was strongly dependent on the support; representative results are shown in figure 2. For alumina, figure 2a, neither the higher temperature reduction nor the calcination-reduction sequence removes much sulfur, but a small amount of Pt-Pt bonds are formed.

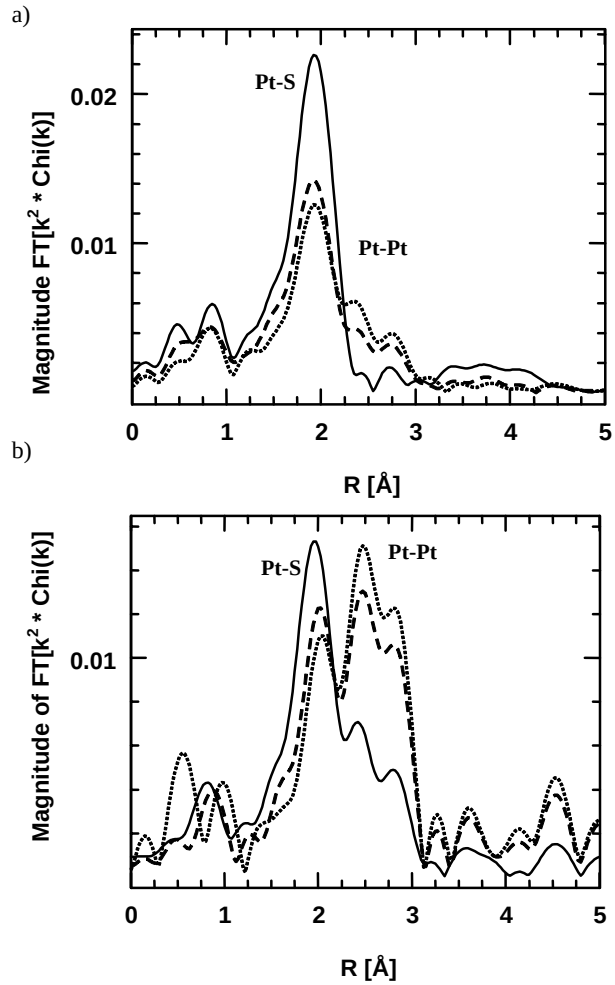


**Figure 2.** Magnitude of Fourier transform of PSA ($k^2$: $\Delta k = 3.0 – 13.0$ Å$^{-1}$), solid: reduced at 300°C, dashed: calcined at 300°C then reduced at 300°C, dotted: reduced at 500°C, on a) alumina, b) silica.

Over silica, figure 2b, much more metallic Pt is formed. However, even in the most S-free sample (500°C reduction) there are on average 0.6 Pt-S bonds and 8.4 Pt-Pt bonds.

The next attempt to remove sulfur was made by reduction-calcination-reduction cycles. A representative result is shown in figure 3 for silica. From the 300°C reduced sample (solid line) which contains about 2 Pt-S bonds and 3.5 Pt-Pt bonds, a 400°C calcination once again removes the Pt-S bonds and an oxide phase is formed with 4.1 Pt-O bonds and 1.6 Pt-Pt bonds (dashed line). Upon re-reduction at 300°C, Pt-S bonds form again with slightly more Pt-Pt bonds than initially (dotted line).

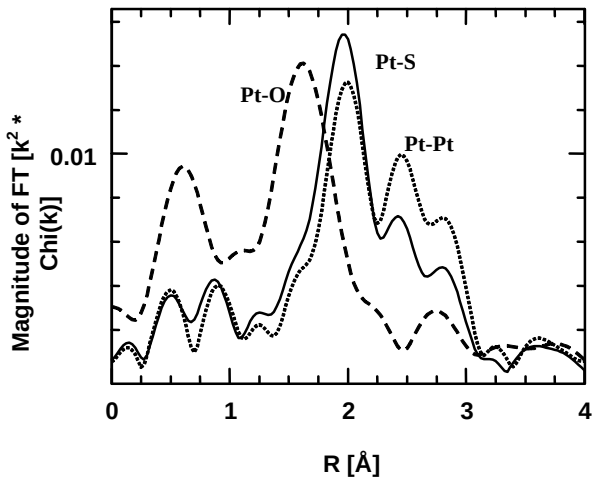


**Figure 3.** Magnitude of Fourier transform of PSA on Silica ($k^2$: $\Delta k$ = 3.0 – 13.0 $Å^{-1}$), solid: reduced at 300°C, dashed: reduced followed by 400°C calcination, dotted: reduced, oxidized, followed by reduction at 300°C.

A final survey of catalyst supports, including carbon black, alumina, magnesia, and silica, is shown in figure 4. After a 500°C reduction in $H_2$, no catalyst is free of sulfur, and the amount of sulfur depends greatly on the catalyst support. Carbon and alumina appear to retain the greatest amount of sulfur, while magnesia and silica appear to retain the least.

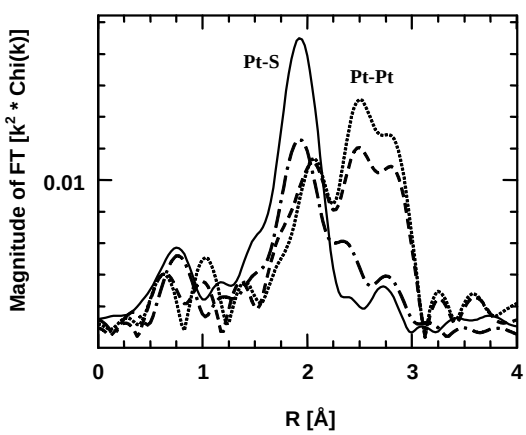


**Figure 4.** Magnitude of Fourier transform of PSA on Different Supports Reduced at 500°C ($k^2$: $\Delta k$ = 3.0 – 13.0 $Å^{-1}$), solid: Carbon black, dot-dash: Alumina, dashed: Magnesia, dotted: Silica

While oxygen replaces S in calcined catalysts (figures 1 and 3), Pt-S reappears upon reduction. These results imply that each catalyst has some mechanism for S storage. This would explain why catalysts with supports that form sulfates, like alumina, retain the most sulfur. Supports that do not form sulfates such as silica do retain some S, perhaps associated with the Pt phase as Pt-O-S linkages.

A final consideration can be made concerning the size of Pt containing particles. While estimation of Pt particle sizes can be made straightforwardly for pure Pt metal particles, from a correlation of Pt-Pt coordination numbers with Pt dispersion measured by $H_2$ chemisorption [4], estimating the size of particles containing a fraction of Pt-S is more tenuous. Nevertheless, an estimate has been attempted and can at least serve to indicate the general trends in the size of Pt-containing particles which result from the PSA precursor.

The data from which estimates where made is given in Table 1. It was assumed that the Pt on Al, V and BP carbons reduced at 300°C was 100% $Pt^{+2}$ (i.e., PtS) since these did not have a Pt-Pt in the EXAFS and the XANES was similar to $Pt^{+2}$. The Pt-S average CN for these three catalysts was 3.4. For all other catalysts reduced at 300°C, the fraction of $Pt^{+2}$ was taken as the Pt-S CN/3.4. The remaining Pt is then metallic. The fitted CN was then divided by the fraction of $Pt^0$ to get the corrected Pt-Pt CN. From that, the fraction of surface Pt atoms in the metallic particle could be estimated (this fraction is not properly termed "dispersion" since they have S on them) using the correlation of $H_2$ chemisorption and Pt-Pt CN. Assuming spherical geometry, size can be estimated as 1/dispersion x 10 Å. For catalyst reduced at 500°C, the same approach was taken. However, 2.9 Pt-S, which is the value for BP carbon reduced at 500C, was used as 100% $Pt^{+2}$.

The fraction of surface atoms and particle sizes should be viewed as very approximate and might be used to classify the particles as small, medium and large. There is a significant fraction (25-50%) of $Pt^{+2}$, i.e., a high fraction of Pt is bonded to S, in most catalysts. For example, while silica yields small particles, they contain a high fraction of sulfur. For most catalysts the fraction of surface Pt atoms is similar to the fraction of $Pt^{+2}$, i.e, atoms with S. Thus, there is not a lot of exposed, reduced Pt. In practice, many (reduced) catalysts are completely poisoned when there is 1 S for every 3 surface Pt atoms. The best support appears to be $Nb_2O_5$, over which the particles are small-medium in size, but have a much smaller fraction of Pt-S, about 10-15%.

**Significance**

While all catalysts show retention of some S, reasonably small particle sizes with relatively little Pt-S can in some instances be produced using PSA. While this synthesis approach would not appear to be very good in general for catalysts used for reforming or other reduction reactions it maybe suitable for those applications such as automobile exhaust catalysts in which the presence of sulfur is not detrimental.

**Acknowledgements**

JRR gratefully acknowledges the support of the National Science Foundation (NSF CTS-0243210). Use of the Advanced Photon Source was supported by the U. S. Department of Energy, Office of Science, Office of Basic Energy Sciences, under Contract No. W-31-109-Eng-38. Work performed at MRCAT is supported, in part by funding from the Department of Energy under grant number DE-FG02-04ER46106.

The submitted manuscript has been created by the University of Chicago as Operator of Argonne National Laboratory under Contract No. W-31-109-Eng-38 with the U.S. Department of Energy. The U.S. Government retains for itself, and others acting on its behalf, a paid-up, nonexclusive, irrevocable worldwide license in said article to reproduce, prepare derivative works, distribute copies to the public, and perform publicly and display publicly, by or on behalf of the Government.

**References**

1. Watanabe et al., J. Electroanal. Chem. 229 (1987) 395
2. Spieker, W. A., Liu, J., Hao, X., Miller, J. T., Kropf, A. J., and Regalbuto, J. R., *Appl. Catal. A: Gen.*, 243, 2003, 53.
3. Miller, J. T., Kropf, A. J., Scheier, M., and Regalbuto, J.R., *J. Catal.* 225, 2004, 203.
4. Miller, J.T., unpublished results.

**Table 1. Composition and Estimated Size of Pt Particles**

| Sample | Pt-Pt CN | Fraction $Pt^{+2*}$ | Fraction $Pt^{0*}$ | Corrected Pt-Pt CN | Fraction Pt Surface Atoms** | Estimated Particle Size, Å*** |
|---|---|---|---|---|---|---|
| Al red 300 | - | 1.0 | - | - | - | No metallic Pt |
| Al cal 300 red 300 | 1.9 | 0.55 | 0.45 | 4.2 | 0.90 | 10 |
| Al red 500 | 2.6 | 0.55 | 0.45 | 5.8 | 0.70 | 15 |
| | | | | | | |
| Si red 300 | 3.5 | 0.60 | 0.40 | 8.5 | 0.40 | 25 |
| Si red 300 ox 400 red 300 | 5.2 | 0.40 | 0.60 | 8.6 | 0.40 | 25 |
| Si cal 300 red 300 | 7.4 | 0.30 | 0.70 | 10.6 | 0.15 | 60 |
| Si cal 500 red 300 | 8.7 | 0.20 | 0.80 | 10.9 | 0.15 | 75 |
| Si red 500 | 8.4 | 0.20 | 0.80 | 10.5 | 0.15 | 60 |
| | | | | | | |
| Mg red 300 | - | 1.0 | - | - | | No metallic Pt |
| Mg red 500 | 6.9 | 0.30 | 0.70 | 9.9 | 0.25 | 40 |
| | | | | | | |
| Nb red 500 | 6.2 | 0.15 | 0.85 | 7.3 | 0.55 | 20 |
| | | | | | | |
| Ti red 300 | 6.0 | 0.35 | 0.65 | 9.2 | 0.35 | 30 |
| Ti cal 500 red 300 | 11.3 | 0.25 | 0.75 | 15 | <0.1 | >100 |
| | | | | | | |
| V carbon red 300 | - | 1.0 | - | - | - | No metallic Pt |
| V carbon red 500 | 3.4 | 0.50 | 0.50 | 6.8 | 0.60 | 20 |
| | | | | | | |
| BP carbon red 300 | - | 1.0 | - | - | - | No metallic Pt |
| BP carbon red 500 | - | 1.0 | - | - | - | No metallic Pt |

*Fraction of $Pt^{+2}$ estimated from Pt-S CN (Pt-S of 3.4 at 300C assumed at 100% $Pt^{+2}$, Pt-S CN of 2.9 assumed at 500C).
**From correlation of Pt-Pt CN and $H_2$ chemisorption (without S)
***Particle size assumed to be 1/dispersion x 10 Å.

# MULTIFUNCTIONAL MESOPOROUS SILICA NANOPARTICLE CATALYSTS FOR CONVERSIONS OF BIO-BASED FEEDSTOCKS TO BIODIESEL AND OTHER VALUE-ADDED PRODUCTS

*Victor S.-Y. Lin,* Daniela R. Radu, and Hung-Ting Chen*

Department of Chemistry and U.S. DOE Ames Laboratory
Iowa State University, Ames, Iowa 50011-3111

## Introduction

Biodiesel, such as soy diesel (methyl soyate), is becoming increasingly useful as a "green fuel", as a carrier solvent, and as an agent for shoreline oil spill clean-up.[1] Apparently, methyl soyate is a viable alternative to traditional petroleum-derived solvents which are of environmental concern and are under legislative pressure to be replaced by biodegradable substitutes. Although interest in biodiesel is rapidly increasing, the process by which biodiesel is synthesized has not changed much. Currently, soy diesel (methyl soyate) is made commercially by an energy and labor-intensive process wherein soybean oil is reacted with methanol at 140-150 °F (sometimes under pressure) in the presence of sodium methoxide.[1] This process is called "transesterification". Isolation of the desired methyl soyate from the highly caustic (toxic) catalyst and other products, such as glycerol, involves a precise neutralization process with strong acids, such as hydrochloric acid (HCl), and extensive washes with water to remove the resulting sodium chloride (NaCl) salt. Also, the glycerol must be separated from the sodium chloride salt by vacuum distillation in an energy intensive operation for this high-boiling product.

As more alkyl soyates with different alkyl functional groups, such as ethyl and isopropyl soyates, being rapidly developed to meet the growing needs of various applications, the level of difficulty in separating the corresponding catalysts, e.g., sodium ethoxide and sodium isoproxide catalysts, respectively, would unavoidably escalate due to the increasing solubility of these basic catalysts in the product solution. Clearly, the successful development of a more effective and economical method to separate the base catalysts from the products is of keen interest to further advance the techniques of biodiesel production.

In addition to the separation issue, the current base-catalyzed transesterification methods also have several other limitations. As producers look for feedstocks other than soybean oil, such as waste restaurant oils and rendered animal fats, they have observed a larger amount of free fatty acids (FFAs) contained in the feedstocks. FFAs can not be converted into biodiesel using the current base-mediated processes. Sulfuric acid, an inexpensive strong acid catalyst, has been used to convert the fatty acids into methyl esters, but the rate is slow. The other limitation of the base-induced process is that saponification of the biodiesel produces soaps as impurities that must be separated before use.

Herein, we report on a new co-condensation method[2] that could generate organically functionalized, MCM-41 type of mesoporous silica nanoparticle (MSN) materials that can catalyze the esterification of free fatty acids.[3] The results of catalytic performance of the MSN materials in comparison to commercial catalysts are reported. In addition, the results of mesoporous silica modified with arenesulfonic groups are presented.

## Experimental

Our method involves the utilization of disulfide-containing organotrimethoxysilanes that have different anionic functional groups, such as 3-(3'-(trimethoxysilyl)-propyl-disulfanyl)-propionic acid (CDSP-TMS), 2-[3-(trimethoxy-silyl)-propyl-disulfanyl]-ethanesulfonic acid sodium salt (SDSP-TMS), and mercaptopropyl-trimethoxysilane (MP-TMS), to electrostatically match with cationic cetyltrimethylammonium bromide (CTAB) surfactant micelles in a NaOH-catalyzed condensation reaction of tetraethoxysilane (TEOS).

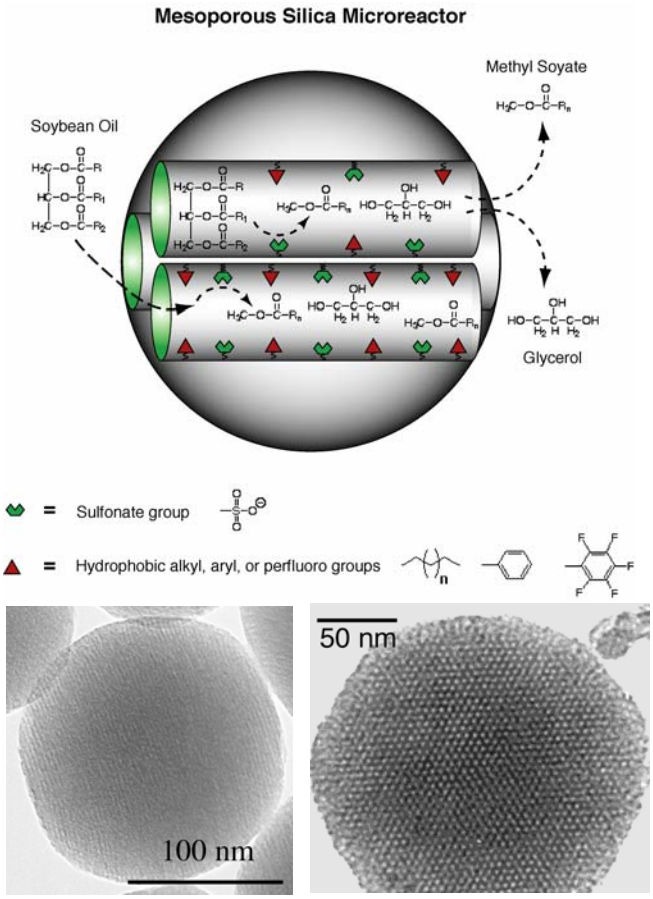


**Figure 1.** Schematic representation of the MSN catalytic system for the synthesis of methyl soyate and glycerol (above). Scanning electron microscopy (SEM) image of the MSN catalyst (lower left). A transmission electron microscopy (TEM) image of the cross-section of the MSN indicating the highly periodic hexagonal lattice units of the porous framework (lower right).

Three organically functionalized mesoporous silica materials, MSN-COOH, MSN-SO3H, and MSN-SH, were prepared by adding an ethanolic solution (2 mL, 2.24 mmol) of CDSP-TMS, SDSP-TMS, and the commercially available MP-TMS, respectively, to an aqueous solution (480 mL, 80°C) of CTAB (2.74 mmol), NaOH (7.00 mmol), and TEOS (22.40 mmol, added at 80°C prior to the addtion of organoalkoxysilanes). The reaction mixture was stirred for 2 h. The solid products were isolated by filtration and washed thoroughly with methanol. Surfactant-removed materials were obtained with an acid extraction. All three materials exhibited spherical particle shape with an average particle diameter of 200 nm (Figure 1). The mesoporous structures of these organically functionalized MSN materials were determined by nitrogen adsorption-desorption surface analysis (BET isotherms and BJH pore size distributions), TEM, and powder X-ray diffraction (XRD) spectroscopy. All three MSN materials exhibited type IV BET isotherms with similar average BJH pore diamerters. Hexagonally packed mesoporous channels were clearly observed in the TEM micrographs of these MSNs (Figure 1). In addition, these materials exhibited diffraction patterns characteristic of hexagonal MCM-41

silicas, including (100), (110), and (200) peaks. The existence of the organic functional groups was confirmed by $^{13}C$ solid state NMR spectroscopy.[2f]

We chemically converted the surface bound organic groups of the MSN-COOH and MSN-SO3H materials to thiol (-SH) by treating them with a disulfide reducing agent, dithiothreitol (DTT). The surface concentration of the *chemically accessible* thiol functional group increases from MSN-SH (0.56 ± 0.01 mmol/g), MSN-COOH (0.97 ± 0.01 mmol/g), to MSN-SO3H (1.56 ± 0.01 mmol/g). We further derivatized these surface-bound thiol functional groups to catalytic functionalities that could efficiently catalyze the FFA esterification reaction for biodiesel formation. Given the fact that *p*-toluene sulfonic acid (*p*-TSA) is a good catalyst for esterification reaction in homogeneous solutions, we treated the thiol-functionalized mesoporous silica materials with 4-vinyl-benzenesulfonyl chloride and α,α'-azoisobutyronitrile (AIBN) in chloroform solutions to yield benzenesulfonyl chloride-functionalized mesoporous silica materials (MSN-SH-BSA, MSN-COOH-BSA, and MSN-SO3H-BSA, respectively) via a modified literature reported procedure.[4] The desired benzenesulfonic acid-derivatized materials were obtained by submersion of the benzenesulfonyl chloride-functionalized mesoporous silicas in either sulfuric or hydrochloric aid aqueous solutions as shown in Scheme 1. As depicted in Figure 1, these benzenesulfonic acid-functionalized mesoporous silica materials have large uniform pore sizes (pore diameter = ~30 Å), high surface areas (> 600 $m^2$/g), good mesoscopic order, and high thermal/hydrothermal stability, all of which are appealing properties for catalyzing the synthesis of biodiesel.

**Scheme 1**

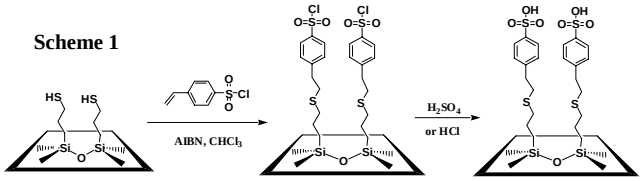


## Results and Discussion

As mentioned previously, utilizing of a heterogeneous solid acid catalyst for the synthesis of biodiesel could circumvent the separation of catalyst problem and eliminate the free fatty acids in the crude FFA-containing feedstocks to prevent the base-induced saponification during the transesterification reaction. Therefore, a highly efficient solid acid catalyst can serve not only as a "pretreatment catalyst" to remove FFA's from the triglycerides, but also as a catalyst for the conversion of the oil to biodiesel as well. To examine the catalytic performance of the MSN solid acid catalysts, we tested the catalytic properties of the sulfonic acid-functionalized mesoporous silicas for the methyl esterification of a common FFA (palmitic acid) with excess methanol.

Shown in Figure 2 is the catalytic activity of MSN-SO3H-BSA for the esterification of palmitic acid relative to MSN-COOH-BSA as well as the MSN-SH-BSA. MSN-SO3H-BSA had significantly higher activity than the other MSN materials. While the overall conversion achieved using MSN-SO3H-BSA was similar to $H_2SO_4$, the initial reactivity of the solid catalyst was higher than for $H_2SO_4$. Esterification of FFAs with methanol releases water that is known to limit the extent of the esterification reaction. The low level of palmitic acid conversion after 60 minutes for MSN-SO3H-BSA might be due to the presence of water with water potentially having a more detrimental impact on the performance of the solid catalyst than the homogeneous catalyst.

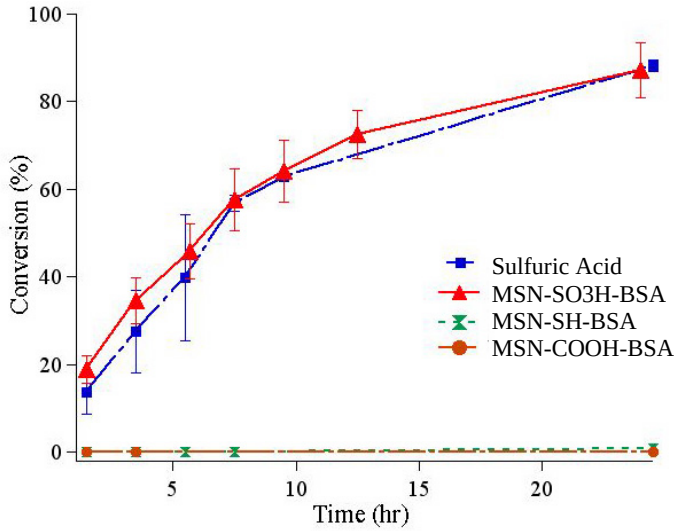


**Figure 2.** Esterification of palmitic acid with methanol catalyzed by sulfuric acid, MSN-SH-BSA, MSN-COOH-BSA, and MSN-SO3H-BSA materials at 35 °C.

## Conclusion

Organosulfonic acid functionalized mesoporous silica nanoparticles have been demonstrated to be able to catalyze the esterification of fatty acids to methyl esters. Tailoring the textural properties of the catalyst structure and tuning the surface concentration of the active site can enhance the performance of the mesoporous materials. Due to the narrow pore size distribution of the mesoporous materials, the pore size effect on internal mass transfer could be definitively determined. Proper choice of the organosulfonic acid group produced a functionalized mesoporous silica with activity at least comparable to $H_2SO_4$. This work demonstrates the potential of organic-inorganic mesoporous materials for rational design of heterogeneous catalysts.

**Acknowledgement.** This research was supported by the U.S. Department of Energy, Office of Basic Energy Sciences, through the Catalysis Science Grant No. AL-03-380-011 and NSF (CHE-0239570).

## References

(1) (a) Bender, M. *Bioresource Technol.* **1999**, *70*, 81. (b) Diasakou, M.; Louloudi, A.; Papayannakos, N. *Fuel* **1998**, ***77***, 1297. (c) Ogoshi, T., and Miyawaki, Y., *J. Am. Oil. Chem. Soc.* **1985**, *62*, 331. (d) Suppes, G.J.; Bockwinkel, K.; Lucas, S.; Botts, J.B.; Mason, M.H.; Heppert, J.A. *J. Am. Oil. Chem. Soc.* **2001**, *78*, 139.

(2) (a) Huh, S.; Wiench, J. W.; Trewyn, B. G.; Song, S.; Pruski, M.; Lin, V. S. Y. *Chem. Commun. (Cambridge)* **2003**, 2364-2365. (b) Huh, S.; Wiench, J. W.; Yoo, J.-C.; Pruski, M.; Lin, V. S. Y. *Chem. Mater.* **2003**, *15*, 4247-4256. (c) Lai, C.-Y.; Trewyn, B. G.; Jeftinija, D. M.; Jeftinija, K.; Xu, S.; Jeftinija, S.; Lin, V. S. Y. *J. Am. Chem. Soc.* **2003**, *125*, 4451-4459. (d) Lin, V. S. Y.; Lai, C.-Y.; Huang, J.; Song, S.-A.; Xu, S. *J. Am. Chem. Soc.* **2001**, *123*, 11510-11511. (e) Lin, V. S. Y.; Radu, D. R.; Han, M.-K.; Deng, W.; Kuroki, S.; Shanks, B. H.; Pruski, M. *J. Am. Chem. Soc.* **2002**, *124*, 9040-9041. (f) Radu, D. R.; Lai, C.-Y.; Huang, J.; Xu, S.; Lin, V. S. Y. *Chem. Commun. (Cambridge)* **2004**, in press. (g) Radu, D. R.; Lai, C.-Y.; Wiench, J. W.; Pruski, M.; Lin, V. S. Y. *J. Am. Chem. Soc.* **2004**, *126*, 1640-1641.

(3) Mbaraka, I. K.; Radu, D. R.; Lin, V. S. Y.; Shanks, B. H. *J. Catal.* **2003**, *219*, 329-336.

(4) Song, C. E.; Yang, J. W.; Ha, H.-J. *Tetrahedron: Asymmetry* **1997**, *8*, 841-844.

# NANOSTRUCTURES IN SYNTHESIS OF HETEROGENEOUS CATALYSTS

*W.M. Xue, Y.W. Suh, M.C. Kung, and H.H. Kung*

Chemical and Biological Engineering Department
Northwestern University
Evanston, IL 60208-3120

## Introduction

One area of rapid development in nanotechnology is the ability to synthesis a wide variety of nanostructures, which, in turn, is a consequence of the availability of a large number of macromolecules of various sizes, shapes, and functionalities. While these macromolecules can be used as catalysts in specific applications, they can also be used to enable preparation of catalysts in a much more controlled manner than what is possible previously. Examples of the latter applications include the well-known synthesis of mesoporous MCM materials, and more recently, preparation of metal nanoparticles using the dendrimer-assisted method. To our knowledge, however, there is not yet any report on the synthesis of cage-like structures in a controlled manner for catalytic applications. Here, we report our synthesis of nano-size cage-like structures for such purposes. In one example, we synthesized internally functionalized silica nanosphere. The functional groups can be used as catalytic sites or as sites to bind catalytic functions. In the second example, we synthesized siloxane cages of controlled sizes that mimic a zeolite cage, but our synthesis offers the ability to vary the cage and window sizes without apparent limitations.

## Internally functionalized silica nanocapsules

Hollow silica nanocapsules, about 2 nm in diameter with imprinted amines in the interior were synthesized using Si-containing amphiphile with carbamate group (Si-surfactant; I, Fig. 1a). The amphiphile was prepared by reaction of aminopropyltriethoxysilane with cetylchloroformate, followed by column chromatographic purification. The structure of I was confirmed by $^{1}$H-, $^{13}$C-, $^{29}$Si-NMR analyses, and mass spectrometry. This Si-surfactant self-assembles into micelles in the mixture of water and ethanol. Dynamic light scattering (DSL) of the surfactant solution showed the presence of micelles in the range of 1–3 nm in diameter, but primarily 2 nm. The ethoxy groups at the Si head group were then hydrolyzed using acidified ethanol-water solution. The hydrolyzed silanol groups were allowed to self-condense, and any remaining ones were reacted with dimethyldimethoxysilane to generate a thin silica shell. Complete hydrolysis was confirmed by $^{1}$H-NMR analysis, and it was shown that the NMR peaks for $–CH_3$ (1.22 ppm) and $–CH_2–$ (3.8 ppm) of the ethoxy groups were shifted to those for $–CH_3$ (1.18 ppm) and $–CH_2–$ (3.6 ppm) of ethanol, which was a product of the hydrolysis reaction. This silica shell was structurally robust, and the structure remained stable even if the solvent was changed. The inside cavity was created by cleaving the C-N bond by reaction with trimethylsilyliodine, which generated the tethered propylamine groups inside the silica capsule (Fig. 1b). Finally, the cleaved-off hydrocarbon chains would be removed by dialysis or solvent extraction. DLS analysis revealed that the micelles at all stages have a very similar size distribution in the range of 1–3 nm. These internal amines are catalytic active sites, can be used to bind metal ions, which could be further transformed into metal nanoparticles inside the nanospheres.

## Siloxane cages

Siloxane cages can function similarly to zeolite cages. However, to our knowledge, there are no reports of controlled synthesis of siloxane cages that could result in predetermined cavity and access window sizes. Here, we report the synthesis of bicyclic siloxane cages of an arbitrary but controlled size. The synthesis method involves stepwise construction of the cages, thereby offering complete control on the composition and size. This was accomplished by variation of the length of each siloxane branch, and the cage structure can be asymmetric. Figure 2 shows the structures of two examples. In each structure, the cavity is defined by three siloxane branches. Cage 1 has two identical branches which have three siloxane unit in each, while the third branch has five siloxane units. Cage 2 has all the three branches of different lengths of three, four, and five siloxane units. The structures of the cage compounds were confirmed by $^{1}$H, $^{13}$C and $^{29}$Si NMR, mass spectra and elemental analysis. Although the mass spectrum of cage 1 did not show the molecular ion (m/z 690), the fragment of $M^{+}$-$CH_3$ (m/z 675) was indicative of the desired structure. Similarly, the mass spectrum of cage 2 showed a fragment of $M^{+}$-$CH_3$ at m/z 749. The $^{13}$C NMR of cage 1 showed three peaks for $Me_2SiO_2$ groups at 1.10, 0.90 and 0.69 ppm, and one for $MeSiO_3$ at -2.93 ppm. Cage 2 showed five different $Me_2SiO_2$ groups in $^{13}$C NMR at 1.27, 1.08, 1.03, 0.90 and 0.72 ppm, and one $MeSiO_3$ group at -2.57 ppm. The $^{29}$Si NMR of 1 shows six peaks at -17.09, -19.54, -20.12, -48.42, -63.94 and -78.36 ppm in a ratio of 2:1:1:1:1:1, corresponding to two identical branches. In cage 2 all the $^{29}$Si NMR showed eight peaks at -19.49, -19.83, -20.49, -20.56, -21.32, -48.33, -66.65 and -80.52, indicating an asymmetric structure and all the three branches were different. These cages can be functionalized, and methods to do so will be presented.

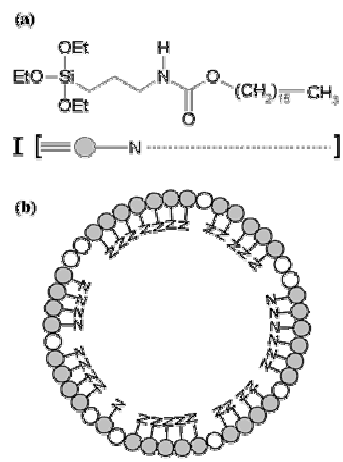


**Figure 1**. Molecular structure of Si-surfactant (a) and hollow silica nanocapsule internally functionalized with amine (b).

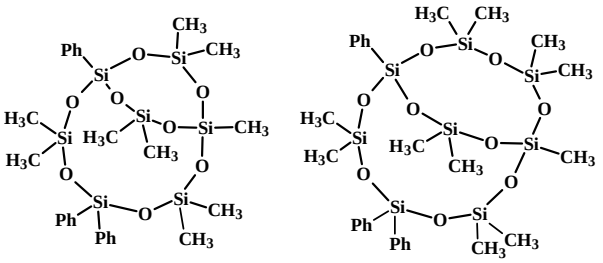

**1** **2**

**Figure 2.** Structures of two siloxane cages (bicyclic siloxane compounds) synthesized using a method that permits controlled of cage and window sizes.

# HOW TO PREVENT THE DEACTIVATION BY COKING OF ACID ZEOLITE CATALYSTS

*M. Guisnet* and P. Magnoux*

Université de Poitiers, Laboratoire de Catalyse en Chimie Organique, UMR CNRS 6503, 40, avenue du Recteur Pineau, 86022 Poitiers Cedex, France
e.mail : michel.guisnet@univ-poitiers.fr

## Introduction

Owing to their remarkable acid properties and their shape selectivity, zeolites are the catalysts most employed in refining (cracking, hydrocracking, hydroisomerization etc.) and petrochemical processes (alkylation, isomerization and disproportionation of aromatics etc.). The deactivation of zeolite catalysts which is observed during these processes is mainly due to the formation of non desorbed heavy secondary products generally designated as "coke" or as carbonaceous deposits. The cost of catalyst deactivation is often very high and mastering catalyst stability has become at least as important as controlling the activity and the selectivity. It is why most contributions to the field of deactivation (and regeneration) originate in industrial laboratories, much of the related data unfortunately remaining proprietary. However, academic laboratories contribute significantly to this field by developing the basic knowledge on the modes of coke formation and deactivation that is indispensable to master catalyst stability.

In this paper, coking and deactivation of acid zeolite catalysts are described, the aim being to use this description for modelling realistically the deactivation by coking of zeolite catalysts and even of all the porous acid catalysts. Indeed, their regular pore system makes of zeolites excellent models for understanding the effect of the catalyst characteristics and of the operating conditions on the rate of coking and on the deactivating effect of coke. Moreover the reactions, coking included, occur essentially within the molecular-size channels and cages, with as a consequence a steric limitation of the growth of coke molecules by the walls of these **nanoreactors** Therefore, coke molecules are not very bulky and the composition of coke can be quantitatively established.

## 1. Characterization of carbonaceous deposits

Part of the non desorbed reaction products which are responsible for zeolite deactivation are not polyaromatic, hence cannot be designated as coke. Therefore, to avoid any confusion the terms carbonaceous deposits or coke between inverted commas ("**coke**") will be applied here to all the non-desorbed products, polyaromatic or non-polyaromatic.

The characterization of carbonaceous deposits is still often limited to the amount and to their elemental composition. In the case of hydrocarbon transformations, the hydrogen to carbon ratio (H/C) is determined by quantitative analysis of $CO_2$ and $H_2O$ resulting from "coke" combustion, sometimes coupled with the determination of the oxygen consumption. The degree of "coke" aromaticity can be estimated from the H/C values. Generally the longer the time-on-stream and the higher the reaction temperature, the lower H/C hence the higher the degree of aromaticity.

Spectroscopic techniques : infrared (IR), Raman, ultraviolet and visible spectroscopy (UV-VIS), electron spin resonance (ESR), carbon 13 nuclear magnetic resonance ($^{13}C$ NMR) etc. are often used for determining the chemical identity of the "coke" components (1,2). With $^{13}C$ NMR, stable carbocation intermediates can also be detected (3). These techniques have the advantage of not modifying the "coked" catalysts which can therefore be characterized successively by several of them (4). Most of the studies have been carried out under static conditions. However, systems in which the deposition of the carbonaceous materials can be observed on the working catalyst have been developed. In particular, IR flow reactor cells with on-line analysis of the reaction products by mass spectrometry or gas chromatography are now currently used. In addition to information on the nature of the carbonaceous deposits, this operando technique can allow to specify the interaction between the deposits and the active sites (e.g. hydroxyl groups) and their effect on the activity and selectivity. Unfortunately, this technique leads often to limited information on the nature of carbonaceous deposits because of their complexity and of the difficulty to assign unambiguously an IR band to a particular species.

The only way to determine the **chemical composition of carbonaceous deposits** (i.e. the complete distribution of their components) is to totally separate them from the catalyst and then to analyze them by appropriate techniques (5). Such a method was developed for specifying the composition of "coke" formed during the transformations of various organic compounds, mainly hydrocarbons and oxygenated compounds over zeolite catalysts (6). In the first step, the carbonaceous compounds are liberated from the zeolite by dissolution of the aluminosilicate matrix in a hydrofluoric acid solution (40 %) at room temperature. In the second step, the soluble components are extracted by $CH_2Cl_2$ as a solvent and the non-soluble components are recovered. Blank tests with samples of an inert solid ($SiO_2$) impregnated with very reactive compounds show that the treatment with the acid solution causes no chemical changes of the carbonaceous compounds. The chemical identity of the components soluble in $CH_2Cl_2$ can be determined using IR, UV-VIS, H and $^{13}C$ NMR, etc. while their developed formula can be deduced from GC MS and GC/MS experiments.

Unfortunately, it is impossible to establish the chemical composition of the insoluble fraction which consists of very polyaromatic compounds (coke). The characterization of this coke is often limited to its elemental composition. Various physical techniques can however be used. Thus, through transmission electron microscopy (TEM) coupled with electron energy loss spectroscopy (EELS), it was shown that with HZSM5 and HOFF, the structure of insoluble "coke" was similar to that of coronene (pregraphitic), while with USHY it was more like that of pentacene (linear polyaromatic) (7). The distribution in mass of the insoluble "coke" components can also be established by laser desorption/ionisation time-of-flight mass spectroscopy (LD-MALDI-TOF-MS) (8).

## 2. How to minimize the rate of coking

**2.1 Modes of "coke" formation.** The modes of formation of carbonaceous deposits ("coke") during the transformation of hydrocarbons over acid catalysts were recently described (2). "Coke" results from the transformation of reactant(s), reaction products, impurities of the feed through various successive steps most of them bimolecular : condensation, hydrogen transfer, etc. (2). Therefore, the rate of coking depends on the parameters which usually affect the rate of catalytic reactions namely : a) the characteristics of the hydrocarbon reactant-active site couple ; b) the characteristics of the zeolite pore structure : in particular the size and the shape of the cages (or channel intersections) in which are located the acid sites ; c) the operating conditions : temperature, pressure, reactant concentration.

However, "coke" has the peculiarity of being a **non-desorbed product**. Therefore, its formation , besides the reaction steps requires the "coke" molecules to be retained inside the zeolite pores or non the outer surface of the crystallites. This retention occurs because "coke" molecules are not volatile enough to be eliminated from the zeolite under the operating conditions or because their size is greater

than the pore aperture (**trapping** in the cages or at channel intersections).

The composition of "coke" formed from various reactants on various zeolites shows that the first cause of retention is predominant at low temperatures (≤ 200°C), the second one at temperatures ≥ 350°C (9). Thus at 120°C, "coke" formed during propene transformation over a HMFI zeolite is constituted of $C_{10}$-$C_{35}$ alkanes, alkenes and dienes with a kinetic diameter (4.3 Å) lower than the micropore diameter (~ 5.5 Å) and with a boiling point (175-480°C) higher than the reaction temperature. In contrast, at 450°C, the soluble "coke" molecules (which are the only "coke" molecules up to 4 wt % coke) : polymethylbenzenes, naphthalenes, fluorenes and pyrenes have a boiling point lower than the reaction temperature but a kinetic diameter larger than the micropore diameter. However, these molecules are not located on the outer surface of the MFI crystallites. Indeed although soluble in $CH_2Cl_2$, they cannot be recovered in this solvent by soxhlet treatment of the coked zeolite. Therefore, these molecules are trapped within the MFI zeolite micropores and most likely located at the channel intersections which are enough large (8.5 Å ∅) to accommodate them (see for instance Fig. 1). For "coke" contents higher than 4 wt % insoluble "coke" appears at the expense of soluble "coke" molecules. Therefore insoluble "coke" molecules results from the growth of soluble "coke" molecules hence have a part of their skeleton located within the zeolite micropores ; the other part overflows onto the outer surface of the zeolite crystallites (7).

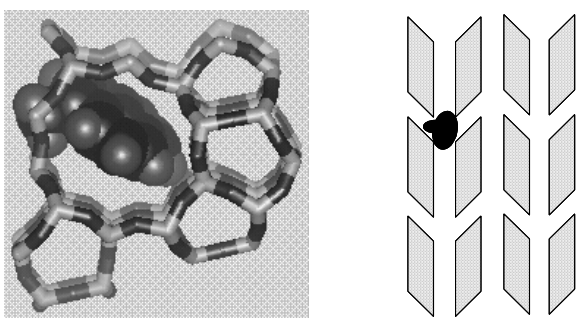

**Figure 1.** Location of the bulkiest soluble coke molecule (methylpyrene) formed from hydrocarbons at 450°C within the micropores of a HMFI zeolite.

**2.2 Pore structure and "coking" rate.** At high temperatures i.e. in the range of temperatures corresponding to most of the refining and petrochemical processes, the pore structure is the main parameter which determines the composition and the rate of "coke" formation (9) : **coking is a shape selective process**. The size and the shape of channels, cages or channel intersections determine the shape and the maximum size of the "coke" molecules which are trapped inside, their minimum size being determined by the size of the micropore apertures. Furthermore, the greater the difference between the size of channels, cages or channel intersections and the size of the pore apertures the easier the trapping hence the faster the formation of "coke". Thus the formation of "coke" during n-heptane transformation at 450°C was found to be ~ $10^3$ times faster with HERI which has **trap cages** (i.e. large cages (15.1 x 6.5 Å) with small apertures (3.6 x 5.2 Å)) than with HMFI in which the channel intersections (8.5 Å ∅) are only slightly larger than the micropore diameter (~ 5.5 Å).

**2.3 Acidity and "coking" rate.** The rate of coking and the selectivity to coke (for instance the coking/desired reaction rate ratio C/P) depends a lot on the **strength and density of the acid sites**. Thus, the rate of "coke" formation during n-heptane cracking at 450°C on USHY exchanged by sodium cations and the coking/cracking rate ratio (C/P) decrease significantly with increasing sodium content, which can be attributed to both a decrease in the strength and in the density of the acid sites. The positive effect of the density of the acid sites on the C/P ratio is clearly demonstrated in the case of dealuminated HY zeolites having similar acid strength (10). Moreover, this ratio is greater when the dealuminated Y samples present extra-framework Al species with a Lewis acidity, which has been related to an increase in the strength of the protonic sites caused by their interaction with these Lewis species (11).

**2.4 Operating conditions and coking rate.** On acid zeolites, coking occurs rapidly from alkenes and polyaromatics or from reactants which can be rapidly tranformed into these **coke-maker molecules** (12). On the other hand, it occurs slowly from the reactants such as linear akanes or monoaromatics whose transformation into alkenes or polyaromatics is slow. Thus, at 450°C on a USHY zeolite, coking occurs more or less at the same rate from propene, cyclohexene and methylnaphthalene ; it is slightly slower from cumene which cracks easily into benzene and propene, 10 times slower from toluene and n-heptane and 100 times slower from benzene. Moreover, from n-heptane and cumene, coke appears as a secondary product resulting from the transformation of the olefinic primary products.

During the transformation of alkenes (propene, cyclohexene ec.) on various zeolites, there is a minimum in the change of the coking rate with the **reaction temperature** T. This complex behaviour can be related to the fact that both the nature of the chemical steps involved in "coke" formation and the cause of trapping within the micropores change with T. From n-heptane, the rate of "coking" increases with T hence with the rate of cracking into alkenes which are coke-maker molecules.

The rate of coking increases generally with the **reactant pressure**. Thus in m-xylene disproportionation on mordenites the coking rate and the coking/disproportionation rate ratio for $P_{m\text{-}xylene}$ = 0.2 bar were about 2 times greater than for $P_{m\text{-}xylene}$ = 0.06 bar. The use of **hydrogen** in the feed was found to decrease the formation of "coke" and to improve the zeolite stability for typical reactions of acid catalysis such as toluene and cumene disproportionation (13). The effect is generally more pronounced when hydrogen is used at high pressure or activated by redox compounds. Obviously, the formation of "coke" is still more significantly reduced when there is a change from an acid to a bifunctional mechanism.

**2.5 General rules for limiting the formation of coke.** From the effect the zeolite characteristics and the operating conditions have on the rate of coking, general rules can be set up for limiting the formation of coke (Table 1).

**Table 1. General Rules for Limiting the Formation of "Coke" (11)**

*Choice and adaptation of the pore structure*

Space available near the active sites : large enough to allow the main reaction but narrow enough to limit the formation of "coke" by steric constraints

Diffusion path (size of the pore apertures, of the crystallites, etc.) allowing a rapid diffusion of "coke" precursors (in particular, no trap cages)

*Adjustment of the acidity*

Lowest density and weakest strength of the acid sites necessary for the selective formation of the desired products

*Choice of the operating conditions*

Conditions avoiding the formation of coke-maker side products (alkenes, polyaromatics)

Use of hydrogen (under pressure and/or activated by redox compounds) for reducing the concentration in "coke" precursors.

**3. How to minimize the deactivating effect of "coke"**

The number of "coke" molecules can be drawn from the amount and composition of "coke" hence the **deactivating effect of "coke" molecules** $D_K$ (and not only the deactivating effect of "coke") can be determined. This was done for n-heptane cracking at 450°C on protonic zeolites with different structures : monodimensional or tridimensional – small, average or large pore apertures – tubular or with cages. Table 2 shows that the $D_K$ values estimated initially and at complete deactivation depend very much on the zeolite (9).

**Table 2. Deactivating Effect ($D_K$) of "Coke" Molecules Formed during n-heptane Cracking over Protonic Zeolites. $D_K$ is the Number of Protonic Acid Sites that one "Coke" Molecule Renders Inactive. A : Initial Values ; B : Values at Complete Deactivation.**

| Zeolite | A | B |
|---|---|---|
| FAU | 5 | 1.3 |
| MOR | 25 | 7.5 |
| MFI | 0.25 | 1.0 |
| ERI | 30 | 7.0 |

This wide-ranging effect of the pore structure leads us to define four modes of deactivation instead of the two (**site coverage and pore blockage**) which are generally proposed. Deactivation could be due to : (a) a limitation of the access of the reactant to the active sites of a cage or a channel intersection in which is located a "coke" molecule, or (b) a blockage of the access ; (c) and (d) a limitation or a blockage of the access of the reactant to the active sites of cages, of channels intersections or parts of channels in which there are no "coke" molecules.

In modes a and b, the limitation or the blockage are either due to steric reasons, namely the diffusion of the reactants in the cage or at the channel intersections is limited or blocked, or chemical reasons – the "coke" molecules are reversibly or quasi-irreversibly adsorbed on the acid sites (site coverage). With these modes, the deactivation of the zeolite is generally limited since only the sites located in the cages or at the channel intersections (often only one site) are partially or totally deactivated.

Modes c and d correspond to what is generally called pore blockage. With these modes the deactivating effect of the "coke" molecules is very pronounced, because a large number of active sites are generally located in the inner pores.

With tridimensional zeolites having no trap cavities such as FAU and MFI, only site coverage (modes a and b) can be observed at low "coke" content while pore blockage appears at high "coke" content caused by coke molecules overflowing on the outer surface of the crystallites (Fig. 2).

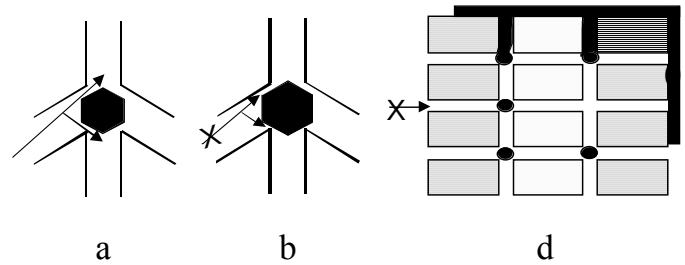


**Figure 2.** Modes of deactivation of a MFI zeolite. a and b : site coverage ; d : pore blockage.

Therefore, with HMFI whose acid sites are of identical strength the greater the "coke" content the greater the deactivating effect of "coke" molecules. The situation is more complex when the acid sites of the zeolites are of different strengths as is the case with HFAU zeolites. Indeed, the strongest acid sites, hence the most active, are the first to be deactivated, resulting in a large apparent deactivating effect of the "coke" molecules at low "coke" content (5).

With **monodimensional zeolites** such as HMOR or with zeolites presenting **trap cages** (large cages with small apertures) such as HERI, the deactivation occurs only through **pore blockage**. With HMOR, one "coke" molecule located in a large channel is able to block the access of the reactant to all the active sites located in this channel resulting in a large deactivating effect of the "coke" molecules. This large deactivating effect is also observed with HERI because the "coke" molecules initially formed, located inside the cages near the outer surface, limit and then block the access of the reactant to the inner cages (5).

Therefore, the pore structure of the zeolite is the main parameter which determines the deactivating effect of "coke" molecules. Hence, only tridimensional zeolites without trap cavities could be used as catalysts for reactions in which "coke" can be rapidy formed because of the presence of coke-maker molecules and operating conditions favouring "coke" formation. However, monodimensional zeolites or zeolites with trap cavities could be stable catalysts for processes in which the formation of "coke" is very slow. A typical example is n-hexane isomerization on a bifunctional PtHMOR catalyst. Modifications of the pore structure can also significantly decrease the deactivating effect of "coke" molecules. This has been shown, in particular, for the transformation of methanol to olefins on HMOR catalysts ; the deactivating effect of "coke" molecules is much lower (> 10 times) in dealuminated samples because mesopores created by dealumination allow a quasi-tridimensional diffusion of reactant molecules (14).

Besides the pore structure, the operating conditions can also affect, though indirectly, the deactivating effect of "coke" molecules. With operating conditions favouring a rapid formation of "coke", "coke" molecules will be formed and deposited in the pores of the outer part of the zeolite crystallites even if the zeolite is not monodimensional and has no trap cavities. These "coke" molecules block the diffusion of the reactant molecules to the acid sites of the core of the crystallites, with a large deactivating effect of "coke" molecules. This **shell blockage** was shown in methylnaphthalene transformation on a USHY zeolite.

Some general rules allowing to minimize the deactivating effect of "coke" are indicated in Table 3.

**Table 3. General Rules for Minimizing the Deactivating Effect of "Coke" (11)**

*Choice (or adaptation) of the pore structure* : Tridimensional zeolites without trap cages (large cages with small apertures) must be employed
*Adjustment of the acidity* : Homogeneous distribution in strength of the acid sites
*Choice of operating conditions* avoiding shell blockage

**References**


(1) Karge, H.G.; *Stud. Surf. Sci. Catal.* **1991**, *58*, 531-570 ; **2001**, *137*, 707-746.
(2) Guisnet, M.; Magnoux, P. *Appl. Catal. A: General*, **2001**, *212*, 83-96.
(3) Luzgin, M.V.; Arzumanov, S.S.; Shmachkova, V.P.; Kotsarenko, N.S.; Rogov, V.A.; and Stepanov, A.G. *J. Catal.* **2003**, *220*, 233-239.
(4) Guisnet, M. *Handbook of Heterogeneous Catalysis* ; Ertl, G.; Weitkamp, J., Eds ; Wiley-VCH, Weinheim, 1997; Vol 2, pp. 626-632.
(5) Guisnet, M.; Magnoux, P. *Appl. Catal.* **1989**, *54*, 1-27.
(6) Magnoux, P.; Roger, P.; Canaff, C.; Fouché, V.; Gnep, N.S.; Guisnet, M. *Stud. Surf. Sci. Catal.* **1987**, *34*, 317-330.
(7) Gallezot, P.; Leclercq, C.; Guisnet, M.; and Magnoux, P. *J. Catal.* **1988**, *114*, 100-111.
(8) Feller, A.; Barth, J.O.; Guzman, A.; Zuazo, I.; and Lercher, J.A. *J. Catal.* **2003**, *220*, 192-200.
(9) Guisnet, M.; Magnoux P.; and Martin, D. *Stud. Surf. Sci. Catal.* **1997**, *111*, 1-19.
(10) Wang, Q.L.; Giannetto, G.; and Guisnet, M. *J. Catal.* **1991**, *130*, 471-482.
(11) Guisnet, M.; Magnoux, P. *Catalysis Today* **1997**, *36*, 477-483.
(12) Guisnet, M.; Magnoux, P.; *Stud. Surf. Sci. Catal.* **1994**, *88*, 53-68.
(13) Absil, R.P.L.; Butt, J.; and Dranoff, J.S. *J. Catal.* **1985**, *92*, 187-196.
(14) Gnep, N.S.; Roger, P.; Cartraud, P.; Guisnet, M.; Juguin, B.; and Hamon, C. *C.R. Acad. Sci. Series II*, **1989**, *309*, 1743-1747.

# STUDY OF ZEOLITE NUCLEATION KINETICS

*Michael W. Deem*

Depts. Bioengineering and Physics & Astronomy
6100 Main Street – MS 142
Rice University
Houston, TX 77005-1892

## Introduction

Zeolites are crystalline microporous materials that have found a wide range of use as catalysts, molecular sieves, and ion exchangers. A typical example is ZSM-5, used as a cracking catalyst in the refinement of crude oil. Essentially all refinement of petroleum occurs through fluid catalytic cracking with a H-ZSM-5 zeolite catalyst. Essentially all reforming occurs with zeolitic catalysts, typically H-ZSM-5 or faujasite-type structures. A significant fraction of air separation into $N_2$ and $O_2$ occurs via a process involving the zeolite Li-X. Roughly 25% by weight of the powdered laundry used in washing machines is the zeolite Na-A, which softens the water for low-phosphate detergents. Finally, zeolites are widely used in remediation applications. For example, victims of the three-mile-island accident were fed ion-exchange zeolites to remove radioactive traces of $^{127}$Cs and $^{90}$Sr.

Zeolites continue to be synthesized at a furious pace. The major current limitation of our ability to synthesize zeolites with tailored properties is an incomplete understanding of the fundamental steps that occur in zeolite synthesis, which is normally carried out at hydrothermal conditions. Important factors that determine which zeolite will be made include the Si/Al ratio, the alkalinity, the cation species, and the presence of templates. A significant amount of experimentation, including NMR spectroscopy, X-ray diffraction, and neutron scattering, has been done in an effort to characterize the growth kinetics of zeolites yet the mechanism of nucleation is still not fully understood. One of the difficulties arises from the accessible length scale in experiments. NMR is able to provide information on the 0.5-1.0~nm scale. Diffraction, on the other hand, is limited to providing detailed information on the 5~nm and above length scale. The nucleation process falls, unfortunately, within this gap and is difficult to be identified directly. High temperature calorimetry provides thermodynamic data but no direct structural information. Recently, it has been possible to access the nucleation scale with a combination of electron microscopy, X-ray, and neutron diffraction methods. A working hypothesis formed is that, at least for template-mediated synthesis of ZSM-5, the nucleation event involves roughly 8 disordered unit cell precursors aggregating into a ``primary unit''. This aggregate forms the nucleation core, to which additional units are added. It is unclear whether the larger 5-10~nm globule is already crystalline or is amorphous. As the globule grows, a small crystallite begins to form. This type of nucleation on the length scale of a few unit cells is consistent with typical nucleation behavior of other electrolytes in aqueous media. In particular, the primary unit size for ZSM-5 is roughly 2 unit cells ona side, consistent with the nucleation scale of 2-3 unit cells for typical electrolytes condensing in aqueous media. Further support is provided by the observed primary unit size of 2.6 nm for zeolite beta (unit cell of 1.3 x 1.3 x 2.4 nm) and 1.6 nm for zeolite SOD (unit cell of 0.9 x 0.9 x 0.9 nm). These primary units were not detected under conditions for which no zeolite was formed (i.e., without template). The concentration of primary units decreased as the initial stages of nucleation and growth took place. All of these data show the strong correlation between the presence of the primary units and the rate of nucleation. This hypothetical mechanism for ZSM-5 synthesis, however, has not been unambiguously demonstrated to be correct.

The hypothetical zeolite nucleation event involves few enough atoms that it may be investigated computationally. Molecular dynamics has been used to examine the early stage of the polymerization process of silicate ions in aqueous solution. This dynamical approach yields important information of the reaction mechanism, but is limited to the case where the system is well above the saturation concentration and the free energy barrier is low. Methods that can investigate the nucleation event for simple solids have recently been developed. Related methods have been developed in the context of ion-induced aerosol nucleation. These methods make use of transition state theory, and so they avoid the time-scale problems associated with a direct simulation of the nucleation event.

As a first step towards fundamental understanding of the zeolite nucleation process, we present here a Monte Carlo study of silicate solutions, using a model with explicit Si and O atoms. We aim at constructing an equilibrium distribution of clusters that provides the free energy barrier of nucleation. Novel reactive moves that alter the connectivities of the silicate clusters, as well as other Monte Carlo moves, are used to equilibrate the system. No a priori building blocks are assumed in the simulation. Experimentally known features of aqueous silicate solutions are used to calibrate the model. We analyze the structure of the clusters found in the silicate nucleation process, and we compare the results with known zeolite structures.

## Discussion

Using an atomic-scale model for silicate solutions, the nucleation process during zeolite synthesis in the absence of a structure directing agent is investigated [1]. Monte Carlo schemes are developed to determine the equilibrium distribution of silicate cluster sizes within the context of this model. How the nucleation barrier and critical cluster size change with Si monomer concentration is discussed. Distance and angle histograms as well as ring size distributions are calculated and1 compared with known zeolite structures. The free energies of critical clusters are compared with those for small clusters of alpha-quartz. The barriers to nucleation are estimated to be on the order of 100 kT, and the critical cluster size is estimated to be between 25 and 50 silicons. Interestingly, the nucleation behavior is rather sensitive to the Si concentration in and the pH of the solution, in accord with experimental experience. Structural analysis shows the results reproduce physical properties of condensed phases of silica, such as the distance distribution and topological features. The smooth distribution of ring sizes suggests the cluster is amorphous up to 200 silicons.

We also survey the size and flatness of rings that occur in known zeolites and also in a set of hypothetical structures [2]. The results suggest that 16-membered rings, while rarely observed in zeolites, are not unique and should be thermodynamically accessible. Conversely, the results also show that rings of a given flatness, or planarity, become exponentially less likely as ring size increases. We compare the geometry of rings in known zeolites with the geometry of unconstrained rings as determined from Monte Carlo simulation. The rings that occur in zeolites are flatter than unconstrained rings due to the constraints imposed by the crystal. The thermodynamic factors that determine the flatness of rings in crystals is investigated by using a reverse umbrella sampling technique. Interestingly, the energy required to bring rings from an unconstrained state to the crystalline flat state is roughly 5 kJ/mol-Si, which is similar to the range to stabilities observed for zeolites and also to the range of interaction energies between zeolites and structure directing agents. Our results suggest that the main stumbling block in the formation of large pores is not

thermodynamics but rather identification of a suitable organo-cations as templating agents.

We discuss creation of a hypothetical zeolite database. Each of the 230 space groups is examined for hypothetical structures consisten with ZEFSAII energetics [3]. Unit cell parameters are varied within typical values (a, b, c, alpha, beta, gamma) as are unit cell densities.

**Acknowledgement.** This work was supported by the U.S. Department of Energy Office of Basic Energy Sciences.

**References**

(1) Wu, M.-G.; Deem, M. W.. *J. Chem. Phys.*, **2002**, *116*, 2125.
(2) Curtis, R. A.; Deem, M. W., J. Phys. Chem. B, **2003**, 107, 8612.
(3) Falcioni, M; Deem, M. W., *J. Chem. Phys.*, **1999**, *110*, 1754.

# PRIMARY STUDY ON MACRO POROUS FCC CATALYSTS PREPARED USING THE NANO POLYSTYRENE PARTICLES AS TEMPLATE

*Yanping Qi, Peng Dong, Sheng-Li Chen*,Bao-jian Shen*

State Key Laboratory of Heavy Oil Processing
and Department of Chemical Engineering,
University of Petroleum, Changping, Beijing 102249, China.

**Key words:** FCC, Catalyst, Macro Porous, Polystyrene Particles, Nanoparticles

## Introduction

The petroleum refining industry has been required to upgrade more and more heavy oil especially the residue with the decrease of light fraction content in crude oil and the great increase of the demand for light fuel oils, such as gasoline and diesel oil. However, due to the large molecular size of the residue, the diffusion of the residual molecules inside the FCC catalysts becomes an important factor that limits the catalyst activity and selectivity. The ideal residue FCC catalyst should have macropores and the macropore structure of catalyst matrix should be accessible for primary cracking of the large hydrocarbon molecules so that the forming smaller molecules can transfer into zeolite channels and further convert to value added product over zeolites sites. Described in this paper is a primary study on the synthesis of macro porous FCC catalysts using the polystyrene particles as template and their residual catalytic cracking performance.

## Experimental

In a typical synthesis, the precursor gel was prepared by mixing sodium silicate, dilute sulfuric acid , sodium aluminate and distilled water with stirring. The prepared FCC catalyst consisted of amorphous 85Wt%$Al_2O_3$-$SiO_2$ and 15Wt% REUSY and the particle size of the catalyst is 0.3~0.45 mm. In addition, the catalyst with macropores was introduced 55Vol% polystyrene spheres in the preparation. The polystyrene particles were removed from the catalyst through burning in air at 550 ℃. REUSY was offered by Zhoucun catalyst factory and the other chemicals were purchased from the market. The fluid catalytic cracking reactions were performed in a fixed bed micro reactor using Daqing atmospheric residua as the feed stock at the temperature of 500℃.

## Results and Discussion

The introduction of polystyrene spheres as template is aim to enhance the quantity of macropores of catalyst system, which reduce the diffuse resistance of large hydrocarbon molecules in catalyst pores. And the macropore diameter of catalysts can be precisely controlled by size of polystyrene spheres. The pore structure of the catalysts was characterized by BET and SEM. The features of Catalyst with macropores were showed figure (a) and (b).

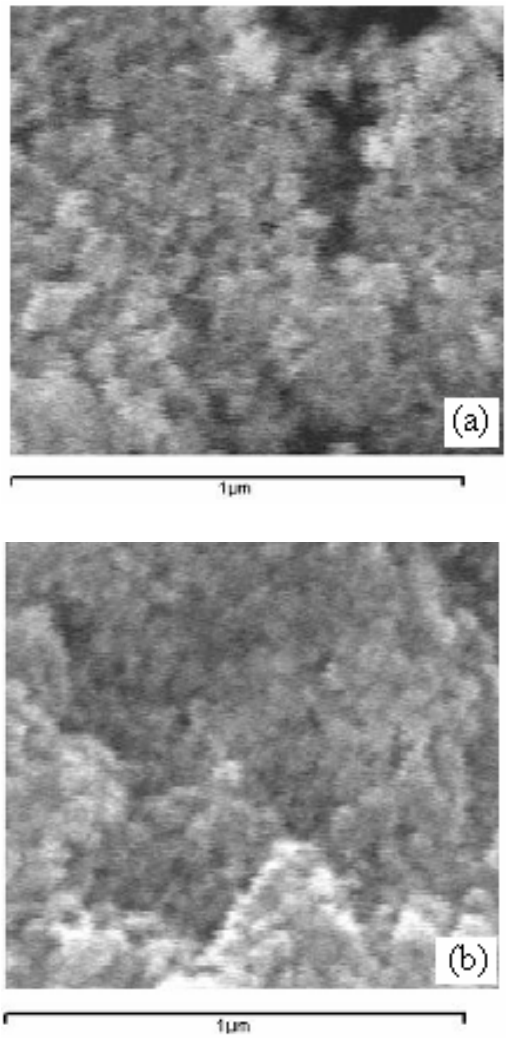


**Figure 1**.SEM feature of catalyst with macropores (a) and (b) introduced by the PS template

**Table 1* MAT result of cracking catalysts※**

| No. | Cat-1① | Cat-2② |
|---|---|---|
| $H_2$ | 0.036 | 0.061 |
| $C_1$～$C_2$ | 0.873 | 1.469 |
| LPG | 5.41 | 12.01 |
| Gasoline | 36.12 | 53.29 |
| Diesel | 24.24 | 18.66 |
| >350℃ oil | 27.43 | 4.98 |
| Coke | 6.133 | 9.525 |

※ The ratio of oil to catalyst is 3.2

① Cat-1 none template was used in the preparation

② Cat-2 the template diameter was 93nm

* The reaction temperature was 500℃

The experimental results showed that, the yield of gasoline was nearly 15Wt% high than the catalyst in whose preparation polystyrene particles were not used as template, and the yields of LPG increased 7.6 percent when the size of the PS template was 93nm. As the ratio of catalyst to oil increased, more LPG and $C_4^=$ were obtained, while the yield of gasoline and diesel have a maximum.

**Acknowledgement.** The authors thank the National Nature Science Foundation of China for support of this work (Grant No. 20376064) .The Foundation of National Key laboratory of Heavy Oil Processing of China in the whole work is also gratefully acknowledged.

*: Corresponding author Professor Sheng-Li Chen

# DESIGNING NANOSTRUCTURED MATERIALS FOR CATALYSIS THROUGH MULTISCALE SELF-ASSEMBLY

*Jun Liu*

Sandia National Laboratories,
Department of Chemical Synthesis and Nanomaterials,
P. O. Box 5800, MS 1411, Albuquerque, NM 87185-1411

## Introduction

Commercial catalysts and catalyst supports are complex and high surface area materials. Although widely used and widely investigated, the catalytic activities of these materials are difficult to understand. Fundamental studies on single crystalline materials, both theoretical and experimental, have made significant contributions to catalytic science. However, the lack of fundamental understanding of the catalytic activities in high surface area catalysts limits the development of effective catalysts for novel applications. In the last few years, great progress has been made in the designing and synthesis of tailored nanostructured materials. This paper summaries our recent efforts to control properties and structures of high surface area materials, from the molecular level to nanometer scale, and to macroscale. We hope that these new materials will make a significant contribution to the development of novel catalysts and to the fundamental understanding of catalytic properties of high surface area catalysts.

## Experimental

The high surface area materials discussed here are based on a surfactant templated approach.[1] Surfactant molecules co-assemble with the inorganic materials into sophisticated nanoscale structures through favorable molecular interactions.[2] The resultant nanoscale materials have extremely high surface area. Not only the scale of ordering (from 1.5 nm to 30 nm) and the crystalline symmetry (hexagonal, lamella, cubic, etc.) can be controlled, the morphology of the particles can be also varied.

The chemical activity is introduced into the porous materials through surface functionalization.[3] Several approaches have been used to incorporate functional groups and molecules into nanoporous materials.[4] Direct silanation of partially hydroxylated mesoporous silica depends on the population density of hydroxyl groups existing on the surface.[5,6,7] High density self-assembled molecular monolayers can be constructed by purposely introducing physically adsorbed layers of water molecules before silanation.[8] Alternatively, co-condensation is a one-step process in which the functional molecules were incorporated into the framework during the preparation of the mesoporous materials.[9]

A molecular lithography[10,11] process was developed from a molecular imprinting technique[12] to create molecular architecture in the molecular monlayers. This process produces heterogeneous, multifunctional molecular monolayers. Template molecules of controlled sizes and shapes, such as triangular (tripods), linear (dipods), and point cavities were deposited onto the nanoporous substrate. Long-chain molecules were then deposited on unoccupied surface of the silica substrates. Subsequently, the template molecules were selectively removed from the substrates to leave the desired cavities in the monolayer coating.

To form large ordered nano- and macroporous structures, we used a combination of self-assembly and controlled crystal growth. Hybrid silanes and bridged organic silsesquioxanes were used as the starting materials.[13-17] Inagaki *et al.* already prepared well-defined hybrid mesoporous crystals using 1,2-bis(trimethoxysilyl)ethane (BTME) as a silica source and hexadecyltrimethylammonium chloride (CTAC) as a surfactant.[18] Here we use BTME along with CTAC to create a new class of supported hierarchical nanoporous crystals through heterogeneous nucleation and growth.[19]

## Results and Discussion

Figure 1a is a TEM image of the hexagonal nanoporous structure. The amazing ordering of the self-assembled periodic nanostructures has been extensively illustrated in the literature, such as the three-dimensional cubic structures reported in the literature, SBA-6 and SBA-16.[20,21]

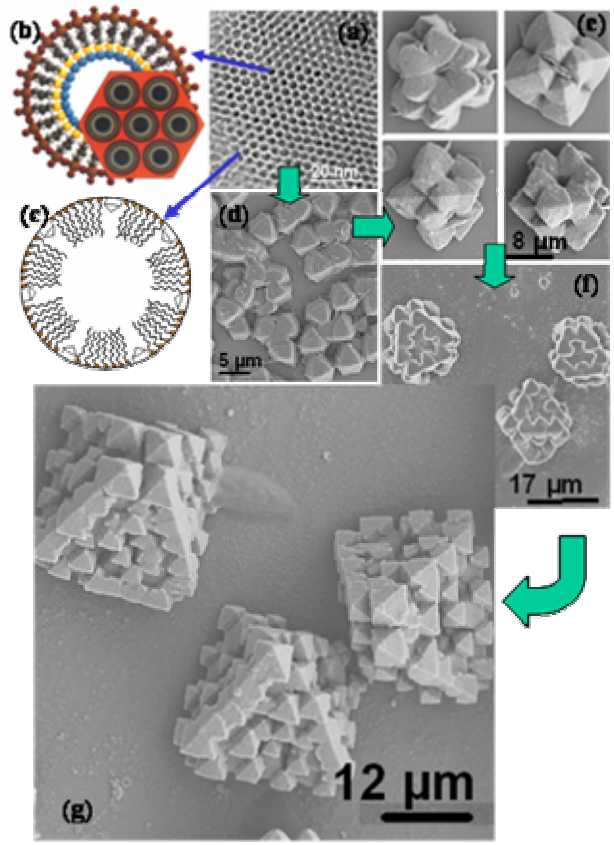


**Figure 1.** Self-assembled porous materials with multiscale ordering. (a) Hexagonally ordered nanopoorus silica. (b) Self-assembled monolayers on nanoporous silica. (c) Microcavities with controlled sizes and shapes created by molecular lithography within self-assembled monolayers. (d) Octahedral crystals made of self-assembled nanoporous silica. (e) Secondary crystals made of 24 individual octahedral crystals. (f) Tertiary structures made of individual octahedral crystals. (g) High order structures made of individual octahedral crystals.

Self-assembled monolayers on nanoporous supports provide new opportunities to tailor the pore size and surface chemistry on a molecular scale (Figure 1b). Key material parameters can be adjusted and independently evaluated. (1) Pore channel size. The actual pore channel spacing is determined by the pore size of the support and the chain length of functional molecules on the surface. Therefore, the pore channel sizes will be varied from Ångstrom level to nanometer scale by adjusting the pore size of the support and the molecular size of the functional groups. (2) Stereochemical interactions. This stereochemical relationship can be adjusted by manipulating the arrangement of the functional groups on the surface (for example, the population density or chain length). (3) Functionality of the surface groups. The functional groups, as well as their spatial distribution, can be substituted and tailored for a particular application.

Furthermore, the molecular lithography technique allows us to create controlled three dimensional architectures within the monolayers (Figure 1c). By properly choosing the template molecules, the size and shape of the cavities can be systematically varied. Zeolite-like properties, such as size and shape selective adsorption and selective catalysis have been demonstrated. The microcavities on the monolayer coatings showed excellent size and shape selectivity during adsorption studies. In addition, we can take advantage of the conformational changes of the long-chain molecules in the monolayer coating to regulate the accessibility of the microporous cavities in the monolayer. Tunable access is a highly sought-after property and is usually observed in biomembranes, but not in inorganic microporous materials. The microcavities are fully accessible in the open position and partially accessible or inaccessible in the closed position.

On the micrometer scale, well-defined and oriented nanoporous crystals were formed through controlled nucleation and growth. Figures 1d shows the primary 5 μm octahedral crystals formed by the {111} planes of the cubic phase. These crystals are rather uniform in shape and size (12 μm wide here). Low angle X-ray diffraction (XRD) and transmission electron microscopy (TEM) indicate that these crystals have a cubic structure (Pm3n, $a_o$ = 98 Å) as reported in the literature.

Hierarchically ordered large crystals and open macroporous structures can be constructed through multiple and self-similar growth. The new self-assembled crystals add to the existing crystals during multiple growth processes. Figure 1e shows a commonly observed rosette-like, secondary structure viewed from different angles, indicating that these crystals are stacked structures made of primary octahedral subunits. The secondary structure is about 11 μm in width, two times the size of the primary structure, and is based on a quartet-octahedron model with 24 edge-sharing octahedral primary subunits. The large crystal contains four surfaces made of six subunits and six corners made of four subunits. Figure 1f shows the tertiary octahedral structures containing three subunits on each side. The width of the tertiary structure is 16 μm, roughly three times the size of the primary crystal.

On a much large length scale, high order structures can be derived by edge-sharing growth (Figure 1g). These large crystals are remarkable in several ways. First, these structures are not close packed and contain large empty spaces (macroporosities), but they still have almost perfect octahedral shapes. Second, the octahedral subunits in the large structure are all about 5 μm in size and are fairly uniform. These subunits are also well aligned throughout the crystal by edge sharing. Finally, the high order octahedral crystals are also rather uniform in size.

**Conclusions**

We developed general solution based approaches to systematically control the crystal shape, morphology, surface and interfacial properties. The control morphologies may allow us to control the reactions on specific model surfaces or interfaces in model high surface area crystals. We discussed our efforts to control the properties of the materials over multiple length scales. Self-assembled monolayers in the nanoporosity enabled us to obtain molecular level control of the active groups on the surfaces, and provided the opportunity to create complex architectures on molecular and nanometer scale. On large length scales, we are developing techniques to form uniform and well-defined crystals, and construct true hierarchical superstructures from such self-assembled crystals with long range ordering and uniform macroporosities.

**Acknowledgement.** This work is supported by the Sandia National Laboratories (SNL) Laboratory-Directed Research and Development Program (LDRD), and by the Division of Materials Sciences and Engineering, Office of Basic Energy Sciences, U.S. Department of Energy. SNL is a multi program laboratory operated by Sandia Corporation, a Lockheed Martin Company, for the Department of Energy under Contract DE-AC04-94AL85000.

**References**

(1) (a) Beck, J. S.; Vartuli, J. C.; Roth, W. J.; Leonowicz, M. E.; Kresge, C. T.; Schmitt, K. D.; Chu, C. T-W.; Olson, D. H.; Sheppard, E. W.; McCullen, S. B.; Higgins, J. B.; Schlenker, J. L. *J. Am. Chem. Soc.* **1992**, *114*, 10834. (b) Kresge, C. T.; Leonowicz, M. E.; Roth, W. J.; Vartuli, J. C.; Beck, J. S. *Nature* **1992**, *359*, 710.

(2) Monnier, A.; Schuth, F.; Huo, Q.; Kumar, D.; Margolese, D.; Maxwell, R. S.; Stucky, G. D.; Krishnamurty, M.; Petroff, P.; Firouzi, A.; Janicke, M.; Chmelka, B. F. *Science* **1993**, *261*, 1299.

(3) Sayari, A. *Chem. Mater.* **1996**, *8*, 1840.

(4) Moller, K.; Bein, T. *Chem. Mater.* **1998**, *10*, 2950.

(5) Cauvel, D.; Renard, G.; Brunel, D. *J. Org. Chem.* **1997**, *62*, 749.

(6) Burkett, S. L.; Simms, S. D.; Mann, S. *J. Chem. Soc. Chem. Comm.* **1996**, 1367.

(7) (a) Mercier, L.; Pinnavaia, T. J. *Adv. Mater.* **1997**, *9*, 500. (b) Mercier, L.; Pinnavaia, T. J. *Envir. Sci. Technol.* **1998**, *32*, 2749.

(8) (a) Feng, X.; Fryxell, G. E.; Wang, L.-Q.; Kim, A. Y.; Kemner, K.; Liu, J. *Science*, **1997**, *276*, 923. (b) Liu, J.; Feng, X.; Fryxell, G. E.; Wang, L.-Q.; Kim, A. Y.; Gong, M. *Adv. Mater.* **1998**, *10*, 161.

(9) Lim, M. H.; Blanford, C. F.; Stein, A. *Chem. Mater.* **1998**, *10*, 467.

(10) Shin, Y.; Liu, J.; Wang, L.-Q.; Nie, Z.; Samuels, W. D.; Fryxell, G. E.; G. J. Exarhos, G. J. *Angew. Chem. Int. Ed*, **2000**, *39*, 2702.

(11) Liu, J.; Shin, Y.; Fryxell, G. E.; Wang, L.-Q.; Nie, Z.; Jeong Ho Chang, J. H.; Samuels, W. D.; Exarhos, G. J. *J. Phy. Chem. A.* **2000**, *104*, 8328.

(12) For a review, see (a) Wulf, G. *Angew Chem. Int. Ed. Engl.* **1995**, *34*, 1812. (b) Davis, M. E.; Katz, A.; Ahmad, W. R. *Chem. Mater.* **1996**, *8*, 1820.

(13) Inagaki, S.; Guan, S.; Fukushima, Y.; Ohsuna, T.; Terasaki, O. *J. Am. Chem. Soc*. **1999**, *121*, 9611.

(14) Lim, M. H.; Stein, A. *Chem. Mater.* **1999**, *11*, 3285.

(15) Asefa, T.; MacLachlan, M. J.; Coombs, N. Ozin, G. A. *Nature*, **1999**, *402*, 867.

(16) Dag, O.; Yoshina-Ishii, C.; Asefa, T.; MacLachlan, M. J.; H. Grondey, H.; Coombs, N.; Ozin, G. A. *Advanced Functional Materials*, **2001**, *11*, 213.

(17) Fan, H. Y.; Reed, S.; Baer, T.; Schunk, R.; Lopez, G. P.; Brinker, C. J. *Microporous and Mesoporous Materials*, **2001**, *44*, 625.

(18) Guan, S.; Inagaki, S.; Ohsuna, T.; Terasaki, O. *J. Am. Chem. Soc.* **2000**, *122*, 5660.

(19) Tian, Z. R.; Liu, J.; Voigt, J. A.; Mckenzie, B.; Xu, H. *Angew. Chem. Int. Ed*, **2003**, *42*, 413.

(20) Zhao, D.; Feng, J.; Huo, Q.; Melosh, N.; Fredrickson, G. H.; Chmelka, B. F.; Stucky, G. D., *Science*, 1998, *279*, 548.

(21) D. Zhao, Q. Huo, J. Feng, B. F. Chmelka, and G. D. Stucky, *J. Am. Chem. Soc.*, **1998**, *120*, 6024.

# DEEP HYDRODESULFURIZATION ON NI-$MOS_2$, CO-$MOS_2$, AND PT-PD CATALYSTS ON $Al_2O_3$ AND ASA

*Roel Prins, Marina Egorova, and Adeline Röthlisberger*

Institute for Chemical and Bioengineering
Swiss Federal Institute of Technology (ETH), Zurich, Switzerland

## Introduction

Nitrogen-containing compounds inhibit hydrodesulfurization (HDS) of sulfur-containing compounds. In the past this was not a problem, because the amount of N-containing molecules in naphtha and gasoil is much smaller than that of S-containing molecules. However, environmental legislation requires a strong reduction of the sulfur content of gasoline and diesel fuel to 10 ppm by the year 2010. At that low sulfur level even small amounts of N-compounds will be harmful because of competitive adsorption.

Dibenzothiophenes are constituents of gasoil and especially 4,6-dialkyldibenzothiophenes react slowly in HDS. Therefore we have prepared 4,6-dimethyldibenzothiophene (DMDBT), 4,6-dimethyl-tetrahydro-dibenzothiophene (DM-TH-DBT), 4,6-dimethyl-hexahydro-dibenzothiophene (DM-HH-DBT), and 4,6-dimethyl-dodecahydro-dibenzothiophene (DM-DH-DBT) and studied the HDS of these sulfur-containing molecules. The influence of N-containing compounds on HDS was studied with 2-methylpyridine and 2-methylpiperidine in the case of metal sulfide catalysts and pyridine and piperidine in the case of noble metal catalysts. As catalysts we used Ni-$MoS_2$, Co-$MoS_2$, and Mo on $\gamma$-$Al_2O_3$ as well as Pt, Pd, and Pt-Pd on $\gamma$-$Al_2O_3$ and amorphous silica-alumina (ASA). The experiments were performed at 5 MPa total pressure and 300-340°C.

## Experimental

**Catalyst preparation.** The NiMo, CoMo and Mo catalysts (8 wt% Mo and 3 wt% Co or Ni) and Pt, Pd, and Pt-Pd catalysts (0.25 or 0.5 wt% for each metal) were prepared by incipient wetness impregnation of $\gamma$-$Al_2O_3$ or ASA with aqueous solutions of $(NH_4)_6Mo_7O_{24}{\cdot}4H_2O$, and Ni or Co nitrate, and $M(NH_3)_4(NO_3)_2$ respectively. After impregnation the catalysts were dried in air at 20°C, then in an oven at 120°C for 15 h, and finally calcined at 500°C for 4 h.

**Reactions.** The HDS and HDN reactions were carried out in a continuous-flow fixed-bed reactor. The NiMo, CoMo and Mo catalysts were sulfided *in situ* with 10% $H_2S$ in $H_2$ at 400°C and 1.0 MPa for 4 h. The metal catalysts were reduced *in situ* with $H_2$ at 300°C and 0.5 MPa for 2 h. After sulfidation or reduction, the pressure was increased to 5.0 MPa, and the liquid reactant was fed to the reactor by means of a high-pressure pump. Experiments were carried out at 300-340°C for the metal sulfide and 300°C for the metal catalysts. The gas-phase feed contained 1 kPa DMDBT and the total pressure was 5.0 MPa in all cases. In experiments over the sulfidic catalysts 1-6 kPa amine and 35 kPa $H_2S$ were added, while over the metal catalysts 0.02-0.5 kPa amine was added. The reaction products were analyzed by off-line gas chromatography with a PTA-5 fused silica capillary column and FID as well as pulsed flame photometric detection. Weight time was defined as the ratio between the catalyst weight and the molar flow to the reactor. The weight time was varied by varying the flow rates of the liquid and the gaseous reactants while keeping their ratio constant. Further experimental details have been published before.[1]

## Results and Discussion

**HDS of DMDBT**. The product distribution in the HDS of DMDBT, DM-TH-DBT, DM-HH-DBT and DM-DH-DBT showed that the HDS of DMDBT occurred as indicated in **Scheme 1** over all catalysts: i) by direct desulfurization (DDS), leading to the formation of 3,3'-dimethylbiphenyl, and ii) by hydrogenation (HYD) yielding DM-TH-DBT, DM-HH-DBT, and DM-DH-DBT, followed by desulfurization to methylcyclohexyl-toluene and 3,3'-dimethylbicyclohexyl. Slow hydrogenation of 3,3'-dimethylbiphenyl to methylcyclohexyl-toluene and methylcyclohexyl-toluene to 3,3'-dimethylbicyclohexyl was observed in the presence of Ni-$MoS_2$, $MoS_2$ and noble metal catalysts.

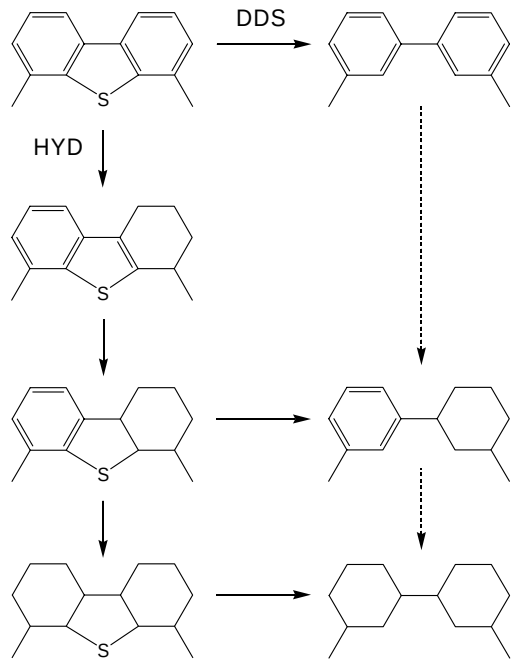


**Scheme 1.** HDS network of 4,6-dimethyldibenzothiophene.

The methyl groups adjacent to the sulfur atom strongly hinder the DDS pathway that occurs via $\sigma$-adsorption of DMDBT, and weakly promote the hydrogenation that requires a $\pi$-adsorption mode. Thus, the conversion of DMDBT predominantly occurs via the HYD pathway.

While over sulfided catalysts only the tetrahydro-intermediate of DMDBT was observed, over the noble metal catalysts also the hexahydro- and dodecahydro-intermediates were detected in significant amounts. Their highest selectivities were found on Pd and Pt-Pd catalysts **(Figure 1)**. This could be due to the relatively weaker direct desulfurization and faster hydrogenation on the metals as well as to the fact that these partially hydrogenated intermediates are desulfurized in the $\sigma$-adsorption mode as was reported for sulfide catalysts.[2] These observations in the HDS of DMDBT were confirmed in the HDS of DM-TH-DBT and DM-HH-DBT over sulfide catalysts. In these reactions the main product was 3,3'-dimethylbicyclohexyl and not methylcyclohexyl-toluene showing the difficulty of the sulfur removal from partially hydrogenated intermediates **(Figure 2)**. Only after complete hydrogenation of DMDBT to DM-DH-DBT the steric hindrance is reduced and the molecule can be desulfurized.

Relatively less direct desulfurization of DMDBT into 3,3'-dimethylbiphenyl and more hydrogenation into DM-TH-DBT was observed over the ASA-supported noble metal catalysts. Thus, the selectivity in the DDS product decreased from 15% on Pt/$Al_2O_3$ to 6% on for Pt/ASA. We ascribe this to the lower metal dispersion on ASA and lower number of edge and kink sites needed for the DDS. Moreover, substantial isomerization of the methyl groups and

cracking of the products into methylcyclohexane and toluene occurred over the acidic ASA-supported catalysts.

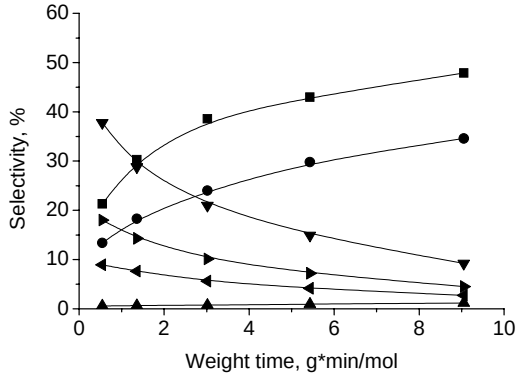


**Figure 1.** Product selectivities in the HDS of DMDBT over 0.5wt% Pd/γ-$Al_2O_3$ as a function of weight time (■ 3,3'-dimethylbicyclohexyl; ● methylcyclohexyl-toluene; ▼ DM-TH-DBT; ► DM-HH-DBT; ◄ DM-DH-DBT; ▲ 3,3'-dimethylbiphenyl).

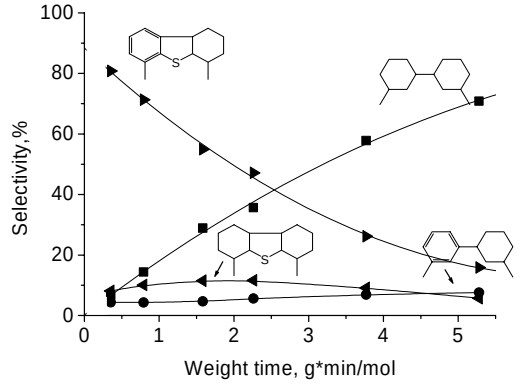


**Figure 2.** Product selectivities in the HDS of DM-TH-DBT over $MoS_2$/γ-$Al_2O_3$ as a function of weight time.

The activity order of the catalysts was Pt-Pd > Pd > Pt > Co-$MoS_2$ ≥ Ni-$MoS_2$ > $MoS_2$ and the ASA-supported noble metal catalysts were more active than the $Al_2O_3$-supported ones.

**Influence of N-compounds.** 2-Methylpyridine and 2-methylpiperidine strongly suppressed the HDS of DMDBT over the sulfidic catalysts. At 2 kPa nitrogen-compounds, the conversion of DMDBT decreased by factors of 3.5-4, 14-16, and 6-10 over Ni-$MoS_2$, Co-$MoS_2$, and $MoS_2$ respectively **(Figure 3)**. The HYD pathway was more strongly inhibited than the DDS pathway, leading to an increase in the 3,3'-dimethylbiphenyl selectivity in the presence of N-containing molecules. 2-Methylpiperidine suppressed the overall HDS and the HYD pathway somewhat stronger than 2-methylpyridine.

Amines also suppressed the HDS of DMDBT over the metal catalysts. In the presence of 0.5 kPa pyridine and piperidine the conversion of DMDBT decreased by a factor of 2.7, 2, and 1.5 over the Pt, Pd, and Pt-Pd on $Al_2O_3$ catalysts respectively **(Figure 4)**. The bimetallic catalyst showed a better resistance toward poisoning. As in the case of the sulfidic catalysts, an increase in the selectivity of the DDS product was observed when increasing the amount of N-containing molecules. This is due to a stronger inhibition of the HYD pathway. On the ASA-supported metal catalysts similar influences were observed and the acid-catalyzed reactions, such as isomerization and cracking of the products, were almost totally suppressed in the presence of the amines.

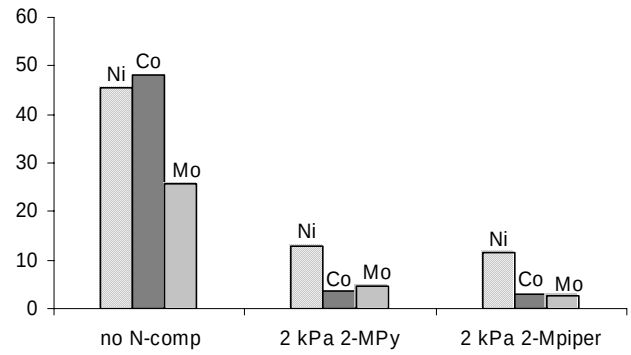


**Figure 3.** Conversion of DMDBT in the absence and in the presence of 2 kPa 2-methylpyridine and 2-methylpiperidine over Ni-$MoS_2$, Co-$MoS_2$, and $MoS_2$ catalysts.

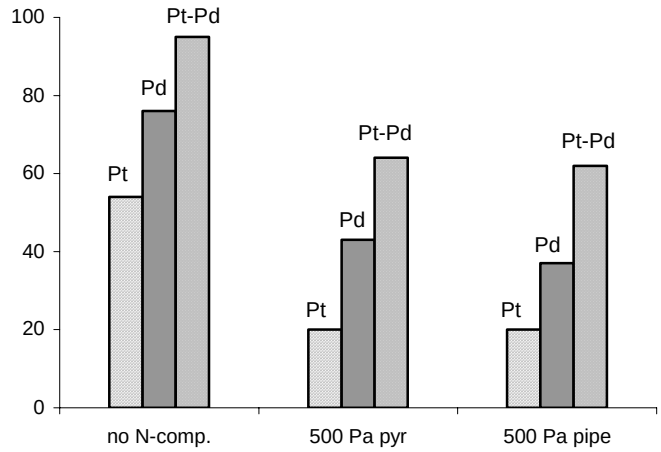


**Figure 4.** Conversion of DMDBT in the absence and in the presence of 0.5 kPa pyridine and piperidine over Pt, Pd, and Pt-Pd alumina-supported catalysts.

## Conclusions

Nitrogen-containing molecules are strong inhibitors of the HDS of DMDBT over all studied catalysts. The main pathway of the HDS of DMDBT is the HYD and it is affected by N-compounds somewhat more strongly than the DDS route. Among the sulfided catalysts Ni-$MoS_2$ is the least sensitive to the presence of 2-methylpyridine and 2-methylpiperidine and Pt-Pd/γ-$Al_2O_3$ is the least susceptible to the presence of pyridine and piperidine among the metal catalysts.

## References


(1) Egorova, M.; Prins, R. *Journal of Catalysis* **2004**, *224*, 278.
(2) Egorova, M.; Prins, R. *Journal of Catalysis* **2004**, *225*, 417.

# HDS & DEEP HDS ACTIVITY OF Co/Mo/S-MESOSTRUCTURED SYNTHETIC CLAYS

*K. A. Carrado[1], C. Song[2], J. H. Kim[2], N. Castagnola[1], R. Fernandez-Saavedra[3], C. L. Marshall[4], M. M. Schwartz[4]*

[1]Chemistry and [4]Chemical Engineering Divisions, Argonne National Laboratory, Argonne, IL
[2]Dept. of Energy & Geo-Environmental Engineering, Pennsylvania State University, University Park, PA
[3]ICMM-CSIC, Madrid, Spain

**Abstract**

Silica sol can be used as the silicon-containing starting material when creating nanoporous layered silicate catalysts, and a certain portion of unreacted sol particles is incorporated into the final matrix. The resulting structure then has mesoporosity and a unique morphology. Hectorite-based clays have been prepared using different silica sols in order to ascertain the importance of sol characteristics on the final matrix. Several techniques have been applied to characterize the materials, including XRD, TGA, $N_2$ porosimetry, and TEM. For hydrodesulfurization (HDS), the conversion of dibenzothiophene (DBT) to biphenyl was examined at 400°C using Co/Mo/S-loaded mesostructured clay supports. Activity was compared to a Crosfield 465 commercial catalyst. No hydrogenation was observed with any of the clay supports. The most active clay was derived from ludox silica sol AS-30, with an activity of 65% DBT conversion (86% for Crosfield 465). For deep HDS, the conversion of 4,6-dimethyldibenzothiophene was tested at 325°C and 350°C and compared to a Criterion 344 commercial catalyst. At 325°C, Cr344 displays 11.4% conversion. This value is nearly attained for the Co/Mo/S-loaded mesostructured clay derived from AM30 silica sol (10.5%). The commercially available synthetic hectorite called Laponite has very low activity (3.0%), indicating that the unique morphology of the mesostructured clays is important. Hydrogenolysis vs. hydrogenation pathways are compared for the deep HDS reaction.

**Introduction**

Because of their characteristic porous structure, surface reactivity, and ion exchange capacity, clays are useful catalysts. Over the years, our group has developed and patented a general technique for the hydrothermal synthesis of magnesium silicate hectorite clays in the presence of inorganic, organic, organometallic and polymeric intercalants[1]. This process involves the hydrothermal crystallization of a gel containing silica sol, magnesium hidroxide sol, lithium fluoride, and an alkylammonium cation or polymer if an organo-hectorite is desired.

A certain portion of unreacted sol particles is incorporated into the final matrix. The resulting structure then has mesoporosity and a unique morphology[2]. Previous reports concerning the feasibility of these materials as supports for HDS have been published[3]. Here we report on the preparation using different silica sols in order to examine the importance of sol particle size, pH, and surface chemistry on the final matrix. The test catalytic reactions are based on hydrodesulfurization reactivity. The importance of new design approaches to ultra-clean diesel fuels by deep desulfurization has been pointed out recently[4].

**Experimental**

**Materials.** The mesostructured clays were prepared according to published methods[1]. The silica sols were obtained from Aldrich and include HS-30, SM-30, AM-30, AS-30, and TM-40. This represents a variety of sol particle sizes, pH values, and counter-ions as shown in Table 1. Both tetrethylammonium (TEA)- and lithium(I) (Li)-containing versions of the clays were made and denoted by the terms TEA-HS30 or Li-TM40, for example. Calcination was performed by heating the clay to 400°C in a $N_2$ atmosphere and then to 500°C in air prior to metal loading for HDS.

**Characterization.** XRD patterns were recorded on a Rigaku Miniflex+ with Cu K radiation, a 0.05 °2θ step size, and 0.5 °2θ scan rate using powders. TEM images were acquired using a FEI TECNAI F30ST operating at 300 kV with a CCD camera. One drop of clay slurry in MeOH (sonicated for 1 hr) was placed onto 3 mm holey carbon Cu grids; excess solution was removed and the grid dried at 100°C for 10 min. $N_2$ porosimetry was obtained on a Micromeritics ASAP2010 after degassing at 110°C for at least 3 hr, and employing the multipoint BET and BJH methods.

**HDS Catalysis.** For catalyst preparation, 4 gm clay support was impregnated with $(NH_4)_6Mo_7O_{24}$•$4H_2O$ (Aldrich) solution to give 6% Mo, dried at 110 ºC for 1 hr, and calcined at 400 ºC for 4 hr. The cooled catalyst was then impregnated with $Co(NO_3)_2 \cdot 6H_2O$ (Baker) solution to give 2% Co, dried at 110 ºC for 1 hr, calcined at 400 ºC for 4 hr. The catalysts were then pelletized in a Carver press, crushed and sieved retaining 10-20 mesh portion, heated under $N_2$ at 280ºC for 1 hr and then sulfided with 8% $H_2S$ in $H_2$ at 350ºC for 2 hr and resieved to 10-20 mesh. 1.0 gm sulfided and sieved catalyst was mixed with 2.0 gm SiC (20 size; Electro Abrasives) and loaded into the trickle-bed reactor, a thick-walled 0.375" ID 316 SS tube that is mounted vertically in a three zone furnace. The catalyst is located in the center of the tube between plugs of quartz wool and on top of a deadman used to minimize the volume between the reactor and the liquid receiver. The liquid test feed consisted of 0.25 wt% sulfur as dibenzothiophene (DBT) in hexadecane (1.4 wt% DBT). The reaction was carried out at 400 °C under 286 psig $H_2$ (400 psig $H_2$ plus $N_2$) with WHSV = 15-18. After a slopped fore-cut of 3 or 4 hr to reach steady-state, 2 or 3 one hour samples were collected, analyzed, and the results averaged. The reproducibility of the conversion measurements was ± 4% of the reported values; mass balances were 100 ± 2%. The reaction products were diluted with mixed hexanes (0.3-0.7g in 10.0 ml), separated using a DB5-MS column, and analyzed using an HP 5890A GC-MS. The reaction products are biphenyl and unconverted DBT.

**Deep HDS Catalysis.** A two-step wet impregnation method was used to load the catalyst. First, 6 wt% Mo is added in water from ammonium heptamolybdate tetrahydrate. After drying, 2 wt% Co is added in water as cobalt(II) nitrate hexahydrate. The catalysts are dried at 110°C overnight, calcined at 500°C for 5 hr, then pre-sulfided at 350°C over a 4-hr ramp and held for 2 hr in 5% $H_2S$-$H_2$ using a flow apparatus. The catalysts were stored in decalin after presulfidation. HDS of 1.23 wt% 4,6-dimethyldibenzothiophene (DMDBT) in decalin solvent was performed at 325 and 350 °C for 30 min under an initial hydrogen pressure of 300 psi (20.4 atm). A microbatch reactor of 25 ml volume was employed using 4.0 gm of feed and 0.10 gm of catalyst.

**Results and Discussion**

**Synthetic Clays.** The various clay supports were first characterized with respect to XRD and $N_2$ porosimetry. The XRD patterns shown in Fig. 1 are from as-prepared clays prior to calcination. This figure contains the TEA-clays only; the d-spacing for these materials is 1.4-1.5 nm. This value is lower, 1.2-1.3 nm, for the Li-clays due to the smaller size of this exchangeable cation. After calcination, the patterns look the same except that the d-spacing (d(001)) collapses to 1.0 nm. The XRD patterns were used as a qualitative measure of crystallinity of the support. Generally, the better the separation of reflections occurring within 20-30 degrees

2θ, the more crystalline the clay. Going by this measure, the most crystalline samples are derived from AM30, AS30, and HS30. The same holds true for the Li-versions (figure not shown). The most intense basal spacing occurs for the AM30 sample.

In terms of $N_2$ porosimetry, the BET surface areas of samples after calcination generally ranged from 194-278 $m^2$/gm. Pore volumes were generally 0.24-0.26 cc/gm for Li-clays and 0.41-0.49 cc/gm for those derived from TEA-clays. The isotherms were all Type IV with hysteresis loops. The vast majority of samples displayed H2 loops, with the remainder having H3 loops. For those with H2 loops, which indicates mesostructuring, the average pore diameter size was typically 4.8-5.5 nm. TEM of all of the clays prior to calcination was also performed. One example is shown in Fig. 2 for TEA-AS30. Here, individual clay flakes and layers are visible as curved features approximately 100-200 nm long. The background is dominated by spherical particles approximately 1.5 nm in diameter, which are the unreacted silica particles. Although this phase appears to be dominant in TEM images due to contrast, it is in fact present at only about the 10 wt% level. Table 1 lists some of the clays used in terms of the precursor silica sol parameters. TEM was used to determine the particle size of the silica phase present in the clay as compared to the size in the sols provided by the supplier. The best catalyst results (vida infra) were invariably obtained from clays that contained 15 nm silica particles (HS30, AM30, AS30).

**HDS of DBT.** Table 2 summarizes these particular catalysis results in terms of %DBT conversion. The selectivity to biphenyl was 100% in all cases since no trace of the hydrogenation product cyclohexylbenzene was observed. The reference, in contrast, which was a Crosfield 465 CoMo/alumina catalyst, displayed a biphenyl yield of 80.8%, a cyclohexylbenzene yield of 5.0%, and a biphenyl selectivity of 94.2%. All catalysts maintained activity during the duration of the test. While %DBT conversions were considerably lower than that of the reference, commercial, catalyst, our interest was in parameters which may cause differences between the clays themselves. No correlation could be found for materials prior to Co/Mo/S loading from $N_2$ porosimetry data. Interestingly, most of the catalysts displaying the highest DBT conversions were derived from the Li-clays (56.1-64.8%); TEA-HS30 was also in this range at 58.3%. The remainder of the TEA-clays, however, were lower at 40.1-49.6%. Possible reasons for this behavior will be discussed in the discussion on catalyst stability.

**Table 1. Synthetic Clays Based on Silica Sol Source**

| clay (exchangeable cation-silica sol) | ave. silica diameter in clay (nm)[1] | precursor silica sol diameter (nm)[2] | precursor silica sol pH[2] |
|---|---|---|---|
| TEA-SM30 | 11 | 7 | 10.2 |
| TEA-HS30 | 15 | 12 | 9.8 |
| TEA-AM30 | 15 | 12 | 8.9 |
| TEA-AS30 | 15 | 22 | 9.2 |
| TEA-TM40 | 24 | 22 | 9.0 |
| Li-TM40 | 24 | 22 | 9.0 |

[1]determined via TEM analysis of the clay product.
[2]as reported by the supplier.

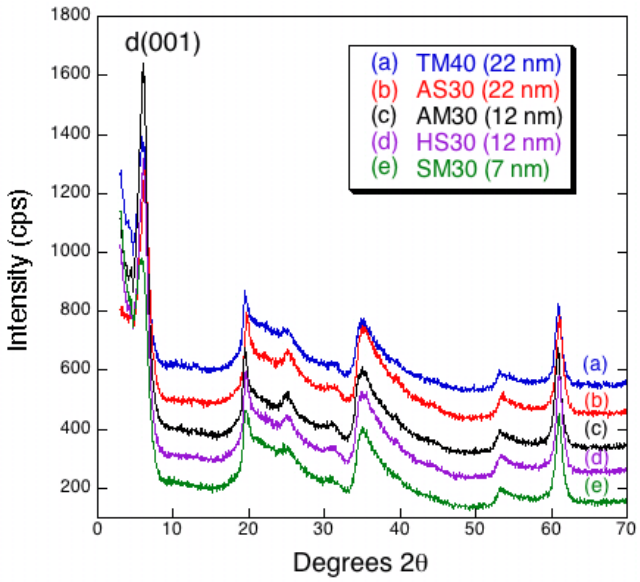


**Figure 1.** XRD patterns of synthetic TEA-hectorite catalyst precursors derived from various silica sols as shown in the legend.

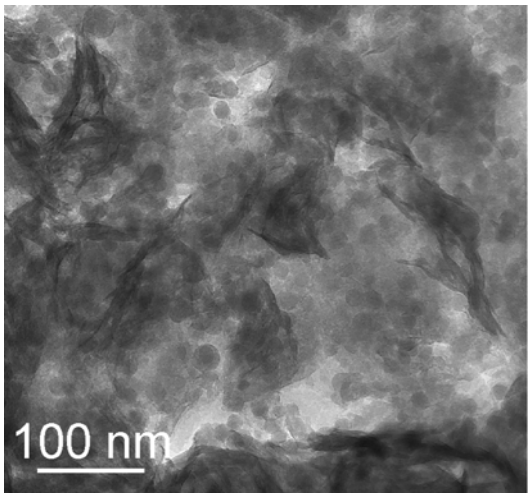


**Figure 2.** TEM image of TEA-AS30 hectorite prior to calcination and catalyst loading.

**Table 2. HDS at 400°C with Co/Mo/S Catalysts**

| Catalyst | %DBT Conversion |
|---|---|
| Crosfield 465 | 85.8 |
| Li-AS30 | 64.8 |
| TEA-HS30 | 58.3 |
| Li-TM40 | 58.2 |
| Li-HS30 | 56.1 |
| TEA-AS30 | 49.6 |
| TEA-TM40 | 45.7 |
| TEA-AM30 | 44.3 |
| TEA-SM30 | 40.1 |

**Deep HDS of DMDBT.** Tables 3 and 4 contain conversion and product selectivity data for this reaaction over many of the same

catalyts. The reference used for these reactions was a commercial Criterion Cr344 Co/Mo/S catalyst. The conversion of DMDBT was kept intentionally low for accurate kinetic studies. At 325°C, the conversion of DMDBT over the Cr344 commercial catalyst was only 11.4% under these conditions. The reactivity of the most active catalylst, TEA-AM30, was quite similar at 10.5%. There have been recent reports comparing the activity of catalysts in terms of hydrogenation (HYG) versus direct desulfurization (DDS) pathways that are operative during deep HDS. Reportedly, after hydrogenation of DMDBT, elimination of the sulfur atom is facilitated due to molecular puckering, which decreases the steric hindrance of the two methyl groups, and and an increase in electron density of the sulfur atom[5]. For comparison, the HYG/DDS ratio at 325°C for Cr344 is 2.2 but it is significantly higher (4.4) for the TEA-AM30 catalyst. DMDBT conversions increased with temperature, as one would expect, ranging from 2.9-10.5% at 325°C and 2.9-16.1% at 350°C. DDS was more limited at lower temperatures, however, causing the HYG/DDS values to be higher here. No DMDCH was observed at 325°C, whereas the more active catalysts displayed up to 3.6% selectivity of this product at 350°C. In summary, the catalysts with higher HYD activities may be suitable for the deep HDS reaction.

**Table 3. Deep HDS with Co/Mo/S-Clay Catalysts**

| Catalyst | %DMDBT conversion at 325°C | HYG/DDS at 325°C[1] | %DMDBT conversion at 350°C | HYG/DDS at 350°C[1] |
|---|---|---|---|---|
| TEA-AM30 | 10.5 | 4.4 | 16.1 | 2.2 |
| TEA-AS30 | 9.5 | 3.6 | 14.2 | 1.9 |
| TEA-TM40 | 5.9 | 2.8 | 10.4 | 1.9 |
| Li-TM40 | 6.0 | 3.5 | 10.1 | 1.5 |
| TEA-HS30 | 7.1 | 3.6 | 10.0 | 2.3 |
| TEA-SM30 | 6.9 | 3.5 | 9.5 | 2.0 |
| Laponite | 3.0 | 2.3 | 2.9 | 1.5 |

[1]Ratio of hydrogenation products (HYG) over direct desulfurization products (DDS) (see Table 4).

**Table 4. Product Selectivity (%) from Deep HDS at 350°C**

| Catalyst | DMBP (DDS)[1] | HDMDBT (HYG)[1] | DMDCH + MCHT (HYG)[1] |
|---|---|---|---|
| TEA-AM30 | 31.8 | 45.8 | 22.4 |
| TEA-AS30 | 34.5 | 46.4 | 19.1 |
| TEA-TM40 | 34.2 | 48.2 | 17.6 |
| Li-TM40 | 39.6 | 42.2 | 18.2 |
| TEA-HS30 | 30.3 | 53.7 | 16.0 |
| TEA-SM30 | 34.0 | 48.7 | 17.4 |
| Laponite | 39.8 | 33.6 | 26.6 |

[1]DMBP = dimethyl biphenyl; HDMDBT = tetrahydrodimethyl dibenzothiophene; MCHT = methylcyclohexyltoluene; DMDCH = dimethyldicyclohexane.

It is known that Ni/Mo/S-catalysts have higher activity for deep HDS than Co/Mo/S-catalysts because Ni has high hydrogenation activity. In fact, a reference Cr424 Ni/Mo/S commercial catalyst showed 24.5% DMDBT conversion under the same conditions at 325°C where the Cr344 Co/Mo/S catalyst showed 11.4% conversion. All of the clay supports show higher HYD activity than Cr344. The TEA-AM30 support, furthermore, displays activities (%DMDBT conversions) that are very similar to the HDS activity of the commercial Co/Mo/S-catalyst. If this material were to be modified further by different preparation methods or pretreatments, it shows potential as a promising deep HDS catalyst. Future studies will focus on testing these supports as Ni/Mo/S-catalysts.

**Catalyst Stability**. XRD, $N_2$ porosimetry, and TEM characterization of some of the materials was done after Co/Mo/S loading and after DBT HDS catalysis. For these purposes, only the most reactive (TEA-HS30, Li-AS30) and least reactive (TEA-SM30) catalysts were examined. Table 5 provides the $N_2$ porosimetry data for these samples.

**Table 5. $N_2$ Porosimetry of Various DBT HDS Catalysts**

| stage | surface area $m^2$/gm | pore volume cc/gm | hysteresis loop type |
|---|---|---|---|
| TEA-HS30 | | | |
| calcined | 225 | .38 | H2 |
| after Co/Mo/S | 143 | .27 | H2 |
| after HDS | 99 | .22 | H2 |
| Li-AS30 | | | |
| calcined | 200 | .24 | H2 |
| after Co/Mo/S | 125 | .15 | H2 |
| after HDS | 65 | .10 | H2 |
| TEA-SM30 | | | |
| calcined | 278 | .46 | H2 |
| after Co/Mo/S | 115 | .25 | H3 |
| after HDS | 78 | .22 | H3 |

As would be expected, the surface areas and pore volumes decrease quite markedly upon Co/Mo/S loading of the supports, and further still after HDS reaction. The one parameter that changes for the least active catalyst (TEA-SM30) that does not change for the active catalysts is the hysteresis loop type. It is apparent that, for whatever reason, the mesostructuring of this material was lost upon metal loading. Possible reasons for this phenomenon remain under investigation. Fig. 3 displays representative isotherm data with the different hysteresis loop types.

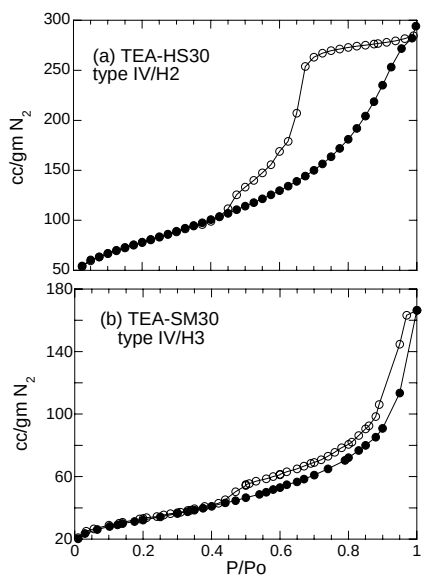


**Figure 3.** $N_2$ isotherms for (a) calcined clay TEA-HS30 and (b) calcined and Co/Mo/S-loaded TEA-SM30; solid circles = adsorption, open circles = desorption.

The high resolution TEM image shown in Fig. 4 is for the Co/Mo/S-Li-AS30 active catalyst. Note the curved layered structure that nearly envelops one of the silica particles and the lattice fringes

in the upper left portion of the image. Both are assumed to arise from the Co/Mo/S-species since neither has been observed in the precursor clay supports.

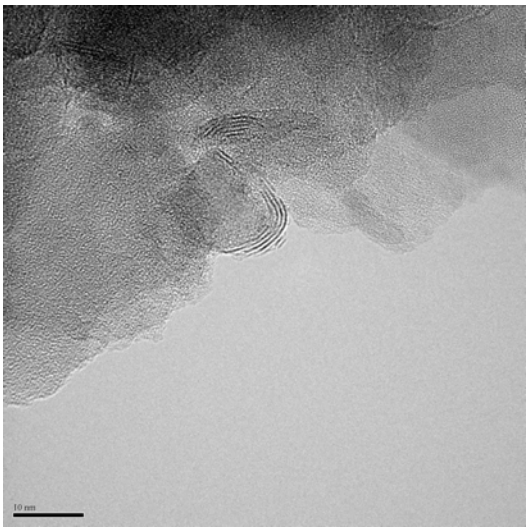


**Figure 4.** HR-TEM image of Co/Mo/S-Li-AS30 (scale bar 10 nm).

**Conclusions**

For an as yet undetermined reason, precursor silica sols that yield silica particles sizes of 15 nm within the synthetic clays appear to be optimum for HDS and deep HDS reactions. Both smaller and larger silica sol sizes were employed, but both showed a negative effect on final catalytic results. It is presumed that the 15 nm sols foster the most crystalline materials (from XRD data) and the optimum mesostructuring (in terms of textural porosity and morphology) of the clay catalyst precursor. This may also have an impact on the optimum Co/Mo/S-species size and/or shape. Variation between the activity of a particular catalyst for HDS vs. deep HDS is not directly comparable due to differences in conditions such as calcination, Co/Mo/S-loading, reaction temperatures, etc. The Li-clays are overall more active for DBT HDS than the TEA-versions. In general, the former have lower pore volumes at 0.24-0.26 cc/gm than the latter (0.41-0.49 cc/gm). High crystallinity is also apparent for the Li-clays from the electron diffraction patterns taken during TEM imaging of these clays, which showed very strong and sharp diffraction rings (data not shown).

**Acknowledgement.** R. E. Cook of MSD-ANL acquired TEM images of pure clay samples at the ANL Electron Microscopy Center. The TEM facility at the Cummings Life Science Center of the University of Chicago is acknowledged. This work was performed under the auspices of the U.S. DOE, Office of Basic Energy Sciences, Division of Chemical Sciences, Geosciences, and Biosciences under contract number W-31-109-ENG-38.

**References**

1. (a) Carrado, K.A. *Appl. Clay Sci.* **2000**, *17*, 1-23 (b) Carrado Gregar, K.; Winans, R. E.; Botto, R. E., *U.S. Patent* #5,308,808, **1994**.
2. Carrado, K.A.; Csencsits, R.; Thiyagarajan, P.; Seifert, S.; Macha, S.M.; Harwood, J.S., *J. Mater. Chem.* **2002**, *12*, 3228-3237.
3. (a) Carrado, K.A.; Xu, L., *Micropor. Mesopor. Mater.* **1999**, *27*, 87-94 (b) Carrado, K.A.; Xu, L.; Marshall, C.L.; Wei, D.; Seifert, S.; Bloomquist, C.A., *Nanoporous Materials II* (Stud. Surf. Sci. Catal.), A. Sayari, M. Jaroniec, T. J. Pinnavaia (Eds), Elsevier: Amsterdam, **2000**, vol. 129, 417-424.
4. Song, C.; Ma, X., *Appl. Catal. B. Environ.* **2003**, *41*, 207-238.
5. (a) Ma, X.; Sakanishi, K.; Isoda, T.; Mochida, I., *Energy & Fuels* **1995**, *9*, 33 (b) Kim, J. H.; Ma, X.; Song, C.; Oyama, S. T.; Lee, Y. K., *ACS Fuel Chem. Div. Prepr.* **2003**, *48*, 40-41.

# NEW SYNTHESIS METHOD FOR METAL PHOSPHIDE HYDROTREATING CATALYSTS

*S. Yang and R. Prins*

Institute for Chemical and Bioengineering, Swiss Federal Institute of Technology (ETH), 8093 Zürich, Switzerland

## Introduction

The need to deeply reduce the sulfur level of fuels has led to a high interest in materials different from the classic hydrotreating catalysts based on $MoS_2$. Whereas metal carbides and nitrides are initially highly active, but not stable in a sulfur-containing atmosphere, the metal-phosphorus and metal-silicon bonds are stronger than the metal-sulfur bond. Under hydrodesulfurization (HDS) conditions the surfaces of molybdenum and nickel phosphide take up sulfur atoms, but the kernels of the metal phosphide particles stay intact.[1, 2] Metal phosphides and silicides may therefore be promising hydrotreating catalysts for deep HDS. Supported metal phosphides of Mo, W, Co and Ni can be prepared from the corresponding metal salts and $(NH_4)_2HPO_4$ by reduction in $H_2$ and the resulting materials have very promising hydrotreating activities.[3-8] Unfortunately, the dispersion of thus-prepared supported metal phosphides is low, because the P-O bond is strong and its reduction requires high temperature. Hydrogen atoms, formed on the metal atoms, spill over to the phosphate and reduce it to phosphorus or phosphine, which can react with the metal particles to a metal phosphide. The high temperature leads to a low dispersion of the resulting metal phosphide particles. We have therefore looked for phosphor-containing species that contain P-X bonds that are easier to break than the P-O bond in phosphates and phosphites. We have found that supported metal phosphide particles of high dispersion can be obtained by treating reduced metal particles on a support by phosphine. In this chemical vapor deposition method there is no need to go to high temperatures, and as a consequence the size of the metal phosphide particles is equivalent to that of the metal particles and can be kept small.

## Experimental

**Catalyst preparation.** Silica-supported nickel phosphide was prepared by reaction of supported Ni and NiO particles with $PH_3$. The supported metal precursor was prepared by pore-volume impregnation. The silica support was dried at 373 K for 12 h prior to impregnation. Three aqueous solutions of nickel nitrate, nickel acetate, and nickel nitrate containing the chelating ligand nitrilotriacetic acid (NTA)[9] were used in the impregnation. The corresponding samples are denoted as N-X (nitrate), A-X (acetate) and NTA-X respectively, where X is the weight percent of nickel in the samples. The dried, impregnated solids were reduced in flowing $H_2$ at 673 K for 2 h. In one experiment, a dried powder impregnated with nickel nitrate was calcined at 773 K for 3 h before reduction in $H_2$. The reduced samples were cooled down to 298 K in flowing $H_2$. The reduced $Ni/SiO_2$ samples were exposed to a flowing 10% $PH_3/H_2$ mixture (20 ml/min) between 298 and 523 K; the final temperature was maintained for 2 h. Then the samples were cooled down to 298 K in flowing $H_2$, flushed with He for 20 min and passivated in a flow of 1 mol% $O_2$/He. In addition, a sample was prepared by the classical phosphate reduction method[3] for comparison (NP-13, nickel loading 13 wt%).

**Catalyst characterization.** The catalysts were characterized by XRD, nitrogen adsorption, and CO chemisorption (in the latter case after re-reduction of the samples in situ in $H_2$ at 623 K for 2 h). $^{31}P$ MAS-NMR spectra were obtained with an Advance 400 WB Bruker spectrometer at room temperature. Samples were packed into a 4-mm-diameter rotor in an inert atmosphere and measured with spinning at 10 kHz. The spectra were obtained by applying the Fourier transformation to the free induction decay signals. The isotropic shifts of the signals were obtained by comparing spectra measured at different spinning rates.

**HDS and HDN activities.** The HDS of dibenzothiophene (1 kPa) and the hydrodenitrogenation (HDN) of orthomethylaniline (3 kPa) were carried out in a continuous–flow microreactor at a total pressure of 3.0 MPa as described before.[7, 10] The passivated catalysts were activated in situ with $H_2$ at 673 K and 0.1 MPa for 3 h. The liquid reactant was fed into the reactor by means of a high–pressure pump using toluene (HDS) and *n*-octane (HDN) as the solvent. The catalyst was stabilized at 643 K and 3.0 MPa for at least 12 h before samples were taken for analysis. The experiments were carried out in the absence of $H_2S$, in the presence of $H_2S$ and after removal of $H_2S$ from the feed. During two weeks of operation there was almost no deactivation of the catalyst.

## Results

After reduction of the impregnated and dried $Ni/SiO_2$ precursors in $H_2$, the XRD patterns of the N-4.8 and N-13 $Ni/SiO_2$ precursors exhibited peaks corresponding to Ni. Using the Scherrer equation, average crystallite sizes of 8 and 10 nm were calculated, respectively. In the XRD patterns of the two reduced 5 wt% $Ni/SiO_2$ precursors, which were prepared with a solution of nickel acetate (A-5) and with a solution of nickel nitrate and NTA (NTA-5), only the features of amorphous silica were visible. It implies that the nickel particles were too small to be detected by XRD, which was confirmed by TEM and $H_2$ chemisorption.

The reduced $Ni/SiO_2$ precursors were treated with a 10% $PH_3/H_2$ mixture (20 ml/min) from 298 to 523 K (2 h), cooled down to 298 K in flowing $H_2$, flushed with flowing He, and then passivated in a flow of 1 mol% $O_2$/He. **Figure 1** shows the XRD patterns of the 13 wt% $Ni/SiO_2$ precursor, prepared from nickel nitrate (N-13), after reaction with phosphine at different temperatures. After reaction at 298 K, the diffraction characteristics of Ni particles are still present, similar to those of the starting $Ni/SiO_2$ precursor.

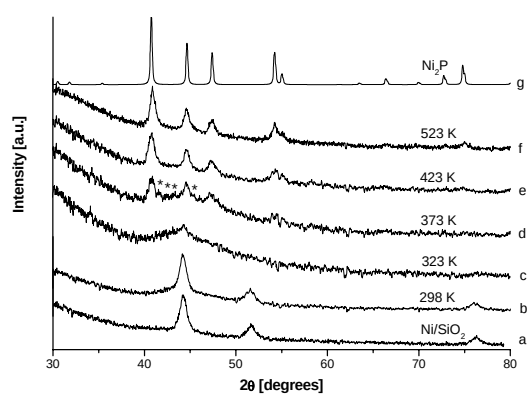


**Figure 1**. XRD patterns of the 13 wt% $Ni/SiO_2$ precursor, prepared from nickel nitrate, after reaction with phosphine at different temperatures. *, $Ni_3P$

The Ni peaks almost disappeared after reaction at 323 K, only a broad Ni peak at ca. 44.6° remained. In the XRD pattern of the $Ni/SiO_2$ precursor after reaction with phosphine at 373 K intense peaks were present at 40.7°, 44.6°, and 47.4° and weaker peaks at 54.2° and 55.0°,

all attributed to $Ni_2P$. Very weak peaks were present at 41.8°, 42.8°, 43.6°, and 45.3°, corresponding to $Ni_3P$. When the reaction temperature was increased to 423 and 523 K, only the $Ni_2P$ diffraction peaks were present, indicating that pure $Ni_2P$ can be prepared on silica by treatment with phosphine above 423 K. The average crystallite size of both $Ni_2P/SiO_2$ catalysts, obtained at 473 and 523 K, was ca. 13 nm. $^{31}P$ MAS-NMR spectra of the samples prepared at 423 and 523 K showed peaks around 4075 and 1200-1700 ppm. Although these peaks are in the region to be expected for $Ni_2P$, the peaks in the region of 1200-1700 ppm were not exactly equal to those of highly crystalline $Ni_2P$.

Metallic $Ni/SiO_2$ precursors, prepared from different metal salts, were treated with 10% $PH_3/H_2$ at 523 K. **Figure 2a** shows that the XRD pattern of the catalyst prepared by the classical phosphate reduction method[3] had sharp peaks; large $Ni_2P$ particles with an average crystallite size of 30 nm had formed. The $Ni_2P/SiO_2$ catalysts, made from nickel nitrate and with Ni loadings of 4.8 and 13 wt%, exhibited broader XRD peaks (Figs. 2b and c) and average crystallite sizes of 11 and 13 nm were calculated, respectively. The XRD patterns of the samples prepared with nickel acetate and with nickel nitrate and NTA showed only the features of amorphous silica, implying that the nickel phosphide particles were too small to be detected by XRD.

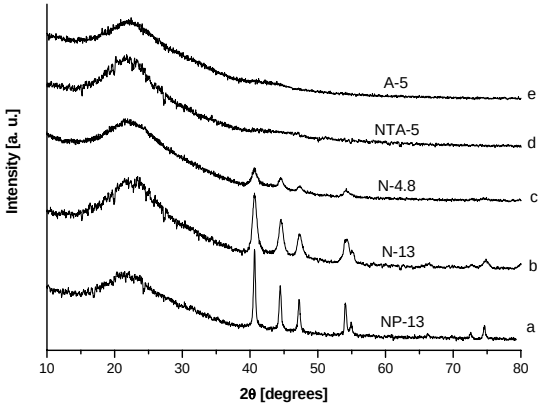


**Figure 2**. XRD patterns of $Ni_2P/SiO_2$ catalysts prepared from different precursors.

To examine if $PH_3$ also reacted with supported NiO, the calcined 13 wt% $NiO/SiO_2$ sample was treated with a 10% $PH_3/H_2$ mixture at different temperatures. The XRD patterns show that, after reaction with phosphine at 523 K for 2 h, the NiO peaks had almost disappeared and that weak peaks at 40.7°, 44.6°, and 47.4° attributed to $Ni_2P$ were present. When the reaction temperature was increased to 623 K, only the diffraction peaks corresponding to $Ni_2P$ were present. This indicates that silica-supported $Ni_2P$ can also be achieved by treating a $NiO/SiO_2$ precursor with phosphine above 623 K.

The hydrotreating activity of the N-13 $Ni_2P/SiO_2$ catalyst was tested in the HDS of dibenzothiophene and the HDN of orthomethylaniline. The activity of $Ni_2P$ in the HDS of DBT was very high. The product distribution was similar to that over sulfided CoMo and NiMo catalysts. The amount of tetrahydro-DBT was very low showing that it is easily desulfurized. Bicyclohexyl was observed only in trace amounts. The further hydrogenation of biphenyl to cyclohexylbenzene and of cyclohexylbenzene to bicyclohexyl did not take place. Also the HDN activity was very good and much higher than that of the metal phosphide catalysts determined before.[7]

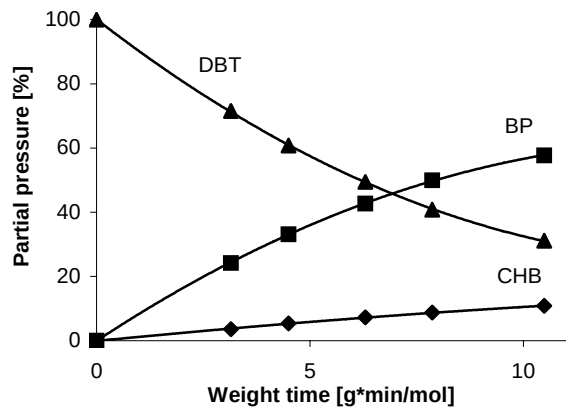


**Figure 3**. HDS of dibenzothiophene over the N-13 $Ni_2P/SiO_2$ catalyst.

**Discussion**

Our results demonstrate that metal phosphide particles on a support can very easily be prepared from metal or metal oxide particles by treatment with phosphine and hydrogen. In case of Ni, the metal particles already became fully phosphided at 423 K, while NiO particles needed 623 K. These temperatures are very much lower than the temperatures required in the phosphate method of preparing metal phosphide. Because of the very strong P-O bond, temperatures of about 1000 K are needed. Such high temperatures lead to the almost exclusive formation of phosphorus (phosphine is not stable at high temperature), which diffuses only slowly into the metal particles. All this leads to sintering and loss of dispersion. At these high temperatures phosphate also reacts with supports like alumina and therefore a large excess of phosphate has to be added in order to make metal phosphide particles. Thus, only alumina-supported metal phosphide catalysts with loadings above 20 wt% have been reported.

**Conclusions**

The phosphine method allows preparing the metal phosphide particles at moderate temperature. As a result, the particle size is equivalent to that of the precursor particle size and small supported metal phosphide particles can be made of any metal or metal oxide precursor that can be made with high dispersion. Even on alumina, low-loading metal phosphide catalysts with high dispersion can be made.

**References**

(1) Wu, Z.; Sun, F.; Wu, W.; Feng, Z.; Liang, C.; Wei, Z.; Li, C. *J. Catal*. **2004**, *222*, 41.
(2) Layman, K.A.; Bussell, M.E. *J. Phys. Chem. B* **2004,** *108*,10930.
(3) Clark, P.; Li, W.; Oyama, S. T. *J. Catal*. **2001**, *200*, 140.
(4) Clark, P. A.; Oyama, S. T. *J. Catal*. **2003**, *218*, 78.
(5) Oyama, S. T. *J. Catal*. **2003**, *216*, 343.
(6) Stinner, C.; Prins, R.; Weber, Th. *J. Catal*. **2001**, *202*, 187.
(7) Zuzaniuk, V.; Prins, R. *J. Catal*. **2003**, *209*, 85.
(8) Phillips, D. C.; Sawhill, S. J.; Self, R.; Bussell, M. E. *J. Catal*. **2002**, *207*, 266.
(9) Medici, L.; Prins, R. *J. Catal*. **1996**, *163*, 28.
(10) Egorova, M.; Prins, R. *J. Catal*. **2004**, *221*, 11.

# MAKING ETHYLENE IN THE FCC

*A. W. Chester*[*], *M.F. Mathias*[§], *K. Liu*[#]

ExxonMobil Research and Engineering Company
Annandale, NJ 08801

## Introduction

The use of ZSM-5 additives in FCC units began in the early 1980s to increase the octane of the FCC gasoline produced, particularly in distillate mode operation where the low severity leads to lower octane[1]. More recently, as the value of gasoline octane has decreased, and the values of petrochemical feedstocks have increased, ZSM-5 is increasingly being used to produce increased quantities of light olefins (particularly propylene and butylenes)[2].

While propylene is the product generally desired as an FCC product for feed for polypropylene, ethylene is also of considerable value if it can be obtained in a practical manner. Ethylene is generally separated cryogenically from the light gas products of thermal cracking. Cryogenic separation is generally not available for FCC off-gas because of the low concentrations of ethylene normally found, but in instances where a thermal cracking process is utilized in the same refinery as an FCC unit, ethylene is often recovered if sufficient capacity exists.

It has been recognized that use of ZSM-5 additives results in increased yields of ethylene, although these are small compared to propylene. Zhao and Roberie investigated the effects of different levels of ZSM-5 additives at two temperatures[3]. They found that with 32% of an additive containing 25% ZSM-5 (8% crystallinity), they could produce about 3.2% ethylene along with close to 15% propylene. In the present investigation, we show how changing catalyst formulations can radically increase the yields of ethylene, as well as the combined light olefin yields, under practical FCC conditions.

## Experimental

FCC conversion experiments were performed in quartz fixed bed reactors similar to those described by Chester and Stover[4]. However, in contrast to the run methodology described by them, all runs were performed at constant WHSV (either 6 or 12) and varying time on stream in order to produce high C/O ratios when catalysts had low activity for overall cracking (as is the case when ZSM-5 additives were used without a USY catalyst component). A Mid-continent Sour Heavy Gas Oil (SHGO) was used as feed.

ZSM-5 additive catalysts were prepared (generally) from low $SiO_2/Al_2O_3$ ZSM-5 crystals (40%) and a matrix containing kaolin clay (30%) and silica sol as binder. Active alumina (5%, except where noted) was added by dispersing suitable quantities of psuedoboehmite with acid prior to addition to the catalyst slurry. Phosphorus (2.3%) was added to the slurry prior to spray drying. Other ZSM-5 crystals with varying $SiO_2/Al_2O_3$ and crystal sizes were obtained from commercial sources.

The base catalyst (designated Octacat) used in blending experiments and as a comparison was obtained from W.R.Grace, Inc. and contained 40% USY (no rare earths) in a silica-sol, clay matrix.

Prior to testing all catalysts were calcined at 538 $^oC$ (1000 $^oF$) for 3 hours after being heated at a rate of 2.8$^oC$/min. Catalysts were then steamed *(except where specified*) by cyclic propylene steaming for 20 hours at 780 $^oC$ (1435 $^oF$) at 4.4 bar (50 psig) with 50% steam in order to simulate aging in an FCC regenerator. In cyclic propylene steaming, 5 min cycles of $N_2$, propylene and air are used throughout the steaming.

## Results and Discussion

In the initial investigation, ZSM-5 catalysts with differing properties were tested at 1200 $^oF$ start-of-run temperature; no large pore zeolite was used to provide high conversion. The results are shown in Table 1, where Octacat is used as a comparison.

Note that the lower $SiO_2/Al_2O_3$ ratio zeolites all produced from 6-8% ethylene. Under the same conditions, USY (Octacat) only produced 1% ethylene, indicating that *thermal* conversions were minimal under the experimental conditions. The best ethylene yield was obtained with low $SiO_2/Al_2O_3$ ZSM-5 with *no* active $Al_2O_3$ in the matrix. Propylene yields followed the same trends as ethylene, and are of the same magnitude as observed with ZSM-5 additives at lower temperatures[3].

However, activities are quite low, as indicated by the Cat/Oil ratios necessary to reach 60% conversion (9-24). Since ZSM-5 does virtually no heavy oil conversion, the matrix bears the load; the active $Al_2O_3$ has no apparent effect, as indicated by comparing the standard catalyst with one with no $Al_2O_3$ in the matrix. Comparatively, the nanocrystalline ZSM-5 is surprisingly active, perhaps because of its high external surface area. In conventional additives, the poorer stability of nanocrystalline ZSM-5 has precluded its use[5], but it has been found that phosphorus stabilization is effective in stabilizing these small crystals[6]. Selective ZSM-5, with much lower activity and inherently larger crystal size and poorer diffusion, is the poorest performer.

Current Address:
*Catalyst Manufacturing Science and Technology Consortium
Department of Chemical and Biochemical Engineering
Rutgers University, New Brunswick, NJ
achester@rci.rutgers.edu
[§]General Motors – Global Alternative Propulsion Center, Honeoye Falls, NY, USA
[#]General Electric Energy and Propulsions Technologies, Irvine, CA, USA

**Table 1. Performance of ZSM, cracking Gas Oil at 1200°F (60% Conversion)**

| Catalyst | Octa-cat | Standard ZSM-5 | no Al in Binder | Nano-crystal ZSM-5 | Select -ive ZSM-5 |
|---|---|---|---|---|---|
| **$SiO_2/Al_2O_3$** | **USY** | **25.0** | **25.0** | **60.0** | **450.0** |
| **Size** | **N/A** | **200-500nm** | **200-500nm** | **20-50nm** | **~1µm** |
| Conversion, wt% | **60.0** | | | | |
| Cat./Oil | 3.3 | 14.3 | 13.8 | 8.9 | 23.9 |
| C2$^-$, wt% | 4.0 | 7.1 | 7.4 | 7.0 | 9.4 |
| **C2$^=$, wt%** | **1.0** | **6.7** | **7.7** | **6.0** | **5.5** |
| **C3$^=$, wt%** | **4.2** | **12.7** | **13.3** | **12.7** | **10.7** |
| C3, wt% | 1.2 | 2.1 | 2.6 | 1.9 | 1.6 |
| **C2$^=$+C3$^=$, wt%** | **5.2** | **19.4** | **21.0** | **18.7** | **16.2** |
| **C4$^=$, wt%** | 5.3 | 7.3 | 7.0 | 7.6 | 7.7 |
| C4, wt% | 1.9 | 0.8 | 0.9 | 0.8 | 0.5 |
| **Gasoline wt%, $C_5$-430°F** | 40.3 | 17.8 | 16.8 | 19.3 | 17.8 |
| **LFO, wt%** | 25.1 | 19.8 | 19.9 | 21.4 | 18.8 |
| **HFO, wt%, 700°F $^+$** | 14.9 | 20.2 | 20.1 | 18.6 | 21.2 |
| **Coke, wt%** | 2.1 | 5.5 | 4.4 | 4.7 | 6.7 |

Cracking at 1200°F Start of run, Mid-continent SHGO

In order to increase the activity of the system, ZSM-5 was blended with Octacat in varying proportions and also tested at 1200 °F. The results are shown in Table 2 at a constant 70% conversion; actual conversions in the midrange blends (30-70%) could be much higher. Higher conversions could be obtained without sacrificing the ethylene yields; with the catalyst containing 70% Octacat/30% ZSM-5, conversions as high as 78% could be attained with ethylene yields of 7%. With that catalyst, total light olefin yields of well over 30% $C_2^=$-$C_4^=$ are obtained even at 70% conversion; coke yields are also low and the Cat/Oil ratio, is well below 10 and within more normal FCC ranges. Investigations of other ZSM-5 catalysts, as described in Table 1, in this system showed that the catalyst without any $Al_2O_3$ in the matrix showed an additional benefit in ethylene yield (about 0.7% at 70% conversion.

**Table 2. Performance of Octacat/ZSM-5 Blends in Cracking to Olefins.**

| Catalyst,% Octacat | 0 | 30 | 50 | 70 | 90 | 100 |
|---|---|---|---|---|---|---|
| Conv., wt% | **70.0** | | | | | |
| Cat./Oil | **22.0** | **22.0** | **15.2** | **7.7** | **4.9** | **4.9** |
| C2$^-$, wt% | 8.9 | 5.9 | 5.8 | 4.8 | 4.8 | 7.9 |
| **C2$^=$, wt%** | **8.5** | **7.7** | **7.0** | **6.0** | **5.3** | **2.6** |
| **C3$^=$, wt%** | **14.3** | **15.8** | **17.1** | **16.3** | **15.6** | **7.3** |
| C3, wt% | 3.1 | 2.6 | 2.4 | 2.3 | 2.2 | 1.9 |
| **C2$^=$+C3$^=$, wt%** | **22.8** | **23.5** | **24.1** | **22.3** | **20.9** | **9.9** |
| **C4$^=$, wt%** | 7.1 | 8.7 | 9.3 | 10.2 | 9.5 | 8.2 |
| C4, wt% | 1.1 | 1.1 | 1.2 | 1.8 | 1.6 | 1.9 |
| **Gasoline wt%, $C_5$-430°F** | 18.9 | 18.3 | 19.9 | 22.9 | 25.2 | 35.4 |
| **LFO, wt%** | 16.7 | 16.3 | 16.8 | 19.6 | 19.1 | 19.9 |
| **HFO, wt%, 700°F $^+$** | 13.3 | 13.7 | 13.2 | 10.4 | 10.9 | 10.1 |
| **Coke, wt%** | 8.1 | 8.4 | 6.0 | 4.1 | 4.4 | 4.7 |

Cracking at 1200°F Start of run, Mid-continent SHGO

Although a process has been proposed for operation at temperatures higher than 1200°F (the CPP Process[7]), operation at such a high temperature is unlikely to be practical in normal FCC units because of metallurgy requirements. So a lower temperature, 1080°F, was tested. This is not an unreasonable riser bottom temperature in current FCCs that operate at above 1000°F riser top temperature. The results are shown in Table 3. Ethylene yields are still high for the standard catalyst, down from 7 to 4.6% for the 50% catalyst. But when $Al_2O_3$ is removed from the matrix, and some steam is added (which simulates real operations), ethylene yields were close to 8%, suggesting that with the right catalyst system and operating conditions, existing FCC units could produce high ethylene yields.

**Table 3. Cracking Results for a 50%Octacat/50% ZSM-5 Catalyst at 1080°F.**

| Catalyst | Standard ZSM-5 | no $Al_2O_3$ in Binder |
|---|---|---|
| Conversion., wt% | **75.0** | |
| Cat./Oil | 17.8 | 9.6 |
| **H2O Co-feed, wt%** | 0.0 | 7.5 |
| **WHSV** | 12.0 | 6.0 |
| C2$^-$, wt% | 4.4 | 4.4 |
| **C2$^=$, wt%** | **4.6** | **7.8** |
| **C3$^=$, wt%** | **16.0** | **14.8** |
| . C3, wt% | 2.8 | 4.4 |
| **C2$^=$+C3$^=$, wt%** | **20.6** | **22.6** |
| **C4$^=$, wt%** | **10.6** | **7.8** |
| C4, wt% | 3.8 | 3.6 |
| **Gasoline wt%, $C_5$-430°F** | **23.1** | **24.2** |
| **Coke, wt%** | **5.3** | **3.4** |

Cracking at 1080°F Start of run, Mid-continent SHGO
Catalyst:50% Octacat/50% ZSM-5

In another experiment, the effect of steaming the ZSM-5 was examined: an unsteamed catalyst (calcined only) was compared to the standard steam treated catalyst. The results are shown in Table 4 and are remarkable.

**Table 4. Effect of Steaming ZSM-5 on Cracking Performance**

| ZSM-5 Treatment | Steamed | Unsteamed |
|---|---|---|
| Conversion, wt% | 75.0 | |
| Cat./Oil | **12.9** | **8.6** |
| $C2^-$, wt% | 7.6 | 7.6 |
| **$C2^=$, wt%** | **6.5** | **9.2** |
| **$C3^=$, wt%** | **16.6** | **14.3** |
| C3, wt% | 2.8 | 3.8 |
| **$C4^=$, wt%** | **9.4** | **7.1** |
| **$C2^=+C3^=+C4^=$,wt%** | **32.5** | **30.6** |
| C4, wt% | 2.3 | 2.0 |
| **Gasoline wt%, $C_5$-430°F** | **22.8** | **25.5** |
| **LFO, wt%** | **15.9** | **16.1** |
| **HFO, wt%, 700°F $^+$** | **9.1** | **8.9** |
| **Coke, wt%** | **7.0** | **5.5** |

Cracking at 1200°F Start of run, Mid-continent SHGO

Catalyst:70% Octacat/30% ZSM-5

Both activity *and* ethylene yield increased by about 50%. This suggests strongly that the high ethylene yields associated with ZSM-5 are in fact catalytic, and thermal mechanisms make no major contributions.

**Mechanistic Considerations**. Note, however, that although the ethylene yield is higher in the higher activity system, propylene has actually decreased, and in fact total light olefins have also decreased. This decrease is offset by an unexpected increase in gasoline yield.

Buchanan[8] has reviewed the mechanisms occurring in the use of ZSM-5 in FCC applications. Olefinic naphtha is produced by cracking of the feed by the base catalyst. A USY catalyst is preferred for making olefins, since its hydrogen transfer activity is much lower than for REY-based catalysts. The olefinic naphtha contains light ($C_5$-$C_7$) and heavy ($C_8^+$) olefins, which are converted to $C_2$-$C_4$ olefins by ZSM-5. Heavy olefins are also cracked to lighter olefins. Naphtha olefins are also isomerized by ZSM-5, increasing gasoline octane; highly branched olefins cannot be cracked by ZSM-5 because of its pore size.

The increased ethylene but decreased total light olefin yield when ZSM-5 activity is increased as in Table 4 can be explained by a combination of *olefin interconversion* and *selective aromatization*. Olefin interconversion is a reaction optimally catalyzed by ZSM-5 and tends to bring olefin distributions closer to their thermal equilibrium distribution, and is thought to occur by a combination of oligomerization, cracking, disproportionation and hydrogen transfer[9]. The detailed mechanism has not been worked out. When ZSM-5 activity is increased, olefin interconversion reactions are accelerated, producing more ethylene. Ethylene is, however, notably unreactive toward aromatization[10], but the increased activity does produce selective aromatization of propylene and butylenes to form aromatics. Thus increased ZSM-5 activity is seen to produce higher ethylene yields, lower propylene and incremental gasoline aromatics that could be used in petrochemical processes and raise gasoline octane.

**Conclusions**

A comparison can be made between the catalyst and process system discussed in this paper with the Sinopec DCC process, which utilizes a ZSM-5 containing catalyst at temperatures of about 1050°F in a conventional FCC. The Sinopec data on a hydrotreated paraffinic feed was compared to an equally paraffinic resid on a 50% Octacat/50% ZSM-5 catalyst. The comparison is shown in Table 5. The DCC yields of ethylene and propylene are considerably inferior.

By proper selection of catalysts, feeds and reaction parameters, it is possible to produce ethylene yields in excess of 10% under conditions attainable in most modern FCC units. This is of particular value in units already associated with petrochemical plants with available cryogenic separation units.

**Table 5. Comparison with Sinopec DCC Process[11]**

| Catalyst | This Work | DCC |
|---|---|---|
| Feed | Gippsland 760°F$^+$ Resid | Hydrotreated Paraffinic Feed |
| Gravity, API | 28.41 | 31.40 |
| Distillation, °F | | |
| IBP | 619 | 315 |
| 10 | 717 | 649 |
| 50 | 827 | 806 |
| EP | 1342 | 1076 |
| **Catalyst** | **50%Octacat / 50%ZSM-5** | **ZRP-1 (ZSM-5)** |
| **H2O Cofeed, wt%** | **7.5, 15** | **~22** |
| **Conversion, wt%** | **82** | |
| C2-, wt% | 5.9 | 5.2 |
| **C2=, wt%** | **12.3** | **5.1** |
| **C3=, wt%** | **20.9** | **17.4** |
| **C2=+C3=, wt%** | **33.2** | **22.5** |
| **Coke, Wt. %** | **3.6** | **~6** |

**References**


(1) Donnelly, S. P. *et al. Preprints - American Chemical Society, Division of Petroleum Chemistry,* **1987**, *32*, 621-6.
(2) Adewuyi, Y. G. *et al. Applied Catalysis a-General,* **1995**, *131*, 121-133.
(3) Zhao, X. *et al. Industrial & Engineering Chemistry Research*, **1999**, *38*, 3847-3853.
(4) Chester, A. W. *et al. Industrial & Engineering Chemistry Product Research and Development,* **1977**, *16*, 285-90.
(5) Cormier, W. E., Jr. *et al. US 4828679* (1989).
(6) Kowalski, J. A. *US 5888378* (1999).
(7) Xieqing, W. *AIChE Meeting, Spring 2002,* **2002**.
(8) Buchanan, J. S. *Catalysis Today,* **2000**, *55*, 207-212.
(9) Ware, R. A. *et al. Hart's Fuel Technology & Management,* **1998**, *8*, 41-46.
(10) Garwood, W. E. *et al. US 4227992* (1980).
(11) Fu, A. *et al. Oil & Gas Journal,* **1998**, *96*, 49-53.

# HYDROGENATION OF LOWER ALDEHYDES OVER REDUCED AND SULFIDED Ni-Mo/$Al_2O_3$ CATALYSTS

*Xueqin Wang, Umit S. Ozkan*

Department of Chemical and Biomolecular Engineering
The Ohio State University
140 West 19th Avenue
Columbus, OH 43210

## Introduction

Oxo process alcohols are a major class of organic chemicals.[1] The oxo process (i.e., hydroformylation) consists of reacting an olefin with carbon monoxide and hydrogen at elevated temperatures and pressures, in the presence of a suitable catalyst, to produce an aldehyde with a carbon number one higher than the starting olefin. The product stream from the Oxo process needs to be hydrogenated to convert the aldehydes to alcohols. Catalysts frequently used for aldehyde hydrogenation include copper chromite, molybdenum sulfide, nickel, and cobalt. Although copper chromite has excellent hydrogenation activity, it is also very sensitive to sulfur poisoning, making it difficult to use with sulfur containing feed streams. Sulfided Ni-Mo/$Al_2O_3$ catalysts provide excellent hydrogenation activity while showing a high tolerance to sulfur compounds, however, a major problem is the selectivity loss due to side reactions.

Although there is ample literature on the application of sulfided Ni-Mo catalysts in hydrotreating, especially in HDN reactions, there have not been many studies focusing on their application in aldehyde hydrogenation reactions. Especially an understanding of how the surface characteristics correlate with different reaction pathways is lacking. This communication presents the results on the catalytic performance of reduced and sulfided Ni-Mo/$\gamma$-$Al_2O_3$ catalysts in hydrogenation of lower aldehydes and their pre-reaction, post-reaction, and *in-situ* characterization using XRD, TEM, XPS, DRIFTS, and chemisorption techniques.

## Experimental

**Catalyst Preparation.** Alumina-supported catalysts with different $MoO_3$ and NiO loadings were prepared by wet co-impregnation of $\gamma$-$Al_2O_3$ with aqueous solutions of ammonium heptamolybdate $[(NH_4)_6Mo_7O_{24}\cdot 4H_2O]$ and nickel nitrate $[Ni(NO_3)_2\cdot 6H_2O]$. The preparation procedure was reported previously.[2] Catalyst compositions are reported as weight percentages of the oxide precursors, i.e., $MoO_3$, NiO. Prior to reactions, the catalysts were sulfided or reduced *in situ*, followed by He flushing at the same temperature for 2 hour and cooling to reaction temperature.

**Catalyst Characterization.** *In-situ* XRD patterns were acquired by a Bruker D8 Advance X-Ray Diffractometer equipped with atmosphere and temperature control capabilities and operated at 40 kV and 50 mA. Reduction was performed *in-situ* under 5% $H_2/N_2$ gas flow using a linear temperature-program between isothermal steps. XPS was performed using an AXIS Ultra XPS spectrometer, operated at 13 kV and 10 mA with monochromatic Al K$\alpha$ radiation (1486.6 eV). Catalysts were mounted on sample holder with conductive tape in dry glove box and transferred to the analysis chamber of the spectrometer with a controlled-atmosphere transporter. Charge neutralization was used to reduce effect of charge built on samples. All binding energies were referenced to Al 2p of 74.4 eV. DRIFTS experiments were performed using a Bruker IFS66 instrument equipped with MCT detectors (operated at -196 $^oC$) and a KBr beam splitter. Catalyst was placed in a sample cup inside a Spectratech diffuse reflectance cell equipped with KBr windows and a thermocouple mount that allowed direct measurement of the surface temperature. NO and $CO_2$ adsorption process was carried out by introducing NO or $CO_2$ into the system at room temperature and followed flushing with He. Pyridine was carried into the chamber by He with a diffusion tube, followed by He flushing. TPD experiments were performed using a system previously described.[3] The reactor effluent composition was continually monitored as a function of sample temperature by a mass spectrometer (Hewlett-Packard, MS Engine 5989A). The volumetric measurements of $CO_2$ and NO chemisorptions (at 30 and –78 $^oC$, respectively) were performed using Micromeritics ASAP2010 instrument.

**Reaction Studies.** Hydrogenation of aldehydes was carried out in a fixed bed flow reactor, which made out of 1/4-in stainless steel tubing. The amount of catalyst loaded into the reactor corresponded to a total surface area of 25 $m^2$ except when otherwise noted. Reaction temperatures were in the range of 140–180 $^oC$ and pressure was kept at 1000 psig. Hexanal, propanal, and other feeds were introduced into the reaction system by saturating a stream in $H_2$ using a bubbler. The concentration of feed was controlled by the temperature of bubbler and verified by GC analysis. The outlet of reactor was connected directly to a condenser, which was cooled in an ice-water bath. Decane was used as the solvent in the condenser. Condensed species were analyzed by GC using the auto liquid injector. The lighter components were analyzed on-line using the gas injection mode of the GC.

## Results and Discussion

The reaction products from hydrogenation of aldehydes were grouped in three categories: alcohol, heavy products and light products. The primary selectivity loss was due to heavy product formation from condensation of aldehydes and aldehyde with alcohol. DRIFTS experiment[4] for bi-metallic Ni-Mo catalysts and FTIR experiment[5] for mono-metallic Mo catalysts showed that NO and $CO_2$ can be used as probe molecules for anion vacancies (i.e., coordinatively unsaturated sites) and surface hydroxyl groups, which may be associated with alumina surface. The correlations of NO and $CO_2$ uptake, measured through a volumetric chemisorption technique, with propanol and heavy product formation rates in propanal hydrogenation over sulfided catalysts are presented in **Figure 1.**

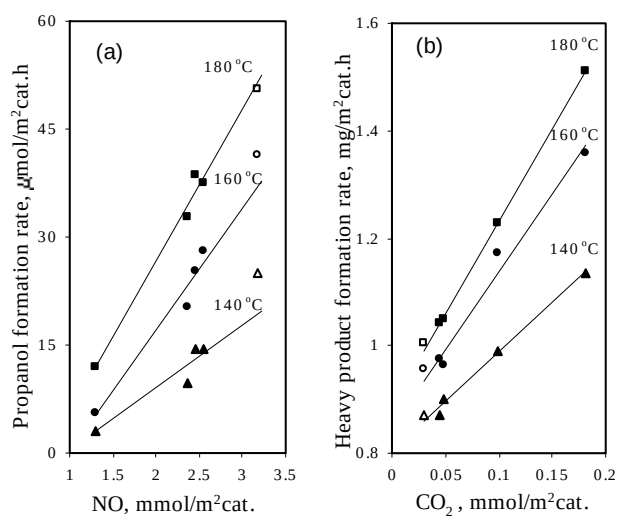


**Figure 1.** Correlations of NO and $CO_2$ adsorptions with formation rates of propanol (a) and heavy products (b). Solid points: Mo catalysts with different loading; Blank points: Ni-Mo catalysts.

Hexanal hydrogenation exhibits similar correlations. Alcohol formation rate varies linearly with NO uptake, implying that the anion vacancies are indeed the active sites for aldehyde hydrogenation to form hexanol. Results obtained by using alcohols as feed molecules showed a higher reactivity for alcohol, suggesting that the "observed" formation rate of propanol may be significantly lower than the actual formation rate due to further reaction of alcohol once it is formed. This would explain the minus formation rates for propanol when NO adsorption is extrapolated to zero. The heavy product formation rate increases linearly with increasing $CO_2$ uptake, suggesting a correlation between the $CO_2$ adsorption sites and the active sites for the heavy product formation. However, the extrapolated lines do not go through the origin, suggesting that there may be additional sites contributing to the formation of heavy products, which are not "probed" by $CO_2$ adsorption. These could be more acidic OH groups as well as the sulfhydryl (SH) groups.

**Figure 2** shows the adsorbed pyridine bands (adsorbed at 150 °C) over 3%Ni-15%Mo/$Al_2O_3$ catalysts treated at different conditions. The spectrum taken over the bare support reduced at 500 °C is also included for comparison.

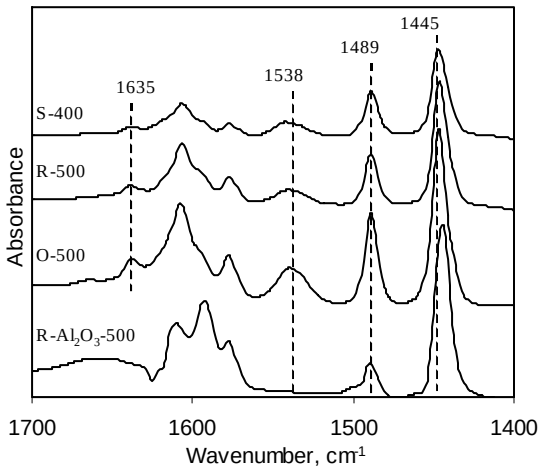


**Figure 2.** DRIFTS spectra of adsorbed pyridine over 3%Ni-15%Mo/$Al_2O_3$ catalysts and $Al_2O_3$ support treated at different conditions. O-oxidized, S-sulfided, R-reduced; numbers present temperatures.

The bands at 1445 and 1538 $cm^{-1}$ are the characteristics of anti-symmetric vibrations of adsorbed pyridine over L and B acidic sites, respectively. The band at 1489 $cm^{-1}$ has contributions from the symmetrical vibrations of both L and B sites. The reduced $Al_2O_3$ support shows strong bands from Lewis acid sites only. No Bronsted acid sites are observed over the bare support. The oxidized sample exhibits strong bands at 1538 and 1635 $cm^{-1}$ (anti-symmetric and symmetric vibration of adsorbed pyridine over Bronsted acidic sites, respectively), signaling the presence of Bronsted acid sites. The spectra taken over the reduced and sulfided samples are very similar, with strong bands arising from pyridine adsorbed on Lewis acid sites along with relatively weak bands from pyridine adsorbed on Bronsted acid sites. One interesting point to note about these results is that pyridine adsorption on Bronsted acid sites over these catalysts was not observed by some researchers, especially when the IR spectra were collected under high vacuum. Other researchers, however, reported the presence of Bronsted acid sites in IR spectra as identified by pyridine adsorption,[6-7] in agreement with our observations. The fact that the DRIFT spectra in our experiments were collected after flushing (without evacuating) the sample chamber with He and by using a high-sensitivity MCT detector (operated at 77 K) can explain why the presence of Bronsted acid sites were clearly visible. It is conceivable that under vacuum conditions, SH- or OH- groups may re-associate with $H^+$ ions and desorb, eliminating the Bronsted acid sites. The fact that the Bronsted acid sites were observed over both reduced and sulfided catalysts seem to support our earlier assertion that the two catalysts may have analogous sites in the form of OH- and SH- groups or S or O vacancies. [8]

*In situ* XRD and DRIFTS experiments and controlled-atmosphere XPS studies showed that sulfidation was not complete at temperatures lower than 400 °C. Higher sulfidation temperatures, on the other hand, led to the formation of sulfate species on the surface. Pre-treatment of the catalyst following sulfidation was also seen to play a major role in the relative abundance of the CUS sites, SH sites and OH sites.

**Table 1. Performance Comparison of Reduced and Sulfided Ni-Mo/$Al_2O_3$ Catalysts in Propanal Hydrogenation.** [a]

| Performance | 180 °C | | 160 °C | | 140 °C | |
|---|---|---|---|---|---|---|
| | S-400 | R-500 | S-400 | R-500 | S-400 | R-500 |
| S%-lights | 2.8 | 0.7 | 1.1 | 0.2 | 0.3 | 0.1 |
| S%-propanal | 57.4 | 69.1 | 38.6 | 54.0 | 29.2 | 49.6 |
| S%-heavies | 39.8 | 30.2 | 60.3 | 45.8 | 70.5 | 50.3 |
| C%-propanal | 53.7 | 67.0 | 25.4 | 40.3 | 13.6 | 21.9 |

[a] Reaction conditions: 1000 psi, 0.35% propanal in 250 $cm^3$ (STP)/min $H_2$, 12.5 $m^2$ catalyst.

Reduced Ni-Mo/$Al_2O_3$ catalysts show superior aldehyde hydrogenation activity and alcohol selectivity than their sulfided counterparts, as shown in **Table 1**. As shown earlier,[8] reduced catalysts, which may be represented as a Ni-Mo-O structure, possess catalytic behavior analogous to Ni-Mo-S catalysts. A reduction temperature of 500 °C appears to be optimum for forming a catalyst surface where majority of Mo species are in a +4 oxidation state and the oxygen anion vacancies are maximized. This temperature also appears to be optimum for minimizing the exposed alumina surface and the OH groups that lead to heavy product formation. The *in-situ* X-ray diffraction, controlled-atmosphere XPS, DRIFTS and chemisorption studies have provided complementary data that support this assertion.

**References**


(1) MeKetta, J. J.; Cunningham, W. A. In *Encyclopedia of chemical processing and design* 33; New York and Basel, 1990; pp. 46.
(2) Ozkan, U. S.; Zhang, L.; Ni, S.; Moctezuma, E. *J. Catal.* **1994**, *148*, 181.
(3) Ozkan, U. S.; Cai, Y.; Kumthekar, M. W.; Zhang, L. *J. Catal.* **1993**, *142*, 182.
(4) Wang, X.; Ozkan, U. S. *J. Catal.* **2004**, *227*, 492.
(5) Millman, W. S.; Segawa, K.; Smrz, D.; Hall, W. K. *Polyhedron* **1986**, *5*, 169.
(6) Topsoe, N. Y.; Topsoe, H.; Massoth, F. E. *J. Catal.* **1989**, *119*, 252.
(7) Rajagopal, S.; Marzari, J. A.; Miranda R. *J. Catal.* **1995**, *151*, 192.
(8) Bunch, A. Y.; Ozkan, U. S. *J. Catal.* **2002**, *206*, 177.

# UV RAMAN SPECTROSCOPIC STUDY OF V/δ-$AL_2O_3$ CATALYSTS IN BUTANE DEHYDROGENATION

*Zili Wu and Peter C. Stair**

Center for Catalysis and Surface Science, Northwestern University, Evanston, IL 60208, USA. pstair@northwestern.edu

## Introduction

The increasing demand for light olefins and the insufficient capacity from current production by steam and catalytic cracking are the driving forces to seek alternative ways to manufacture these chemicals. The most feasible processes on a commercial scale at present are catalytic dehydrogenation (DH) and oxidative dehydrogenation (ODH) of light alkanes. Commercial catalysts for alkane DH process are supported chromium oxide and platinum metal. Supported vanadium oxides ($VO_x$) have also been recently reported to be very active and selective for the DH of light alkanes.[1, 2] However, the structure of supported $VO_x$ and the deactivation/coke deposits under DH conditions are not well understood.

The focus of this study is the application of Raman spectroscopy to investigate the structural changes of surface $VO_x$ and the coke formation process during butane DH over V/δ-$Al_2O_3$ catalysts with various surface $VO_x$ densities (0.03 – 14.2 V/nm$^2$). A better understanding of coke formation chemistry and the role of different $VO_x$ species in coke formation could facilitate optimization of catalysts and possible reduction of side reactions leading to coke.

## Experimental

**Sample preparation.** Supported $VO_x$ samples were prepared via incipient wetness impregnation of aluminas (δ-$Al_2O_3$: Johnson Matthey, UK, $S_{BET}$ = 101 m$^2$/g) with aqueous $NH_4VO_3$ solutions. Surface $VO_x$ density varied in the range 0.03 – 14.2 V/nm$^2$. A V/$Al_2O_3$ sample with surface $VO_x$ density of *Y* V/nm$^2$ will be denoted as *Y*V in the following text

**Raman Studies.** When doing butane DH reactions, the sample was first either calcined (5% $O_2/N_2$) at 823 K or reduced (5% $H_2/N_2$) at 873 K in a fluidized bed reactor[3] and then exposed to 3% butane/$N_2$ at different temperatures for 30 min. The sample was purged with He at reaction temperature for another 10 min before spectral collection. The reaction of 1-butene, cis-2-butene, trans-2-butene, and 1,3-butadiene (all the $C_4$ olefins are around 3% in $N_2$) with supported $VO_x$ was conducted on a 1.2V sample in the similar way as butane DH.

Most Raman spectra were collected at room temperature in flowing He on the UV Raman instrument built at Northwestern University.[4]

## Results and Discussion

We selected several V/δ-$Al_2O_3$ catalysts (0.03V, 1.2V, 4.4V, and 14.2V) for butane DH studies because our Raman study[5] suggests that these catalysts contain surface $VO_x$ species with different structures. 0.03V possesses exclusively isolated $VO_x$ in tetrahedral coordination. 1.2V contains both isolated and polymerized $VO_x$ species. A mixture of polyvanadates with different polymerization degrees and crystalline $V_2O_5$ are present on 4.4V and 14.2 V samples. We expect that a Raman study of butane DH over these samples may provide a correlation between the nature of coke species and the structure of the catalysts.

Taking 1.2V sample as an example, the Raman spectra collected during butane DH at different temperatures are shown in Fig. 1. At temperatures below 673 K, a weak Raman band at around 1605 cm$^{-1}$, due to C=C stretching in polyaromatics,[6] is observed together with the two bands at 1022 and 910 cm$^{-1}$ due to V=O and V-O-Al modes

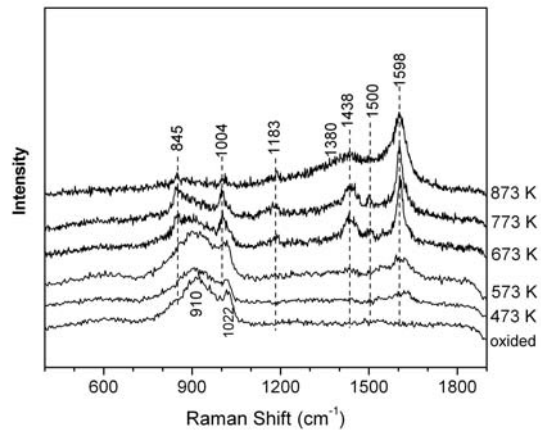


**Figure 1.** Raman spectra from butane dehydrogenation over calcined 1.2V/δ-$Al_2O_3$ at different temperatures

of surface $VO_x$ species,[5] respectively. After butane DH at 673 and 773 K, an intense band at 1598 cm$^{-1}$ due to polyaromatics develops. Simultaneously, bands at 1500, 1438, 1183, 1004, and 845 cm$^{-1}$ are observed. Meanwhile, Raman bands due to surface $VO_x$ are no longer observable, due to absorption of radiation by surface coke species. The band at 1500 cm$^{-1}$ can be assigned to conjugated polyolefins or cyclopentadiene species.[7, 8] The band at 1438 cm$^{-1}$ is due to the bending mode of $CH_3/CH_2$ or C-H in aromatic rings. C-C stretching in aromatics usually shows up around 1180 cm$^{-1}$. The two sharp bands at 1004 and 845 cm$^{-1}$ can be either ascribed to surface $VO_x$ species or coke species. They are confirmed to be due to coke deposits on the surface by doing the same reaction on an oxygen-18 exchanged V/δ-$Al_2O_3$ sample. Their assignment will be addressed later. As the DH temperature goes up to 873 K, the Raman bands below 1500 cm$^{-1}$ decrease greatly in intensity. The intensity ratio $I_{1598}/I_{1438}$ increases as the temperature increases, indicating the formation of more dehydrogenated coke species at higher reaction temperatures. Raman spectra obtained from the reaction of butane with pre-reduced 1.2V are quite similar to those on pre-oxidized 1.2V (Fig. 1). It seems that the initial valence state of surface V does not affect the nature of coke species.

The Raman spectra of butane DH over other V/δ-$Al_2O_3$ samples (0.03V, 4.4V, and 14.2V) show similar Raman bands to those on 1.2V sample, indicating that similar coke species are formed on these catalysts. The band intensity patterns suggest that the coke species formed on supported $VO_x$ have a sheet-like topology.[8] However, some slight spectral differences can be distinguished. The intensity ratio $I_{1598}/I_{1438}$ increases not only as the reaction temperature rises but also as surface $VO_x$ density increases, implying that highly dehydrogenated coke species are more easily formed on polyvanadates than on monovanadates. Moreover, conjugated polyolefins with a Raman band at ca. 1500 cm$^{-1}$ are not formed on 0.03V sample. These differences show that the nature of the coke formed on the surface is somehow related to the structure of $VO_x$ species. It is also noted that Raman bands due to surface $VO_x$ are still observable, with decreased intensity, only for the 0.03V sample after butane DH. The decrease in intensity of the bands suggests a reduction of surface $VO_x$ under butane DH conditions.

$C_4$ olefins (1-butene, 2-butenes, and 1,3-butadiene) are supposed to be the primary products from butane DH. So Raman studies of their reaction with the supported $VO_x$ catalysts will not only help to assignment of the two Raman bands at ca. 850 and 1005

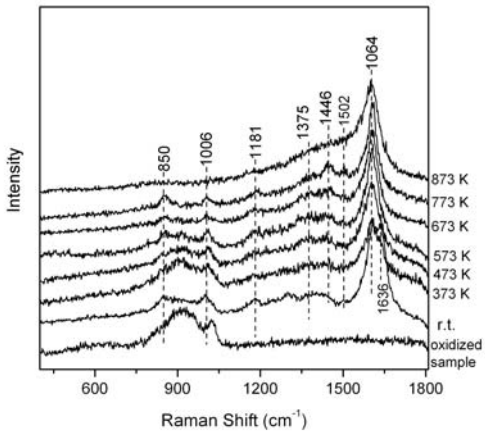


**Figure 2.** Raman spectra from 1,3-butadiene dehydrogenation over calcined 1.2V/δ-$Al_2O_3$ at different temperatures

$cm^{-1}$ but also provide information on which of these olefins are the coke formation intermediates.

Raman spectra from the reaction of the $C_4$ olefins on 1.2V sample show quite similar features to each other and to those from butane DH at temperature above 573 K This indicates that the four $C_4$ olefins are possible coke precursors in butane DH reaction on supported $VO_x$ catalysts.

Raman spectra (Fig. 2) from 1,3-butadiene DH on 1.2V sample show some different features from other olefins and butane at reaction temperatures below 573 K A comparison of these Raman spectra can be helpful for the interpretation of the two bands at around 850 and 1006 $cm^{-1}$. It is interesting to see that these two bands are readily formed upon room temperature adsorption of 1,3-butadiene on the 1.2V sample and persist from reaction temperature up to 773 K (see Fig. 2). The two bands observed at room temperature can be removed after heating in He at 573 K, suggesting they are due to adsorbed 1,3-butadiene on the V/δ-$Al_2O_3$ sample. Thus the bands at 850 and 1006 $cm^{-1}$ can be assigned to $=CH_2$ rocking and =CH bending, respectively. But the bands appearing at higher temperature (above 473 K) are quite stable upon desorption. Therefore, we propose that the two bands at ca. 850 and 1006 $cm^{-1}$ observed upon the reaction of $C_4$ olefins and butane on $VO_x$ samples are related to a $–CH=CH_2$ structure but not exactly 1,3-butadiene. This group is possibly connected to aromatic rings because the two bands seem to be from the same coke species as the bands at 1183, 1438, and 1598 $cm^{-1}$ which are due to polyaromatics.

Regeneration of the coked samples by 2% $O_2/N_2$ at different temperatures is also carried out to reveal the oxidation behavior of coke species. It turns out that the total oxidation temperature of the coke species also depends on the surface $VO_x$ density, i.e., the structure of surface $VO_x$ species. Coke species formed on polymerized $VO_x$ are more easily removed than on isolated $VO_x$. The structure of V/δ-$Al_2O_3$ is fully regenerated after the coke removal

**Acknowledgement.** This work is financially supported by ATHENA and the Chemical Sciences, Geosciences and Biosciences Division, Office of Basic Energy Sciences, Office of Science, U.S. Department of Energy under Grant No. DE-FG02-97ER14789. The Athena project is funded by the Engineering & Physical Sciences Research Council (EPSRC) of the U.K. and Johnson Matthey plc

## References

(1) Mamedov, E. A.; and Cortes-Corberan, V. *Appl. Catal.* **1995**, *127*, 1.
(2) Harlin, M. E.; Niemi, V. M.; and Krause, A. O. *J. Catal*. **2000**, *195*, 67.
(3) Chua, Y. T., and Stair, P. C. *J. Catal.* **2000**, *196*, 66.
(4) Li, C., and Stair, P. C. *Stud. Surf. Sci. Catal.***1996**, *101*, 881.
(5) Wu, Z. L.; Kim, H. S.; Rugmini, S.; Jackson, S. D.; and Stair, P. C. *J. Phys. Chem. B, submitted.*
(6) Kuba, S.; and Knözinger, H. *J. Raman Spectrosc*. **2002**, *33*, 325.
(7) Chua, Y. T.; Stair, P. C.; Nicholas, J. B.; Song, W.; Haw, J. F. *J. Am. Chem. Soc.* **2003**, *125*, 866.
(8) Chua, Y. T., and Stair, P. C. *J. Catal.* **2003**, *213*, 39.

# HYDROGENATION OF AROMATICS VIA RF PLASMA DERIVED NI CATALYSTS

*Chalita Ratanatawanate, Monyka Macias, Ai-Min Zhu and Ben Jang*

Chemistry Department, Texas A&M U.-Commerce, Commerce, TX 75429-3011

## Introduction

Hydrogenation of aromatic compounds is an important research area due to stringent environmental regulations on the content of aromatics in fuels. Ni catalysts have been widely studied for the reaction because of their high activity and relatively low cost [1]. This study focuses on the development of the RF plasma technique to improve the activity and stability of Ni catalysts for benzene hydrogenation to cyclohexane because plasma based techniques for catalyst preparation have recently been used to develop catalytic materials with unusual catalytic properties including high metal dispersion and better stability [2,3]. The goal is to demonstrate the unique capability of RF plasma technique to improve the efficiency of various catalytic processes by controlling the metal dispersion and the interaction between metals and supports.

## Experimental

20-40 mesh alumina particles with or without plasma pre-treatments are impregnated with calculated nickel nitrate solution using the incipient wetness technique. The support material with plasma treatments before impregnation are designated as (B), for example air(B) representing catalyst with plasma treatment before impregnation with nickel nitrate. The catalysts treated with plasmas are designated as (A), for example $H_2$(A) representing catalyst with $H_2$ plasma treatment after nickel nitrate impregnation.

Plasma treatments were carried out in the custom-designed 360° rotating RF plasma system. The detail of the system is described in the previous publication. [4] 400 mtorr and 160 watt were used for both $H_2$ and air plasmas in this study. Typically, one gram of catalysts is loaded in the plasma chamber for plasma treatments. The time for plasma treatment ranges from 10 to 30 minutes with a continuous wave.

5%Ni/$Al_2O_3$ catalysts tested include air(B), $H_2$(B) un-calcined and air(A) and $H_2$(A). Reaction study was carried out with a space velocity of ~63,000 cc/h-g catalyst at temperatures from 50-150°C with hydrogen to benzene ratio of 18 to 1.

## Results and Discussion

The activities of catalysts as a function of time on stream after reduction in $H_2$ at 450°C are shown in Figure 1. The activity goes through an initial fast decrease and quickly stabilizes followed by a slow decrease with time. The activity order of five different 5%Ni/$Al_2O_3$ catalysts after 8 hours on stream is air(B) > $H_2$(B), air(A) > $H_2$(A), un-calcined. The results suggest both air and $H_2$ plasma modifications before the impregnation of nickel precursor are effective in improving the activity. However, only the air plasma modification after nickel precursor impregnation slightly improves the activity while the $H_2$ plasma has negligible effect. The improved activity of catalysts with plasma modifications is hypothesized to be resulted from cleaned surfaces to stabilize smaller Ni metal particles to achieve higher dispersion.

To determine the plasma effect on catalytic stability we use an extended reduction in $H_2$ at 600°C for 5 hours to speed up the deactivation. The activities of all catalysts are tested again under the same reactions as the catalyst with a reduction at 450°C. The results of conversion versus time are shown in Figure 2. The activity order after 8 hours on stream is air(A), $H_2$(A) > air(B), $H_2$(B) > un-calcined. The relative stability of catalysts is calculated based on the percent decrease from the activity with 450°C reduction to the activity with 600°C reduction. The result is summarized in Table 1. The percent decrease order for all five catalysts is $H_2$(A) < air(A) < $H_2$(B) < air(B), un-calcined.

## Summary

Plasma modifications before and after impregnation of metal precursors are effective in improving the activity of Ni catalysts for benzene hydrogenation. Plasma modification before impregnation is slightly more effective than the plasma modification after impregnation. However, plasma modifications after impregnation increase the stability of catalysts much more than that of catalysts with plasma modification before the impregnation. The economic benefit of much improved stability of Ni catalysts for hydrogenation of benzene is significant. Via RF plasma techniques similar benefits for various catalysts and other industrial processes can be expected.

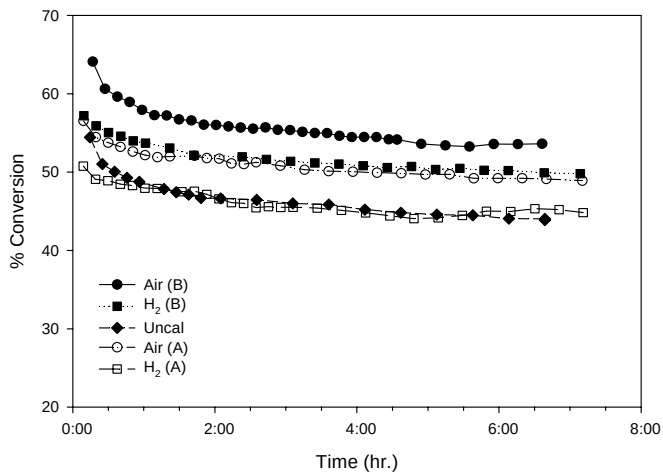


**Figure 1.** Activities of Ni catalysts versus time for benzene hydrogenation at 150°C after reduction at 450°C.

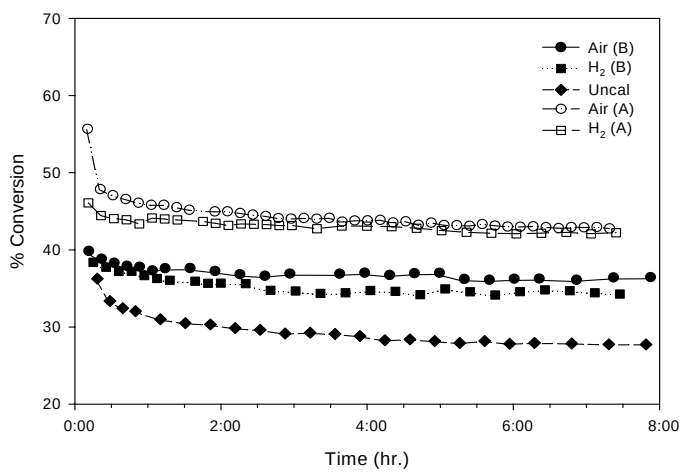


**Figure 2.** Activities of Ni catalysts versus time for benzene hydrogenation at 150°C after extended reduction at 600°C.

**Table 1. Activity and stability of Ni catalysts for benzene hydrogenation at 150°C.**

| Catalyst | % benzene conversion after 8 hours on stream | | Percent decrease of activity |
|---|---|---|---|
| | Reduction at 450°C | Reduction at 600°C | |
| **Air(B)** | 55.8 | 36.9 | 38.8 |
| **$H_2$(B)** | 52.1 | 35.2 | 32.4 |
| **Un-calcined** | 46.9 | 29.5 | 37.2 |
| **Air(A)** | 51.2 | 44.2 | 13.6 |
| **$H_2$(A)** | 46.3 | 43.0 | 7.1 |

**Acknowledgement.** The authors wish to acknowledge the financial support partly by the Welch Foundation and the Organized Research Grant of Texas A&M U.-Commerce.

**References**

1. Stanislaus, A and Cooper, B.H., *Catal. Rev. Sci. Eng.*. **1994**, *36*, 75.
2. Liu, C.-J.; Vissokov, G.P.; Jang, B.W.-L. *Catalysis Today*, **2002**, *72*, 173.
3. "Plasma Technology and Catalysis" edited by Jang et al. *Catalysis Today*, **2004**, 89(1-2).
4. Zhan, Jason; Boopalachandran, Praveen; Jang, Ben W.-L., Cho, Jai and Timmons, Richard B.; *Am. Chem. Soc., Div. of Fuel Chem. PREPRINTS*, **2004,** *49(1)*, p176.

# TRANSFORMATION OF FERROUS SULFATE-BASED CATALYST DURING HYDROGENATION OF COAL

*Lian Zhang[1,2], Jianli Yang[1*], Zhenyu Liu[1] and Hang Gao[1]*

[1]State Key Laboratory of Coal Conversion
Institute of Coal Chemistry, Chinese Academy of Sciences
P.O.Box 165, Taiyuan 030001, P. R. China

[2]Department of Applied Chemistry, Chubu University
1200 Matsumoto-cho, Kasugai, Aichi 487-8501, Japan

## Introduction

Iron based catalysts exhibit high activity and selectivity in hydrogenation of coal (1-2). Ultra fine iron based catalysts is desirable due to the presence of a larger percentage of unsaturated coordination sites on surface and intimate contact with coal during hydrogenation (2). In situ impregnation of iron based catalyst is even better because the nano-size iron species form not only on coal surface but also in coal's pore network. Correspondingly, significant enhancements in coal hydrogenation conversion can be achieved using in situ catalyst impregnation compared to those using physical mixing of ultra fine catalysts and coal. The objective of this study is to investigate chemical transformation of impregnated ferrous sulfate based catalysts during hydrogenation of a Chinese coal. To overcome the interference of coal matrix on analysis, X-ray diffraction (XRD) and X-ray photoelectron spectroscopic (XPS) were used to study the catalyst composition in the bulk and on the surface of coal samples before and after the hydrogenation. The neighbouring coordination structure of iron element was also determined by the extended X-ray adsorption fine structure (EXAFS)

## Experimental

Yanzhou coal (YZ), a Chinese bituminous coal, was used. Its properties are listed in Table 1. It was ground to <170μm and dried under vacuum before use.

**Table 1. Properties of Yanzhou Coal**

| Proximate analysis, **wt%** | | | |
|---|---|---|---|
| Moisture, as | Ash, as | | Volatile Matter, daf |
| 2.7 | 2.84 | | 44.71 |
| Ultimate analysis, wt%, daf | | | |
| C | H | N | S |
| 81.49 | 5.86 | 1.27 | 2.70 |
| Petrographic Composition, wt% | | | |
| Vitrinite | semi-vitrinite | exinite | Inertinite |
| 76.7 | 2.5 | 2.9 | 17.9 |

"as" denotes as received; "daf" denotes dry ash free.

The catalyst precursor was impregnated on coal. The impregnation procedures had been reported earlier (2). Three samples were prepared using different reagents. Sample YZ1 was prepared by impregnation of $FeSO_4$ onto YZ coal; sample YZ3 by co-impregnation of $FeSO_4$ and $Na_2S$; and sample YZ4 by co-impregnation of $FeSO_4$ and urea. The iron loadings of the three samples are 2.0 wt%. The hydrogenations were carried out in a 25 ml tubing bomb reactor at 400°C under an initial $H_2$ pressure of 7.0 MPa without using a solvent. Detailed experimental procedures have been reported elsewhere (2).

∗ Corresponding author. Tel: +86-351-4048571; Fax: +86-351-4041153; E-mail address: jyang@sxicc.ac.cn.

XRD analysis was made on a Dmax-rA X-ray diffractometer with a Cu Kα radiation operated at 40kV and 50mA. XPS analysis was carried out in 2202-XL ESCA. Carbon (1s) at 284.0 eV was used as the reference for binding energy. EXAFS characterization was conducted at a beamline of 4W1B at Beijing Synchrotron Radiation Facility. The X-ray energy was varied from approximately 200 eV below the Fe K-shell absorption edge to 800 eV above the edge using a double crystal Si (111) monochromator.

## Results and discussion

Activity of the catalysts in hydrogenation of the coal is defined as the percentage conversion of coal to THF soluble materials on dry-and-ash-free base. Compared to the YZ coal, the conversions of the iron loaded samples are significantly high (38% for YZ, 54% for YZ1, 77% for YZ3 and 70% for YZ4). The activities of the catalysts on YZ3 and YZ4 are higher than that on YZ1, indicating promotive effect of $Na_2S$ and urea on the activity of $FeSO_4$.

XRD analysis showed well-developed crystals in YZ1 corresponding to $FeSO_4{\cdot}H_2O$ and a small amount of β-$Fe_2O_3$ (see figure 1 and Table 2). The existence of $FeSO_4{\cdot}H_2O$ species is consistent with what reported by Artork et al (3). The presence of β-$Fe_2O_3$ may result from air oxidization of the highly dispersed iron element on coal surface. XRD patterns of YZ3 and YZ4 are significantly different from that of YZ1. $FeS_2$ was found in YZ3 as the main species, which is consistent with the stoichiometry of the reaction between $FeSO_4$ and $Na_2S$. FeOOH was also observed in YZ3, possibly resulted from hydrolysis of sulfide ion and oxidization of ferric ion in the basic solution of $Na_2S$. Iron oxides, such as β-$Fe_2O_3$, FeOOH and $Fe_3O_7(OH){\cdot}7H_2O$, are the main species in YZ4, which is similar to the form of super-acid catalyst ($Fe_2O_3/SO_4$).

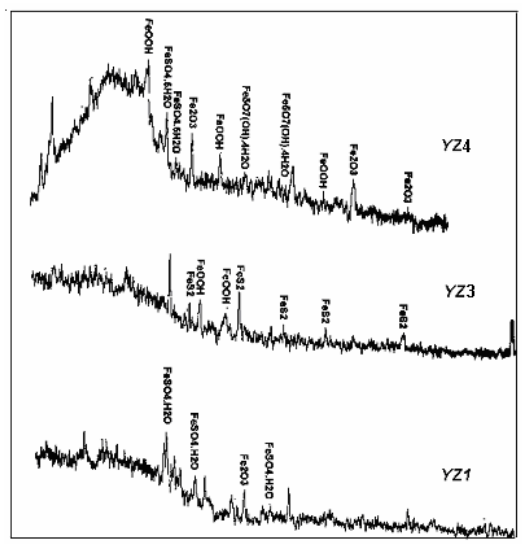


**Figure 1.** XRD patterns for the raw coal and the coal impregnated with the catalyst precursors.

**Table 2. Results from XRD Analyses**

| Sample | Major species | Minor species |
|---|---|---|
| YZ 1 | $FeSO_4.H_2O$ | β-$Fe_2O_3$ |
| YZ 3 | $FeS_2$, FeOOH | |
| YZ 4 | FeOOH, $Fe_3O_7(OH).7H_2O$, β-$Fe_2O_3$ | $FeSO_4.6H_2O$ |

XPS analysis revealed that oxygen, iron, carbon and sulfur elements exist distinctly on the surface （see figure 2）. It was found that the surface Fe/C ratio on YZ1 is lower than the theoretic value ($4.62x10^{-3}$ vs. $5.5710^{-3}$), suggesting some iron penetrated into the pore network of the coal. The surface Fe/C ratio for YZ3 and YZ4 are higher than the theoretic value ($7.58\ x10^{-3}$ and $11.34\ x10^{-3}$ vs. $5.5710^{-3}$), resulting from the fast precipitation between the iron ions and the promoters (S ions and OH ions) during the impregnation. It was also found that about 1/2 of the surface Fe in YZ1 is in the form of $FeSO_4$ and about 1/5 of that in the form of $Fe_2O_3$. However, about 1/2 of the surface Fe in YZ3 and YZ4 is in the form of FeOOH and 1/10-1/5 of that in the form of $Fe_2O_3$. Correspondingly, most of the surface S in YZ1 is in the form of $SO_4^{2-}$ and about 1/10 of that in organic sulfur form. On the contrary, more organic sulfur appears on the surface of YZ3 and YZ4.

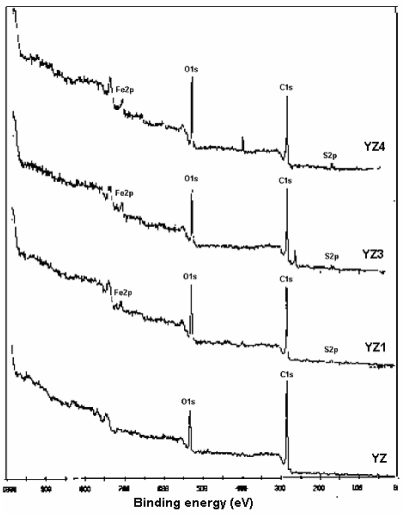


**Figure 2.** XPS spectra for the raw coal and the coal impregnated with the catalyst precursors.

EXAFS analyses indicate that, before the hydrogenation, most of the iron coordinates with oxygen and sulfur, and $FeSO_4$ character is weak or is overlapped with Fe/S coordination. Radial structure function (RSF) of the pure compounds and the impregnated samples are shown in figures 3 and 4. The position and shape of Fe/O and Fe/S coordination peaks vary with the promoters. It indicates the iron in deferent samples presents with different forms and concentrations, which can be related to different hydrogenation activity.

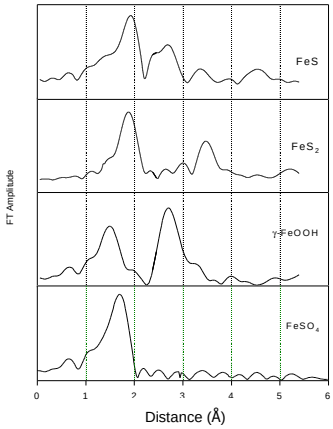


**Figure 3.** Radial structure function (RSF) of pure compounds.

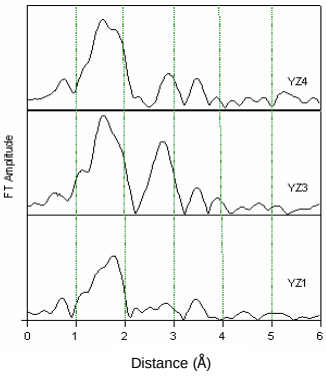


**Figure 4.** Radial structure function (RSF) of the impregnated samples.

The residues from the hydrogenation generally exhibit $Fe_{1-x}S$ (pyrrhotite) characteristics. This agrees with the common understanding that pyrrhotite is the active species for hydrogenation of coals. However it was also found that the iron species in YZ3 sample ($Na_2S$ as the promoter) completely transforms to the form of $Fe_{1-x}S$ while part of iron element in YZ4 sample (urea as the promoter) existed in the form of $FeSiO_3$ ($FeO{\cdot}SiO_2$) after 12 min reaction. XPS analyses showed that as the progress of the hydrogenation, the surface concentrations of oxygen and sulfur decrease and the surface concentration of carbon increase, and FeOOH and $Fe_2O_3$ transform into FeS. the concentration of $SO_4^{2-}$ decreases for YZ3 residue and increases for YZ4 residue with the increasing of the reaction time. In addition to the higher Fe/O character of YZ4 residue, it suggests that urea may promote the transform of super acid, $Fe_2O_3/SO_4^{2-}$.

## Conclusions

Impregnation of $FeSO_4$ alone leads to slightly increase the coal conversion than that without any catalyst. However, the co-impregnation of $FeSO_4$ and promoter, $Na_2S$ or urea, results in a remarkable increase of the conversion, which is nearly twice as much as that of the raw coal.

When $FeSO_4$ is impregnated alone on the coal, the iron form generally remains unchanged but with a small amount of iron oxides on the coal surface. Co-impregnation of $FeSO_4$ and $Na_2S$ leads to the occurrence of FeS and FeOOH species. Co-impregnation of $FeSO_4$ and urea results in complete surrounding of iron element by oxygen.

In spite of the different iron forms, most of the iron transforms to $Fe_{1-x}S$ after 12 min hydrogenation reaction, although some of iron oxides still exist after the 12 min reaction in the presence of urea. The oxide is in combination with $SiO_2$ (from coal ash). The co-impregnation of $FeSO_4$ and urea on the coal may lead to formation of super acid sites during hydrogenation of coal.

**Acknowledgment.** The Natural Sciences Foundation of China (90210034), the National Basic Research Program (2004CB217602) and Chinese Academy of Sciences are gratefully acknowledged for the financial supports. The Beijing Synchrotron Radiation Facility (BSRF), professors Tiandou Hu, Tao Liu and Yaning Xie are also acknowledged for providing the facility and technical support.

## References

(1) Kaneko T; Tazawa K; Okuyama N; Tamura M; Shimasaki K. *Fuel*, **2000**, *79*, 263.
(2) Zhang L; Yang J; Zhu J; Liu Z; Li B; Hu T; Dong B. *Fuel*, **2002**, *81*, 951.
(3) Artork L; Schobert H.H; Davis A. *Fuel Processing Technology*, **1992**, *32*, 87.

# STUDYING SULFURATION CONDITIONS OF NI CATALYST FOR $C_4$ FRACTION TO REMOVE BUTADIENE

*Fan Zhang, Xingliang Huang*

(Faculty of Chemical Science & Engineering, the Key Laboratory of CNPC, University of Petroleum, Beijing 102249, China)

**Abstract**

There is a bit of butadiene in $C_4$ fraction, and it does great harm to the parts of further process. The simplest and most economical measure is transforming butadiene to butylenes by selective hydrogenation. Non-noble metal Ni is the active ingredient in these experiments, we investigate the pretreated conditions of the catalyst, including the sulfuration mode、sulfur solution concentration and sulfuration time.

**Keyword:** $C_4$ fraction, butadiene, selective hydrogenation, $Ni/Al_2O_3$

Since the 1990s, because of the progress in the separating technology, the application of $C_4$, which is used as the raw material of chemical petroleum, achieves fast development [1]. However a bit of butadiene in $C_4$ fraction does great harm to the parts of next processes. In order to resolve these problems, the simplest and most economical measure is transforming butadiene to butylenes by selective hydrogenation. At present, there is a lot of study on noble metal Pd, or adding a small amount of auxiliary agents, such as Cu、Ag、Fe、Co、Au、Zn、Pb、Cr、Ga、In [2-5]. But Pd catalysts have more shortcomings: high price; polymerization reaction may lead to the selectivity descends, the polymers pollute the surface of catalysts, then make the stability decline; it is poisoned by mercaptan、carbonyl sulphur and arsenic etc. Therefore the exploitation of non-noble metal, which is inexpensive and has high activity、stability and anti-sulfur ability, has obvious significance [6].

## 1 Experiment

**1.1 Catalyst preparation.** Φ 1-2 mm $\gamma$-$Al_2O_3$ ,which is provided by the Petroleum Chemical Third Plant of Fushun, is calcined through high temperature. A certain amount of nickel is loaded in $\gamma$-$Al_2O_3$ carrier by impregnation. Then the catalyst is dried and calcined at given temperature. Before the usage, the catalyst is reduced by $H_2$ and pretreated in special sulfuration conditions.

**1.2 Analysis measure.** The catalyst is estimated in the up-flow fixed-bed reactor, which includes gas、liquid and solid three phases . The inner diameter of the reaction pipe is 11mm. The raw material is sent to the reactor by pump, and the reactions take place in liquid phase. The gas specimens of the raw material and products are analyzed by model sq206 gas-phase chromatographic instrument. The length of chromatographic column is 50m; inner diameter is 0.53mm, the chromatographic column fixed liquid is AT. $Al_2O_3$ /S. Collection and analysis of the chromatographic data are done by AnaStar chromatographic workstation.

**1.3 Raw material.** The raw material is liquid petroleum gas, whose compositions are listed in table 1. The reaction conditions are as follows: the temperature70℃、pressure1.3MPa、LHSV $9h^{-1}$、ratio of hydrogen to $C_4$ fraction 2:1(in reaction conditions).

**Table1. The Mass Composition of Raw Material**

| component | content /wt% | component | content /wt% |
|---|---|---|---|
| isobutane | 36.1800 | isobutylene | 15.6638 |
| butane | 10.2508 | cis- butylene -2 | 10.4948 |
| anti- butylene -2 | 14.9082 | 1，3-butadiene | 0.1159 |
| butylene | 12.3865 | sulphur | 246mg/$m^3$ |

## 2 Results and Discussions

**2.1 The necessity of sulfuration.** Because the catalyst has some strong active sites, diolefin tends to deep hydrogenation. So it is necessary that the catalyst is pretreated before the usage, and the strong active sites are deactivated, to ensure the selectivity and stability of the catalyst. It can be seen from Fig 1 that, in the same reaction condition, selectivity and activity of the catalysts, which are pretreated before the usage, are better. The sulfurating reagent is the accepting body of electrons, and its adsorption ability is more than olefin, but less than diolefin. So it can restrain olefin hydrogenation effectively. When the catalyst is pretreated, strong active sites are occupied by sulfides, the chance that butadiene contacts with hydrogen decreases; at the same time, the concentration of butadiene in the surface of the catalyst is diluted by sulfides, the conversation of butadiene declines; the middle production olefin is easy to be desorbed from the surface of the catalyst, then it can avoid the olefin hydrogenation. So it is necessary that sulfuration of the catalyst before the usage.

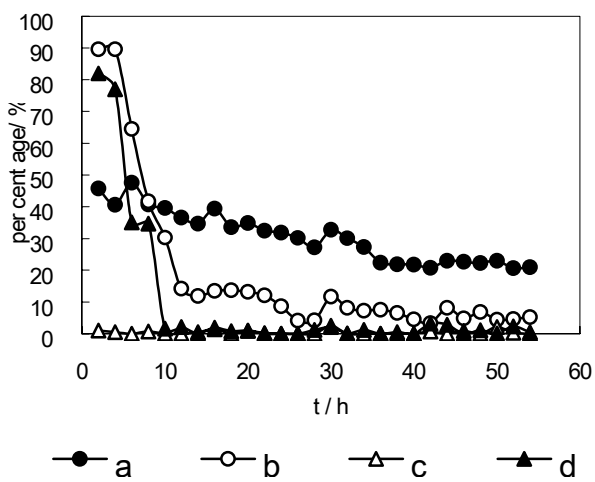


a- conversion of butadiene with sulfuration
b- conversion of butadiene without sulfuration
c- increment rate of butane with sulfuration
d- increment rate of butane without sulfuration

**Figure 1.** The compare activity and selectivity sulfuration

**2.2 Effect of S concentration in the sulfur solution on the activity of the catalyst.** It can be seen from Fig 2 that the effect of S concentration in the sulfur solution on the activity of the catalyst are obvious. If the sulfuration time and volume of the sulfur solution is the same, the S concentration in the sulfur solution increase, the effect of sulfuration may become better. When the catalyst is pretreated by the sulfur solution whose S concentration are 0.07mol/L and 0.035mol/L, the former is better. For the 0.07mol/L, because the sulfides absorb in the active sites more, the original

activity is lower, but the stability is higher. If S concentration of the sulfur solution is too high（0.7mol/L），the active sites absorb too much sulfides, so the number of active center is too few, then the activity of catalyst may decline very low. Therefore the reasonable S concentration in the sulfur solution is 0.007mol/L.

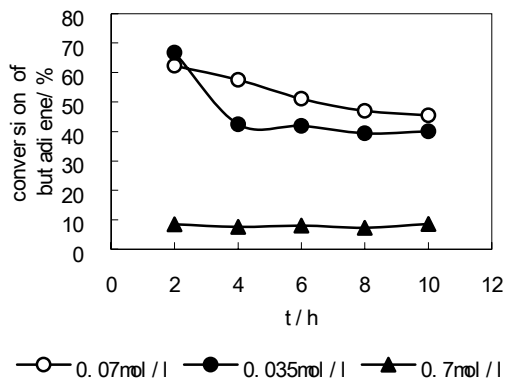


**Figure 2.** Effect of S concentration in the sulfur solution on the activity of the catalyst

**2.3 Effect of sulfuration mode on the activity of the catalyst.** It can be seen from Fig 3 that, using interior sulfuration mode, the original activity is higher, but the stabilization is slower, and the final activity is inferior; while the exterior sulfuration is opposite. Because that with interior sulfuration mode, the time of sulfuration is short, the sulfuration is inadequate, the number of active centers is more, and the original activity is higher. After a period of reaction, because the effect of sulfuration isn't good, the sulfides in the raw material absorb in the active sites, so the catalysts lose activity, which lead to the final activity is inferior. Though the sulfur solution volume is the same in both exterior sulfuration and interior sulfuration, the effect of sulfuration by soak is better than that by stream. The sulfides which absorb in the active sites from the sulfur solution is more, the effect of sulfuration is better, so the catalyst keeps stabilization soon, and the final activity is higher. So in the same condition, the effect of sulfuration by exterior sulfuration is better than that by interior sulfuration.

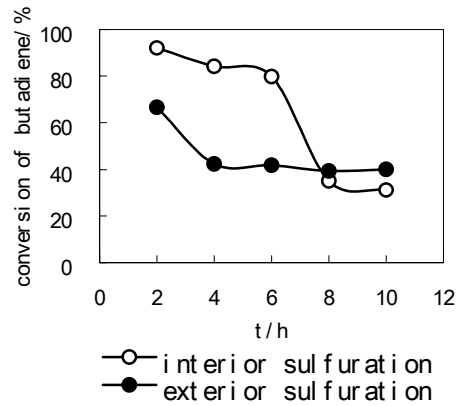


**Figure 3.** Effect of sulfuration mode on the activity of the catalyst

Though the effect of sulfuration by exterior sulfuration is better, the catalysts contacts with the oxygen in air, when they are put into the sulfur solution. Then some strong active sites may be oxygenated, and the catalysts lose activity. In order to avoid this question, we can prolong the sulfuration time. Therefore interior sulfuration is the preferable sulfuration mode.

**2.4 Effect of sulfuration time on the activity of the catalyst.** The Fig 4 reflects the effect of different sulfuration time on the activity of the catalyst. When the sulfuration time is too short (20min), the activity declines fast, because the catalyst is pretreated inadequately, the strong active centers are not deactivated fully. This lead to the original activity of the catalyst is very high, along with the reaction going on, the catalyst will absorb the sulfides from the raw material. The stronger the active center is, the more sulfides it will absorb. Then the number of active centers will decrease rapidly, the activity of the catalyst also declines fast. Mounting up the sulfuration time, the activity can keep stable, because the sulfurating reagent acts perfectly. During the reaction, there are competing absorption relationships between diolefin and sulfide to the catalyst in the raw material. Because the activity of the catalyst is tempered, the diolefin absorbs in the catalyst firstly, in the absorption process. Therefore the absorption of sulfide is very slow, and this can ensure the catalyst has stable hydrogenation activity. If the sulfuration time is too long (90min), the active centers of the catalyst react with too much sulfides, then lose activity. Therefore the best sulfuration time is 60min.

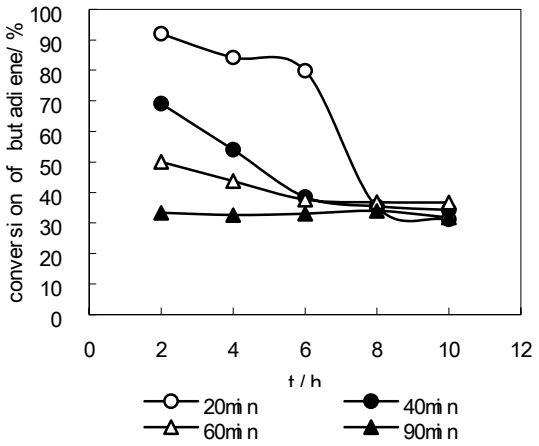


**Figure 4.** Effect of sulfuration time on the activity of the catalyst

**3 Conclusions**

We pretreated the catalyst, and selected the fittest pretreated conditions: S concentration in the sulfur solution（0.007mol/l）、the sulfuration mode(interior sulfuration)、and the sulfuration time（60min）. Therefore the activity and stability of the catalyst can be improved.

**References**

(1) Bao Shizhong. Petroleum Refinery Engineering, 2002，（32）5：18-20

(2) J W.Hightower.B.K.Furtong.A.Sarkany, L.Guczi, Proc10th Int Congr Catal, Akedemia Kiado, Budapest,1993,Vol.C,pp.2305-2308

(3) H Miura,M.Terasasaka,K.Oki and T.Matsuda,in L.Guczi,F.Solymosi and P.tetenyi(Editors),Proc 10th Int Congr Catal, Akedemia Kiado, Budapest, 1993,Vol.C,p.2379-2385

(4) A.Borgna.B.Moraweck,J.Massardier and A.J.Renouprez, J.Catal.1991,128,99-103

(5) A.Sarkany,Z.Zsoldos, B.K.Furlong, J.W.Hightower and L.Guczi, J.Catal., 1993,141,566-568

(6) J.A. Pena etc. Chemical of catalysis.1996,159,313-32

# $NO_X$ STORAGE MECHANISM OVER Pt-Ba/$Al_2O_3$ LEAN $NO_X$ TRAP CATALYSTS

*Isabella Nova, Lidia Castoldi, Luca Lietti, Enrico Tronconi, Pio Forzatti*

Dipartimento di Chimica, Materiali e Ingegneria Chimica "G. Natta", Centro NEMAS - Nano Engineered MAterials and Surfaces, Politecnico di Milano, Italy

## Introduction

The demand to improve the fuel efficiency of vehicles and the need to decrease the $CO_2$ emissions has recently led to the introduction of the so-called lean-burn engine technology. However, the presence of excess oxygen strongly decreases the efficiency of the catalytic reduction of $NO_x$ of the Three Way Catalyst. A possible solution involves the use of a Lean $NO_x$ Trap (LNT) catalyst: a LNT catalyst consists of a storage component (e.g. BaO) and a precious metal, generally Pt, dispersed on a high-surface area carrier, e.g. $Al_2O_3$. One typical example of this class of catalysts is the Pt-Ba/γ-$Al_2O_3$ system [1,2]. The LNT catalysis is based on a cyclic process during which the storage of $NO_x$ is accomplished under lean conditions and the subsequent catalyst regeneration is carried out during a short period under rich conditions. For this reason they are also referred to as NOx Storage/Reduction (NSR) catalysts.

In spite of the fact that a number of papers have been published on the catalytic behavior of Pt-Ba/$Al_2O_3$ catalysts, still the mechanism of the NOx adsorption and of their subsequent reduction has not been completely clarified so far. In our Labs, an extensive investigation was started with the aim of elucidating the $NO_x$-storage capability of Pt/$Al_2O_3$, Ba/$Al_2O_3$ and Pt-Ba/$Al_2O_3$ catalyst samples, and the characteristics of the adsorbed $NO_x$ species. In particular, NO and $NO_2$ adsorption experiments have been carried out at different temperatures in the presence and in the absence of oxygen. FT-IR spectroscopy and the transient response method (TRM) have been used for this purpose as complementary techniques. The collected data are herein presented and addressed, and a novel pathway for $NO_x$ storage that implies the direct uptake of NO in the presence of oxygen in the form of nitrites [3] at Ba sites nearby Pt will be presented and discussed. This adsorption route implies a proximity between Pt and Ba sites: therefore, in order to better elucidate the role of the Pt-Ba interaction on NOx storage and reduction, the adsorption of NOx/$O_2$ and their subsequent reduction was then investigated over model Pt-Ba/$Al_2O_3$ samples with Ba loadings in the range 0-30% w/w. The results have also been compared with those obtained on a physical Pt/$Al_2O_3$-Ba/$Al_2O_3$ mixture, and a kinetic literature model for $NO_x$ storage over Pt-Ba/$Al_2O_3$ [4] has been adapted to our catalytic system in order to simulate the transient $NO_x$ adsorption over the different considered catalytic systems [5].

Finally, the results of studies aimed at a better understanding of the effect of the operating conditions (reaction temperature, presence of $CO_2$ and/or $H_2O$ in the feed, use of $H_2$ or $C_3H_6$ in the regeneration step, lengths of lean and rich steps) on the $NO_x$ adsorption/reduction is herein addressed and discussed.

## Experimental

**Catalyst preparation**. The γ-alumina support was obtained by calcination at 700°C of a commercial alumina material (Versal 250 from La Roche Chemicals). Pt/$Al_2O_3$ (1/100 w/w) and Ba/$Al_2O_3$ (20/100 w/w) catalysts were prepared by incipient wetness impregnation of the alumina support with aqueous solutions of dinitrodiammine platinum (Strem Chemicals, 5% Pt in ammonium hydroxide) or barium acetate (Strem Chemicals, 99%). The powders were then dried overnight in air at 80°C and finally calcined at 500°C for 5 h. The Pt-Ba/$Al_2O_3$ (1/x/100 w/w) samples at different barium loading (5-30%) were prepared by impregnation of calcined Pt/$Al_2O_3$ with different solutions of barium acetate.

**Characterization techniques.** Absorption/transmission IR spectra were performed on a Perkin-Elmer FT-IR 1760-X spectrophotometer equipped with a Hg-Cd-Te cryo-detector, working in the range of wavenumbers 7200-580 $cm^{-1}$ at a resolution of 2 $cm^{-1}$ (number of scans ~60). For IR analysis powder samples were pelletized in self-supporting discs (10-15 mg $cm^{-2}$) and placed in a quartz IR cell allowing thermal treatments in vacuo or in controlled atmosphere. Pellets were activated by heating in vacuo at 773 K (1023 K in some cases) subsequently in dry oxygen at the same temperature and cooled down in oxygen.

**Catalytic activity tests.** The $NO_x$ storage-reduction capability of the catalyst has been investigated by transient experiments performed in a flow micro-reactor system equipped with a mass spectrometer for product analysis [3,5,6]. The dynamics of the $NO_x$ adsorption-reduction has been investigated by alternating rectangular step feed of NO or $NO_2$ (1000 ppm) in He + 3% v/v $O_2$ and of propylene (1000 ppm) or hydrogen (2000 ppm) in He, separated by a He purge in between. Experiments have been performed at different temperatures in the range 250-400°C. In each run 120 mg of catalyst (75-100 μm) were used and a total flow rate of 200 $cm^3$/min STP was maintained in the different phases. The experiments have been performed in the absence and in the presence of carbon dioxide (2000 ppm) and/or water (1%).

## Results and discussion

**Nature of the barium species involved in the $NO_x$ storage process**. A conditioning procedure of the catalyst, i.e. some storage-reduction cycles, must be performed in order to obtain reproducible results [6]. **Figure 1** shows the results collected during the three initial $NO_x$ storage cycles performed at 350°C onto a calcined Pt-Ba(16)/$Al_2O_3$ catalyst sample after *in-situ* calcination in dry air at 500°C, in terms of $NO_x$, $H_2O$ and $CO_2$ outlet concentration as a function of time. In the first $NO_x$ storage cycle (section I of **Figure 1**) upon the NO step addition at t = 0 s the $NO_x$ outlet concentration presents a delay of about 50 s, and then slowly increases with time eventually reaching the inlet concentration value. A significant evolution of $CO_2$ is also monitored with a time delay about 50 s. The data prove that $NO_x$ is first adsorbed at BaO and then at $BaCO_3$ (with release of $CO_2$), in line with the greater basic character of the former site. Indeed IR analysis and XRD spectra indicate that in the fresh calcined catalyst sample Ba is present as Ba carbonate. The decomposition of part of $BaCO_3$ during the *in-situ* calcination in dry air leads to the formation of BaO. Accordingly $BaCO_3$ (that is predominant) and BaO, but not $Ba(OH)_2$, are present on the fresh catalyst sample before $NO_x$ adsorption, and this explain the sequence observed upon $NO_x$ adsorption. In the second $NO_x$ storage run (section II of **Figure 1**), performed after reduction with diluted $H_2$ at the same temperature, it appears that the time delay in the $NO_x$ outlet concentration is greater (250 s vs 50 s), water evolution becomes evident and occurs with a time delay of 150 s, $CO_2$ evolution is significantly reduced and is now observed after 250 s. The data prove that the storage of $NO_x$ occurs first at BaO, then at $Ba(OH)_2$ and finally at $BaCO_3$, in line with the basic character of the different Ba adsorption sites, and that the storage at $BaCO_3$ is of lower importance.

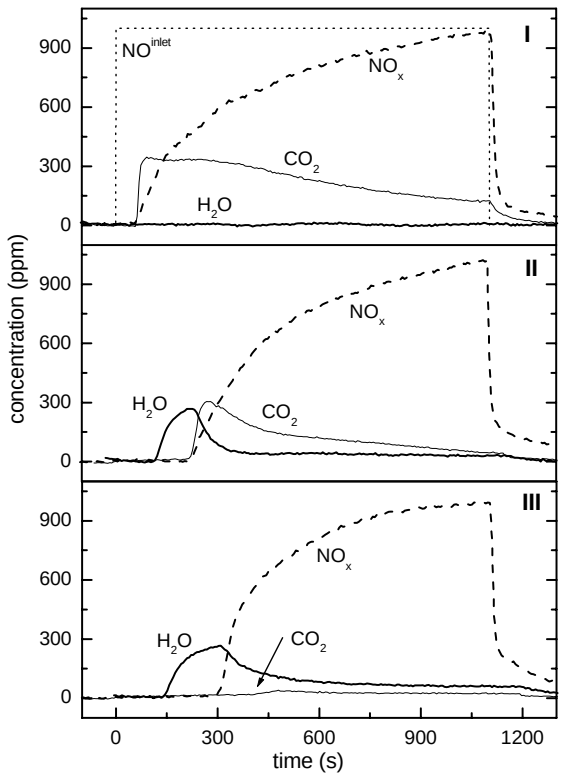


**Figure 1**. Subsequent $NO_x$ storage runs at 350°C on the fresh Pt-Ba(16)/γ-$Al_2O_3$ sample: $NO_x$, $H_2O$, $CO_2$ outlet concentration and NO inlet concentration.

In the third adsorption cycle (section III of **Figure 1**), again performed after reduction of the catalyst with $H_2$ at 350 °C, the $NO_x$ adsorption is further enhanced and the transformation of barium carbonate into barium oxide and barium hydroxide is almost complete, so that the catalyst appears to be fully conditioned after three cycles. Besides water evolution is increased whereas that of $CO_2$ is almost negligible because the transformation of $BaCO_3$ into BaO and $Ba(OH)_2$ has proceeded further.

The stability order of the different Ba species involved in the $NO_x$ storage process reflects their increasing acid character:

$$BaO < Ba(OH)_2 < BaCO_3$$

$NO_x$ are stored on barium carbonate, barium hydroxide and barium oxide depending on the characteristics of the regeneration step. The catalytic surface is mainly constituted by barium hydroxide and barium oxide when the reduction run is performed using hydrogen as reducing agent; and it is mainly constituted by barium carbonate and barium oxide when the reduction run is performed using propylene. Obviously, the presence of other species in the feed gases (e.g. water and $CO_2$) affects the features of the $NO_x$ adsorption by modifying the nature of the surface Ba species involved in the $NO_x$ storage.

**NOx adsorption mechanism.** In order to achieve a complete qualitative and quantitative comprehension of the mechanism that govern the NOx adsorption phase, NO and $NO_2$ adsorption experiments were carried out over model $Al_2O_3$-supported Pt-Ba, Ba and Pt samples. Both the FT-IR spectroscopy and the transient response method (TRM) were used as complementary techniques.

Upon NO admission, small amount of $NO_x$ species are adsorbed on Ba/γ-$Al_2O_3$ sample, identified by IR as bidentate nitrites. On the other hand, on Pt-Ba/γ-$Al_2O_3$ catalyst, a higher $NO_x$ adsorption is observed, with formation of nitrite and in minor amounts of nitrate ads-species.

Upon $NO_2$ admission, the $NO_x$ adsorption process on the Ba/ and Pt-Ba/γ-$Al_2O_3$ samples is important and a simultaneous release of NO is evident, following a disproportionation stoichiometry: $O^{2-} + 3\ NO_2 \rightarrow 2\ NO_3^- + NO\uparrow$. On Pt-Ba/γ-$Al_2O_3$ $NO_2$ decomposition to NO and $O_2$ is also evident, catalyzed by the Pt presence. IR spectra showed that on both samples $NO_2$ is stored with formation of only nitrate species, mainly of ionic type.

At variance, NO + $O_2$ adsorption over both Ba/γ-$Al_2O_3$ and Pt-Ba/γ-$Al_2O_3$ showed important $NO_x$ adsorption with formation of nitrite species at first, which then evolve to ionic and in minor extent bidentate nitrates. This evolution is slow and only partial on Ba/γ-$Al_2O_3$, while nitrites are very rapidly and completely oxidized to nitrates in the presence of Pt.

On this basis, the reaction pathway depicted in **Scheme 1** is suggested for $NO_x$ adsorption over supported Pt-Ba catalysts. According to the proposed scheme, in the presence of NO/$O_2$ mixtures (the actual gases in the exhausts), $NO_x$ are stored on Ba neighbouring to Pt sites in the form of nitrite ad-species (step a). Nitrite ad-species are then progressively oxidized to nitrates, which are prevailing at saturation (step b). Our data point out that routes (a) + (b) ("nitrite route") occur on the binary Ba/γ-$Al_2O_3$ catalyst as well, although in to a negligible extent if compared to Pt-Ba/γ-$Al_2O_3$. Hence the presence of neighbouring Pt and Ba sites is important for this route.

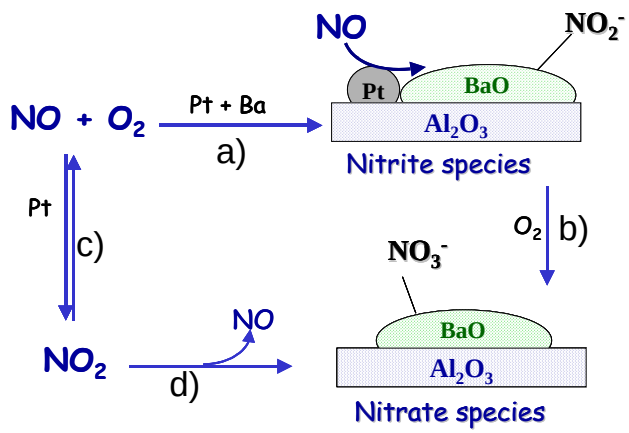


**Scheme 1** - $NO_x$ storage pathway

In parallel with the "nitrite route", the oxidation of NO to $NO_2$ on Pt sites by gaseous oxygen can also occur (step c); the $NO_2$ thus formed is stored on BaO directly in the form of nitrates ("nitrate route" = steps (c) + (d)), i.e. without the intermediacy of nitrites, according to a disproportionation reaction (step (d)).

The "nitrite" and "nitrate" pathways operate simultaneously during the NO/$O_2$ storage but the first one, which is responsible for the formation of nitrites, dominates over the disproportionation route since nitrites are the most abundant species before $NO_x$ breakthrough.

**Effect of Ba loading on $NO_x$ storage.** Characterization measurements (XRD, BET surface area, $H_2$ chemisorption) performed over Pt-Ba(x)/$Al_2O_3$ catalysts indicated that the addition of Ba affected negatively both the morphological properties and the noble metal dispersion for the systems with Ba loading higher than 10%. Nevertheless, the increase in the Ba loading resulted in a strong increase of the NOx adsorption at breakthrough and in the percentages of Ba involved in the storage: a maximum value of 25%

ca. was evaluated for the system with 23 % w/w of Ba content. As a matter of facts, this clearly appears in **Figure 2**, where the outlet NO, $NO_2$ and $NO_x$ ($NO+NO_2$) concentration curves recorded upon NO step addition are displayed as a function of time for the Pt-Ba(x)/γ-$Al_2O_3$ catalysts, along with that of the NO inlet concentration. In all cases NO and $NO_2$ are detected at the reactor outlet, $NO_2$ formation being ascribed to the occurrence of the oxidation of NO by $O_2$ on Pt sites. The dead time observed in the $NO_x$ concentration profile indicates that during the initial part of the pulse the NO fed to the reactor is completely stored on the catalyst surface.

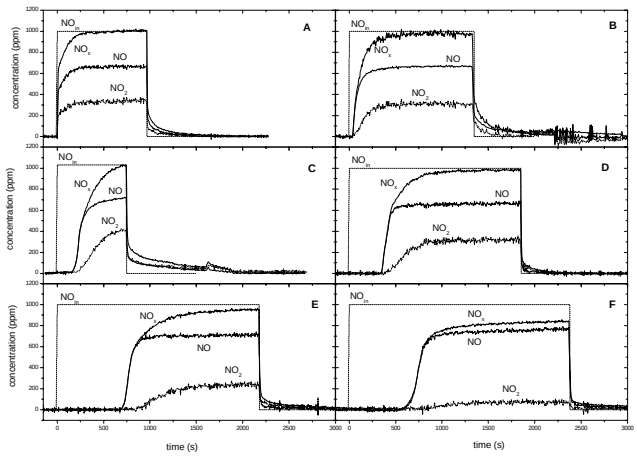


**Figure 2**. NO, $NO_2$ outlet concentration and NO inlet concentration vs time upon NO addition on the Pt-Ba(x)/γ-$Al_2O_3$ catalysts at 350°C: A) Ba(0); B) Ba(5); C) Ba(10); D) Ba(16); E) Ba(23) and F) Ba(30) catalysts.

According to the "nitrite" route invoked in Scheme 1, a cooperative effect between Pt-Ba neighboring couples appears to be relevant in favoring the step-wise oxidative adsorption of NO in the form of nitrite-like ad-species on the Ba sites. Hence, it can be speculated that upon increasing the Ba loading (up to a maximum value) the number of Pt-Ba neighboring couples increases, along with the $NO_x$ stored via the "nitrite" route. Accordingly neighbors Pt-Ba species would favor the $NO_x$ storage process according to the "nitrite" pathway, thus resulting in a better utilization of the Ba component.

Data also indicated that the higher the Ba content the lower was the $NO_2$ concentration value at catalyst saturation, this effect being marked for the highest Ba loadings. This behavior can be explained considering that a decrease in the Pt content of the catalysts was associated with the Ba addition to the Pt/$Al_2O_3$ binary sample, but also that a masking of Pt sites is possibly occurring when the Ba coverage approaches and exceeds the monolayer coverage. The fact that the $NO_x$ storage capacity seems to be independent from the oxidative capability of the catalysts apparently contrasts with the $NO_x$ adsorption mechanism reported in the literature [4], which considers the oxidation of NO to $NO_2$ as the first necessary step for the storage of $NO_x$ species.

Our data were quantitatively analyzed by using a detailed literature kinetic model [4]. The results, discussed in [5], have shown that the model satisfactorily accounts for the dynamics of both NO/$O_2$ and $NO_2$ adsorption over Pt-Ba/$Al_2O_3$ and on the mechanical mixture Pt/$Al_2O_3$ - Ba/$Al_2O_3$. However, it was also pointed out that in order to account for the $NO_x$ breakthrough, the model overestimates the oxidation of NO to $NO_2$, i.e. is not able to account independently for the $NO_x$ adsorption and NO oxidation. Besides, upon adsorption of NO/$O_2$ or $NO_2$, the model foresees the formation of an unique intermediate species whose nature does not depend on the inlet gas composition. This intermediate species is then slowly transformed into nitrates. This result contrasts with FTIR data which showed the intermediacy of nitrites species in the case of NO/$O_2$ adsorption, and the formation of nitrates only when starting from $NO_2$. Work is currently in progress in order to gain a better adequacy of the model to our data, e.g. by including an additional NO adsorption pathway according to the above proposed nitrite route; preliminary results obtained in this direction seem very promising.

**Reduction of the stored $NO_x$ species.** The reduction of the stored $NO_x$ species has been carried out over all the investigated systems (including the physical mixture) by step-wise addition of $H_2$ in He at 350°C. If one exclude the physical mixture, for all the investigated catalysts the stored $NO_x$ species are readily reduced to $N_2$ and $H_2O$. When the Ba content of the samples was higher than 16%, at the end of the $N_2$ production ammonia appears at the reactor outlet: accordingly these catalysts were characterized by a lower selectivity, which was close to 30% for the Pt-Ba(30) sample. Hence, the bulk of data collected evidenced that the reduction process is very complex and that it can lead to nitrogen and/or ammonia depending on the formulation and properties of the catalysts. Notably, in the case of the physical mixture, no reduction of the stored $NO_x$ was achieved: this clearly indicates that the simultaneous presence of Pt and Ba on the same support is required for catalyst regeneration.

A comprehensive and detailed picture explaining the mechanism of the reduction process and in particular of its selectivity is currently under investigation in our laboratories

**Effect of the operating conditions on the storage of $NO_x$.** *Reaction temperature* - The storage of $NO_x$ in the presence of 3% oxygen over the fully conditioned Pt-Ba(16)/γ-$Al_2O_3$ sample has been investigated in a wide temperature range, extending from 200°C to 400°C. In all cases $H_2$ was used in the regeneration step, hence BaO and $Ba(OH)_2$ are the Ba sites involved in the $NO_x$ storage, as discussed above.

On increasing the temperature up to 400°C a maximum in the $NO_x$ breakthrough was observed at 350 °C. In all cases, after breakthrough the $NO_x$ outlet concentration increased and approached asymptotically the NO inlet concentration value. During $NO_x$ storage a small amount of water was released indicating that the adsorption of $NO_x$ species occurs on BaO and on $Ba(OH)_2$ sites, leading to formation of nitrites and nitrates species according to reaction pathway in **Scheme 1**.

Calculations showed that considerable amounts of $NO_x$ are stored onto the Pt-Ba/γ-$Al_2O_3$ catalyst during the storage, up to 0.58 mmoles/g catalyst at 300°C. The corresponding % Ba involved up to catalyst saturation was roughly 24%; the % Ba that was involved up to the $NO_x$ breakthrough was significantly lower at any temperature, and increased with temperature up to about 14% at 300°C, at which temperature it levels off. Based on the amounts of water which was released, it can be estimated that the relative amounts of $Ba(OH)_2$ involved in the $NO_x$ storage process was large (≅ 50-60%) at low temperature but diminished significantly with temperature (down to 10-15%), as expected.

*$CO_2$ presence* - The influence of 0.3% $CO_2$ on the $NO_x$ storage was investigated in the range 150-400°C. Due to the presence of $CO_2$, $BaCO_3$ was the most abundant barium-species present at the catalyst surface. At any temperature the $NO_x$ breakthrough was remarkably reduced in the presence of 0.3% $CO_2$, as observed in **Figure 3** where the comparison was made for a temperature of 300 °C. Notably, i) no water was released upon $NO_x$ storage but only $CO_2$; ii) no delay was observed in the evolution of $CO_2$, suggesting that the catalyst surface was fully carbonated. The shorter time delay in the $NO_x$ breakthrough

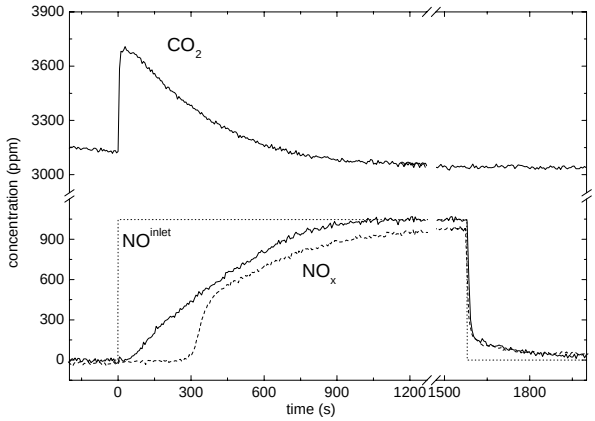


**Figure 3.** Storage of $NO_x$ at 300°C over Pt-Ba(16)/γ-$Al_2O_3$ in the absence (dashed line) and in the presence (solid line) of $CO_2$: $NO_x$ and $CO_2$ reactor outlet concentration

and the slower rise of the $NO_x$ concentration can be ascribed to lower reactivity of $BaCO_3$ towards NO with respect to BaO and $Ba(OH)_2$.

Accordingly, the net amount of $NO_x$ that was stored was significantly lower than in the absence of $CO_2$ and was twice the net amount of $CO_2$ that was released from the catalyst. Notably, the effect of $CO_2$ was much more relevant on the amounts of $NO_x$ which are stored up to $NO_x$ breakthrough rather than up to saturation.

*$H_2O$ presence* - The presence of water in the feed gas during the $NO_x$ storage was studied in the range 150-400°C over the Pt-Ba(16)/γ-$Al_2O_3$ catalyst. Data indicated that the storage of $NO_x$ was always accompanied by a simultaneous release of water (without dead time), suggesting that the adsorption of $NO_x$ occurs primarily on $Ba(OH)_2$ sites. Besides a striking effect of water was the increase at low temperature and a decrease at high temperature of the time delay of $NO_x$ outlet concentration. It seems that water has a promoting action at low temperature and a negative effect at high temperature on the reactions involved in the $NO_x$ storage process.

*Nature of the reducing agent* – As previously shown, the $NO_x$ storage was affected by the nature of the Ba sites (BaO, $Ba(OH)_2$ or $BaCO_3$) involved in the process. $N_2$ and $H_2O$ are formed upon regeneration of the adsorbed $NO_x$ species with hydrogen whereas $N_2$, $CO_2$ and $H_2O$ are released when propylene is used as reducing agent: accordingly it was expected that different Ba species are formed on the catalyst surface during regeneration (i.e. BaO / $Ba(OH)_2$ in the case of $H_2$, BaO / $Ba(OH)_2$ / $BaCO_3$in the case of propylene) thus affecting the subsequent $NO_x$ storage process.

The results obtained at 300 and 350 °C over the Pt-Ba(16)/γ-$Al_2O_3$ sample when propylene or hydrogen are used as reducing agents show that at both temperatures the $NO_x$ breakthrough was lowered when the regeneration was carried out with propylene. This is likely related to the fact that less active $BaCO_3$ species are left on the catalyst after regeneration with propylene. On the other hand, if $NO_x$ adsorption is carried out in the presence of $CO_2$, similar results are obtained after propylene and hydrogen regeneration, because in both cases the $NO_x$ storage occurs on $BaCO_3$ sites.

**Lean-rich cycles.** In order to further investigate the catalytic performances of Pt-Ba/$Al_2O_3$ catalyst in more representative conditions, lean-rich experiments have been performed in which the lengths of both the lean and the rich phases have been changed, and the effects of these variations on the efficiency and selectivity in the removal of $NO_x$ have been analyzed. Lean-rich cycles have been carried out using stoichiometric and over-stoichiometric conditions: stoichiometric conditions are those in which the theoretical amount of reducing agent is used to remove adsorbed $NO_x$ according to the stoichiometry: $Ba(NO_3)_2 + 5H_2 \rightarrow BaO + N_2 + 5H_2O$.

In the case of stoichiometric conditions, $NO_x$ adsorption was carried out up to breakthrough (200 sec), estimated from a fully regenerated catalyst. Upon cycling the catalyst, the NO breakthrough progressively decreases from 200 s to 185 s. At this point the $NO_x$ breakthrough was always observed at 185 s. Since the adsorption phase has been maintained for 200 s, $NO_x$ are observed at the reactor outlet during the lean phase; in addition, NO was detected during the reduction phase. No $H_2$ slip was observed during the rich phase.

When the lean-rich $NO_x$ cycles were performed with an over-stoichiometric rich phase (i.e. when the reduction time is increased by 10% with respect to the stoichiometric one) the NO breakthrough time was found to be always constant (ca.200 sec). In this case, NO production (300ppm) was observed only during the reduction phase, pointing out that or the reduction of adsorbed species is not totally selective to $N_2$ and/or that a thermal decomposition of surface nitrates takes place, due the to exothermic reduction reactions. Furthermore, in these conditions $H_2$ slip is observed.

Lean-rich $NO_x$ cycles have also been performed progressively reducing the adsorption time ($NO_x$ breakthrough, ¾ of $NO_x$ breakthrough, ½ of $NO_x$ breakthrough) and keeping an over-stoichiometric rich phase. In all cases, NO is never observed during the storage phase, being performed before breakthrough; furthermore, on decreasing the storage time, the amount of NO produced during the reduction phase decreases as well. In particular, when the storage phase length corresponds to half of the $NO_x$ breakthrough, no $NO_x$ are evolved during both the lean and the rich phase. Accordingly, the $NO_x$ abatement efficiency (i.e. $NO_x$ reduced / $NO_x$ fed to the reactor) increases by decreasing the storage period, approaching the 100% when the storage phase is ½ of $NO_x$ breakthrough.

The bulk of the collected data indicated that the catalytic performances of the catalysts strongly depends on the length of both lean and rich periods. In particular, by maintaining the $NO_x$ adsorption phase at or slightly below breakthrough, NO production is observed only during the regeneration period. This can be ascribed to a thermal desorption of the adsorbed species and/or to a not selective reduction process. On the other hand, when the storage is limited, complete $NO_x$ abatement efficiency is achieved. It can be speculated that when the lean phase is short, below $NO_x$ breakthrough, $NO_x$ are adsorbed at Ba sites neighbor to Pt and are more selectively reduced. Work is presently ongoing to check the mechanism of the reduction process, particularly addressing selectivity.

**Acknowledgment**

The authors gratefully thank Prof. G. Ghiotti and Dr. F. Prinetto (University of Turin), Dr. V. Dal Santo and Prof. R. Psaro (ISTM-CNR of Milan) and Prof. S. Recchia (University of Insubria) for the valuable contribution to the FT-IR and DRIFT studies.

**References**

1. Shinjoh, H., Takahashi, N., Yokota, K., Sugiura, M., *Appl.Catal. B:Environmental*, **1998**, *15*, 189.
2. Epling, W.S., Campbell, L.E., Yezerets, A., Currier, N.W., Park II, J.E., *Catal.Reviews*, **2004** ,*46*(2), 163.
3. Nova, I., Castoldi, L., Prinetto, F., Ghiotti, G., Lietti, L., Tronconi, E., Forzatti, P., *J.Catal*, **2004,** *222*(2), 377.
4. Olsson, L., Persson, H., Friedell, E., Skoglundh, M., Andersson, B., *J. Phys.Chem. B*, **2001,** *105*, 68.
5. Scotti, A., Nova, I., Tronconi, E., Castoldi, L., Lietti, L., Forzatti, P., *Ind.Eng.Chem.Res.*, **2004**, *43*, 4522.
6. Lietti, L. Forzatti, P., Nova, I: Tronconi, E., *J.Catal*, **2001,** *204* (1), 175.

# NMR STUDIES OF SCR OF $NO_x$ WITH $NH_3$ ON Ga-EXCHANGED FERRIERITES

*M. Mecarova and T. Pietraß*

Department of Chemistry
New Mexico Tech
Socorro, NM 87801

## Introduction

Emissions abatement strategies for lean burn engines are challenging, because of the need to reduce $NO_x$ in the excess of oxygen that exists in lean burn exhaust[1]. Various types of de$NO_x$ catalysts are under consideration[2-6]. Critically important is the acidity of the support. Acidity favors the formation of $N_2$ over $N_2O$, another green house gas, yet carbon deposition deactivates the catalyst if there are too many acid sites[7].

Gallium-exchanged zeolites have been reported to be very active in the selective catalytic reduction (SCR) with high selectivity for the formation of $N_2$[8]. They are diamagnetic which makes these systems suitable for study by NMR techniques. We attempt to understand the role of the gallium (III) ions in Ga-exchanged ferrierites in the SCR reduction of $NO_x$ with ammonia under flow conditions using $^{15}N$ NMR spectroscopy. In addition, we exploit the sensitivity of the $^{15}N$ NMR chemical shift of ammonia to probe the acidity of the ferrierites.

## Experimental

Zeolite ferrierite was obtained from Tosoh (TOS) and Zeolyst (ZEO). The gallium-exchanged samples were prepared by ion-exchange from the ammonium form of the parent zeolites. An aqueous solution of gallium (III) nitrate was mixed with ammonium-ferrierite. The solution was stirred at room temperature for two days. After 24 hours, the solids were isolated from the solution by centrifugation, and fresh gallium solution was added for an additional period of 24 hours. The solids were again isolated and washed repeatedly by centrifugation, dried and calcined at 400-500ºC. Elemental analysis and sample identifications for the ferrierite catalysts are summarized in **Table 1**.

**Table 1. Elemental Analysis of Ferrierite Sample**.

| Sample ID | ZEO | ZEO-Ga | TOS | TOS-Ga |
|---|---|---|---|---|
| Sample Description | Zeolyst | Zeolyst/Ga | Tosoh | Tosoh/Ga |
| Ga (wt%) | | 0.47 | | 0.76 |
| K (wt%) | 0.0141 | <0.09 | 4.165 | 4.81 |
| Na (wt%) | 0.0282 | 0.027 | 0.6012 | 0.21 |
| Si/Al ratio | 10 | | 7.3 | |
| Al/Fe ratio | 231 | | 112 | |

The NMR data were acquired on an Apollo (Tecmag)/MSL-400 (Bruker) NMR spectrometer operating at a Larmor frequency of 40.545 MHz for $^{15}N$. The samples in NMR tubes were heated for 12 hours at 400ºC under vacuum and then exposed to 0.1 MPa $^{15}N$ labeled $NH_3$. NMR data were acquired directly after the gas was loaded. Then, the samples were heated to 300ºC over a period of 30 min, kept at this temperature for 30 min, quenched, and analyzed by NMR at ambient temperature. Consecutive heating cycles were repeated up to a total heating time of 2 hours.

For the *in situ* experiments, the catalyst was loaded into a U-shaped NMR tube and heated under a flow of helium for 12 hours at 300ºC. The reaction mixture consisted of 20% $NH_3$ and 20% NO, each in a balance of He. The two gas mixtures were stored separately in stainless steel bottles so that the flow rate of each component could be controlled individually. After passing through the calibrated flow meters, the two components were mixed and then admitted to the sample. The reaction was monitored using $^{15}N$ NMR spectroscopy.

It should be noted that NO is NMR inactive due to its paramagnetism.

## Results and Discussion

**$NH_3$ Adsorption Experiments.** We used $^{15}N$ NMR spectroscopy to monitor ammonia adsorption on the ferrierites. The chemical shift is indicative of the zeolite acidity. With increasing acidity (both Lewis and Brønsted), the ammonia is more strongly bound, which leads to an increase in the $^{15}N$ NMR chemical shift.

When compared to the free gas, we observed an increase in line width and a loss in resolution of the $^{15}N$-$^{1}H$ J couplings due to a decrease in mobility brought about by adsorption. At ambient temperature, the chemical shifts may be affected by water which is formed in the reaction (**Figure 1**). After heating, the $^{15}N$ NMR chemical shifts for ammonia adsorbed on ZEO and ZEO-Ga, are the same within experimental error, while there is a significant difference in shifts between TOS and TOS-Ga.

The $^{15}N$ NMR chemical shifts can be discussed in light of Brønsted and Lewis acidity. The Tosoh ferrierite has fewer Brønsted acid sites in agreement with the presence of more $K^+$ and $Na^+$ having exchanged for $H^+$. The elemental analysis suggests that some of $Na^+$ was exchanged with $NH_4^+$ and subsequently $Ga^{3+}$. It is anticipated and has been shown that Ga exchange in the zeolite decreases the Brønsted and increases the Lewis acidity[9]. Extra-framework hydrated gallium, however, increases the Brønsted acidity due to formation of Ga-OH groups[10].

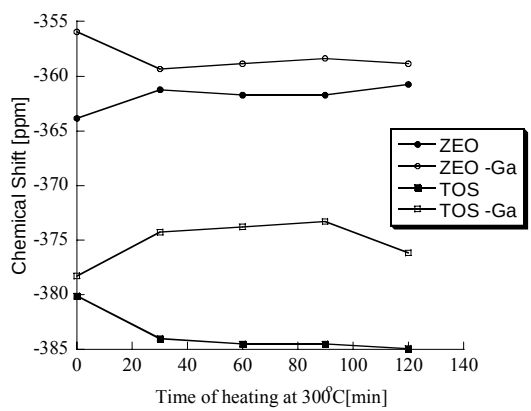


**Figure 1.** The dependence of the $^{15}N$ NMR chemical shift of ammonia with respect to heating time at 300ºC for ZEO (●), ZEO-Ga (○), TOS (■), TOS-Ga (□). The pressure of ammonia is 0.1 MPa. The number of scans is 8000 and the recycle delay is 250 ms using a 90º pulse duration of 28.5 µs. The error bars are smaller than the size of the symbols used.

The ammonia resonances of the ZEO samples are shifted downfield with respect to the TOS samples, indicating a higher number of acid sites of the ZEO ferrierites. The presence of gallium does not affect the chemical shifts in ZEO as, on average, ammonia preferentially samples the stronger Brønsted binding sites. In TOS, gallium increases the number of Lewis sites.

Therefore, the chemical shifts of $^{15}N$ NMR ammonia resonances are shifted farther downfield, indicative of more strongly bound ammonia.

***In Situ* Flow Experiments.** In light of the catalytic experiments under flow conditions, we investigated the interplay between spin-lattice relaxation time $T_1$ and flow rate. Briefly, if the dwell time of the gas in the NMR pick-up coil region is longer than $T_1$, the time constant measured in an inversion recovery experiment should be close to the $T_1$ measured under static conditions. If the flow rate is sufficiently high to reduce the dwell time below the static $T_1$, the time constant will be smaller than the true $T_1$. Thus, a measure of the relaxation time under flow conditions is an indirect measure of the contact time of the gas with the catalyst. In order to optimize our experimental conditions for maximum signal intensity, we measured the apparent $T_1$ at different flow rates. These data are summarized in **Table 2**.

**Table 2. Time Constants of Ammonia at Different Flow Rates**.

| Flow rate [ml/min] | | Time constant $T_1$ [ms] |
|---|---|---|
| 10 | ($NH_3$ mixture alone) | 29.4±3.1 |
| 10 | ($NH_3$ mixture on ZEO) | 29.8±1.3 |
| 50 | ($NH_3$ mixture on ZEO) | 24.6±0.4 |
| Static | ($NH_3$ mixture on ZEO) | 53.3±0.5 |

As a baseline, we also measured the apparent $T_1$ for 20% $NH_3$ in He balance in the absence of a catalyst (**Figure 2**). At a flow rate of 10 ml/min, this time constant is significantly shorter (by two orders of magnitude) then the static $T_1$ for pure ammonia gas at 1 atm (1.4 s). At a cell volume of 0.5 $cm^3$, we can estimate from the flow rate a dwell time of 50 ms. This result is in acceptable agreement with the time constant measured of 30 ms.

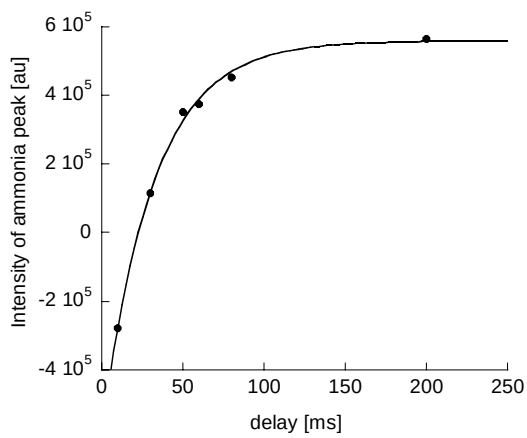


**Figure 2.** Inversion recovery of $NH_3$ alone in the U-shaped sample tube at 10 ml/min. The gas mixture contains 20% of $NH_3$ in He balance.

For the $NH_3$/He mixture in the presence of the catalyst, we measured a static $T_1$ of 50 ms. At a flow rate of 10 ml/min, this time constant is reduced to 30 ms, the same value that was observed without a catalyst (**Figure 3**). This strongly indicates that the ammonia is rapidly exchanging with the gas phase and easily swept out of the coil region. At an increased flow rate of 50 ml/min, the time constant is further reduced. For an empty sample tube, the dwell time should be reduced to 10 ms. The observed change is much less dramatic, indicating binding to the surface sites.

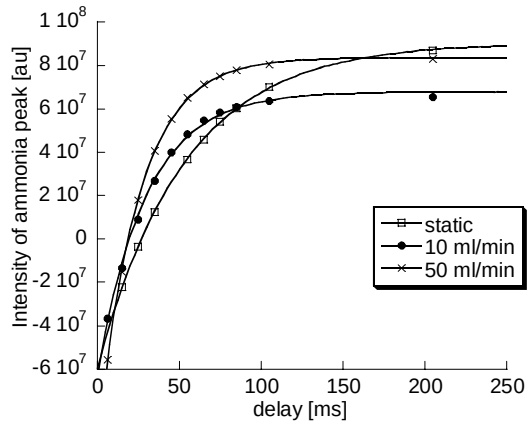


**Figure 3.** Inversion recovery of $NH_3$ on ZEO in U-shaped sample tube under static conditions (□), with flow of 10 ml/min (●), and with flow of 50 ml/min (x). The gas mixture contains 20% of $NH_3$ in He balance.

Previous data[11] showed that under batch-mode conditions, ZEO had the greatest catalytic activity due to its high acidity. We studied the reaction of ammonia with nitric oxide on ZEO under flow conditions at room temperature. First, we purged the catalyst with the $NH_3$/He mixture in the U-shaped sample tube located inside the NMR instrument for 1 hour. Then, the flow of $NH_3$ was stopped and the NO/He mixture was allowed to flow at a rate of 10 ml/min. The $^{15}N$ NMR signal intensity of ammonia was monitored every 5 minutes. The results are summarized in **Figure 4**.

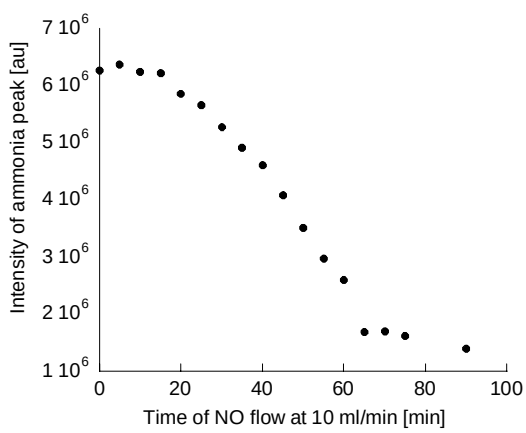


**Figure 4.** Intensity of $^{15}N$ $NH_3$ peak with respect to time of flow of NO. The gas mixture contains 20% of NO in He balance. The space velocity is 10 ml/min.

During the first 15 min, the signal intensity was, within experimental error, constant, indicative of an induction period to allow for NO adsorption on the sample. After 15 min, the signal intensity decreased as the reaction proceeded. The reaction product, nitrogen gas, however, was not detected. This is most likely due to the fact that the small and weakly interacting $N_2$ molecule (diameter of 3 Å) is swept out of the region of the NMR

pick-up coil by the gas flow. A continuous decrease in ammonia signal intensity was observed for 60 min. At this point, the flow of NO was stopped, and the gas mixture left in the now closed system. A spectrum acquired after 4 h showed two resonances, one for ammonia and one for nitrogen. This observation confirms the hypothesis that the $N_2$ is swiftly transported out of the coil region. When re-starting the flow of NO/He, the nitrogen signal disappeared once again and the ammonia signal intensity further decreased after an induction period of about 15 min.

**Conclusions**

$^{15}N$ NMR of ammonia adsorbed on the zeolites provides a measure for the Brønsted acid strength and reveals that the ZEO samples have stronger binding sites than TOS. The increase in the number of Lewis sites in the gallium-exchanged TOS sample is reflected in the downfield shift of the $^{15}N$ resonance. For ZEO, where a large number of Brønsted sites is available, this effect is not measurable.

It is concluded, that the ferrierite itself is sufficient for catalytic reduction of $NO_x$ with ammonia at room temperature. No metal exchange nor increased temperature are needed. This is in agreement with our previous results. Experiments with higher temperatures (up to 300ºC) are currently in progress.

Preliminary flow studies show that nitrogen binds only weakly to the surface of the zeolite and is rapidly swept out of the catalyst region by the flowing gas. Ammonia is more strongly bound to the surface than NO. Nevertheless, exchange of adsorbed phase ammonia with the gas phase is occurring.

**Acknowledgement.** Financial support by the Research Corporation under Contract No. RA0302 and ACS PRF #39255-AC5S are gratefully acknowledged. We thank Dr. Kevin C. Ott from Los Alamos National Laboratories for providing the samples and helpful discussions.

**References**

(1) König, A.; Herding, G.; Hupfeld, B.; Richter, T.; Weidmann, K. *Top. Catal.* **2001**, *16/17*, 23
(2) Han, P. H.; Lee, Y. K.; Han, S. M.; Rhee, H. K. *Top. Catal.* **2001**, *16/17*, 165.
(3) Liotta, L. F.; Macaluso, A.; Arena, G. E.; Livi, M.; Centi, G.; Deganello, G. *Catal. Today* **2002**, *75*, 439.
(4) Macleod, N.; Lambert, R. M. *Appl. Catal. B* **2002**, 35, 269.
(5) Burch, R.; Breen, J. P.; Meunier, F. C. *Appl. Catal. B* **2002**, *39,* 283.
(6) Seijger, G. B.F.; van Kooten Niekerk, P.; Krishna, K.; Calis, H. P. A.; van Bekkum, H.; van den Bleek, C. M. *Appl. Catal. B* **2003**, *40,* 31.
(7) Fendler, A. G.; Denton, P.; Boreave, A.; Praliaud, H.; Primet, M. *Top. Catal.* **2001**, 16/17, 237.
(8) Ott, K. C.; Clark, N. C.; Rau, J. A. *Catal. Today* **2002**, *73*, 223.
(9) Occelli, M. L.; Eckert, H.; Hudalla, C.; Auroux, A.; Ritz, P.; Iyer, P. S. *Prog. Zeolite Microporous Mater*. **1997**, *105*, 1981.
(10) Challoner, R.; Harris, R. K.; Barri, S. I. E.; Taylor, M. J. *Zeolites* **1991**, *11*, 827.
(11) Mecarova, M.; Miller, N. A.; Clark, N. C.; Ott, K. C.; Pietrass, T. *Appl. Catal. A* **2004**, submitted

# REACTIVITY OF Pt/BaO/$Al_2O_3$ FOR $NO_x$ STORAGE/REDUCTION: EFFECTS OF Pt AND Ba LOADING

*Ja Hun Kwak, Do Heui Kim, Janos Szanyi, Tamas Szailer, and Charles H.F. Peden*

Chemical Sciences Division
Pacific Northwest National Laboratory
P.O. Box 999, MS K8-93
Richland, WA 99352

## Introduction

The control of $NO_x$ (NO and $NO_2$) emissions from combustion processes, including vehicle engines, remains a challenge particularly for systems operating at high air-to-fuel ratios (so-called ' lean' combustion). The current "3-way", precious metal-based catalytic converters are unable to selectively reduce $NO_x$ with reductants (e.g., CO and residual unburned hydrocarbon) in the presence of excess $O_2$. In the last few years, worldwide environmental regulations regarding $NO_x$ emissions from diesel engines (inherently operated ' lean') have become significantly more stringent resulting in considerable research efforts to reduce $NO_x$ under the highly oxidizing engine operation conditions. Urea selective catalytic reduction (SCR) and non-thermal plasma assisted $NO_x$ reduction have been explored as possible technologies. In recent years, alkaline and alkaline earth oxide-based $NO_x$ storage/reduction catalysts (especially BaO/$Al_2O_3$) have been developed, and have shown promising activities for lean-$NO_x$ reduction [1,2].

The $NO_x$ storage/reduction catalysts have dual catalytic functions. One is the oxidation of NO to $NO_2$ and its subsequent uptake as nitrate under lean condition, and the other is reduction of the released $NO_x$ under rich condition. Both of these processes are facilitated by a noble metal, in particular Pt. The actual NOx storage material is BaO in most practical applications. Although it is understood that $NO_2$, formed on Pt, is stored on the BaO phase as $Ba(NO_3)_2$ and the interaction between Pt and BaO is important, the effect of this interaction on the reactivity is not clear [2]. In this presentation, we will elucidate the role of Pt and BaO components, and the interaction between these two constituents during the NOx storage/reduction process by studying Pt-BaO/$Al_2O_3$ catalysts with varying BaO loadings, and different Pt particle sizes.

## Experimental

**Materials**. A series of catalysts with different barium oxide loadings were prepared by conventional impregnation methods. First, $Ba(NO_3)_2$ was loaded by repeated incipient wetness and drying on a high surface area gamma-alumina (Condea, 200$m^2$/g), followed by the impregnation of $Pt(NH_3)_4(NO_3)_2$ with the same incipient method and drying. The dried samples were calcined at 500$^o$C for 2 hrs in flowing air, which resulted in 2wt% Pt with 2, 8, and 20wt% BaO supported on $Al_2O_3$.

**Reactivity Studies**. The reaction studies were carried out in a plug-flow quartz reactor with simulated diesel exhaust. The $NO_x$ levels in the inlet (~200ppm) and outlet gases were measured with a chemiluminescence $NO_x$ analyzer. The $NO_x$ conversion was defined as the ratio of the amount of $NO_x$ stored to the amount of inlet $NO_x$ during lean cycle over different time intervals (typically 4 min and 30 min), prior to the rich cycle for 1 min.

**Characterization Methods.** The samples were characterized by XRD and BET. Catalyst samples were also pressed onto a fine tungsten mesh, and placed into the in-situ cell used for FTIR and temperature-programmed desorption (TPD) studies. The cell was connected to a gas handling/pumping station, and through both a leak and a gate valve to a mass spectrometer. This set up allowed us to conduct TPD experiments (open gate valve), and to analyze the gas composition in the IR cell (through the leak valve).

## Results and Discussion

**Figure 1** shows the TEM image for different BaO samples with variable loading. In spite of the significant difference in BaO loading, all of the samples show highly dispersed Pt clusters of less than 2 nm.

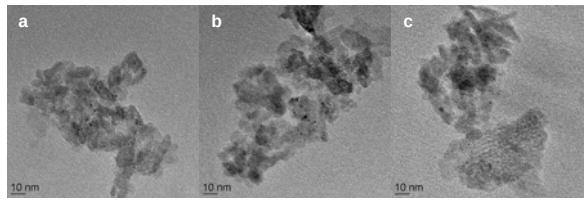


**Figure 1**. TEM image of 2%Pt/2%BaO/$Al_2O_3$ (a), 2%Pt/8%BaO/$Al_2O_3$ (b), and 2%Pt/20%BaO/$Al_2O_3$ (c).

**Figure 2** shows $NO_x$ conversion at various temperatures, and $NO_x$ uptake profiles at 250$^o$C for these three samples. $NO_x$ conversion increased with BaO loading over the whole temperature range, as did the time for $NO_x$ breakthrough. However, $NO_x$ conversion for 30 min was not linearly proportional to the amount of barium oxide; in other words, the BaO portion participating in $NO_x$ storage decreased with barium loading. For the case of 2%Pt/20%BaO/$Al_2O_3$ catalyst, only 12% of the BaO was converted to barium nitrate. This percentage of the participating BaO, for Pt-BaO/$Al_2O_3$ catalysts with 2 wt% and 8wt% BaO loading, was calculated to be 68% and 40%, respectively.

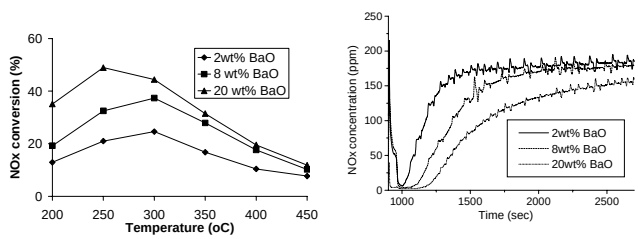


**Figure 2**. $NO_x$ conversion for 30 min and $NO_x$ uptake profiles (at 250 $^o$C) over Pt-BaO/$Al_2O_3$.

Low BaO efficiency cannot be explained by the insufficient production of $NO_2$ arising from the deactivation of Pt because all three samples contain nearly the same size and loading of Pt. However, the fact that $NO_x$ breakthrough increases with BaO loading may imply that the step of transferring $NO_2$ to the neighboring barium sites determines the $NO_x$ uptake. For example, it has been proposed that an intimate interaction between Pt and BaO is required for facile transfer of $NO_2$ to BaO, this step perhaps being a key one for obtaining higher $NO_x$ storage.

The availability of Pt sites was checked with CO adsorption at 300K. On 2%Pt-8wt%BaO/$Al_2O_3$, three intense bands were observed. The absorption feature at 2085 $cm^{-1}$ is associated with linearly adsorbed CO on $Pt^0$. The other two bands indicate the formation of carbonates upon CO exposure, mainly of bidentate type (bands at 1650-1550, 1350-1250 $cm^{-1}$). There is another low intensity peak at 2220 $cm^{-1}$ which can be associated with CO chemisorbed on $Al^{3+}$ Lewis acid sites [3,4]. This feature indicates that part of the $Al_2O_3$

surface is available for CO adsorption. On 2%Pt-20wt%-BaO/$Al_2O_3$, linear CO was also observed on Pt at 2079 $cm^{-1}$. The intensity of this CO band is similar on the two catalysts, indicating that the accessibility of Pt particles is not hindered at the higher BaO loading of 20wt%. On the other hand, carbonate formation was enhanced on the 2%Pt-20wt%-BaO/$Al_2O_3$ catalyst which might originate from the higher Ba-content. After CO adsorption, TPD experiments were conducted. As the IR spectra of **Figure 3** indicate, CO is very stable on these catalysts and higher Ba content seem to lowers the strength of Pt-CO binding, although the surface accessibility of Pt remains the same. $NO_2$ exposure of the $CO_{ads}$-Pt-BaAl samples results in the disappearance of the CO absorption features at much lower temperatures (~400K), due, at least in part, to the Pt-catalyzed reaction between CO and $NO_x$.

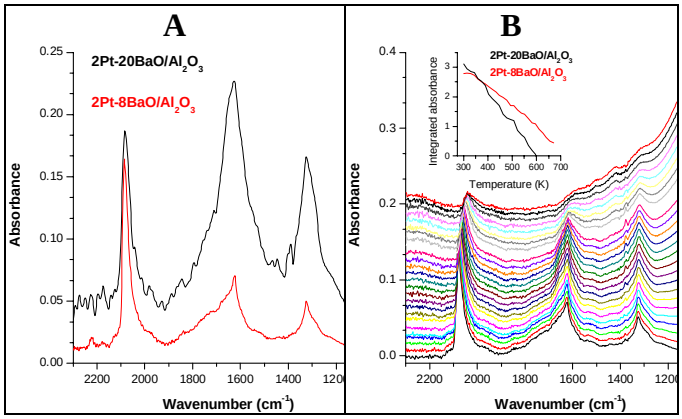


**Figure 3**. IR spectra after CO adsorption on 2%Pt-8wt%-BaO/$Al_2O_3$ and 2%Pt-20wt%-BaO/$Al_2O_3$ catalysts at 300K (A). A series of IR spectra collected during TPD after CO adsorption on 2%Pt-8wt%-BaO/$Al_2O_3$ (B). The insert on (B) shows the integrated intensities of the CO band as a function of catalyst temperature for both materials.

$NO_2$ adsorption onto a CO pre-covered surface was carried out at different $NO_2$ exposures (1, 5, and 10 Torr). Two different types of nitrates were found: surface (bidentate) and bulk (ionic) nitrates. Using spectral deconvolution, changes in the individual absorption features as a function of $NO_2$ exposure were obtained for both catalysts. Increasing the amount of adsorbed $NO_2$ the ratio between these two surface $NO_x$ species changed. Monitoring the gas phase composition during the adsorption, NO, $N_2O$ and $N_2$ were detected. FTIR spectra collected during TPD showed that surface nitrates were transformed to bulk nitrates as the temperature was increased. The distribution of gas phase products was dependent upon the amount of adsorbed $NO_2$.

**Acknowledgment.** This work was supported by the Office of Energy Efficiency and Renewable Energy, FreedomCar and Vehicle Technologies Program, U.S. Department of Energy. The research described in this paper was performed at the Environmental Molecular Sciences Laboratory, a national scientific user facility sponsored by the DOE Office of Biological and Environmental Research and located at PNNL. The Pacific Northwest National Laboratory is operated for the U.S. DOE by Battelle Memorial Institute under Contract No. DE-AC06-RLO1830.

**References**

1. Takeuchi, M.; Matsumoto, S., *Topics in Catal*. **2004**, *28*, 151.
2. Epling, W.S.; Campbell, L.E.; Yezerets, A.; Currier, N.W.; Parks II, J.E., *Catalysis Reviews*., **2004**, *46*, 163-245.
3. F. Prinetto, G. Ghiotti, I. Nova, L. Lietti, E. Tronconi, and P. Forzatti *J. Phys. Chem. B* **2001**, *105*, 12732.
4. Y. Su, M. D. Amiridis *Catalysis Today* **2004**, *96*, 31.

# REFORMER-ASSISTED LEAN NOx CATALYSIS FOR EMISSIONS CONTROL

*KG Rappé, RT Rozmiarek, CL Aardahl*, DN Tran, and DR Herling*

Pacific Northwest National Laboratory
P.O Box 999
Richland, WA 99354
*christopher.aardahl@pnl.gov

**Abstract**

Presented here is an approach for active lean NOx catalysis and so-called 'assisted' lean catalytic processes, where the reductant is treated in some fashion prior to reaction over the NOx catalyst. It consists of a modified lean NOx catalytic approach where diesel or natural gas is treated in a fuel reformer to provide highly active oxygenated species for NOx reduction, and this reformed mixture is injected into the exhaust upstream of the lean NOx catalyst to promote reduction. The process employs a millisecond contact time reformer[1] to convert either diesel or natural gas to largely syngas components in addition to minimal amounts of carbon dioxide. The syngas is then pressurized to 200-300 psi and passed over a Cu/Zn catalyst at 240-280$^{o}$C to form a mixture of dimethyl ether (DME), methanol (MeOH), hydrogen, carbon monoxide, carbon dioxide, and nitrogen. This mixture is then fed into the exhaust upstream of a lean NOx catalyst.

Efforts to date have focused on optimization of the three stages of the system: syngas production, reductant synthesis, and lean NOx catalysis. Results have shown that DME and MeOH are highly selective for NOx reduction in simulated exhaust streams. Current efforts are examining the impact of residual syngas on lean NOx activity with DME-MeOH reductants. In addition, syngas production and reductant synthesis are being optimized and integrated. Progress on these activities will be presented in addition to developments in lean NOx catalysts for this system.

**Introduction**

The diesel engine is attractive due to its ability to deliver power efficiently at high load conditions, and its extended operational lifetime. These attributes lead to a dominant engine in commercial trucking and heavy equipment. However, the diesel engine is burdened with significant particulate and nitrogen oxides (NOx) emissions. Engine burn strategies and passive particulate filters are expected to drop particulate emissions levels to below regulatory limits. However, meeting future regulatory requirements for NOx emissions have proven to remain a significant concern. NOx adsorber traps have shown promise and are simplistic in their design, however they are vulnerable to sulfur poisoning and the cost of the precious metal loading is of significant concern. Selective catalytic reduction (SCR) which utilizes urea has been successfully demonstrated in on-board configurations, however it is burdened with relying on the infrastructure needed for urea distribution and concerns with ammonia slip still remain. Alternative approaches include lean NOx catalysis & plasma-facilitated lean NOx catalysis, however lean NOx catalysis has not shown relatively high activity levels, and plasma-facilitated lean NOx catalysis suffers from high fuel-penalty losses.

One approach being examined is active lean NOx catalysis and 'assisted' lean NOx catalytic processes. In this presentation, we will present a modified lean NOx catalytic approach where diesel or natural gas is treated in a fuel reformer to provide highly active oxygenated species for participation in the 'assisted' catalytic lean NOx reduction process.

In the 'assisted' lean NOx catalytic process, NOx species undergo selective catalytic reduction (SCR) to $N_2$ on the surface of an appropriate catalyst. The SCR process employs a reducing agent (typically hydrocarbon-based) to facilitate the reduction of NOx species. The effect of the active reducing agent on the NOx SCR process has been reported by this group[1]. Results have shown that the appropriate reducing agent & catalyst combination can enhance the NOx SCR process and broaden the effective temperature range for the SCR process. Current investigations of dimethyl ether (DME) as the active reducing agent have shown high selectivity for NOx reduction in simulated exhaust. Investigations have also shown high activity employing methanol (MeOH) as the active reducing agent.

The approach presented here will demonstrate progress on the synthesis of a DME/MeOH mixture from fuel that will be employed as the active reducing agent in the NOx SCR process. A fuel reformer will be employed to facilitate the reformation of fuel to a DME/MeOH mixture in a two-step process: (1) the reforming of fuel to syngas, and (2) the synthesis of DME/MeOH from the syngas. The DME/MeOH mixture is then injected into the exhaust upstream of the lean NOx catalyst to promote the reduction of NOx to $N_2$.

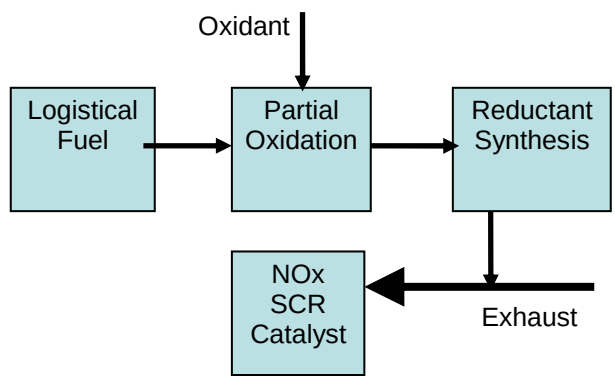


**FIGURE 1.** Overall schematic of the 3-stage NOx reduction process: includes (1) the conversion of fuel to syngas, (2) the synthesis of DME/MeOH from the syngas stream, and (3) the catalytic reduction of NOx in diesel exhaust assisted by the injection of the DME/MeOH mixture into the exhaust.

**Experimental**

Reforming of logistical fuels to hydrogen is a topic of great interest in automotive and fuel-cell related fields due to the large relative energy density of the logistical fuels and the elaborate distribution networks currently in place. Steam reforming, partial oxidation, and autothermal conversion are approaches considered for the conversion of fuel to syngas. Steam reforming (SR) has been shown to effectively produce high ratios of $H_2$:CO [$C_nH_m + nH_2O \rightarrow nCO + (m/2 + n)H_2$]. SR is an equilibrium-based process, and the water-gas shift (WGS) reaction [$H_2O + CO \leftrightarrow H_2 + CO_2$] can be employed in the presence of excess steam to produce additional $H_2$ at lower temperatures. However SR is energy intensive as the reaction is largely endothermic, and SR catalysts will sulfur poison. Additionally, SR has the tendency to form soot when processing large alkanes. However the most significant drawback for the application at hand is the requirement to have significant amounts of water available for the SR process.

Partial oxidation (POx) is an exothermic process and requires no additional energy for operation [$C_nH_m + (n/2)O_2 \rightarrow nCO_2 + (m/2 + n)H_2$]. However it does suffer from dilution effects as a result of using air as the oxygen source, and produces a lower $H_2$:CO ratio in

respect to SR. Due to the significant amounts of water required for SR, POx has been chosen as the current path forward for the production of syngas from fuel. The process shown here employs a millisecond contact time reformer[2] to convert either diesel or natural gas to largely syngas components in addition to minimal amounts of carbon dioxide.

The POx reformer facilitates the vaporization of fuel in air and then passes this air-fuel mixture over a Rh-based γ-alumina catalyst which facilitates the fuel POx process. Fuel vaporization is assisted by a fuel injector that forms a spray to create a film of fuel on the inside of the reactor wall. Vaporization of fuel then takes place from this film in a boundary layer void of oxygen, thus avoiding autothermal ignition. The Rh catalyst consists of a γ-alumina layer deposited onto an 80-ppi reticulated ceramic support (Hi-Tech Ceramics), with Rh deposited onto the γ-alumina layer via Rh-nitrate solution. Blank reticulated ceramic supports are placed directly upstream and downstream of the catalyst for heat shielding, and a blank support is placed upstream from this assembly to promote mixing and facilitate plug flow. Characterization of the POx product stream is performed with a gas chromatograph (GC) equipped with a thermal conductivity detector (TCD) and a mass selective detector (MSD).

The catalytic chemical synthesis of DME/MeOH from syngas is an exothermic process that is equilibrium favored at relatively low temperatures (240-280°C) and relatively high pressures (200-600psig). Synthesis gas conversion to DME/MeOH is equilibrium hindered by nitrogen dilution (from the POx reaction) via a decrease in the partial pressure of $H_2$ and CO. The equilibrium calculations of DME & MeOH formation at various temperatures & pressures will be presented. The effect of nitrogen dilution on the equilibrium conversion numbers will also be presented.

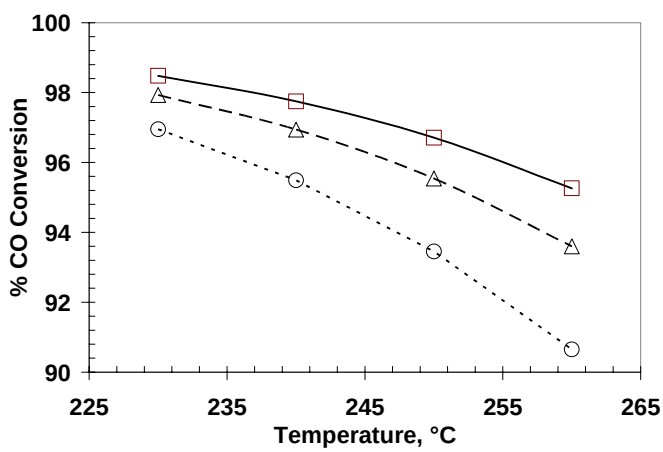


**FIGURE 2.** Equilibrium DME (& MeOH) production versus temperature from 2:1 $H_2$/CO syngas at three (3) pressures: (□) 50 atm, (Δ) 40 atm, and (◊) 30 atm.

The syngas stream produced from the fuel POx reformer is pressurized to 200-300 psi and passed over a Cu/Zn catalyst at 240-280°C to form a mixture of DME, MeOH, hydrogen, carbon monoxide, carbon dioxide, and nitrogen[3]. The current testing apparatus utilizes simulated syngas which is delivered via Brooks mass flow controllers. The simulated syngas is pre-heated before entering an oil-heated catalytic reactor at the desired reaction pressure. The product gas mixture from the reactor is then chilled to remove condensable constituents prior to analysis via an Agilent four (4) column micro-GC which utilizes TCD detectors.

The performance of the NOx SCR process is characterized by flowing simulated exhaust with active reducing agents over powder catalysts packed inside a 1-inch quartz tube inside of a Thermodyne tubular furnace. Steady-state NOx reduction efficiencies are determined by measuring the presence of NOx species before and after the catalyst. NOx measurements are made via a California Analytical 600-HCLD chemiluminescent NOx detector

**Results and Discussion**

Efforts to date have focused on optimization of the three stages of the system: syn-gas production, reductant synthesis, and lean NOx catalysis. The main variables investigated in the syngas production are catalyst formulation, support characteristics, carbon to oxygen ratios and contact times. The main variables of reductant synthesis have been pressure, temperature, contact time and partial pressure reduction. The variables for lean NOx catalysis have been temperature, catalyst formulation, reductant to NOx ratio and specific reductant effect.

Results have shown that DME and MeOH are highly selective for NOx reduction in simulated exhaust streams. Steady-state results will be shown demonstrating the effectiveness of DME as the reductant on undoped γ-alumina catalyst. Steady-state results will also be shown investigating the effect of Ag-doping the NOx reduction catalysts. Figure 3 shows the steady-state NOx reduction efficiency on one undoped and four (4) Ag-doped γ-alumina catalysts. At 400°C using DME at $C_1$:NOx ratio of 4 and 44000 GHSV, undoped γ-alumina catalyst demonstrates NOx conversion above 70% from 400°C to 460°C and above 60% from 380°C to almost 500°C. DME combustion activity appears to be too high on Ag-doped γ-alumina catalysts to result in significant NOx reduction, even at extremely low silver loading.

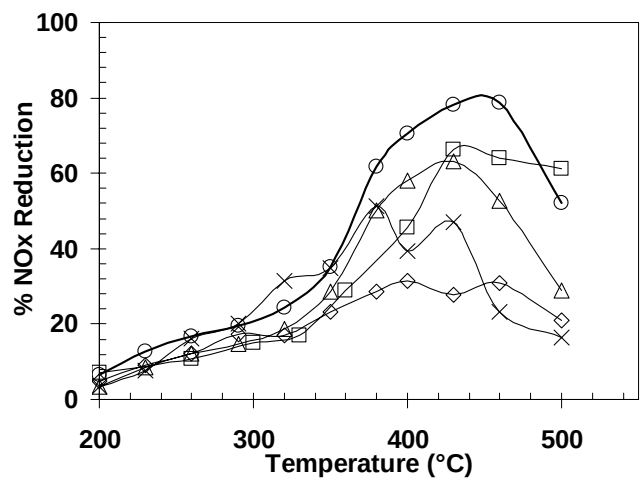


**FIGURE 3.** Steady-state NOx reduction performance versus temperature with DME at $C_1$:NOx ratio of 4 and 44000 GHSV on five (5) γ-alumina based catalysts: (○) undoped, (□) 0.0635-wt% Ag, (Δ) 0.253-wt% Ag, (◊) 0.522-wt% Ag, and (X) 1.020-wt% Ag.

Several proprietary catalyst formulations are currently being investigated for NOx reduction activity with DME and MeOH as reductants. Specific precious metal mixtures have shown increased steady-state NOx reduction activity, and these results will be presented.

Additional efforts are currently underway examining the impact of residual syngas on lean NOx activity with DME-MeOH

reductants. Testing is underway investigating the effect of $H_2$, CO, & syngas on the SCR of NOx. Preliminary results indicate minimal effect of the presence of varying amounts of $H_2$ & CO separately on the NOx reduction activity of undoped γ-alumina. However an adverse effect is seen resulting from varying amounts of syngas. These preliminary results will be presented and discussed.

Performance of the millisecond contact time reformer is being optimized for syngas production; testing is currently underway with n-decane. The C:O ratio for combustion of n-decane is 0.323, and 1 for syngas. Thus, C:O ratios of 0.7 to 2.5 are being examined, resulting in catalyst operating temperatures of >1200°C to <700°C (respectively). Contact times in the reformer of 6 and 12 milliseconds are being examined. Results have shown promise for syngas production from n-decane, with optimum performance appearing at the lower contact time and lower C:O ratios. However operating temperature of the catalyst is of concern, as elevated temperatures (>1200°C) witnessed at lower C:O ratios can result in catalyst deactivation and Rh mobility. The results of these investigations will be presented.

Reductant synthesis results with varying temperatures, pressures, syngas ratios, syngas compositions will be presented and discussed. The effect of contact time will also be shown, with all results compared to thermodynamic equilibrium.

And finally, progress on the integration of the POx reformer & DME/MeOH synthesis apparatus will be addressed and discussed.

**Acknowledgment.** This work was funded by the U.S. Department of Energy, Office of FreedomCAR.

**References**

1. Rappé, et al., *SAE Tech Paper Series* 2001-01-3570.
2. Krummenacher et al., *J. Catal.* **215** (2003) 332-343.
3. Ng et al. *Chem Eng Sci* **54** (1999) 3587-3592.

# NATURE OF NITRATE SPECIES ON BAO/AL$_2$O$_3$ NSR CATALYSTS

*János Szanyi[1], Ja Hun Kwak[1], Do Heui Kim[1], Jonathan C. Hanson[2], Charles H.F. Peden[1]*

[1]Chemical Sciences Division, Pacific Northwest National Laboratory
Richland, WA 99352 USA
[2]Chemistry Department, Brookhaven National Laboratory
Upton, NY 11937 USA

## Introduction

Internal combustion engines operating under lean-burn conditions exhibit high fuel efficiency. Removal of harmful $NO_x$ gases from the exhaust in the presence of excess oxygen, however, presents a great challenge to the catalysis community. Traditional three-way catalysts are ineffective under these conditions. Therefore, new approaches toward $NO_x$ reduction have been sought in the last decade. Urea selective catalytic reduction (SCR), plasma assisted $NO_x$ reduction, and $NO_x$ storage/reduction (NSR) are three promising technologies for diesel emission control.

In the NSR technology, an active oxides (alkaline and alkaline earth) material takes up $NO_x$ under lean engine operation conditions and stores them as nitrates [1]. In a brief rich cycle these nitrates are released form the active oxide catalyst component, and reduced to $N_2$ on the precious metal component, almost exclusively Pt. The precious metal also plays a key role in the storage cycle as well; it converts NO to $NO_2$ that, in turn, can adsorb on the active oxide component. The most commonly used catalyst in this technology is Pt/BaO/$Al_2O_3$. Both the uptake and release of $NO_x$ have been extensively studied on these BaO-based systems. Although the $NO_x$ uptake mechanism is fairly well understood today [2-6], the nature of the nitrate species formed is poorly characterized. For instance, it has been reported that during temperature programmed desorption (TPD) two distinct $NO_x$ features appear. At lower temperature the only desorbing species was $NO_2$, while at higher temperature NO+$O_2$ were seen to desorb. The origin of these two desorption features has not been discussed unambiguously.

Here we report the results of our multi-spectroscopy study in which we set out to understand the nature of different nitrate species formed during $NO_2$ uptake on BaO/$Al_2O_3$ $NO_x$ storage materials. To this end, we investigated $NO_2$ adsorption and desorption on $Al_2O_3$, 8wt%-, and 20wt%-BaO/$Al_2O_3$ catalysts using FTIR, TPD, $^{15}$N solid state NMR spectroscopies. We also followed the changes in catalyst morphology during these processes using time resolved XRD (TR-XRD) and TEM.

## Experimental

BaO/$Al_2O_3$ catalysts were prepared by incipient wetness of γ-$Al_2O_3$ (200 m$^2$/g) with an aqueous $Ba(NO_3)_2$ solution. Prior to adsorption studies the samples were calcined at 773K in air flow in order to decompose the nitrates and form the active oxide phase. For FTIR and TPD experiments the powder catalyst sample was pressed onto a tungsten mesh, which, in turn, was attached to a copper sample holder assembly. This sample mounting allowed us to heat the sample resistively to ~1000K. The IR cell consists of a 2 ¾" stainless cube with $CaF_2$ windows, and is connected to a gas handling manifold, pumping station, and a mass spectrometer (UTI 100C). A Mattson Research Series FTIR spectrometer was used throughout the study, operated at 4 cm$^{-1}$ resolution, and each spectrum collected was the average of 64 scans. Prior to acquiring an IR spectrum a background spectrum was recorded with the catalyst sample in the IR beam to eliminate the contribution of the oxide materials. TPD experiments were carried in two different systems: in the IR cell, and in a flow through reactor. Desorbed $NO_x$ species were followed either by a mass spectrometer (IR cell) or by a chemiluminescence $NO_x$ analyzer (flow through cell).

$^{15}$N solid-state NMR spectra were acquired on a Varian/Chemagnetics CMX Infinity 300 MHz instrument, equipped with a Varian/Chemagnetics 7.5 mm HX MAS probe operating at a spectral frequency of 30.40651 MHz. In the in-situ NMR cell 0.5 g of catalyst sample was pretreated under vacuum (<1x10$^{-7}$ torr) at 773K for 2 hrs. $NO_2$ saturation of the samples was conducted at 673K. The $NO_2$ saturated samples were transferred into the gas-tight rotor (7.5 mm O.D.) for solid state $^{15}$N-NMR measurements. All $^{15}$N NMR spectra were externally referenced to $^{15}$N-ammonium chloride at 0 ppm. All spectra were obtained spinning at 5 kHz and using a 10 seconds recycle delay.

The TR-XRD experiments were carried out at the beam line X7B of the National Synchrotron Light Source (NSLS), at Brookhaven National Laboratory. In these experiments the decomposition of the $Ba(NO_3)_2$ phase in the as-prepared catalysts, as well as the formation and decomposition of nitrate species upon $NO_2$ uptake and release were followed.

## Results and Discussion

TEM images of the as-prepared $Ba(NO_3)_2/Al_2O_3$ show the presence of large $Ba(NO_3)_2$ crystallites on the $Al_2O_3$ support. EDS analysis revealed that the Ba distribution was uneven on the alumina support; there were Ba-rich regions (where the $Ba(NO_3)_2$ particles reside) and Ba-free areas. XRD pattern recorded from this material also indicated the presence of large crystals of $Ba(NO_3)_2$. TR-XRD analysis suggested that the average particle size of the $Ba(NO_3)_2$ crystals remained constant until the sudden disappearance of the $Ba(NO_3)_2$ phase. TEM images from 8wt%-, and 20wt%-BaO/$Al_2O_3$ showed no BaO particles on the alumina support, and the evenly distributed BaO phase was confirmed by EDS measurements. The morphologies of the two Ba-containing materials were identical to that of the alumina support. TR-XRD results indicated that some of the BaO was present as nano particles. When these BaO/$Al_2O_3$ samples were exposed to $NO_2$ at 300K, the formation of nano-sized (~5nm) $Ba(NO_3)_2$ crystals were seen. Heating the sample in $NO_2$ flow to 573K resulted in the formation of large $Ba(NO_3)_2$ crystallites (~15nm).

TPD spectra acquired in the flow through reactor form the $Al_2O_3$, 8wt%-, and 20wt%-BaO/$Al_2O_3$ following $NO_2$ adsorption show in Fig. 1. A broad $NO_2$ desorption feature is seen from the alumina support in the 500-800K temperature range. In the TPD spectrum from the 8wt%-BaO/$Al_2O_3$ sample two desorption features can be distinguished: a low temperature $NO_2$ peak, and a high temperature NO feature. This high temperature NO desorption feature is always accompanied by an $O_2$ feature, suggesting that in this range the nitrates formed in the $NO_2$ uptake cycle decompose as NO+$O_2$. The same two desorption features are observed on the 20wt%-BaO/$Al_2O_3$ system, however, the intensity ratio of these two features is very different from that seen for the 8wt%-BaO/$Al_2O_3$. Based on the morphology changes discussed above, and the IR an NMR results we will discuss next, we propose that the lower temperature peak ($NO_2$) in TPD represents desorption of surface nitrates formed on a monolayer of BaO interacting strongly with the underlying $Al_2O_3$ support. BaO present on the support in excess of a monolayer forms bulk-like $Ba(NO_3)_2$ crystallites and decomposes as NO+O2 similarly to unsupported $Ba(NO_3)_2$. This proposal is supported by the observation that the integrated area under the lower temperature desorption peak is directly proportional to the surface area of the catalyst.

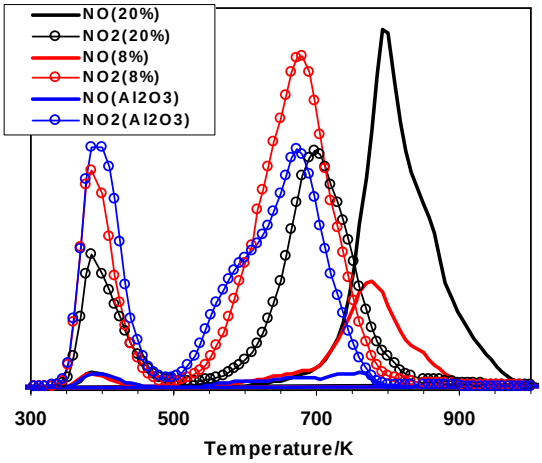


**Figure 1.** TPD spectra form $Al_2O_3$, 8wt%, and 20wt% BaO/ $Al_2O_3$ after $NO_2$ saturation at 300K.

The existence of different nitrate species on these $BaO/Al_2O_3$ samples is further supported by the results of our FTIR and $^{15}N$ SS NMR studies. IR spectra obtained after NO2 adsorption at both 300K and 673K on $Al_2O_3$, 8wt%-, and 20wt%-$BaO/Al_2O_3$ catalysts are displayed in Fig. 2. In agreement with the results of previous studies [2-6] both bridging bidentate (1300 and 1575 $cm^{-1}$) (surface) and ionic (1300 and 1420-1480 $cm^{-1}$) (bulk-like) nitrates are formed on both BaO-containing catalysts. The relative intensities of these two features, however, are vastly different on the two samples. On 8wt%-$BaO/Al_2O_3$ the intensity of the surface nitrate features are much higher than that of the bulk nitrates. It is also evident that at this low BaO coverage not the entire $Al_2O_3$ surface is covered with BaO, while in the case of the 20wt% sample no $NO_2$ adsorption on the alumina support is seen. Heating the samples to 673K in the presence of $NO_2$ does not affect the IR spectrum of $Al_2O_3$, while changes in the IR spectra of the BaO-containing samples are evident. On the 8wt%- $BaO/Al_2O_3$ the intensities of the surface nitrates increase, while those of the bulk nitrates decrease, suggesting some redistribution of the $Ba(NO_3)_2$ phase on the alumina support at high temperatures. On the 20wt% sample we see changes in much smaller extent: the intensities of the surface nitrate peaks decrease, while those of the bulk nitrates increase as we form larger $Ba(NO_3)_2$ particles at higher $NO_2$ uptake temperatures.

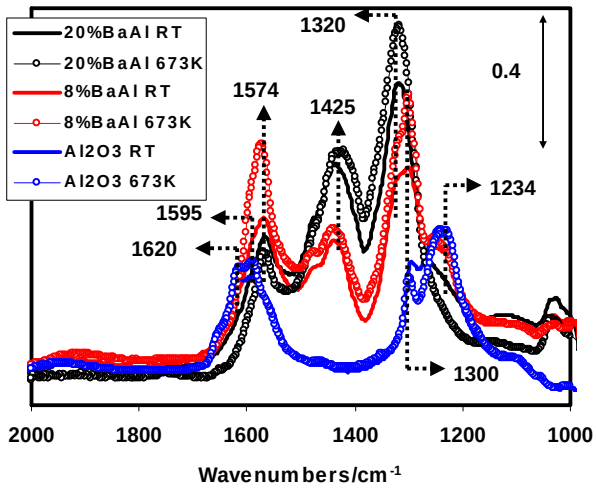


**Figure 2.** IR spectra from $Al_2O_3$, 8wt%, and 20wt% BaO/ $Al_2O_3$ after $NO_2$ adsorption at 300K (solid lines), and 673K (open circles).

$^{15}N$ solid state NMR spectra obtained form the three samples are shown in Fig. 3. On $Al_2O_3$ only one broad peak is seen at 313ppm. We assign this feature to surface nitrates on the $Al_2O_3$ support. The broadness of this peak shows the heterogeneity of the adsorption sites on this support. On 8wt%-$BaO/Al_2O_3$ three distinct features are seen in the NMR spectra: at 313, 337, and 340.5ppm chemical shifts. The presence of the 313ppm feature shows that the alumina support is not fully covered by BaO, and available for $NO_2$ adsoprtion. The two features at higher chemical shifts can be assigned to nitrates [7,8], specifically to surface (337ppm) and bulk (340.5ppm) nitrates. Increasing the BaO content of the catalyst to 20wt% results in a large increase in the intensity of the bulk nitrate feature, while the surface nitrate peak is very similar to that of the 8wt% sample. Also, on the 20wt%-$BaO/Al_2O_3$ catalyst no alumina surface is available for $NO_2$ adsorption as it is completely covered with BaO.

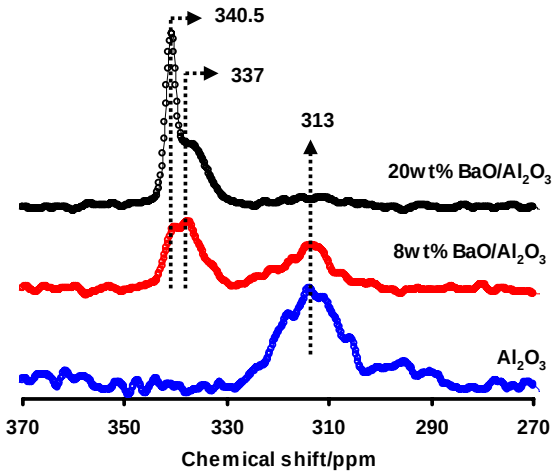


**Figure 3.** $^{15}N$ solid state NMR spectra form $Al_2O_3$, 8wt%, and 20wt% BaO/ $Al_2O_3$ after $NO_2$ saturation 673K.

## Conclusions

The results of this multi spectroscopic study clearly show the formation of a monolayer BaO on the alumina support during catalyst preparation. This film adsorbs $NO_2$ in a bridging bidentate configuration, and releases $NO_x$ as $NO_2$. As the concentration of BaO exceed that of a monolayer, BaO particles form. These particles are then converted to bulk-like $Ba(NO_3)_2$ upon $NO_2$ adsorption and release $NO_x$ as $NO+O_2$ during temperature programmed desorption.

**Acknowledgement.** This work was carried out at the Pacific Northwest National Laboratory, operated for the US DOE by Battelle Memorial Institute and at Brookhaven National Laboratory. Funding for this work was provided by the DOE, Office of Basic Energy Sciences, Division of Chemical Sciences.

## References

(1) Takahashi, N., Shinjoh, H., Iijima, T., Suzuki, T., Yamazaki, K., Yokota, K., Suzuki, H., Miyoshi, N., Matsumoto, S., Tanizawa, T., Tanaka, T., Tateishi, S., and Kasahara, K., *Catal.Today* **1996,** *27,* 63.
(2) Prinetto, F., Ghiotti, G., Nova, I., Lietti, L., Tronconi, E., and Forzatti, P., *J.Phys.Chem. B.* **2001,** *105*, 12732.
(3) Nova, I., Castoldi, L., Lietti, L., Tronconi, E., Forzatti, P., Prinetto, F., and Ghiotti, G., *J.Catal.* **2004**, *222*, 377.
(4) Broqvist, P, Gronbeck, H., Fridell, E., and Panas, I., *J.Pys.Chem. B,* **2004**, *108*, 3523.
(5) Fanson, P.T., Horton, M.R., Delgass, W.N., Lauterbach, J., *Appl.Catal.B: Environmental*, **2004**, *46*, 393.
(6) Anderson, J.A., Patterson, A.J., and Fernanadez-Garcia, M., *Stud.Surf.Sci.Catal.*, **2000**, *Vol. 130*, 1331 (Eds. Corma, A., Melo, F.V., Mendioroz, S., and Fierro, J.L.G).
(7) Szanyi, J., Kwak, J.H., Burton, S., Rodriguez, J.A., Peden, C.H.F., J.Elect.Spectr.Rel.Phen, *submitted*
(8) Anderson-Altmann, K.L., and Grant, D.M., *J.Phys.Chem.* **1993**, *97*, 11096.

# LOW TEMPERATURE CATALYTIC OXIDATION OF CO OVER SILICA SUPPORTED PALLADIUM CATALYST

*Anil.C.Banerjee, Dipankar Koley, Ekua Okoso-Amaa*

Department of Chemistry
Texas A&M University—Commerce
Commerce, Texas-75429, USA

## Introduction

Catalytic oxidation of carbon monoxide on platinum group of metals has been well studied. Supported palladium catalysts have shown good possibilities for low temperature CO oxidation[1]. Pre-oxidized $Pd/Al_2O_3$ catalysts produced 20% CO conversion at $210^0$C and the pre-reduction did not change the catalytic activity[2]. The dependence of catalytic activity on methods of preparation, pH, temperature of calcination has been reported for some catalysts[3, 4]. However, systematic studies on the effect of catalyst preparation including the effect of drying conditions (temperature, atmosphere, drying rate etc) on palladium catalysts are missing. The results of preliminary studies on drying atmosphere and rate are reported in this paper.

## Experimental

**Catalyst Preparation.** Catalysts were prepared by adsorption of tetraaminepalladium (+2) nitrate to silica slurry. 50grams of silica were slurried in 400ml $H_2O$. The pH was adjusted to 9.5 by addition of conc. $NH_4OH$. Separately 2gm of Pd $(NH_3)_4(NO_3)_2$ was dissolved in 50ml of $H_2O$ and added to the basic silica solution and stirred for 3 hours. The slurry was dried at room temperature in static air. This sample was then further dried in a microreactor in helium or oxygen atmosphere at different heating rates (1, 5, $10^0$C/min). The flow rate of the drying gas was maintained at 50cc/min. The temperature was ramped up to $100^0$C at different drying rates, soaked at 1this temperature for 3hr and then calcined at $300^0$C for 3hr, followed by reduction in hydrogen at $300^0$C for another 3hr.

**Catalytic Activity studies.** Catalysts activities were studied in a fixed bed flow micro reactor. The reactor was interfaced through a multi-loop sample collector and an injection valve to analyze the effluent gases from the reactor on line by gas chromatography (Shimadzu 14B) using carboxen column and TC detector. The reacting gas (1%CO, 10% oxygen and balanced He) at 60cc/min was passed through the reactor containing 0.2 gm of catalyst and the temperature was raised up to 250°C at 2°C/min. The effluents were analyzed by GC to determine the concentrations of CO and $CO_2$.

**FTIR Spectroscopy.** A thin transparent wafer of the catalyst was prepared by mixing with KBr in an IR dye and press and place in the sample chamber of an in-situ IR cell (ISRI, Inc.). The IR cell was placed in the beam path of the FTIR spectrometer (Shimadzu Prestige 21). The catalyst wafer was pretreated in hydrogen for three hr at $200^0$C before reaction. The reacting gas (pure CO or 1% CO, 10%$O_2$, and balance He) was passed at a flow rate of 60cc/min and the temperature of the IR cell was ramped at $2^0$C/min until $250^0$C. The transmission infrared spectra were recorded at a resolution of 2cm-1 and 30 scans/ spectrum in the computer using IR solution software. The spectra were obtained in the absorbance mode after subtraction of the background spectrum of the catalysts disk under He atmosphere.

## Results and Discussion

The activities in terms of conversion at different temperatures for two drying rates are reported in Figure1. The conversion increased by 10% with increase in drying rate at 90 and $110^0$C. The influence of drying atmosphere (helium and oxygen) on activity is shown in Figure 2. The conversion increased by about 7% in oxygen atmosphere at $70^0$C and then rapidly from 46 %( in He) to 91 %( in oxygen) at $110^0$ C. The preliminary results indicate the noticeable effect of drying atmosphere and rate on catalyst activity and further detailed studies including drying temperature and flow rate are being continued.

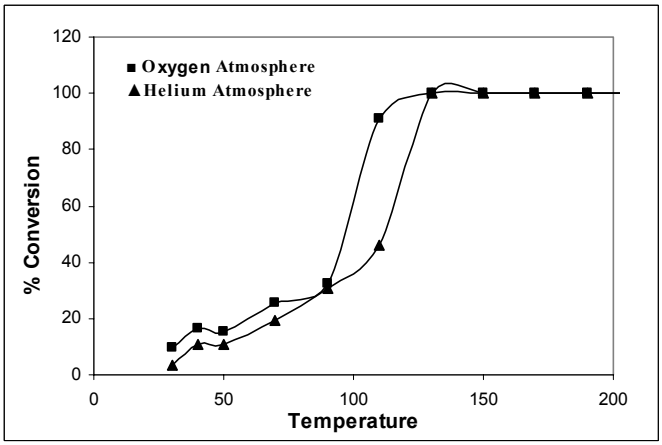


**Figure1**. Effect of drying atmosphere on activity

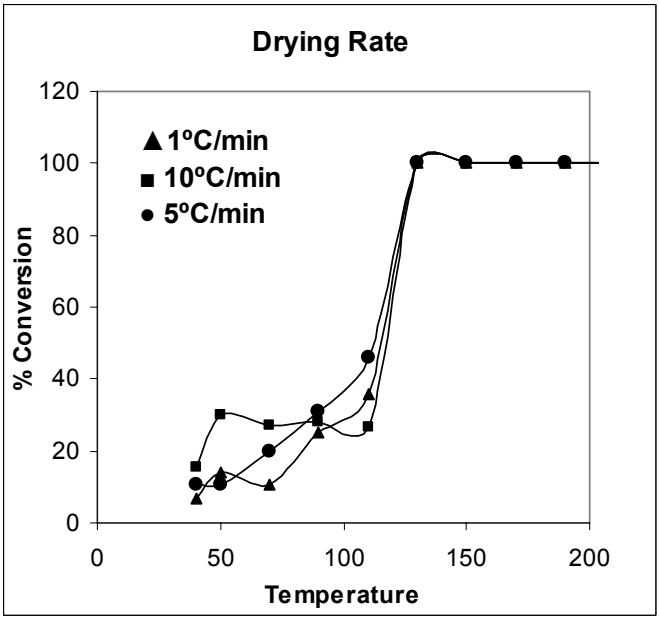


**Figure 2**.Effect of drying rate on activity

The FTIR spectra in Figure 3 are reported for the catalyst dried in helium at 5°C/min. The gas phase CO is in the region (2100-2200 $cm^{-1}$). The IR peaks due to various modes of adsorbed CO vibrations (terminal and bridging) are in the region of 1700 -1900 $cm^{-1}$. These data are in conformity with earlier reported results[5]. The

absorbance due to gas phase CO decreased with increasing temperature due to oxidation. The absorbance due to CO adsorbed species also changed with temperature.

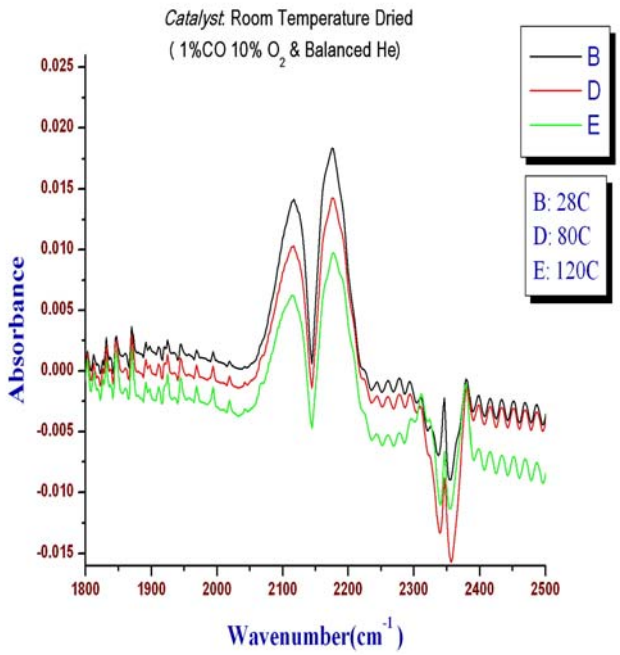


**Figure3**. FTIR spectra

**Significance**

Our results indicate that $Pd/SiO_2$ catalyst remove 90-100% CO at 110-130°C. Further work on the catalyst is under progress for developing a low temperature catalyst for CO oxidation.

**Acknowledgment.** This work was supported by Welch Foundation and Organized Research grant from Texas A&M University Commerce, USA.

**References**

1. Searles, R.A., *Stud. Surf. Sci. Catal*. **1998**,116, 23.
2. Maillet, T.; Solleau, C.; .Barbier Jr.; Jacques, D., *Applied Catalysis B: Environmen*tal 1997, 14, 885-95.
3. Miller, J.T.; Schreier, M.; Kropf, A.a.; Ragalbuto, J.R., *J. Catal.*, **2004**, 225,203-212.
4. Lee, S.; Gavriilidis, A. ; Pankhurst, Q. A. ; Kyek, A. ; Wagner, F. E. ; Wong, P.; Yeung, K. L., *J. Catal*., 2001,200,298-308.
5. Skotak, M.; Karpinski, Z.; Juszczyk, W.; Pielaszek,J.; Kepinski,L., Kazachkin,D.V.; Kovalchuk,V.I.; d'Itri,J.L., *J. Catal.*, 2004, 227,11-25.

# K AND Pd DOPED $CuMnZrO_2$ CATALYSTS FOR CO CONVESION

*Cheng Yang, Minggui Lin, Jiangang Chen, Wenhuai Li, Yuhan Sun**

State Key Laboratory of Coal Conversion,
Institute of Coal Chemistry, Chinese Academy of Sciences,
Taiyuan 030001 P.R.China

## Introduction

Considerable interest remains in carbon monoxide hydrogenation reactions for either the synthesis of hydrocarbons, methanol or higher alcohols. In these synthesis reactions, efforts have been made to limit the selectivity to methane in preference to other products such as alcohols or alkenes. It is widely recognized that higher alcohols together with methanol can be produced from syngas by appropriate modification of methanol synthesis catalysts and reaction conditions [1-2]. However, such reaction conditions are hardly consistent with the preservation of a high dispersion of the active phase in conventional CuZnAl catalyst. It has been demonstrated that active catalyst for the synthesis of methanol can be prepared by dispersing Cu on $ZrO_2$ [3]. The most efficient catalysts ($CuMnOxZrO_2$, or $CuLa_2Zr_2O_7$) for methanol synthesis have been shifted towards higher alcohols under mild conditions using K and FT-elements (Fe, Co and Ni, etc.) as promoters either in our previous work or in the literatures [4-6]. Palladium is also well known as an active phase for CO hydrogenation. Indeed, an alkalized $PdZnMrZrO_2$ catalyst has been developed for methanol-isobutanol synthesis, as $ZrO_2$ was claimed to be active for iso-synthesis [7]. The catalyst for the process also requires high temperatures (>400°C) and pressures (>12 MPa) and produce isobutanol with relatively low productivity (<100 g/kg-cat·h). Moreover, the addition of palladium into other metal catalysts can lead to a substantial improvement in catalytic properties due to its excellent candidates of activate hydrogen, which could then spread over the neighboring phases through a hydrogen-spillover mechanism. Thus, the modification is further made in the alkalized $CuMnZrO_2$ catalyst by Pd to increase the production of higher alcohols without simultaneously increasing unwanted methanation in this work.

## Experimental

**Catalysts preparation.** Catalytic formulations of $CuMnZrO_2$ and $PdCuMnZrO_2$ were prepared by co-precipitation in constant pH conditions about 10-11 using the corresponding metal nitrates as precursors with aqueous sodium carbonate solution, followed by aging, washing and drying. Alkalization was carried out by wetness impregnation $K_2CO_3$ with the precipitates, and then the samples were calcined at 350℃ for 4 h under air. The prepared catalysts were denoted as K-CMZ and K-PCMZ. Another Pd doped catalyst named K-P-CMZ was prepared by successive impregnating of $CuMnZrO_2$ with aqueous $Pd(NO_3)_2$ and $K_2CO_3$, and then the samples were dried and calcinatin in each step as above. The real metal content in the prepared K and Pd doped $CuMnZrO_2$ catalyst analyzed by ICP was as follows: K(3.4wt%), Pd(0.91wt%), Cu(18.5wt%), Mn(7.1wt%), Zr(42.6wt%).

**Catalytic activities test.** CO hydrogenation tests were carried out using a stainless steel fixed-bed reactor, which contained 1.0ml catalyst. All the catalysts were reduced in $H_2$ (5% in $N_2$) flow at 300 ℃ and atmospheric pressure for 6 hr before syngas exposure. Shimazu-8A GC was used to analyze the products. $H_2$, CO, $CH_4$ and $CO_2$ were determined by thermal conductivity detector (TCD) equipped with a TDX-101 column. The water and methanol in liquids were also detected by TCD with a GDX-401 column. The alcohols and hydrocarbons were analyzed by flame ionization detector (FID) with a Propake-Q column.

## Results and Discussion

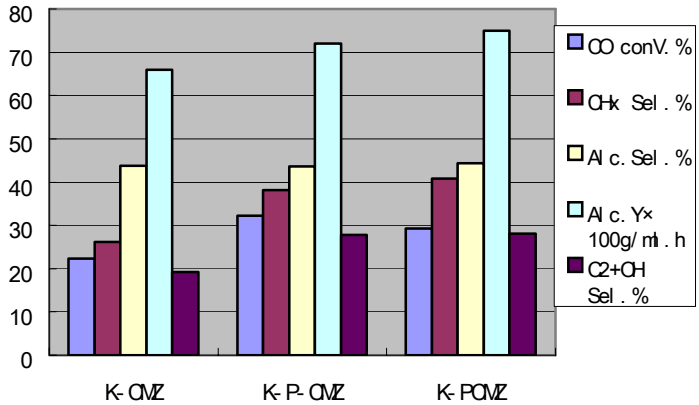


**Figure 1.** The activity and selectivity of K and Pd modified $CuMnZrO_2$ catalysts for CO hydrogenation
Reaction conditions: P=12.0 MPa, T=340$^0$C, GHSV=10000 $h^{-1}$, $H_2$/CO (molar)=1.0: 1

K was usually used as a promoter for methanol synthesis shifted towards higher alcohols. As shown in **Figure 1**, K-CMZ catalyst showed a relatively high activity for CO hydrogenation at the reaction conditions. The space-time-yield of alcohols was about 0.66 g/ml-cat.h with the content of $C^{2+}OH$ about 20wt%. Unlike that of methanol synthesis under mild reaction conditions, the selectivity of alcohol in the products was only 42.4% because amount of hydrocarbons (mainly $CH_4$, see **Figure 2**)) and $CO_2$ was formed. Apparently, the activity was remarkably promoted by Pd addition to K-CMZ catalyst. Though the selectivity of alcohols was slightly increased, their space-time yields and the content of $C^{2+}OH$ were both remarkably improved. This might due to Pd as an excellent candidate of activate hydrogen, which could spread over the neighboring phases through a hydrogen-spillover mechanism, then improved the rate of carbon hydrogenation. Unfortunately, the selectivity of hydrocarbons was also increased either on K-P-CMZ or K-PCMZ catalyst, though the production of $CO_2$ was effectively suppressed.

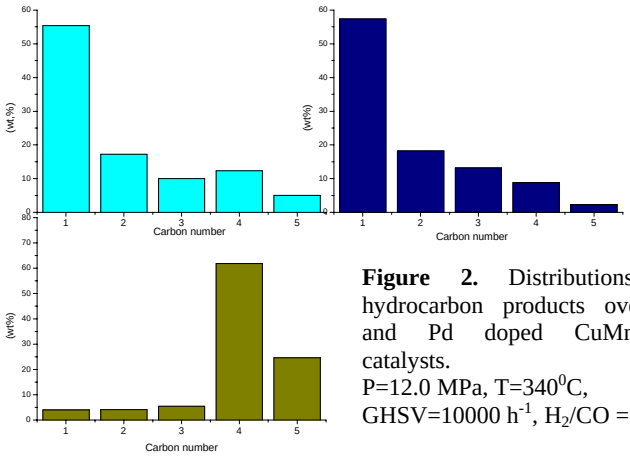


**Figure 2.** Distributions of hydrocarbon products over K and Pd doped $CuMnZrO_2$ catalysts.
P=12.0 MPa, T=340$^0$C, GHSV=10000 $h^{-1}$, $H_2$/CO =1.0.

* Corresponding author. Fax: +86-351-4041153. E-mail address: yhsun@sxicc.ac.cn

**Table 1. The catalytic performance of K-PCMZ catalyst for CO hydrogenation at virous temperatures.**

| Reaction temp. (ºC) | CO conv. (mol%) | Selectivity (C-mol%) | | | Alcohol yield (g/ml.h) | Alcohol distribution (wt%) | | | | |
|---|---|---|---|---|---|---|---|---|---|---|
| | | CHx | $CO_2$ | ROH | | $C_1OH$ | $C_2$ OH | $C_3$ OH | $C_4$ OH | $C_{5+}$ OH |
| 320 | 26.5 | 37.3 | 11.0 | 51.7 | 0.81 | 88.4 | 4.80 | 3.06 | 2.93 | 0.82 |
| 340 | 29.3 | 40.8 | 14.8 | 44.4 | 0.75 | 81.9 | 6.32 | 5.15 | 4.75 | 1.89 |
| 355 | 22.6 | 41.9 | 20.4 | 37.7 | 0.41 | 71.3 | 7.92 | 8.44 | 8.33 | 4.16 |

Reaction conditions: P=12.0 MPa, GHSV=10000 $h^{-1}$, $H_2$/CO (molar)=1.0: 1

Interestingly, it was found that the distribution of hydrocarbons on K-PCMZ was distinctive with that on K-P-CMZ catalyst (**see Figure 2**). The quantity of methane produced on K-PCMZ was less than 5wt%, and the $C_4$ hydrocarbons were the main gas-phase product with iso-butylene above 80wt%. But the hydrocarbon products over K-P-CMZ were mainly methane as same as that on K-CMZ catalyst. This results suggested that the doped manner of Pd in $CuMnZrO_2$ greatly changed the active site for CO conversion, which will be discussed elsewhere.

**Table 1** gave the results of CO hydrogenation over K-PCMZ catalyst at different temperatures. The liquid products were mainly alcohols with a small amount of water and oils. The space-time yield of alcohols decreased with the rising of reaction temperatures as amount of $CO_2$ produced, but the content of higher alcohols ($C_{2+}OH$) in the liquid-phase increased, which reached about 30% at 355ºC. Hydrocarbons (mainly $C_4$ iso-butylene) were also facile to be produced over the catalyst with the selectivity of about 40%.

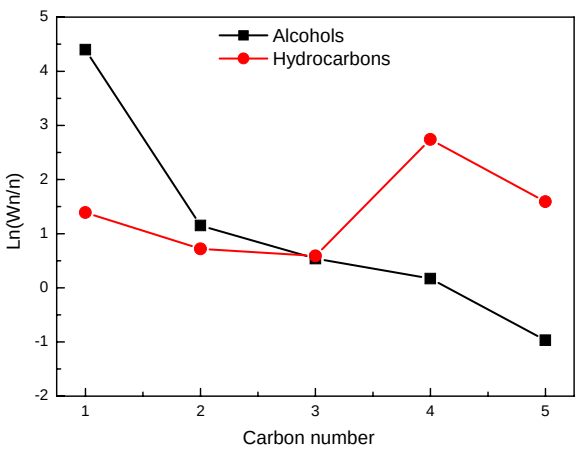


**Figure 3.** The Schulz-Flory-Anderson plots for the distributions of alcohols and hydrocarbons,(Date derived from CO hydrogenation over K-PCMZ catalyst at 340ºC.)

Although several mechanisms had been proposed for either higher alcohols or iso-butylene synthesis from CO hydrogenation, there was still controversy regarding the detailed reactions [8,9]. It was promised that the modifications of the catalyst composition and the reaction conditions greatly influenced the products of CO hydrogenation reaction. It could be seen that the distribution of hydrocarbons obtained from the developed catalyst and process did not obey the conventional Schulz-Flory-Anderson role for the F-T reaction (see **Figure. 3**). A discontinuity at $C_4$ was observed for iso-synthesis. For the distribution of alcohols, methanol was distinctive deviation from the ASF plot, and a little higher of $C_4$ due to the branched alcohols included. This was in line with the results of the synthesis of higher alcohols over alkalized methanol synthesis catalyst.

## Conclusions

A catalyst for CO hydrogenation reactions and the process involving in mixed alcohols synthesis and isosynthesis for coal or natural gas conversion via lean hdydrogen syngas had been developed. These produced a single-phase liquid product of $C_1$ to $C_5$ alcohols with iso-butylene as the main gas-phase hydrocarbon product The space-time-yield of mixed alcohols and iso-butylene were high, and the operating conditions were less severe than the priors.

**Acknowledgements.** The financial support from the State Key Foundation Project for Development and Research of China (G1999022400) and Academic Innovation Project for Acknowledge and Engineering of China (KGCX2-302) is gratefully acknowledged.

## References

1. Herman R. G., *Catal. Today*, **2000**, *55*, 233-245
2. Stiles A. V., et. Al., *Ind. Eng. Chem. Res*., **1991**, 30, 811-821
3. Sun Y. H., Sermon P. A., *J.Chem.Soc.Chem.Commun*., **1993**, 16, 1242-1244.
4. Kiennemann A., Diagne C., Hindermann J. P., *Appl. Catal*., **1989**, 53, 197-206
5. Zhao N., Xu R., Wei W.,Sun Y.H., *React.Kinet.Catal.Lett*., **2002**, 75, 29-33
6. Xu R., Ma Z.Y., Yang C., Wei W., Li W.H., Sun Y.H, *J. Mol. Catal. A:Chem*.,**2004**, 218,133-140.
7. Keim W., Falter F., *Catal. Lett*., **1989**,3, 59-64
8. Xu X. D., Doesberg E. B. M., Scholten J. J. F., *Catal. Today*, 1987, 2, 125-134
9. Tseng S. C., Jackson N. B., Ekerdt J. G., *J. Catal*., 1988, 109, 284-292.

# THE EVIDENCE OF DUAL ACTIVE SITES OF $CO/SIO_2$ CATALYSTS FOR F-T SYNTHESIS

*Jiangang Chen and Yuhan Sun*

*State Key Laboratory of Coal Conversion, Institute of Coal Chemistry, Chinese Academy of Sciences, Taiyuan, 030001, P.R China*
*yhsun@sxicc.ac.cn or chenjg@sxicc.ac.cn*

## Introduction

$Co/SiO_2$ catalysts were widely investigated with regards to conversion of natural gas into clean liquid fuels. The metal dispersion of $Co/SiO_2$ catalysts was determined by either the support porosity or the preparation parameters. For instance, Khodakov [1] showed that the dispersion and reducibility of Co/MCM-41 was dependent on the porosity. Van Steen [2] reported that the solvent category, the cobalt precursor modified the cobalt structure.

The catalysts structure was tentatively correlated with the performance of cobalt catalysts in FT synthesis. Iglesia [3] showed that the TOF was invariable no matter what the support or dispersion was. Similarly, Ho [4] found TOF of Co was independent of Co dispersion or surface texture if the surface contamination was avoided and the degree of reduction was hold to certain degree. Nonetheless, the relationship between structure and selectivity was controversial. Reuel [5] suggested that the product selectivity was a function of the dispersion as well as the extent of reduction. Khodakov [1] observed that the small Co species located in narrow pores yielded higher $CH_4$ selectivity than larger cobalt particles did. Besides, Anderson [6] proposed that the diffusion constants of $H_2$ and CO in wax-filled pore made the difference in selectivity. Iglesia [7] taught that the alpha-olefin re-adsorption was essential to change of hydrocarbon distribution.

In the work, several $Co/SiO_2$ catalysts with well-defined structure were studied in FT synthesis. The structure was correlated with the $CH_4$ yield or $C_2^+$ yield rather than with CO conversion or $CH_4$ selectivity. To our surprise, it was found that the $CH_4$ was formed non-selectively on total cobalt whereas the $C_2^+$ hydrocarbon was merely formed on reduced cobalt. The active phase of dual sites was thus proposed.

## Experimental

The silica supports were prepared by hydrolysis of tetraethylorthosilicate and the control of silica porosity was realized by tuning the pH value of the gel process. The gel is dried at 393K and calcined at 773K.The $Co/SiO_2$ catalysts were prepared by incipient wetness impregnation with aqueous cobalt nitrate, followed by drying at 393K and calcined at 673K.

The content of cobalt and possible impurities were measured with Ion Coupled Plasma (ICP). The BET surface area, pore volume and average pore diameter was derived by $N_2$ physisorption with an automated Micromeritics ASAP2010 system. XRD was taken in a Dmax-γA diffractometer operating at 40kV, 100mA. The scan was taken in the range of 35-38° at a speed of 0.125°/min and the NaCl standard was used as a reference substance. TPR was performed with a catalyst loading of 40mg at a heating rate of 10K/min in $H_2$/Ar (5% vol.). The selection of experimental parameters satisfied the criterion of $\beta S_0/FC_0 \leqslant 15K$ (where $S_0$ is the amount of reducible species in the sample, $FC_0$ is the hydrogen feed to the reactor and β is the heating rate) to achieve high resolution of peaks. The $H_2$ consumption was monitored with TCD. The extent of reduction was measured with pulse $O_2$ titration at 673K. The $O_2$ uptake was quantified by rating the GC-MS area with a pulse loop of known volume.

The performance of catalysts was evaluated in a pressured fixed-bed reactor. The FT synthesis was carried out at 2MPa, $2000h^{-1}$, $H_2$/CO ratio of 2 and a temperature range from 463 to 493K. The products were collected with a hot trap and a cold trap in sequence. The gaseous effluent was analyzed by two on-line GC-8A chromatographs. The liquid was analyzed with a GC-920 chromatograph equipped with OV-101 capillary column. The carbon balance and mass balance was 100±3%.

## Results and Discussion

ICP showed that Na or S impuritys, which usually presented in commercial silica, were not detected in the silica. The density of surface silanol was measured with TG in the flow of inert gas, and the density was almost a constant value, e.g. 4.5 per square nanometer. The acidic property of silanol was evaluated by monitoring the pH value of slurry consisting of distilled water and silica powder. It was shown that the silanol was neutral in spite of adopting ammonia in silica preparation. In summary, the surface property of the silica was homogenous, apparently due to the same preparation route. $N_2$ adsorption showed that the pore diameter of silica increased gradually and the specific surface area decreased in the sequence from Si(1) to Si(7) (see Table 1). Hence, such silica provided a window to study the influence of silica porosity on structure and performance of $Co/SiO_2$ catalysts.

The metal loading in the catalysts was determined by ICP and the Co loading was about 12%. In XRD pattern, only diffraction peaks assigned to $Co_3O_4$ were observed. By calculating the width of peak of 311 crystal plane and applying Scherrer equations, the size of $Co_3O_4$ in calcined catalyst was calculated. As shown in Table 1, the $Co_3O_4$ size decreased monotonously as the function of pore size. Such a relationship was well stated in impregnated metal catalysts [2,8]. In TPR profiles, there were four element peaks after

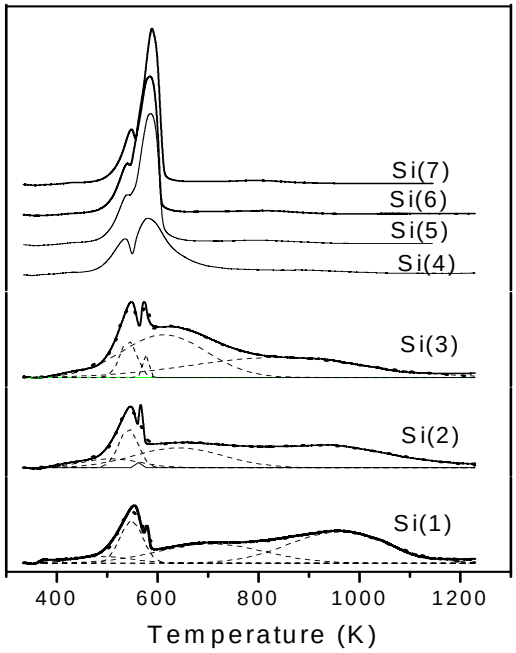


**Figure 1.** The TPR profiles of several $Co/SiO_2$ catalysts

deconvolution. The fixed location of those peaks suggested that there were four Co-containing species in $Co/SiO_2$ catalysts. However, the ratio of the species changed as the silica pore size increased, with the low-temperature peaks (547, 588K) enlarging at expense of high temperature peaks (700, 950K). It was commonly accepted that the

twin peaks at low temperature were stepwise reduction of $Co_3O_4$ [9], the peak at 700K was cobalt oxide interacting with support, and the highest was cobalt silicate or hydrated cobalt silicate [1]. So, a large amount of cobalt silicate was formed in narrow-pore silica supported $Co/SiO_2$ catalysts. Since no diffraction peak of this species was discerned in XRD, it was speculated that the species was highly amorphous. The extent of reduction of the catalysts was determined by the titration of $O_2$ at 673K (see Table1). The reduction degree increased with the increase of pore diameter. All this suggested that the dispersion and reducibility were intervened each other, and both of them could be correlated with the amount of silicate-like species.

**Table 1. The structural and kinetic constants of $Co/SiO_2$ catalysts**

| Cat. | surface area ($m^2g^{-1}$) | Pore diameter (nm) | $Co_3O_4$ size[a] (nm) | Degree of reduction[b] (%) | Reaction 1[c] | | Reaction 2[d] | |
|---|---|---|---|---|---|---|---|---|
| | | | | | Pre-exponential factor | Active energy (kJ/mol) | Pre-exponential factor | Active energy (kJ/mol) |
| Si(1) | 710.5 | 2.2 | 10 | 51 | $1.3\times10^{10}$ | 116.1 | $4.9\times10^{8}$ | 99.8 |
| Si(2) | 649.9 | 2.4 | 11 | 53 | $4.2\times10^{10}$ | 119.8 | $7.8\times10^{13}$ | 147.1 |
| Si(3) | 622.1 | 3.0 | 12 | 61 | $2.9\times10^{7}$ | 89.8 | $1.4\times10^{14}$ | 148.9 |
| Si(4) | 523.8 | 5.1 | 15 | 73 | $1.8\times10^{9}$ | 106.6 | $3.0\times10^{12}$ | 131.2 |
| Si(5) | 366.5 | 8.7 | 16 | 84 | $1.3\times10^{8}$ | 96.4 | $4.9\times10^{13}$ | 143.8 |
| Si(6) | 298.7 | 11.8 | 20 | 87 | $3.4\times10^{8}$ | 101.0 | $5.0\times10^{13}$ | 143.5 |
| Si(7) | 268.2 | 15.1 | 22 | 100 | $3.3\times10^{10}$ | 119.6 | $8.2\times10^{13}$ | 144.8 |

a: measured by line broadening method of XRD
b: measured with $O_2$ titration at 673K
c: $CO+H_2$—$CH_4+H_2O$;
d: $CO+H_2$—$(CH_2)_{8.5}+H_2O$

The $CH_4$ selectivity as well as the CO conversion changed greatly as a function of catalyst structure. However, the reactivity was not taken to correlate with the structure here. Instead, the concept of absolute yield of $CH_4$, which was defined as the amounts of $CH_4$ per unit cobalt per time, was introduced. So was the absolute $C_2^+$ yield. The two values of the catalysts were plotted against the reduction degree. The $CH_4$ yield was insensitive to the reducibility whereas the $C_2^+$ yield responded to reducibility regularly (see Fig.2). This meant that the $CH_4$ formation depended on the total cobalt, no matter if it was reduced. On contrast, the $C_2^+$ products (featured with carbon chain formation) only formed on reduced Co.

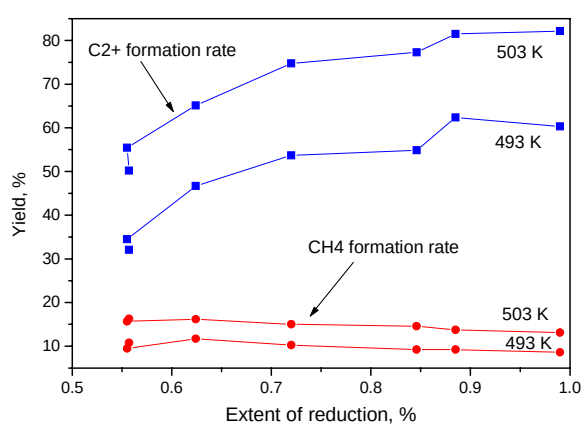


**Figure 2.** The absolute yield of $CH_4$ or $C_2^+$ relating to extent of reduction

In light of the above results, the F-T synthesis over cobalt was modeled as two parallel reactions with the same feedstock. The product of reaction 1 was $CH_4$ and that of 2 was $(CH_2)_{8.5}$, which was the molar average of paraffin expected by ASF rule. If the reactions

$$\ln k_1^{\,0} - \frac{E_1}{RT} = \ln\left\{\frac{F_{V0}\phi}{VRT}\left[-\left(1+\delta_A y_{A\,0}\right)\ln\left(1-x_A\right)-\delta_A y_{A\,0}x_A\right]\right\}$$

**Figure 3.** The kinetic equation of the parallel reaction mechanism. $k_1^{\,0}$: preexpoential factor of reaction 1; $E_1$: activation energy of reaction 1; $\phi$:$CH_4$ sel.; $\delta_A$: contract factor; $x_A$: conversion.

were first order to $H_2$ partial pressure, an equation describing the integrated fixed bed was obtained (see Fig.3). By substituting the experimental data into the equation, the pre-exponential factors and active energies of component reactions were derived (see Table 2). The difference in kinetic constants between two reactions was remarkable and this evidenced the presence of two kinds of active sites.

**Acknowledgment**

This project was supported by the National Nature Science Foundation of China with Grant No. 20303026

**References**

[1] 1. A.Y. Khodakov, A.G. Constant, R.Bechara, V. Zholobenko, J. Catal., **2002,** 206, 230.
[2] E.V.Steen, G.S.Sewell, R.A. Makhothe, et al, J. Catal., **1996 ,**162, 220.
[3] Iglesia, E., Appl. Catal. A., **1997,** 161, 59.
[4] S. W. Ho, H. Marwan, M. H. David, J. Phys. Chem. **1990,** 94, 6396.
[5] R. C. Reuel, C.H. Bartholomew, J. Catal., **1984,** 85, 78.
[6] R.B. Anderson, The Fischer–Tropsch Synthesis, Academic Press, New York, 1984, P78.
[7] Iglesia E., Reyes SS.C., Soled S.L., Reaction transport selectivity models and the design of Fischer-Tropsch catalysts, in: E.R. Becker (Eds), New York, **1993**, P199.
[8] Jacek A. Lapszewicz, Hans J. Loeh and Jan R. Chipperfield, Prepr. Acs. Divi. Pet. Chem. **1993,** 819.
[9] David G. Castner, Philip R. Watson and Ignatius Y. Chan, J. Phys. Chem. **1990,** 94, 819.

# SELECTIVE OXIDATION OF METHANE TO METHANOL OVER $WO_3$/CO-FE-MO-O CATALYSTS

*Xiao-qiang Yang, De-hua He*, Guo-li Dong*

Innovative Catalysis Program, Key Lab of Organic Optoelectronics & Molecular Engineering(Ministry of Education), Department of Chemistry, Tsinghua University, Beijing 100084, China

## Introduction

Methanol is not only a great important chemical raw material, but also a green cleanly fuel. The selective oxidation of methane to oxygenates such as methanol and formaldehyde over oxide catalysts has been of great interesting because it is an alternative route for the conversion of natural gas to high additional value products. Great efforts have been done for developing effective catalyst systems for the selective oxidation of methane to methanol.[1~3]

The reducibility of oxide catalysts and the lattice oxygen in the surface and bulk of oxide catalysts may play important role in the selective oxidation of methane and lower alkanes or olefins.[4~7] Lattice vacancies in oxides are favorable for the mobility of the lattice oxygen. It has been reported that the mobility of the lattice oxygen of $CoMoO_4$ could be greatly improved by the replacement of a part of $Co^{2+}$ by $Fe^{3+}$.[8] This paper reports our recent research results of methane oxidation over $WO_3/Co_{1-n}Fe_nMoO_y$ catalysts.

## Experimental

**Catalyst preparation.** $Co_{1-n}Fe_nMoO_y$ (n=0~0.2) serials supports were prepared by citric acid method.[9] $(NH_4)_6Mo_7O_{24}\cdot 4H_2O$, $Co(NO_3)_2\cdot 6H_2O$, $Fe(NO_3)\cdot 9H_2O$, citric acid and nitric acid were dissolved in the distilled water. The solution was condensed at 80℃ for 4h and then frothed at 110℃ for 8 h. The obtained solids were dried at 110℃ for 12h and calcined at 600℃ for 8h to give the supports. The 10 wt% $WO_3/Co_{1-n}Fe_nMoO_y$ catalysts were prepared by impregnation of the support powers with ammonium tungstate aqueous solution. The catalyst precursors were dried at 110℃ for 8 h and followed the calcination at 600℃ for 8h.

**Catalyst test.** The selective oxidation of methane over the catalysts was carried out in a specially designed high-pressure continuous-flow quartz-lined reactor ( ϕ 7.0mm × 420mm), which was tightly fixed in a stainless steel line. The reaction conditions were 400~460℃, 2.0 MPa, 10/1 ratio of methane/oxygen and 1g catalyst. The effluent passed through a condenser and the liquid products were collected, while the gas phase products were analyzed with an on-line gas chromatograph (TDX-01 Column). The liquid products were analyzed with off-line GC (GDX-403 Column).

**Catalyst characterization.** The crystal phase structures of the prepared samples were identified with XRD by D8 Advanced diffractometer ( Bruker Company ), CuKα ( λ =0.15406nm )，40kV and 20mA.

## Results and Discussion

**Figure 1**. shows the XRD patterns of the samples. The crystalline phases of $CoMoO_4$ and $Fe_2(MoO_4)_3$ were identified as $CoMoO_4$ and $Fe_2(MoO_4)_3$ ( **Fig. 1.** (1) and (5) ). When a part of $Co^{2+}$ in $CoMoO_4$ was replaced by $Fe^{3+}$ ( Fe/Co<1/9 ), the crystalline structures of the supports were same as $CoMoO_4$ and no free Fe oxide phases were observed. When Fe/Co ratio in $Co_{1-n}Fe_nMoO_y$ was 1/9 or 2/8, small amount of free $CoO/MoO_3$ phases were observed besides $CoMoO_4$ phase.(**Fig 1.** (3) and (4) ). When $WO_3$ was loaded on the supports, no $WO_3$ crystalline phase was detected by XRD. It is deduced that amorphous and well-dispersed $WO_3$ formed on the surface of the supports.

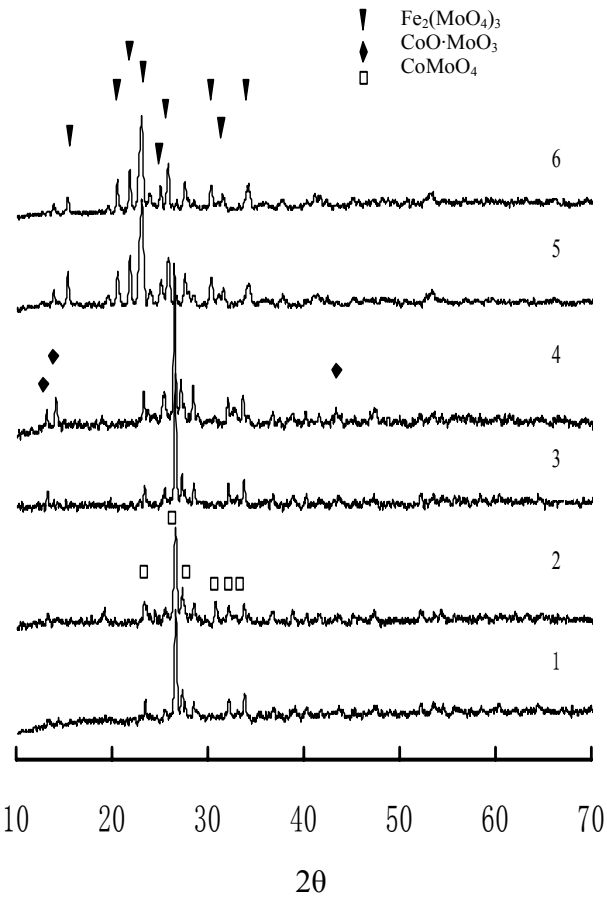


**Figure 1**. XRD patterns of different supports and catalysts. 1: $CoMoO_4$; 2: 10%$WO_3/CoMoO_4$; 3: $Co_{0.9}Fe_{0.1}MoO_x$; 4: 10%$WO_3$/ $Co_{0.9}Fe_{0.1}MoO_x$; 5: $Fe_2(MoO_4)_3$; 6: 10%$WO_3$/ $Fe_2(MoO_4)_3$

**Table 1** shows the catalytic performances of the supports and catalysts in the oxidation of methane. It can be seen from Table 1, when using $Co_{1-n}Fe_nMoO_y$ supports alone, only CO and $CO_2$ with no $CH_3OH$ were detected. In the test of 10% wt $WO_3/Co_{1-n}Fe_nMoO_y$ catalysts, only when Fe/Co ratio was 1/9 or 2/8, a certain amount of methanol as well as trace amount of formaldehyde were detected in the products. $WO_3/CoMoO_4$ and $WO_3/Fe_2(MoO_4)_3$ showed no methanol formation activities under 400~480℃ and 2.0MPa. When Fe/Co ratios were less than 1/9, no methanol was found in the reaction products over $WO_3/Co_{0.97}Fe_{0.03}MoO_y$ and $WO_3/Co_{0.97}Fe_{0.03}MoO_y$ under 400~480℃ and 2.0MPa.

The effect of reaction temperatures on the conversion of methane and oxygen over $WO_3/Co_{0.9}Fe_{0.1}MoO_y$ is shown in **Figure 2**. The oxygen conversion increased sharply to 100% in a narrow temperature range (420~440℃) and the methane conversion reached about 8% at 440℃.

**Figure 3** shows the influence of temperatures on the formation of $CH_3OH$ over $WO_3/Co_{0.9}Fe_{0.1}MoO_y$ and $WO_3/Co_{0.8}Fe_{0.2}MoO_y$ catalysts. The formation of $CH_3OH$ increased with the temperatures from 420℃ to 440℃ and decreased when the temperatures were above 440℃.

**Table1**. **Results of Catalytic Partial Oxidation of $CH_4$**

| Catalyst | T / ℃ | $CH_4$ Conv ./% | Formation Rate /($10^{-4}$mol/g·h) | | |
|---|---|---|---|---|---|
| | | | MeOH | CO | $CO_2$ |
| $CoMoO_4$ | 440 | 2.1 | 0 | 39.9 | 16.3 |
| $Co_{0.9}Fe_{0.1}MoO_y$ | 440 | 8.8 | 0 | 108.4 | 127.2 |
| $Co_{0.8}Fe_{0.2}MoO_y$ | 440 | 8.5 | 0 | 95.6 | 132.0 |
| $WO_3/CoMoO_4$ | 440 | 8.5 | 0 | 120.7 | 107.0 |
| $WO_3/Co_{0.97}Fe_{0.03}MoO_y$ | 440 | 9.0 | 0 | 139.8 | 101.2 |
| $WO_3/Co_{0.93}Fe_{0.07}MoO_y$ | 440 | 8.4 | 0 | 123.8 | 101.2 |
| $WO_3/Co_{0.9}Fe_{0.1}MoO_y$ | 440 | 8.5 | 5.1 | 134.3 | 88.8 |
| $WO_3/Co_{0.8}Fe_{0.2}MoO_y$ | 440 | 8.0 | 4.3 | 113.6 | 96.4 |
| $WO_3/ Fe_2(MoO_4)_3$ | 440 | 8.3 | 0 | 166.7 | 55.6 |

Reaction conditions: $n(CH_4)/n(O_2)$=10:1; SV=6.6 L/(g·h); P=2.0 MPa;

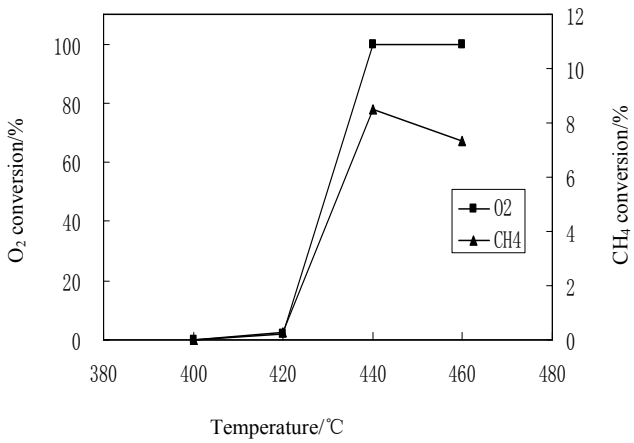


**Figure 2**. $CH_4$ conversion and $O_2$ conversion over the catalyst of 10% $WO_3/Co_{0.9}Fe_{0.1}MoO_y$; Reaction conditions: $n(CH_4)/n(O_2)$=10:1; SV=6.6 L/(g·h); P=2.0 MPa

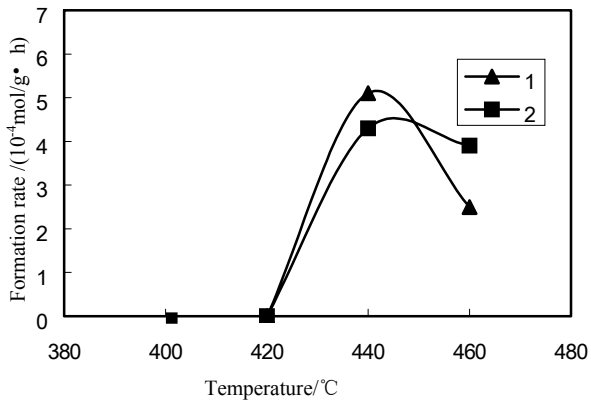


**Figure 3**. Formation rate of $CH_3OH$ over the catalysts. 1: 10% $WO_3/Co_{0.9}Fe_{0.1}MoO_y$; 2: 10% $WO_3/Co_{0.8}Fe_{0.2}MoO_y$; Reaction conditions: $n(CH_4)/n(O_2)$=10:1; SV=6.6 L/(g·h); P=2.0 MPa

## Conclusions

The supports of $Co_{1-n}Fe_nMoO_y$ were not active for the formation of $CH_3OH$ in the oxidation of methane under given conditions. A certain amount of Fe added into $CoMoO_4$ (Fe/Co=1/9 or 2/8) could improve the properties of the catalysts and give the ability for $CH_3OH$ formation in the selective oxidation of $CH_4$ over 10wt%$WO_3/Co_{0.9}Fe_{0.1}MoO_y$ and 10wt%$WO_3/Co_{0.8}Fe_{0.2}MoO_y$.


## Acknowledgement.

We acknowledge the financial support from the National Key Fundamental Research Project Foundation of the Ministry of Science and Technology of China (G199902240-06) and the Research Foundation of Tsinghua University.


## References


1. Graham, JH; et al., Catalysis Today, **1999**, 49: 105
2. Tabata, K.; et al., Catalysis Reviews, **2002**, 44(1): 1
3. Sokolovskii, VD; et al., Catalysis Today, **1998**, 42: 191
4. Banaes, MA; et al., New Frontiers in Catalysis, **1992**, 1131
5. Zanthoff, HW; et al., Chemical Engineering Science, **1999**, 54 (20): 4397
6. Hahm, HS; Park, ES; Cheon, HJ; et al., Journal of Chemical Engineering of Japan, **2004**, 37(2):152
7. Choi, WJ; Park, JY; Kim, MS; et al., Journal of Industrial and Engineering Chemistry, **2001**, 7(4):187
8. Tamaru. K, et al. Dynamic Processes on solid surfaces, Plenum Press: New York, **1993**
9. Zhang X, et al. Chinese Journal of Catalysis, **2003**, 24(4) 305